

ADA 252998

OSAI Society of America

OSAI Society of America

SOFT X RAY

PROTECTION

PROCEEDINGS

Edited by  
Jeffrey Baker

April 10-12, 1991 in Monterey, California

Volume 12

# REPORT DOCUMENTATION PAGE

Form Approved  
OMB No. 0704-0188

Public reporting burden for this collection of information is estimated to average 1 hour per response, including the time for reviewing existing data sources, gathering and maintaining the data needed, and completing and reviewing the collection of information. Send comments regarding this burden estimate or any other aspect of this collection of information, including suggestions for reducing this burden, to Washington Headquarters Services, Directorate for Information Operations and Reports, 1215 Jefferson Davis Highway, Suite 1204, Arlington, VA 22202-4302, and to the Office of Management and Budget, Paperwork Reduction Project (0704-0188), Washington, DC 20503.

|   |  |                                |   |
|---|--|--------------------------------|---|
| 1. AGENCY USE ONLY (Leave blank)  |  | 2. REPORT DATE<br>May 22, 1992 | 3. REPORT TYPE AND DATES COVERED<br>Final 1/1/91-12/31/91 |
| 4. TITLE AND SUBTITLE<br>Organization of the 1991 Optical Society of America Photonic Science Technical Meeting Series Vol 12   |  |                                | 5. FUNDING NUMBERS<br>G - AFOSR-91-0176                   |
| 6. AUTHOR(S)<br>Jarus W. Quinn  |  |                                |   |
| 7. PERFORMING ORGANIZATION NAME(S) AND ADDRESS(ES)<br>Optical Society of America<br>2010 Massachusetts Ave. NW<br>Washington, DC 20036  |  |                                | 8. PERFORMING ORGANIZATION REPORT NUMBER<br>8 05 13       |
| 9. SPONSORING/MONITORING AGENCY NAME(S) AND ADDRESS(ES)<br>US Air Force Office of Scientific Research<br>Department of the Air Force<br>Bolling Air Force Base<br>Washington, DC 20332-6448<br>Schlossberg  |  |                                | 10. SPONSORING/MONITORING AGENCY REPORT NUMBER<br>2305/A1 |
| 11. SUPPLEMENTARY NOTES   |  |                                |   |
| 12a. DISTRIBUTION/AVAILABILITY STATEMENT<br>Approved for public release<br>Distribution unlimited   |  |                                | 12b. DISTRIBUTION CODE                                    |
| 13. ABSTRACT (Maximum 200 words)<br>Attach list of reports supported by Optical Society of America<br>Photorefractive Materials, Effects, and Devices<br>Integrated Photonics Research<br>Nonlinear Guided Wave Phenomena<br>Optical Amplifiers and Their Applications<br>Optical computing<br>Picosecond Electronics and Optoelectronics<br>Quantum Optoelectronics<br>Photonic Switching<br>Microphysics of Surfaces: Beam Induced Processes<br>Soft X-ray Projection Lithography<br>Short Wavelength Coherent Radiation, Generation & Applications<br>Persistent Spectral Hole-Burning: Science & Applications |  |                                |   |
| 14. SUBJECT TERMS<br>92616110   |  |                                | 15. NUMBER OF PAGES<br>92-15681                           |
| 16. PRICE CODE  |  |                                | 17. LIMITATION OF ABSTRACT                                |



## Contents

|                   |    |
|-------------------|----|
| Preface . . . . . | xi |
|-------------------|----|

---

### **X-Ray Projection Systems**

---

|   |    |
|---|----|
| High-Resolution Soft-X-Ray Projection Imaging . . . . .   | 2  |
| <i>O. R. Wood II, J. E. Bjorkholm, J. Bokor, L. Eichner,<br/>R. R. Freeman, T. E. Jewell, W. M. Mansfield, A. A. MacDowell,<br/>L. H. Szeto, D. M. Tennant, W. K. Waskiewicz, D. L. White,<br/>D. L. Windt, and J. H. Bruning</i> |    |
| Soft-X-Ray Projection Lithography System Design . . . . .   | 5  |
| <i>N. M. Ceglio and A. M. Hawryluk</i>  |    |
| Soft-X-Ray Reduction Lithography Using a Reflection Mask . . . . .  | 11 |
| <i>H. Kinoshita, K. Kurihara, T. Mizota, T. Haga, Y. Torii,<br/>H. Takenaka, and Y. Ishii</i>   |    |
| Soft X-ray Projection Optics . . . . .  | 16 |
| <i>David Shafer</i>   |    |
| Throughput Estimate of an X-Ray Projection Lithography System . . . . .   | 18 |
| <i>Masaaki Itou, Tsueno Terasawa, and Shigeo Moriyama</i>   |    |
| Design and Analysis of Multimirror Soft-X-Ray Projection Lithography Systems . . . . .  | 22 |
| <i>David L. Shealy, Cheng Wang, and V. K. Viswanathan</i>   |    |
| Illumination Requirements for Optical Projectors and How to Think about Them . . . . .  | 27 |
| <i>Douglas S. Goodman</i>   |    |

|  |    |
|--|----|
| Development of Reflective Optical Systems for XUV Projection Lithography . . . . .   | 30 |
| <i>V. K. Viswanathan and Brian E. Newnam</i>   |    |
| Specifying Optical Fabrication Tolerances for Soft X-ray Projection Lithography Systems . . . . .  | 34 |
| <i>James E. Harvey</i>   |    |
| Analysis of Thermally Induced Distortion of Optics for Soft-X-Ray Projection Lithography . . . . .   | 37 |
| <i>R. D. Watson and R. H. Stulen</i>   |    |
| Optical Alignment for Lithography . . . . .  | 42 |
| <i>Norman Bobroff and Alan E. Rosenbluth</i>   |    |
| Reflection Mask Technology for Soft-X-Ray Projection Lithography . . . . .   | 45 |
| <i>A. M. Hawryluk, N. M. Ceglio, D. W. Phillion, D. P. Gaines,<br/>R. Browning, R. F. Pease, D. Stewart, and N. Economou</i>   |    |
| Design of an Extended Image Field Soft-X-Ray Projection System . . . . .   | 51 |
| <i>F. Bijkerk, H. -J. Voorma, E. J. Puik, E. Louis, G. E. van Dorssen,<br/>M. J. van der Wiel, J. Verhoeven, E. W. J. M. van der Drift,<br/>J. Romijn, and B. A. C. Rousseeuw</i>  |    |
| Soft-X-Ray Projection Imaging Using a Laser Plasma Source . . . . .  | 54 |
| <i>D. A. Tichenor, G. D. Kubiak, M. E. Malinowski, R. H. Stulen,<br/>S. J. Haney, K. W. Berger, L. A. Brown, R. R. Freeman,<br/>W. M. Mansfield, O. R. Wood II, D. M. Tennant, J. E. Bjorkholm,<br/>T. E. Jewell, D. L. White, D. L. Windt, and W. K. Waskiewicz</i> |    |
| Schwarzschild microscope at $\lambda = 7$ nm . . . . .   | 58 |
| <i>K. A. Tanaka, M. Kado, H. Daido, T. Yamanaka, S. Nakai,<br/>K. Yamashita, and S. Kitamoto</i>   |    |



---

## Soft-X-Ray Sources

---

|   |    |
|---|----|
| Source Issues Relevant to X-Ray Lithography . . . . .   | 62 |
| <i>Khanh Nguyen, David Attwood, and T. K. Gustafson</i>   |    |
| X-Ray Production Efficiency at 130 Å from Laser-Produced Plasmas . . . . .                                    | 68 |
| <i>Robert L. Kauffman and Donald W. Phillion</i>  |    |
| Laser-Produced Plasma Soft-X-Ray Generation . . . . .   | 72 |
| <i>C. Cerjan and M. D. Rosen</i>  |    |
| XUV Conversion Efficiency in a Low-Intensity KrF Laser Plasma for<br>Projection Lithography . . . . .         | 76 |
| <i>Paul D. Rockett, John A. Hunter, Ron Kensek,<br/>Richard E. Olson, Glenn D. Kubiak, and Kurt W. Berger</i> |    |

---

## Multilayer Optics

---

|  |     |
|--|-----|
| Interface Imperfections in Metal/Si X-Ray Multilayer Structures . . . . .  | 82  |
| <i>David L. Windt, R. Hull, and W. K. Waskiewicz</i>   |     |
| Multilayers for Soft-X-Ray Optics . . . . .  | 87  |
| <i>Takeshi Namioka, Masaki Yamamoto, Mihiro Yanagihara, and<br/>Masato Koike</i>   |     |
| Multilayer Uniformity and Performance of Soft-X-Ray Imaging Optics . . . . .   | 92  |
| <i>J. B. Kortright and R. N. Watts</i>   |     |
| Achieving Uniform Multilayer Coatings on Figured Optics . . . . .  | 97  |
| <i>W. K. Waskiewicz, D. L. Windt, J. E. Bjorkholm, L. Eichner,<br/>R. R. Freeman, T. E. Jewell, W. M. Mansfield, A. A. MacDowell,<br/>L. H. Szeto, D. M. Tennant, D. L. White, and O. R. Wood II</i> |     |
| Tungsten/Carbon Multilayers Prepared by Ion-Beam Sputtering . . . . .  | 101 |
| <i>Katsuhiko Murakami, Hiroshi Nakamura, Tetsuya Oshino, and<br/>Hideo Nikaido</i>   |     |

---

## Holography and Phase Effects

---

|   |     |
|---|-----|
| Technique for Projection X-Ray Lithography Using Computer-Generated Holograms . . . . . | 108 |
|---|-----|

*Malcolm R. Howells and Chris Jacobsen*

|   |     |
|---|-----|
| Effect of Amplitude and Phase Dispersion on Images in Multilayer-Coated Soft-X-Ray Projection Systems . . . . . | 113 |
|---|-----|

*Tanya E. Jewell*

---

## Photoresists

---

|                                       |     |
|---------------------------------------|-----|
| Surface-Imaging Lithography . . . . . | 120 |
|---------------------------------------|-----|

*Mark A. Hartney*

|   |     |
|---|-----|
| Resist Characterization at Soft-X-Ray Wavelengths . . . . . | 124 |
|---|-----|

*G. D. Kubiak, E. M. Kneidler, K. W. Berger, R. H. Stulen,  
J. E. Bjorkholm, W. M. Mansfield, and H. Windischmann*

|  |     |
|--|-----|
| Effects of Absorption on Resist Performance in Soft-X-Ray Projection Lithography . . . . . | 129 |
|--|-----|

*W. M. Mansfield, J. E. Bjorkholm, A. A. MacDowell,  
R. R. Freeman, L. H. Szeto, G. N. Taylor, D. M. Tennant,  
W. K. Waskiewicz, D. L. Windt, D. L. White, O. R. Wood II,  
R. M. D'Souza, and A. R. Neureuther*

---

## Metrology and Characterization

---

|   |     |
|---|-----|
| Angstrom-level noncontact profiling of mirrors for soft x-ray lithography . . . . . | 134 |
|---|-----|

*Paul Glenn*

|   |     |
|---|-----|
| Nonspecular Scattering from X-Ray Multilayer Structures . . . . . | 137 |
|---|-----|

*J. B. Kortright*

|   |     |
|---|-----|
| National Institute of Standards and Technology Metrology for Soft-X-Ray Multilayer Optics . . . . . | 142 |
|---|-----|

*R. N. Watts, D. L. Ederer, T. B. Lucatorto, and M. Isaacson*

|   |     |
|---|-----|
| Surface Figure Metrology for X-ray Optics . . . . . | 145 |
| <i>W. Tyler Estler and Chris J. Evans</i>           |     |

---

**Proximity X-Ray Lithography**

---

|  |     |
|--|-----|
| Proximity X-ray Nanolithography . . . . .    | 148 |
| <i>Henry I. Smith and M. L. Schattenburg</i> |     |

|                 |      |
|-----------------|------|
| Index . . . . . | .151 |
|-----------------|------|

## Preface

In the future era of 256-Mb dynamic random access memory (DRAM) chips, as minimum feature dimensions in very large scale integrated circuits shrink to 0.25  $\mu\text{m}$  and below, it is widely understood that the conventional approach to projection optical lithography, using even deep ultraviolet (250-nm wavelength) radiation, will no longer be applicable. This is due to the fundamental diffraction limit, which holds that features cannot be printed with a resolution finer than that of the wavelength of the imaging radiation.

Proximity x-ray lithography has received a great deal of attention as a candidate replacement for conventional optical projection lithography. In this approach, a thin membrane is used as a semi-transparent mask substrate for x rays with a wavelength of 0.8-1.2 nm, and a heavy metal absorber pattern is created on its surface. This mask is brought into close proximity (5-50- $\mu\text{m}$  gap) to a silicon wafer coated with an x-ray sensitive photoresist and then is exposed to the x rays, thus replicating the mask pattern in the photoresist. With this method a faithful 1:1 shadow print can be obtained with resolution finer than 0.25  $\mu\text{m}$ . Synchrotron storage rings as well as laser-produced plasmas are both candidates for the x-ray source. A major issue with this technique is the high cost to produce, inspect, and repair the thin membrane mask, which must have absorber features on it that are as fine as those to be produced on the wafer. Thermal distortion of the thin membrane owing to absorbed x rays is also a concern. By contrast, in today's projection optical lithography systems, a high-performance lens demagnifies a mask pattern, typically by 5 $\times$ , onto the wafer.

A new approach to lithography targeted for the 256-Mb generation and beyond is now being explored. The idea is to attempt to realize an all-reflective, demagnifying, projection optical system suitable for soft-x-ray wavelengths in the 5-50-nm wavelength range. A patterned reflecting mask on a thick, robust, thermally stable substrate is under consideration as a way around the difficulties of the membrane mask. This approach was inspired by the recent advances in the technology of producing and manipulating x rays in this wavelength region. The realization of a practical soft-x-ray projection lithography system will, however, require aggressive development of a number of critical component technologies.

The OSA Topical Meeting on Soft-X-Ray Projection Lithography was organized to bring together researchers working on these diverse issues. The meeting was held April 10-12, 1991, at the Monterey Conference Center in Monterey, California. As these proceedings show, significant progress is being made in all of the important research fronts, but much remains to be done in order to overcome the difficult, yet exciting, challenges that lie ahead.

Jeffrey Bokor  
*AT&T Bell Laboratories*

OSA Proceedings on  
**SOFT-X-RAY PROJECTION  
LITHOGRAPHY**

**Volume 12**

**Edited by  
Jeffrey Bokor**

DTIC QUALITY INSPECTED 2

**Proceedings of the Topical Meeting  
April 10-12, 1991  
Monterey, California**



*Sponsored by  
Optical Society of America*

*Supported by  
Air Force Office of Scientific Research*

Optical Society of America  
2010 Massachusetts Avenue, NW  
Washington, DC 20036  
(202) 223-8130

|                    |  |
|--------------------|--|
| Accession For      |  |
| NTIS GRA&I         | <input checked="checked" type="checkbox"/> |
| DTIC TAB           | <input type="checkbox"/>                   |
| Unannounced        | <input type="checkbox"/>                   |
| Justification      |  |
| By                 |  |
| Distribution/      |  |
| Availability Codes |  |
| Dist               | Avail and/or<br>Special                    |
| A-1                |  |

Articles in this publication may be cited in other publications. In order to facilitate access to the original publication source, the following form for the citation is suggested:

Name of Author(s), Title of Paper, OSA Proceedings on Soft-X-Ray  
Projection Lithography, Jeffrey Bokor, ed. (Optical Society of  
America, Washington, DC 1991), Vol. 12, pp. xx-xx.

ISBN Number 1-55752-187-5

LC Number 90-63176

Copyright © 1991, Optical Society of America

Individual readers of this proceedings and libraries acting for them are permitted to make fair use of the material in it, such as to copy an article for use in teaching or research, without payment of fee, provided that such copies are not sold. Copying for sale is subject to payment of copying fees. The code 1-55752-187-5/91/\$2.00 gives the per-article copying fee for each copy of the article made beyond the free copying permitted under Sections 107 and 108 of the U.S. Copyright Law. The fee should be paid through the Copyright Clearance Center, Inc., 21 Congress Street, Salem, MA 01970.

Permission is granted to quote excerpts from articles in this proceedings in scientific works with the customary acknowledgment of the source, including the author's name, name of the digest, page, year, and name of the Society. Reproduction of figures and tables is likewise permitted in other articles and books provided that the same information is printed with them and notification is given to the Optical Society of America. Republication or systematic or multiple reproduction of any material in this proceedings is permitted only under license from the Optical Society of America; in addition, the Optical Society may require that permission also be obtained from one of the authors. Address inquiries and notices to the Director of Publications, Optical Society of America, 2010 Massachusetts Avenue, NW, Washington, DC 20036. In the case of articles whose authors are employees of the United States Government or its contractors or grantees, the Optical Society of America recognizes the right of the United States Government to retain a nonexclusive, royalty-free license to use the author's copyrighted article for United States Government purposes.

The views and conclusions in this proceedings are those of the author(s) and should not be interpreted as necessarily representing endorsements, either expressed or implied, of the editors or the Optical Society of America.

Printed in the U.S.A.

**OSA Proceedings on**

**SOFT-X-RAY PROJECTION LITHOGRAPHY**

**Volume 12**

---

## **Technical Program Committee**

---

**Jeffrey Bokor, Cochair**

*AT&T Bell Laboratories*

**John Bruning, Cochair**

*GCA Tropel*

**Natale Ceglio**

*Lawrence Livermore National Laboratory*

**James Clemens**

*AT&T Bell Laboratories*

**Daniel Ehrlich**

*MIT Lincoln Laboratories*

**James Forsythe**

*Hampshire Instruments*

**Herbert W. Friedman**

*Lawrence Livermore National Laboratory*

**Hiroo Kinoshita**

*NTT LSI Laboratories, Japan*

**Jeffrey Kortright**

*Lawrence Berkeley Laboratory*

**Mitch Ruda**

*Talandic Corporation*

**William Silfvast**

*CREOL-University of Central Florida*

**Richard Stulen**

*Sandia National Laboratory*

**John Warlaumont**

*IBM*



# **X-Ray Projection Systems**



92-19482



## High-Resolution Soft-X-Ray Projection Imaging

O. R. Wood II, J. E. Bjorkholm, J. Bokor, L. Eichner,  
R. R. Freeman, T. E. Jewell, W. M. Mansfield, A. A. MacDowell,  
L. H. Szeto, D. M. Tennant, W. K. Waskiewicz, D. L. White, and  
D. L. Windt

AT&T Bell Laboratories, Room 4C-434, Holmdel, New Jersey 07733

J. H. Bruning

GCA/Tropel, 60 O'Connor Road, Fairport, New York 14450

### ABSTRACT

Sub-tenth-micron resolution projection imaging has recently been demonstrated in the soft-x-ray spectral region using multi-layer-coated reflective optics.

### INTRODUCTION

The principal motivation for carrying out projection imaging with soft-x-rays instead of with visible or ultraviolet light lies in the dramatic improvement in resolution that can be obtained (while maintaining a usable depth of focus). Although there are many reports of soft-x-ray imaging in the literature [1-6], soft-x-ray imaging with truly high resolution has only recently been demonstrated [7]. In this talk we describe the results of several experiments which have demonstrated projection imaging in the soft-x-ray spectral region with a resolution approaching the Rayleigh limit,  $1.22\lambda/2NA$  where  $\lambda$  is wavelength and  $NA$  is the numerical aperture of the imaging system.

### CHOICE OF ILLUMINATION WAVELENGTH

Projection imaging with short wavelength radiation is not simple because at wavelengths below 100 nm all materials become highly absorbing. Because of this, short wavelength imaging systems must be entirely reflective and because soft-x-rays are strongly absorbed in air the

imaging system must be operated in a vacuum. Furthermore, as shown in Fig. 1, except for a few very narrow wavelength bands where layered synthetic materials (LSM) provide a usable reflectivity, the normal incidence reflectance of all materials falls precipitously at short wavelengths. Finally, if the projected images are to be recorded in a resist film, because of the high resist absorption at short wavelengths (the absorption coefficient of the resist PMMA (poly methyl methacrylate) is approximately  $6.2 \text{ um}^{-1}$  at a wavelength of 14 nm) only thin layers of resist can be used.

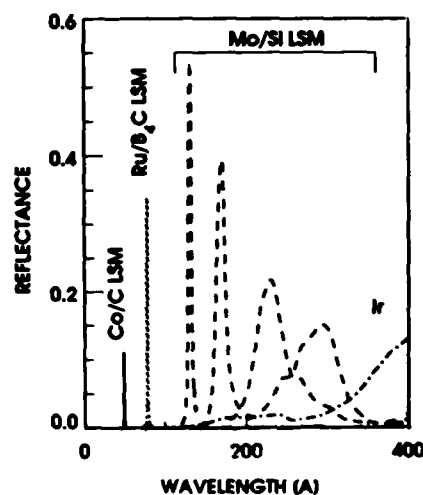


Figure 1. Reflectance of some coating materials for use in the soft-x-ray region.

Hence, the choice of optimum illumination wavelength must strike a balance between the following factors: The resolution increases at shorter wavelengths as indicated by the above formula for the Rayleigh limit. The resist absorption decreases at shorter wavelengths because most resist materials are comprised of large organic molecules that exhibit a more or less monotonically decreasing absorption with decreasing wavelength until the carbon edge at 4.4 nm is reached. The reflectivity is highest for Mo/Si multilayer coatings and can exceed 60% for wavelengths near 13 nm. Hence, at present the choice of illumination wavelength is relatively simple; a practical soft-x-ray imaging system must be illuminated at or near 13 nm. However, if a new efficient LSM were to become available at a shorter wavelength it would have an important impact on imaging in the soft-x-ray region.

#### CHOICE OF IMAGING SYSTEM

In recent experiments we used the third harmonic of an undulator that is installed in the vacuum ultraviolet synchrotron storage ring at the National Synchrotron Light Source to demonstrate projection imaging at wavelengths near 14 nm with 20X reduction over a small image field (roughly 25  $\mu\text{m}$  x 50  $\mu\text{m}$ ) [8]. We used the output from an undulator because it provides a highly collimated beam of narrow bandpass radiation that can be tuned in wavelength to coincide with the peak reflectance of the LSM coated imaging system by adjusting the gap between the magnets. The imaging system was a Schwarzschild optic fabricated by the Tropel Division of GCA Corporation. The mirrors were coated at AT&T Bell Laboratories with 20 layer pairs of a Mo/Si LSM that had a measured reflectance peak of 38% at 13.8 nm and a bandpass of 0.7 nm FWHM. As shown in Fig. 2, the optic was used with off-axis illumination and at a reduced numerical aperture ( $\text{NA} = 0.16$ ) to avoid obscuration by the primary mirror. With this optic a pattern of lines and spaces in the form of a resolution test chart was transferred from a transmission mask consisting of a Ge absorber on a 0.6  $\mu\text{m}$  thick silicon membrane onto a silicon wafer coated with a 60 nm thick layer of

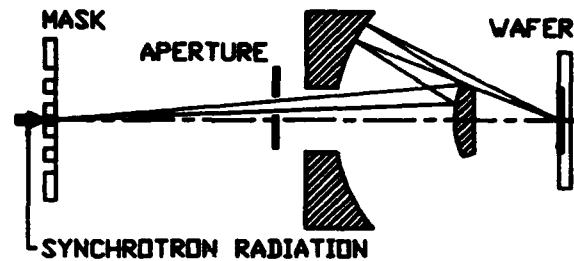


Figure 2. The experimental arrangement used to demonstrate soft-x-ray projection imaging with the Schwarzschild optic.

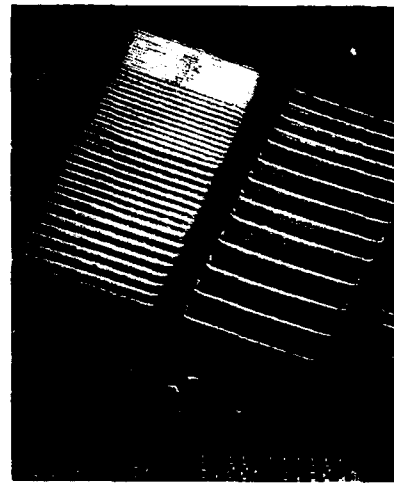


Figure 3. A scanning electron micrograph of developed images in 60 nm thick films of PMMA on Si. The pattern of lines and spaces ranges in size from 0.5  $\mu\text{m}$  to 0.05  $\mu\text{m}$ .

PMMA. As shown in Fig. 3, lines and spaces as small as 0.05  $\mu\text{m}$  were cleanly printed. We have recently been using a reflection mask constructed by patterning a Mo/Si multilayer coated silicon wafer. The multilayer coating was etched entirely away by reactive ion etching exposing the bare silicon substrate everywhere except in the patterned area. The images printed with the reflection mask are comparable to those obtained with the transmission mask. Because the imaging with the Schwarzschild optic was essentially diffraction-limited we have concluded that the spherical mirrors used in our optic must have had extremely good surface figure over the small areas used.

At present we are using the fundamental of the undulator at

wavelengths near 40 nm to demonstrate projection imaging with unity magnification over a larger image field (roughly 2 mm x 0.2 mm) using an Offner ring-field optic [9] fabricated by Perkin-Elmer. The mirrors were coated by Acton Research with a 17 nm thick layer of iridium that has a reflectance of about 10% at 40 nm. This optic, shown in Fig. 4, is used at a numerical aperture ( $NA = 0.135$ ) chosen to provide a balance between maximum cutoff frequency and minimum aberrations [10]. At a wavelength of 42 nm, lines and spaces as small as 0.2  $\mu\text{m}$  have been transferred from an open-stencil transmission mask to a silicon wafer coated with a 60 nm thick layer of PBS (polybutene-1 sulfone). These features are close to the cutoff frequency for coherent illumination of the ring-field optic at this wavelength and numerical aperture. At a wavelength of 46 nm, more complicated patterns with minimum features sizes of 0.35  $\mu\text{m}$  have been transferred from a gold-on-silicon reflection mask to a silicon wafer coated with a 60 nm thick layer of PBS. An example of an image printed using a reflection mask is shown in Fig. 5.

In the future, we intend to use radiation near 13 nm to demonstrate soft-x-ray projection imaging with a resolution of better than 0.1 micron over image fields exceeding 1  $\text{cm}^2$  using a more complex imaging system [11]. Our design studies have indicated that such a system will probably be composed of four mirrors, some of which will have aspheric surfaces. A larger image field means that a larger area of the mask will need to

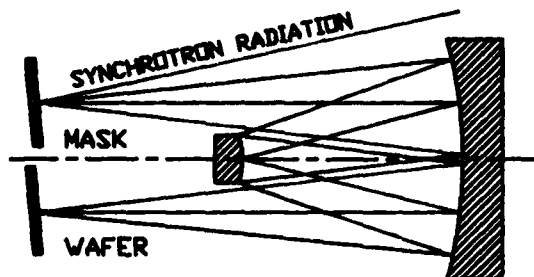


Figure 4. Sketch of the experimental arrangement used to demonstrate soft-x-ray projection imaging with a ring-field optic.



Figure 5. An optical micrograph of developed images in a 60 nm thick film of PBS on Si. The pattern is the gate level of a ring-oscillator circuit.

be illuminated. As a result, it will be necessary to use a soft-x-ray source having a larger beam size and etendue than the undulator beam.

#### REFERENCES

1. A. B. C. Walker, R. B. Hoover, T. W. Barbee, Jr., and J. F. Lindblom, *Science* **241**, 1781-1787 (1988).
2. C. M. Brown, U. Feldman, J. F. Seely, M. C. Richardson, H. Chen, J. H. Underwood, and A. Zigler, *Opt. Comm.* **68**, 190-195 (1988).
3. L. Golub, M. Herant, K. Kalata, I. Lovas, G. Nystrom, F. Pardo, E. Spiller, and J. Wilczynski, *Nature* **344**, 842-844 (1990).
4. J. A. Trail and R. L. Byer, *Opt. Lett.* **14**, 539-541 (1989).
5. H. M. Hertz and R. L. Byer, *Opt. Lett.* **15**, 396-398 (1990).
6. H. Kinoshita, K. Kurihara, Y. Ishii, and Y. Torii, *J. Vac. Sci. Technol. B* **7**, 1648-1651 (1989).
7. D. W. Berreman, et al., *Opt. Lett.* **15**, 529-531 (1990).
8. J. E. Bjorkholm, et al., *J. Vac. Sci. Technol. B* **8**, 1509-1513 (1990).
9. A. Offner, *Optical Engineering* **14**, 130-132 (1975).
10. O. R. Wood, II, W. T. Silfvast and T. E. Jewell, *J. Vac. Sci. Technol. B* **7**, 1613-1615 (1989).
11. T. E. Jewell, J. M. Rodgers and K. P. Thompson, *J. Vac. Sci. Technol. B* **8**, 1519-1523 (1990).

AD-P007 227



## Soft-X-Ray Projection Lithography System Design

N. M. Ceglio and A. M. Hawryluk

Lawrence Livermore National Laboratory, University of California,  
P.O. Box 5508, Livermore, California 94550

### ABSTRACT

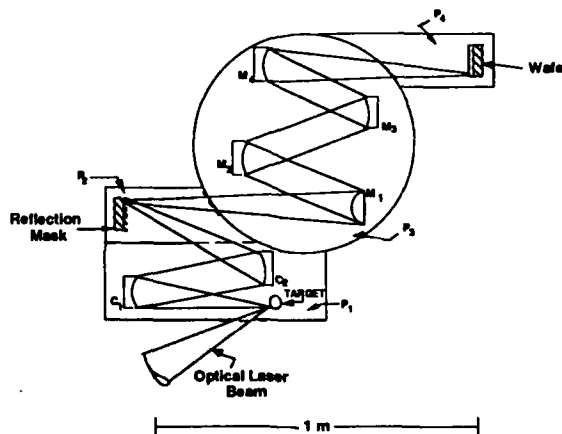
A baseline design for a Soft X-Ray Projection Lithography (SXPL) system is presented. This design is intended to serve as a starting point, and provide an overview of the likely form and structure of a SXPL prototype. Technical performance specifications for system components are presented along with analyses supporting the specification choices.

### Introduction

Since the early papers which first proposed [1,2] and then demonstrated [3] the resolution capability of projection lithography using soft x-rays, there has been a great deal of coordinated activity to define the parameters of such a lithography system [4]. Indeed, there has emerged a fairly broad consensus of what a Soft X-ray Projection Lithography (SXPL) system would look like. However, to date no one has formalized this common view, nor has anyone formally quantified the parameters for such a SXPL system. In this paper we present a baseline or starting point design for a SXPL system, and attempt to specify, as much as is practical at this early stage, the important technical parameters of the system.

Figure 1 provides an artist's sketch of a prototype SXPL tool. Key features of this design concept are the following:

- The working radiation is a narrow band of soft x-rays ( $\Delta\lambda \sim 3\text{\AA}$ ) around  $\lambda_x \sim 130\text{\AA}$ . This choice results from the existence of high performance multilayer optics at  $\sim 130\text{\AA}$  - i.e. wavelengths just longer than the silicon L-edge.
- The x-ray source is a laser produced plasma generated by the interaction of laser light (intensity  $>10^{11}\text{ watt/cm}^2$ ) with a high Z target material. A laser source is proposed because it offers the dual advantages of modularity (i.e., one tool:one laser source) and modest capital investment.
- The x-rays from the target are efficiently collected by a pair of multilayer-coated condenser mirrors ( $C_1, C_2$ ).
- The condenser mirrors project the narrowband radiation onto a mask or master-reticle which works in reflection. Indeed, the mask is a thin, IC metallization pattern atop a multilayer coating, which in turn is supported by a flat, highly polished, massive substrate (e.g., made of bulk silicon).
- The radiation pattern reflected from the mask is imaged by a high precision, 4 mirror imaging system. While there are a number of different designs for the imaging optical system [5], it



$C_1, C_2$ : condenser optics  
 $M_1, M_2, M_3, M_4$ : imaging optics  
 $P_1, P_2, P_3, P_4$ : four different vacuum environments

Figure 1 Design concept for a prototype SXPL system.

generally can be characterized as follows: it is a ring-field imaging system providing for step and scan exposure of the wafer; it's  $f\#$  will be  $f/6$  or smaller, to provide resolution  $\leq 0.1 \mu\text{m}$  at the wafer; it will provide virtually distortion-free imaging over the ring field (distortion  $< 0.01 \mu\text{m}$  at the wafer); one or more of the imaging mirrors will be aspheric; it will be a de-magnifying system with a reduction factor of order 5x; the overall physical dimensions of the optical layout will be of order 1 meter.

- There will likely be four separate vacuum environments:  $P_1, P_4$ : low vacuum because of target debris and resist outgassing;  $P_2, P_3$ : high vacuum to preserve the surface quality of the masks and imaging mirrors.
- There will likely be three vacuum windows separating  $P_1, P_2, P_3, P_4$ . These can be thin Si or a silicon compound such as silicon nitride, allowing for good x-ray transmission at  $\lambda_x \sim 130\text{\AA}$ .
- Narrowband x-rays emerging from the target will undergo seven reflections and three window transmissions before reaching the resist-coated wafer.

### Technological Requirements

Transforming the vision represented by Figure 1 into a practical lithography system is a formidable challenge requiring the solution of a broad range of technical problems [6]. Among the technological requirements that are clearly beyond the current state of the art are the following:

1. Virtually defect-free x-ray reflection masks. No one has yet addressed the problem of depositing high performance, defect-free, x-ray multilayer reflectors over large areas. [7]
2. Precision overlay registration during step-and-scan differential mask and wafer movement. A registration accuracy of order 10 nm will be required.
3. The high resolution imaging system will require precision optical substrates (some aspheres) made from a low expansion material (e.g. Zerodur), having diameter  $\geq 10$  cm, with a total figure error-budget (per mirror)  $< 1$  nm, and a surface roughness  $< 0.2$  nm rms.

In addition to the above technical requirements, the viability of a SXPL technology will demand:

- a.) High reflectivity x-ray multilayer coatings: ( $R$ )
- b.) A practical, high sensitivity resist operating at  $\lambda_x \sim 130 \text{\AA}$ : ( $S$  ( $\text{j}/\text{cm}^2$ ))
- c.) Efficient production of narrowband soft x-rays from the laser produced plasma: ( $\eta$ )

d.) Efficient collection of x-rays by the condenser mirrors: ( $d\Omega$  (sr))

e.) An adequate optical laser driver:  
( $P_L$  (watt) = average power)

f.) Thin vacuum windows having high x-ray transmission at  $\lambda_x = 130\text{\AA}$ : ( $W$ )

Indeed, the exposure-limited throughput  $T(\text{cm}^2/\text{sec})$  of the SXPL system of Figure 1 may be written

$$T = \frac{P_L R^7 W^3 \eta \frac{d\Omega}{\pi}}{S} \quad (1)$$

### System Specifications

In providing even a crude system design, reasonable specifications (or goals) must be chosen for the technical parameters in equation (1). A wide range of choices are possible. Our design specifications are given below:

$$\text{Design Specifications: } \left\{ \begin{array}{l} R = 0.7 \\ W = 0.7 \\ S = 2 \text{ mj}/\text{cm}^2 \\ \eta = .01 \\ T = 2.5 \text{ cm}^2/\text{sec} \end{array} \right\} \quad (2)$$

### Discussion

#### -Mirror Reflectivity-

The strong dependence of throughput on mirror reflectivity ( $T \propto R^7$ ) makes multilayer fabrication a high leverage technology for SXPL. This is illustrated in Figure 2 showing the effect of a variation in mirror reflectivity on wafer cost (all other parameters held constant) [8]. Note that a decrease of mirror reflectivity from 70% to 50% increases wafer cost by an order of magnitude!

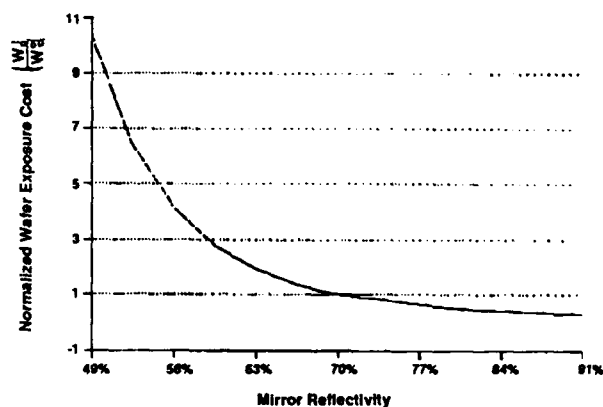


Figure 2 Normalized wafer exposure cost vs. mirror reflectivity for the system in Figure 1. A reduction in mirror reflectivity dramatically increases wafer cost.

The importance of high reflectivity mirrors is further emphasized by the appreciation that poor mirror reflectivity cannot simply be compensated by increased source power. As mirror reflectivity is decreased (and source power increased to maintain throughput, as in equation 1), system throughput will ultimately be limited by thermal distortion in the precision imaging mirrors. Indeed it can be shown, [9], that for the system of Figure 1 the maximum throughput may be written:

$$T_{\max} = \frac{WR^4}{S(1-R)} L_{\max} \quad (3)$$

where  $L_{\max}$  is the maximum allowable power absorbed by the first imaging mirror. Figure 3 shows a plot of  $T_{\max}$  vs.  $R$  using  $L_{\max}$  50 mwatt,  $S = 2$  mj/cm<sup>2</sup>, and  $W = 0.7$ . [10] Figure 3 shows that in order to maintain the throughput design goal of 2.5 cm<sup>2</sup>/sec, mirror reflectivity must be greater than ~ 52%, independent of the source power available.

The choice of  $R = 70\%$  in the design specifications is based upon the recent achievement of 64% normal incidence reflectivity for Mo/Si mirrors, [11] and the expectation of continued rapid progress in multilayer mirror development. There are a number of metal/Si multilayer systems for which the calculated ideal reflectivity is greater than 70%. [12] These are being actively investigated in the laboratory.

#### -X-ray Conversion Efficiency-

Laser-plasma simulations using the 2-D Lasnex hydrodynamics code have been carried out to investigate the experimental parameters (i.e. laser wavelength, pulse duration, intensity on target, target material) that serve to optimize the x-ray conversion ( $\eta$ ) from optical laser light into narrowband ( $\Delta\lambda \sim 3\text{\AA}$ ) soft x-rays around  $\lambda_x \sim 130\text{\AA}$ . Preliminary results [13] indicate that the operational parameter space is fairly

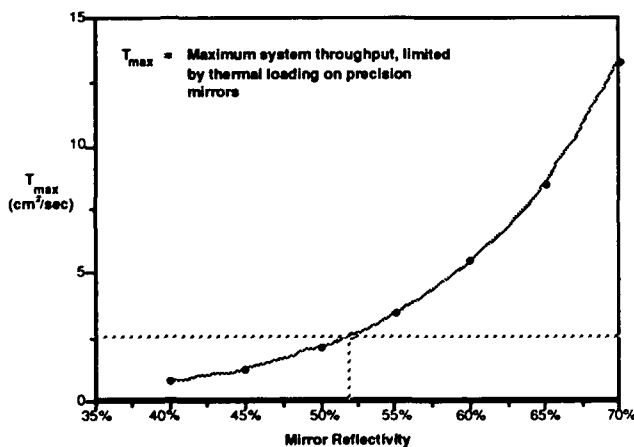


Figure 3 In order to achieve the design goal of  $T = 2.5$  cm<sup>2</sup>/sec, mirror reflectivity greater than 52% is required—independent of available source power.

broad, centering on the values/choices listed in Table I, and that the  $\eta = 1\%$  design specification (equation 2) is not unreasonable. Although  $\eta = 1\%$  has not yet been demonstrated in the laboratory, recent experimental results [14] appear to confirm the parameter space conclusions drawn from the simulations.

#### -Resist Sensitivity-

Anticipation of a high resolution, high sensitivity ( $S \sim 2$  mj/cm<sup>2</sup>) resist for use at  $\lambda_x = 130\text{\AA}$  is based primarily on scaling arguments applied to existing commercial x-ray resists. While there is appreciable resist data for x-rays at 13Å, [15] there is not a large body of experimental data for resist performance at 130Å. However, because x-ray resists have a volumetric dose threshold, the sensitivity should scale as

$$S_{130\text{\AA}} = S_{13\text{\AA}} \left( \frac{\ell_{130\text{\AA}}}{\ell_{13\text{\AA}}} \right) \quad (4)$$

where  $\ell_\lambda$  is the absorption depth in the resist for x-rays at wavelength  $\lambda$ , and  $S_\lambda$  is the resist sensitivity (mj/cm<sup>2</sup>) at  $\lambda$ . For polymer-based resists:

$$\begin{aligned} \ell_{13\text{\AA}} &\sim 1.7 \mu\text{m} \\ \ell_{130\text{\AA}} &\sim 0.2 \mu\text{m} \end{aligned}$$

So that,

$$S_{130\text{\AA}} = \frac{S_{13\text{\AA}}}{8.5}$$

The sensitivity of x-ray resists at 130Å should be roughly an order of magnitude 'better' than at 13Å, although single step resist processing may be sacrificed in achieving higher sensitivity. So then, high resolution x-ray resists with sensitivities in the 10-20 mj/cm<sup>2</sup> range at 13Å may be expected to meet our design specifications at 130Å.

#### -Throughput-

The wafer exposure rate of 2.5 cm<sup>2</sup>/sec corresponds to sixty, 6" wafer-level exposures/hour, a rate similar to current production levels. While it is difficult to project future production rates for an advanced lithographic technology, it is unlikely that industry will readily accept a decline in throughput.

The specification for window transmission = 70% presumes a 0.25  $\mu\text{m}$  silicon window operating at  $\lambda_x = 130\text{\AA}$ .

#### -Laser System-

A key component of the SXPL system is the x-ray source and associated radiation collection and transport optics—commonly referred to as the "front end" (See Figure 1). Design and specification of the front end can

| Table I                    |   |                |                                      |  |
|----------------------------|---|----------------|--------------------------------------|--|
| Material                   | Wavelength                              | Pulse Duration | Intensity on Target                  | Conversion Efficiency ( $\Delta\lambda \sim 3\text{\AA}$ ) |
| High Z<br>(eg. Ta, Au, Pb) | (0.5 $\mu\text{m}$ or 1 $\mu\text{m}$ ) | $\sim 5$ nsec  | $4 \times 10^{11}$ w/cm <sup>2</sup> | $\eta \sim 1.7\%$  |

Table I: Results from laser plasma simulations define a region of optimal x-ray conversion efficiency.

be a complex affair in that it requires integrating state-of-the-art technologies in x-ray optics, high power lasers, and laser-plasma physics. A more detailed discussion of these trade-offs and associated analyses are presented in Appendix I. Our "front-end" specifications are listed in Table II:

As indicated earlier, these design specifications are intended to serve as a reasonable starting point for further discussion. As the engineering constraints on practical laser, condenser, and target illumination systems become clearer, different trade-off choices between system parameters may appear more reasonable.

Our choices were driven by an attempt to: stay close (within a factor of 2) to the guidelines of Table I, keep the laser peak power well below a gigawatt, and keep the repetition rate below a khertz. We chose a challenging (but reasonable) goal for the condenser collection solid angle ( $d\Omega = 0.2$  sr), and the choice of Critical versus Köhler illumination is by no means central to our design concept. Critical illumination allows for a more direct calculation of exposure areas and perhaps a simpler scan strategy, but Köhler illumination could provide additional flexibility in the system design. The fact of the matter is that there is not yet a complete condenser system design for SXPL!

The "exposure logistics" choices indicate that the etendu of the front end ( $dA d\Omega = \text{x-ray source area} \times \text{condensor solid angle}$ ) will be smaller than that for the imaging optics ring field. This is necessary to keep the laser intensity on target sufficiently high for efficient x-ray production. Note also that at only 2 laser shots per exposure field our design does not allow for much statistical averaging of shot-to-shot variations in laser performance. This was again necessary to keep the laser intensity on target sufficiently high. Details of these trade-offs are provided in Appendix I.

#### Summary

A baseline design for a SXPL system is provided. The design concept is presented in Figure 1. Quantitative design specifications are provided in Equation (2), Table I, and Table II. These specifications (requirements) are beyond the current state-of-the-art.

#### Acknowledgments

The authors wish to recognize the technical contributions of their co-workers: D.P. Gaines, D.G. Stearns, R.L. Kauffman, C. Cerjan, E.M. Campbell, and W. Sooy. This work would not have been possible without the support of E. Storm and J.I. Davis of the LLNL Laser Program. \*This work was performed under the auspices of the U.S. Department of Energy by Lawrence Livermore National Laboratory under contract No. W-7405-Eng-48.

Table II

| Laser System<br>( $\lambda = 1\mu\text{m}$ ) |              |                                   |                 |                 |
|--|--------------|-----------------------------------|-----------------|-----------------|
| Average Power                                | Peak Power   | Pulse Duration                    | Energy/Pulse    | Repetition Rate |
| 280 watt                                     | 280 megawatt | 2.5 nsec                          | 0.7 joule       | 400 hertz       |
| Condenser System                             |              |                                   |                 |                 |
| $d\Omega = 0.2\text{sr}$                     |              | Critical Illumination             |                 |                 |
| Target Physics                               |              |                                   |                 |                 |
| Intensity on Target                          |              | Target Area                       | Target Material |                 |
| $2 \times 10^{11} \text{ watt/cm}^2$         |              | $1.4 \times 10^{-3} \text{ cm}^2$ | High Z          |                 |
| Exposure Logistics                           |              |                                   |                 |                 |
| Exposure Field at Wafer                      |              | Exposure Statistics               |                 |                 |
| $1.25 \times 10^{-2} \text{ cm}^2$           |              | 2 laser shots/exposure field      |                 |                 |

Table II: Front end design specifications for a SXPL system.



## References and Notes

- 1) A.M. Hawryluk and L.G. Seppala, "Soft X-ray projection lithography using an x-ray reduction camera", *J. Vacuum Science Technology* **6**, 2162 (1988).
- 2) K. Hoh and H. Tanino, "Feasibility study on extreme UV/soft x-ray projection-type lithography", *Bull Electrotech. Lab. (Japan)* **49**, 47 (1985)
- 3) D.W. Berreman, et. al., "Soft X-ray projection lithography printing of 0.2 mm features using 20:1 reduction", *Optics Letters* **15**, 529 (1990)
- 4) N.M. Ceglio, editor, "Proceedings of the first technical symposium on soft x-ray projection lithography", Lawrence Livermore National Laboratory; Document #CONF-9001104 (Jan, 1990)
- 5) M. Suzuki, et. al. "X-ray reduction projection exposure system of reflection type", *European Patent Application # 873060370* (Filed July 8, 1987).
- 6) N.M. Ceglio, et.al., "Soft x-ray projection lithography", *J. Vacuum Science Technology* **B8**, 1325 (1990)
- 7) In this context we define a defect to be a 0.5  $\mu\text{m}$  (or larger) region with significantly reduced reflectivity in the multilayer coating. The total mask coating area of interest will be of order 225  $\text{cm}^2$  (i.e. 15 cm x 15 cm at the mask—using 5x reduction)
- 8) N. M. Ceglio and A. M. Hawryluk, "Normalized wafer cost analysis for soft x-ray projection lithography", *J. Vacuum Science Technology* (to be published Nov/December 1991).
- 9) A.M. Hawryluk and N. M. Ceglio, "Power loading limitations in soft x-ray projection lithography", *J. X-ray Science and Technology* (to be published, 1991).
- 10) The guidance for  $L_{\text{max}} \sim 50$  mwatt derives from a 2-D thermal analysis of the surface distortion in a Zerodur optic having a Diameter/Thickness aspect ratio of 4:1, and a total allowable thermal distortion of  $\sim 2\text{\AA}$  (See Reference [9]).
- 11) D. G. Stearns, et. al., "High Performance multilayer X-ray optics", this conference
- 12) D. G. Stearns, private communication.
- 13) C. Cerjan and M. Rosen, "Simulation of soft x-ray production by laser irradiation", this conference
- 14) R. L. Kauffman and D. W. Phillion, "X-ray production efficiency at 130  $\text{\AA}$  from laser produced plasmas", this conference
- 15) M. Schattenburg, et.al., "Fabrication and testing of 0.1  $\mu\text{m}$  linewidth micro-gap x-ray masks", *J. Vacuum Science Technology* **B8**, 1604 (Nov/Dec-1990)

## Appendix I

In the design of the "front-end" illumination system we presume (for simplicity) that a critical illumination condenser geometry is used. If a target area  $dA_T$  (per laser shot) is illuminated by the laser, then the area exposed (per laser shot) at the wafer will be  $dA_w$ , and

$$dA_T = \frac{d\Omega_I dA_w}{d\Omega_c} \quad (\text{A1})$$

where  $d\Omega_c$  is the collection solid angle of the condenser optics and  $d\Omega_I$  is the collection solid angle of the imaging optics (at the wafer). For an  $f/6$  system,

$$\begin{aligned} d\Omega_I &= \frac{\pi}{4} \left( \frac{1}{f\#} \right)^2 \\ &= 2.18 \times 10^{-2} \text{ sr.} \end{aligned} \quad (\text{A2})$$

For the purpose of design simplicity we presume the exposure area geometry at the wafer may be represented as a rectangle (eg. ring field): 2.5 cm x y (cm), where y now becomes a design parameter of the illumination system. So then:

$$dA_T = 5.45 \times 10^{-2} \left( \frac{y}{d\Omega_c} \right) \quad (\text{A3})$$

where  $dA_T$  is in  $\text{cm}^2$ ; y is in cm;  $d\Omega_c$  is in sr.

Since the exposed field size at the wafer is 2.5 y  $\text{cm}^2$ , and the specified exposure rate is  $T = 2.5 \text{ cm}^2/\text{sec}$ , then the required number of exposed fields/sec at the wafer will be  $(1/y)$  fields/sec. A field need not necessarily be exposed by a single laser shot. If we require Q laser shots to expose a single field, then the required laser repetition rate, R, will be:

$$R = Q/y \quad (\text{A4})$$

where R is the laser repetition rate in hertz, y is in cm., and Q is an integer greater than or equal to 1.

We note from equation (1) in the text that the average laser power,  $P_L$ , depends only on  $d\Omega_c$ , since all the other parameters are specified. So using the specification from equations (2) we get:

$$P_L = \frac{55.6}{d\Omega_c} \quad (\text{A5})$$

where  $P_L$  is in watts, and  $d\Omega$  is in sr.

Knowing the average laser power,  $P_L$ , and the repetition rate, R, we can calculate the required energy/pulse,  $\epsilon = \frac{P_L}{R}$ . So that

$$\epsilon = 55.6 \left( \frac{y}{Q d\Omega_c} \right) \quad (\text{A6})$$

Where  $\epsilon$  is in joules,  $y$  is in cm.,  $d\Omega_c$  is in sr, and  $Q \geq 1$  (integer).

Determination of the peak laser power,  $P_{pk}$ , requires a choice of the laser pulse duration,  $\tau$ . The peak power will be

$$P_{pk} = 5.56 \times 10^{10} \left( \frac{y}{Q \tau d\Omega_c} \right) \quad (A7)$$

where  $P_{pk}$  is the peak laser power in watts,  $y$  is in cm,  $\tau$  is the laser pulse duration in nsec,  $d\Omega_c$  is in sr, and  $Q \geq 1$  (integer).

Similarly we can get the laser intensity on target from (A7) and (A3):

$$I = \frac{10^{12}}{Q \tau} \quad (A8)$$

where  $I$  is the laser intensity on target in watt/cm<sup>2</sup>,  $\tau$  is in nsec, and  $Q \geq 1$  (integer).

In this design study the key equations are (A3), (A4), (A5), (A6), (A7) and (A8). The (free) design parameters are  $Q$ ,  $\tau$ ,  $d\Omega_c$ , and  $y$ . In achieving the design specifications outlined in Table II of the text the design parameter choices are:

$$\begin{aligned} d\Omega_c &= 0.2 \text{ sr} \\ Q &= 2 \text{ pulses/field} \\ \tau &= 2.5 \text{ nsec} \\ y &= 5 \times 10^{-3} \text{ cm.} \end{aligned}$$

Other design choices are clearly possible.



## Soft-X-Ray Reduction Lithography Using a Reflection Mask

J-P007 228



H. Kinoshita, K. Kurihara, T. Mizota, T. Haga, and Y. Torii  
*NTT LSI Laboratories, 3-1 Morinosato Wakamiya, Atsugi-shi,  
 Kanagawa 243-01, Japan*

H. Takenaka and Y. Ishii  
*NTT Applied Electronics Laboratories, 3-9-11 Midoricho, Musashino-shi,  
 Tokyo 180, Japan*

A soft-x-ray reduction lithography using a multilayer reflection mask has been developed. To obtain a high throughput and a large exposure area, a reduction system consisting of two-mirror optics and a reflection mask with a scanning mechanism is adopted as a first generation system. A full 4-inch wafer reflection mask with a high contrast and an uniform quality throughout has been fabricated using a new process. Mo/B<sub>4</sub>C multilayer is used to shorten the exposure wavelength and to refine interfaces of multilayer and to obtain a fine pattern. And fine patterns less than 0.2  $\mu\text{m}$  at a demagnification of 1/8 have been obtained with a reflection mask and Mo/B<sub>4</sub>C multilayer optics in the area of 0.8 mm x 0.15 mm.

### 1. INTRODUCTION

Advances in multilayer fabrication technology have enabled applications(1-5) that employ normal-incidence optics. Among the more important ones is soft x-ray reduction lithography using multilayer mirrors. At NTT, work on this began some time ago, and by 1986(6), 4  $\mu\text{m}$  demagnified patterns had been fabricated using a schwartzchild type objective and a Si stencil mask. By 1989(7), 0.5  $\mu\text{m}$  patterns had been made using a reflection mask. And in 1990(8), AT&T announced the replication of 0.05  $\mu\text{m}$  patterns. These results are sufficient to demonstrate the feasibility of creating a soft x-ray projection lithography system.

Such system has the following advantages; 1) a magnifying mask can be used; 2) the mask is rigid and can be cooled since a transmission mask is no longer necessary; and 3) ultra fine patterns of less than 0.05  $\mu\text{m}$  can be replicated. Furthermore, this seems to be the

only type of system which holds any promise of being able to mass produce 0.1- $\mu\text{m}$  pattern.

This paper concerns the problems involved in using a multilayer to form an image and the fabrication of a reflection mask. It also presents some results on the replication of patterns with a reflection mask.

### 2. SYSTEM DESIGN

In order to use such a system for the actual fabrication of ULSI's serious problems regarding the size of the exposure field and the throughput must be solved. There are two ways to widen the exposure field. One is design the demagnifying optics to have a large field( > 10mm x 10 mm). This requires several aspherical mirrors to eliminate the various types of aberration. The other way is to use a ring field ( > 10 mm X 0.2 mm) without any aberration and a scanning mechanism to synchronize the movements of the wafer and the mask.

During the past few years, a great deal of works has been done on optics design (7),(9-12). The most common approach is to use full-field optics with 3 or 4 aspherical mirrors. However, as the number of mirrors increases, the throughput goes down, there are serious problems with mirror alignment, and the difficulty of matching the wavelength with the Bragg reflection peak lowers the efficiency.

On the other hand, using a scanning mechanism, two mirrors optics(7) can be used since the area in which aberration must be eliminated is restricted to a thin stripe. The problem here is that the scanning mechanism must be extremely accurate. At NTT, our first-generation system utilizes this approach.

In either case, further work on the fabrication of a suitable multilayer with a very high reflectivity is

needed to obtain an adequate throughput.

Another consideration is designing the x-ray projection system so as to optimize the exposure wavelength. Our group has previously reported(7) that wavelengths in the range of 45 to 130 Å are most suitable for x-ray projection lithography. But as yet, no multilayer with a high enough reflectivity of over 10 % for normal incidence at a wavelength of around 50 Å has been developed. The reason is that, as the layer become thinner, it is increasingly difficult to control the thickness of the layers and to obtain a continuous layer.

So, our system uses a wavelength of 130 Å, at which the higher reflectivity of over 50 % is obtained. However, assuming that the exposure depth is only determined on x-ray absorption coefficient, the exposure depth penetrated at the wavelength of 100 Å shows two times as large as that of 130 Å. And that of 70 Å become to be four times as large as that of 130 Å. Therefore, in order to obtain a fine pattern with a high aspect ratio, it is important to shorten the exposure wavelength. If in the near future a multilayer with the characteristics mentioned above is developed, it will be possible to achieve a much higher resolution and a higher aspect ratio without changing the numerical aperture of the demagnifying optics.

### 3. EXPERIMENT

#### 3.1 DESIGN OF THE DEMAGNIFYING OPTICS

Fig.1 shows the configuration of the experimental setup used to evaluate the characteristics of the demagnifying optics. The system consist of an SR source, a carbon filter to cut out long wavelength over about 400 Å, a reflection mask, ring slit, 2 spherical mirrors for the demagnifying optics, and a wafer. And the movements of the mask table and wafer table are synchronized to widen the exposure field.

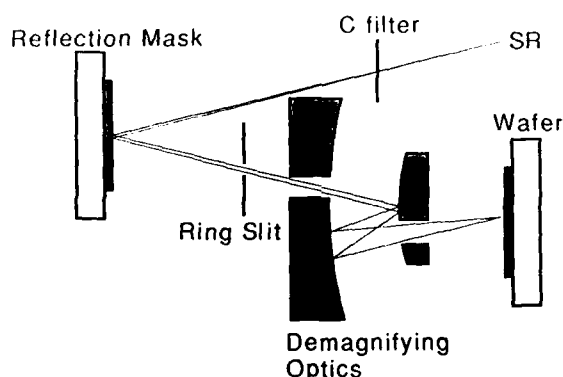


Figure 1 Schematic illustration of the experimental setup to evaluate the image forming characteristics.

The incident angle of the SR beam is critical, which means that the beam must be aligned very precisely with the mask. So, all these components are mounted on a rotating stage. The incident angle for both the mask and wafer is about 3 degrees, which keeps the shift of the image to less than 0.05 μm for a defocusing of 1 μm. The image field is about 0.8 mm x 0.15 mm in size, and the demagnification is 1/8. The optics designed for a wavelength of 100 Å. The numerical aperture size is 0.1. Fig.2 shows the calculated modulation transfer function of the demagnifying optics for incoherent illumination. For 100 Å radiation, the MTF is 40% at 5000 cycle/mm.

The mirrors are made of Mo/B<sub>4</sub>C multilayer deposited by a magnetron sputtering on spherical substrate with an rms surface roughness of 1.2 Å.

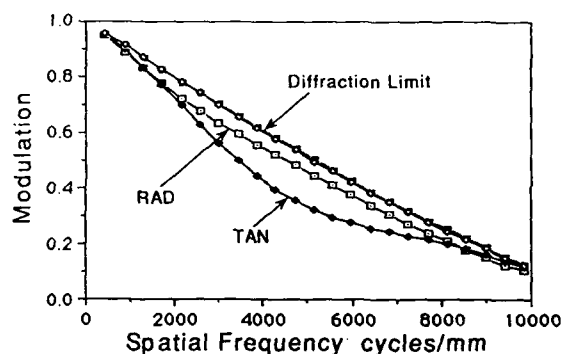


Figure 2 Calculated MTF curves for the two-mirror objective with spatially incoherent illumination at 100 Å.

#### 3.2 FABRICATION OF THE REFLECTION MASK

The reflection mask is the key component of the system. It requires a high contrast, a high reflectivity, a broad bandwidth, and homogeneous reflectivity across a full 4-inch wafer. The process for fabricating such a mask is illustrating in Fig.3.

First, a multilayer is deposited on a Si or SiC base plate with a super-smooth surface. Next, resists are coated onto the multilayer. Then, the patterns to be magnified are delineated with photo or EB lithography and developed. After that, the patterns are transferred to the multilayer by dry etching; and finally, the resists are removed. The advantages of this process, are that the surface of the multilayer is not roughened by the etching process, and the width of the patterns doesn't change when they are transferred to the multilayer.

Fig.4 shows photograph of a reflection mask. The original patterns have a minimum feature size of 2 μm. Sulfur hexafluoride gas as an etchant for Mo/B<sub>4</sub>C

multilayer is used. It is applicable to a full 4-inch wafer and has uniform quality throughout.

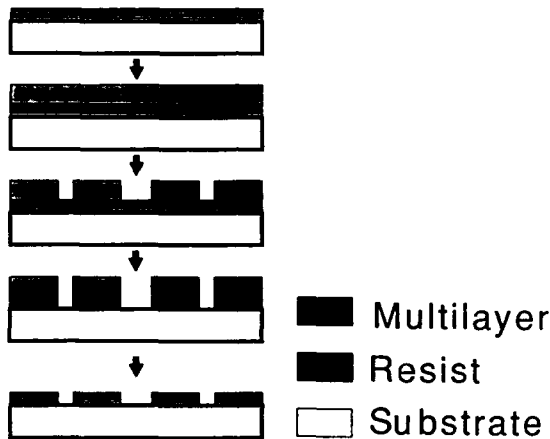


Figure 3 A procedure of a multilayer reflection mask fabrication.

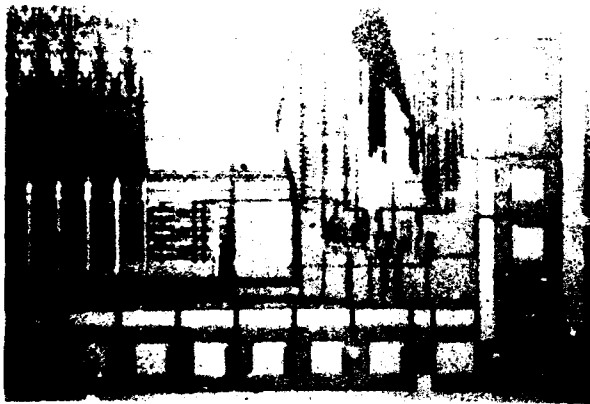


Figure 4 A photograph of a reflection mask pattern.

### 3.3 FABRICATION OF THE MULTILAYER

Multilayer mirrors with a reflectivity of over 50 % at wavelengths greater than 124 Å have been developed. However, cross-sectional TEM images reveal that the interfaces of Mo/Si multilayers are not well-defined because of a composite layer that results from the mixing of the two elements. In addition, as many researchers(13-14) have pointed out, the Mo partially crystallizes into grains that can be as large as the thickness of the Mo layer itself. There doesn't seem to be any correlation between this and the reflectivity of the multilayer; but it does seem to cause some degradation of the quality of the image.

Of the various approaches(15) to solving this

problem, one of the most promising is the use of amorphous Mo, and B<sub>4</sub>C instead of Si. The reason for using B<sub>4</sub>C are; 1) it has a high heat resistance; 2) it enables the use of shorter wavelength; 3) it is easier to obtain a smooth surface and sharp interfaces because of weak chemical reaction. Each of these points is discussed below. Generally, a multilayer is used in an environment where the X-rays are intense enough to degrade its performance. So, a high heat resistance is required. B<sub>4</sub>C has a high melting point, and is very hard and stable. And the heat extension coefficient of B<sub>4</sub>C is almost the same as that of Mo.

Fig.5 shows how the reflectivity of Mo/Si and Mo/B<sub>4</sub>C multilayer changed during a heat cycle test. For the Si spacer, the reflectivity measured by x-ray diffractometer decreased in proportion to the annealing temperature. At the 600 °C, the reflectivity goes down to 9 % but for B<sub>4</sub>C, the reflectivity of over 50 % is obtained, it is found not to have any particular damage as compared with Si.

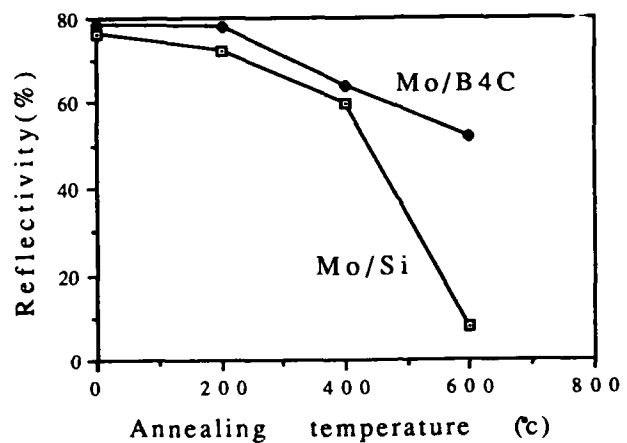


Figure 5 Reflectivity change of the Mo/Si and Mo/B<sub>4</sub>C multilayer with thermal annealing temperature after one hour annealing.

From the standpoint of the resist characteristics, it's desirable to use a wavelength below 130 Å. But since the L absorption edge of Si lies at 123 Å, the reflectivity of Mo/Si multilayer decreases significantly at wavelengths shorter than this. The calculated reflectivity of Mo/Si and Mo/B<sub>4</sub>C multilayers ( $\theta = 5^\circ$ ,  $N = 30$ ) is plotted in Fig.6 for wavelengths between about 70 and 150 Å. At a wavelength of around 100 Å, the peak reflectivity for Mo/B<sub>4</sub>C is 45 %, while for Mo/Si is only 13 %. This shows one of the big advantages of using a B<sub>4</sub>C spacer.

In Fig.7 the cross-sectional TEM photographs of Mo/B<sub>4</sub>C and Mo/Si multilayers are shown. It is found that the interfaces of the Mo/B<sub>4</sub>C multilayer are very sharp and well-defined, and there is no interdiffusion at all.

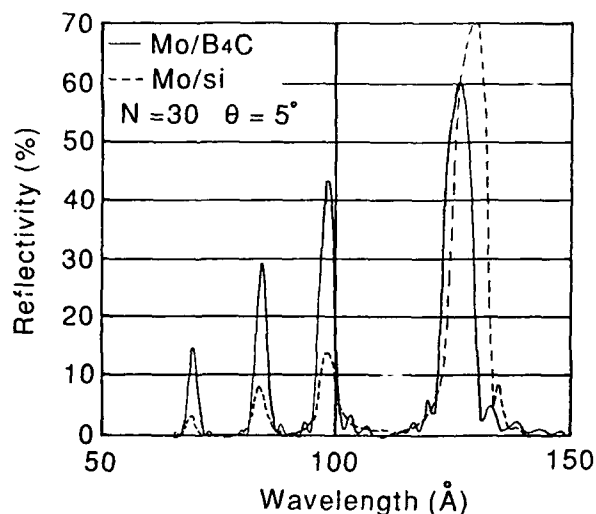


Figure 6 Calculated reflectivity of Mo/Si and Mo/B<sub>4</sub>C.

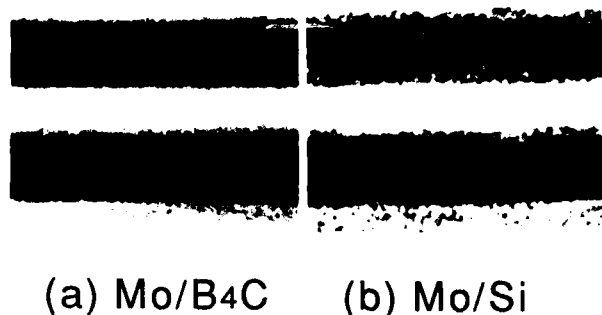


Figure 7 Cross-section TEM photographs of Mo/Si and Mo/B<sub>4</sub>C multilayer.

#### 4. RESULTS AND DISCUSSION

The whole image of a ring field for a line-and-space pattern is shown Fig.8. The exposure area was 0.8mm x 0.15mm and the magnification was 1/8. The optics are made of Mo/B<sub>4</sub>C multilayer which has a measured peak reflectivity of 30 % at the wavelength of 130 Å. For an underdose, the pattern becomes patchy because of irregularities in the reflected radiation. At the proper dose, however, the patchiness disappears and very fine patterns can be obtained.

The pattern in Fig.9 was replicated in a tri-layer resist system consisting of the chemical amplified resist SAL, amorphous Si, and the AZ resist (OFPR). The thickness of the layer were 0.05 μm, 0.01 μm, and 0.45 μm, respectively. Fig.9(a) shows the line and space pattern of 0.25 μm. And (b) shows the isolated line of 0.15 μm. The irregularity in the pattern seem to be caused by the edge of the reflection mask.

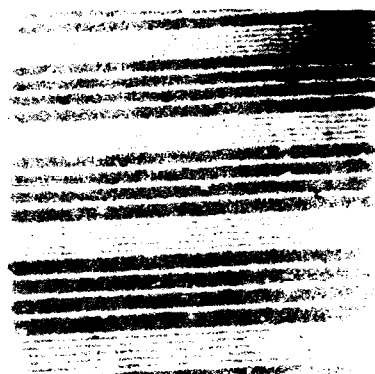


Figure 8 A whole image of a ring stripe field.

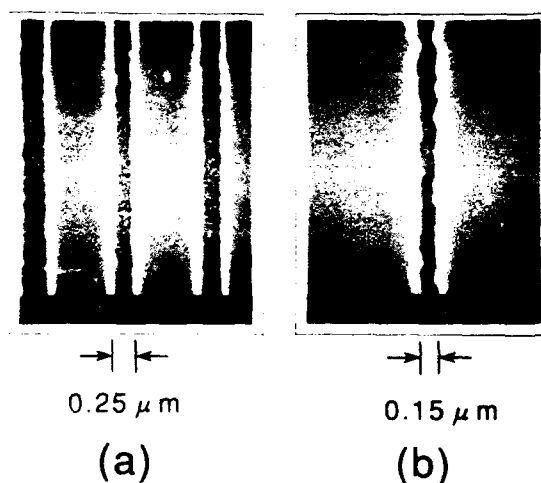


Figure 9 SEM photographs of results obtained using the tri-layer resist: (a) 0.25 μm lines and spaces patterns, (b) 0.15 μm isolated pattern.

#### 5. CONCLUSION

A new soft X-ray reduction lithography system using 2 mirrors and a reflection mask has been developed, and demagnified patterns of less than 0.2 μm have been replicated experimentally in an area of 0.8 mm x 0.15 mm. The key element of the optics and the mask is a Mo/B<sub>4</sub>C multilayer, which has very sharp interfaces. It produced no observable degradation of the image, and the properties are well-suited to this type of lithography.

## ACKNOWLEDGMENT

The authors would like to thank E.Arai for many helpful discussions, and K.Honma and T.Yabe for skillful experimental work.

## REFERENCE

- 1) I. Lobas, W. Stanty, E. Spillar, R. Tibbetts and J. Wilczynski, SPIE 316, 90 (1981)
- 2) J. H. Underwood, T. W. Barbee, D. L. Shealy, SPIE 316, 79 (1981)
- 3) B. Lai and F. Cerrina, SPIE 563, 174 (1985)
- 4) K. A. Tanaka, M. Kado, r. Kodama, M. Ohtani, S. Kimoto, T. Yamanaka, K. Yamashita, and S. Nakai, SPIE Vol. 1140, 502 (1989)
- 5) A. M. Hawryluk and L. G. Seppala, J. Vac. Sci. Technol. B6, 2162 (1988)
- 6) H. Kinoshita, T. Kaneko, H. Takei, N. Takeuchi, and S. Ishihara, In Conf. of Appl. Phys., (28p-zf-15, Jpn. Soc. Appl. Phys. 1986)
- 7) H. Kinoshita, K. Kurihara, Y. Ishii and Y. Torii J. Vac. Sci. Technol. B3, 1581 (1989)
- 8) D. W. Berreman, J. E. Bjorkholm, M. Becker, L. Eichner, R. R. Freeman, T. E. Jewell, W. M. Mansfield, A. A. Macdowell, M. L. O'Malley, E. L. Raab, W. T. silftvast, L. H. Szeto, D. M. Tennant, W. K. Waskieewicz, D. L. White, D. L. windt, and O. R. Wood, Appl. Phys. Lett. 56(22), 28 May (1990)
- 9) T. E. Jewell, J. M. Rodgers, and K. P. Thompson, J. Vac. Sci. Technol. B8(6), 1519 (1990)
- 10) D. L. Shealy, R. B. Hoover, T. W. Barbee, Jr., Arthur B. C. Walker, Jr., Optical Eng., Vol. 29(7) 721 (1990)
- 11) D. L. Shealy, V. K. Viswanathan, Proc., SPIE, July (1990).
- 12) N. M. Ceglio, A. M. Hawryluk, D. G. Stearns, D. P. Gaines R. S. Posen, and S. P. Vernon J. Vac. Sci. Technol. B8(6), 1990
- 13) A. K. Petford Long, M. B. Stearns, C. H. Chang, S. R. Nutt, D. G. Stearns, N. M. Ceglio, and A. M. Hawryluk, J. Appl. Phys. 61(4) 1422 (1987)
- 14) K. Holloway, K. B. Do, and R. Sinclair, J. Appl. Phys. 65(2), 474 (1989)
- 15) H. Takenaka, Y. Ishii, H. kinoshita, and K. Kurihara, Proc., SPIE, July (1990)

Soft X-ray projection optics

David Shafer

David Shafer Optical Design

56 Drake Lane. Fairfield, Ct. 06430

#203-259-4929

AD-P007 229  


**92-19485**



Summary

There is a surprising variety of interesting optical designs for possible use in soft X-ray lithography. The requirements for the projection system are more difficult than those for the beam handling and mask illuminator optics, and it is only the projection optics that will be discussed here.

Only normal incidence types of designs, using multi-layer coatings to get acceptable reflectance, will be treated in any depth. There are other, grazing incidence, designs that will be briefly reviewed but these are not yet mature designs. The normal incidence designs have such reflection losses that it is necessary to minimize the number of surfaces, to 3 or 4. It is assumed that a reflective mask will be used. This places additional constraints on the design. Finally, the use of aspheric surfaces, if any, would ideally result in very small deformations from a sphere - to ease fabrication and test to the required extremely tight x-

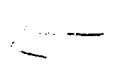


ray tolerances.

Despite the heavily constrained nature of the design problem, and the use of only a few design variables - due to the small number of surfaces allowed - there are many different and useful designs possible. These have quite different geometrical configurations. Finding these separate solution regions is quite difficult, and there is no guarantee that all have been discovered.

What has been found is that to meet .1 micron feature sizes at 130 Angstroms and have the necessary distortion correction drives the designs to the use of several aspherics. The design problem is easiest if a ring-field scanning system is chosen instead of a full-field stepper type. The latter is possible with fairly large chip sizes, but leads to mirror diameters well beyond present x-ray multilayer coating capabilities.

It is interesting that some relaxation in the required feature size allows the use of much more attractive designs. It is very myopic to have the attitude that only .1 micron features are worth doing, and that a .2 micron features machine is a piece of junk. The latter can be done with just spherical surfaces. If it comes to that, what is so shabby about a soft x-ray design, with no aspherics, that does .5 micron features at 4X or 5X magnification, with a huge depth of focus compared to the very small depth of focus of current .5 micron features deep u.v. designs?





## Throughput Estimate of an X-Ray Projection Lithography System

Masaaki Itou, Tsueno Terasawa, and Shigeo Moriyama

Central Research Laboratory, Hitachi, Ltd., Kokubunji, Tokyo 185, Japan

# 92-19486



### Abstract

The feasibility of X-ray projection lithography is discussed with emphasis on throughput issues. A lithography system using 13nm radiation from a compact storage ring was designed. This system consists of a grazing incidence condenser mirror, a multilayer reflection mask, an imaging system with four multilayer mirrors, and an X-ray window. Calculations show that the X-ray power incident onto a wafer is 0.5mW. A highly sensitive resist is required to achieve practical wafer throughput.

imaging, which reduces the stringent requirement on mask pattern accuracy.

From a practical point of view, throughput is one of the most crucial issues in lithography. Hawryluk predicted the exposure time for an XRPL system using 4.5nm radiation from a laser-produced plasma source[1]. However, at a wavelength  $< \sim 10\text{nm}$ , the reflectivity of existing multilayer mirrors is significantly lower than that of deal ones.

We have designed a lithography system to investigate the feasibility of XRPL in terms of throughput. A wavelength of 13nm was chosen, at which multilayer mirrors provide a high reflectivity. Our system uses synchrotron radiation (SR) as an X-ray source. Because SR is emitted within a small angle vertically, a highly efficient illumination system can be designed using a grazing incidence mirror. This paper presents the system design and estimate of the X-ray power incident onto a wafer.

### Introduction

Advances in multilayer-coated reflective optics have aroused great interest in X-ray projection lithography (XRPL) [1-4]. In particular, recent experiments using a Schwartzchild objective have demonstrated a near diffraction-limited resolution  $< 0.1\mu\text{m}$  at 14nm wavelength, although the field of view is limited[5-6]. To print  $\sim 0.1\mu\text{m}$  features over a large field, several imaging systems have been proposed[7]. The primary advantage of XRPL over X-ray proximity printing is reduction

### Lithography system

The design goal for our imaging system is to print  $0.1\mu\text{m}$  features with  $1\mu\text{m}$  depth of focus. The

required field size is  $>10\text{mm}$ . In addition, the imaging system should be distortion free and telecentric at the image plane.

Figure 1 shows a  $5\times$  reduction imaging system with a numerical aperture of 0.08. This system is rotationally symmetric around an optical axis. An X-ray beam strikes a reflection mask at  $60\text{mm}$  from the optical axis. A mask pattern is then imaged onto a wafer with three elliptical mirrors:  $M_1$ ,  $M_2$ , and  $M_3$ . An additional plane mirror,  $M_4$ , deflects the X-ray beam to prevent the wafer obscuring the optical path. All five reflection surfaces, including the mask, are coated with Mo/Si multilayers.

Ray-tracing calculations were carried out to evaluate the imaging performance. Figure 2 shows point spread functions for three off-axis objects. At each point, FWHM is  $\sim 0.1\mu\text{m}$ , showing a near diffraction-limited resolution over a ring field whose radius is  $12\text{mm}$  and width is  $0.8\text{mm}$ .

The imaging system is integrated into a scanning lithography system, as shown in Fig.3. A condenser mirror focuses the X-ray beam from a source point into an entrance pupil of the imaging system. A vertical acceptance of  $3\text{mrad}$  is sufficient to illuminate the width of the ring field. To ensure uniform illumination, horizontal acceptance is limited to  $40\text{mrad}$ , leading to a field length of  $14\text{mm}$ . The mask and the wafer are synchronously translated to expose a whole area. An X-ray window separates an ultra high vacuum system, in which all the optical elements are installed, from a coarse vacuum system, where the resist-coated wafer is placed. In addition, the X-ray window absorbs the longer wavelength radiation which would otherwise cause a reduction in resolution.

#### X-ray power estimate

To estimate the X-ray power

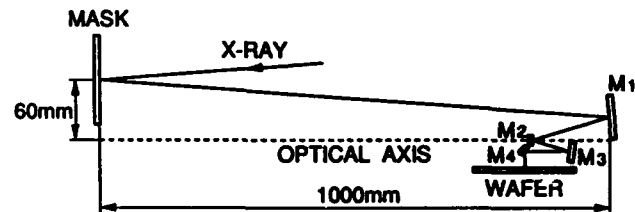
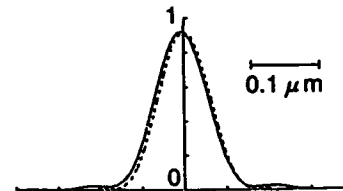
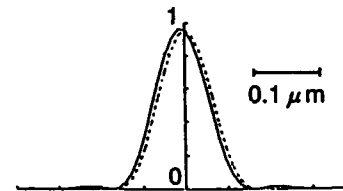


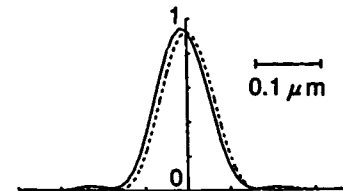
Figure1. Arrangement of imaging system.



(a) OBJECT HEIGHT :  $62\text{mm}$



(b) OBJECT HEIGHT :  $60\text{mm}$



(c) OBJECT HEIGHT :  $58\text{mm}$

Figure2. Point spread functions at three off-axis objects.

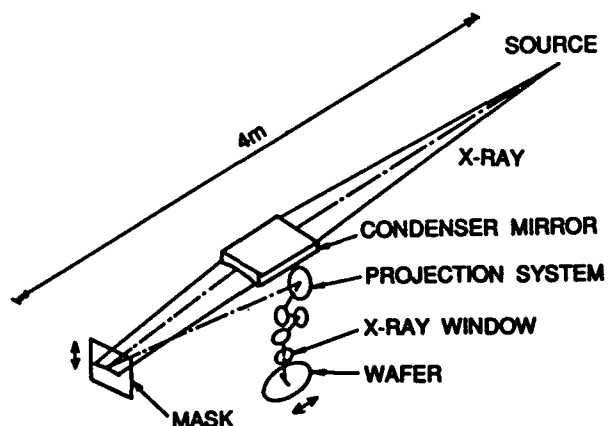


Figure3. Schematic layout of lithography system.

incident onto a wafer, we have calculated the storage ring output and transmission loss throughout the system.

The characteristics of SR primarily depends on the electron energy  $E$  and the magnetic field strength  $B$ . To optimize for the X-ray power at 13nm wavelength, we chose  $E=0.35\text{GeV}$  and  $B=1.2\text{T}$ . These parameters give a bending radius of 1m, so that the storage ring is compact. The intensity distribution of SR is horizontally uniform, while vertically the radiation has a Gaussian-like profile, as shown in Fig.4. As noted above, the acceptance of our system is  $3\text{mrad} \times 40\text{mrad}$ . The condenser mirror collects more than 90% of the total power emitted vertically. Assuming an electron beam current of 500mA, the storage ring output amounts to 16mW in 1% bandwidth.

The X-ray beam strikes the condenser mirror at an incidence angle of  $4^\circ$ . A gold surface gives a reflectivity of 87%. The X-ray throughput of the imaging system is obtained by multiplying reflectivity of each multilayer mirror. We discuss the case where the X-ray beam strikes five Mo/Si multilayer mirrors at an incidence angle of  $5^\circ$ . The period of the multilayer mirror is 6.74nm and the number of layer pairs is 60. As shown in Fig.5, calculated peak reflectivity and bandwidth of the multilayer mirror are 52% and 2.9%, respectively. An X-ray throughput of 3.6% and a bandwidth of 1.6% are predicted for the imaging system. An element with low absorption coefficient is suitable for the X-ray window material. Using a carbon foil with  $0.1\mu\text{m}$  thickness, a transmittance of 61% is obtained.

The X-ray power incident onto a wafer  $W$  is given by

$$W = PR\epsilon T \Delta\lambda / \lambda,$$

where  $P$  is the storage ring output,  $R$  is the reflectivity of the condenser mirror,  $\epsilon$  and  $\Delta\lambda/\lambda$  are

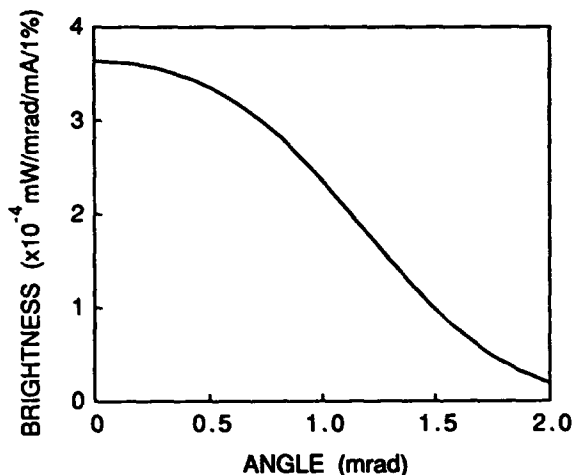


Figure4. Intensity distribution of synchrotron radiation.

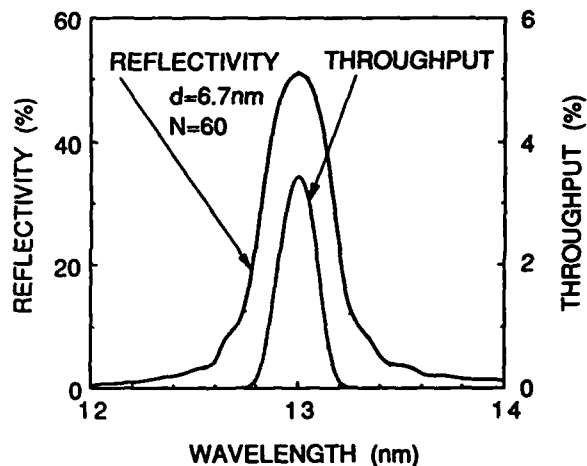


Figure5. Reflectivity of Mo/Si multilayer mirror and X-ray throughput of the imaging system.

the X-ray throughput and the bandwidth of the imaging system,  $T$  is the transmittance of the X-ray window. Substituting the values described above gives  $W=0.5\text{mW}$ . It should be noted that the X-ray power is 2-3 orders of magnitude lower than that achieved with X-ray proximity printing. The exposure time  $t$  is given by

$$t = S/W,$$

where  $S$  is resist sensitivity. Figure 6 shows the exposure time and wafer throughput as a function

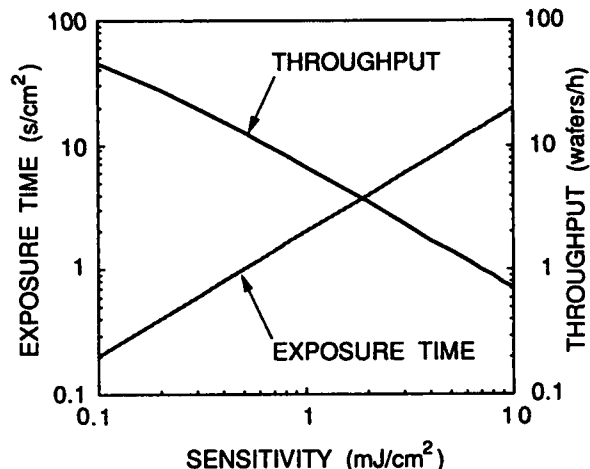


Figure 6. Exposure time and wafer throughput vs. resist sensitivity.

of resist sensitivity. The calculation assumes an exposure field of  $250\text{cm}^2$  and overhead time (alignment and loading) of 30s for an 8" wafer. A resist with  $\sim 0.3\text{mJ}/\text{cm}^2$  sensitivity is required to achieve a reasonable wafer throughput ( $\sim 20$  wafers/h). In contrast, the sensitivity of existing resists is probably  $10\text{--}100\text{mJ}/\text{cm}^2$ .

### Conclusions

We have designed an XRPL system using 13nm radiation from a compact storage ring with five multilayer reflection surfaces. Although this system can achieve  $0.1\mu\text{m}$  resolution

over a large field, the X-ray power incident onto a wafer is very small. Development of a highly sensitive resist is vital to put XRPL into a production tool.

### References

1. A. M. Hawryluk and L. G. Seppala, "Soft x-ray projection lithography using an x-ray reduction camera," *J. Vac. Sci. Technol.* **B6**, 2162(1988).
2. H. Kinoshita, K. Kurihara, Y. Ishii, and Y. Torii, "Soft x-ray reduction lithography using multilayer mirrors," *J. Vac. Sci. Technol.* **B7**, 1648(1989).
3. A. M. Hawryluk, N. M. Ceglio, and D. P. Gaines, "Reflection mask technology for x-ray projection lithography," *J. Vac. Sci. Technol.* **B7**, 1702(1989).
4. N. M. Ceglio, et al., "Soft x-ray projection lithography," *J. Vac. Sci. Technol.* **B8**, 1325(1990).
5. T. E. Jewell, et al., "20:1 Projection soft X-ray lithography using tri-level resist," *Proc. SPIE* **1263** 90(1990).
6. J. E. Bjorkholm, et al., "Reduction imaging at 14nm using multilayer-coated optics: Printing of features smaller than  $0.1\mu\text{m}$ ," *J. Vac. Sci. Technol.* **B8**, 1509(1990).
7. T. E. Jewell, J. M. Rodgers, and K. P. Thompson, "Reflective systems design study for soft x-ray projection lithography," *J. Vac. Sci. Technol.* **B8**, 1513(1990).



## Design and Analysis of Multimirror Soft-X-Ray Projection Lithography Systems

David L. Shealy and Cheng Wang

*Department of Physics, University of Alabama at Birmingham,  
Birmingham, Alabama 35294*

V. K. Viswanathan

*Los Alamos National Laboratory, Los Alamos, New Mexico 87545*

### Abstract

A differential equation method has been developed for the design of soft x-ray projection lithography systems. This method yields numerical values for the sag and slope of two surfaces within a multi-mirror projection system such that the Abbe Sine condition and the constant optical path length condition are satisfied. Application of this design method to three- and four-mirror systems is in progress. Results are compared to optical performance of similar systems designed by conventional methods.

### Introduction

With the evolution of the computer industry, a trend has been to increase the density of devices on chips. Ever smaller geometries will be needed. Chip manufacturers are evaluating lithography processes which will yield a high throughput of chips with small features at a low cost. During recent years, soft x-ray projection lithography has become a very promising process to use in fabrication of high performance microelectronic devices.

Since soft x-ray projection lithography was proposed [1-4], many efforts have been made to obtain projection systems capable of achieving sub-micron or subtenths-micron resolution over a large field of view with very low distortion. There has been a number of reports [4-6] where a two-mirror inverted Schwarzschild microscope, coated with appropriate multilayers [7,8], has been used in soft x-ray projection lithography experiments. Resolutions as small as 50 nm have been reported [9]. A projection optical design survey [10] has indicated that due to its inherent limitations, the two-mirror Schwarzschild type optics can only have a field of view less than 1 mm with resolution of 0.1 microns.

Four-mirror projection optical systems appear to be promising to yield large field systems with 0.1 microns

resolution. Using conventional design techniques, some four-mirror systems [10,11] have been reported to have resolutions less than 0.1 microns over at least 10 mm x 10 mm field of view. Although the four-mirror projection systems display better optical performance than the two-mirror Schwarzschild projection systems, the complexity in the layout, system alignment, and tolerances of four-mirror systems must be considered in practical applications.

Canon Inc. of Japan has disclosed a number of three-mirror projection systems for lithography applications [12]. These systems were reported to yield 0.25 micron resolution over a large field of view. Also, several telescope designs with three aspheric mirrors have been modified for lithography applications, including the three-mirror long (TML) system [13], three-mirror compact (TMC) system [14], and the inverse Baker system [15]. The TML system has a usable flat field of 6.6 mm x 15.2 mm with a diffraction limited performance at 0.08 NA (resolution is 0.1 microns).

Due to low mirror reflectivities, it is desirable to have a minimum number of reflections. Thus, it would be desirable to develop a three-mirror projection system with a simple design comparable to two-mirror systems, but achieve the large field, high resolution performance of four-mirror projection systems.

Based on Korsch's method [16] to design and optimize three-mirror telescopes for high resolution, the authors have developed a differential equation design method (DEDM) to optimize three-mirror projection systems for x-ray lithography applications. The following sections will give the basic conditions for DEDM. Then, DEDM will be applied to optimization of example of three-mirror projection designs. Optical performance will be compared to that of systems designed by conventional methods.

### Differential Equation Design Method

Aplanatism is the basic condition for DEDM. It is known that only two surfaces are needed to obtain

aplanatism. In a three-mirror system, a pair of joining mirrors can be used to achieve the aplanatism, and the third mirror will be used to minimize other residual aberrations.

The basic configuration of a three-mirror projection system is shown in Fig.1.

Here

$$d_0 = \overline{OO_1}, d_1 = \overline{O_1O_2}, d_2 = \overline{O_2O_3}, d_3 = \overline{O_3O_4}.$$

Aplanatism requires the system to satisfy the constant optical path length condition and the Abbe Sine condition. The constant optical path length condition for this system requires

$$s_0 + s_1 + s_2 + s_3 = c, \text{ a const.} \quad (1)$$

with

$$c = d_0 + d_1 + d_2 + d_3.$$

The Abbe Sine condition for this system is given by

$$\sin \alpha = M \sin \beta \quad (2)$$

where  $M$  is the magnification of the system.

In this configuration, all three mirrors have a common optical axis. They are all rotationally symmetric about the optical axis. So we can suppose the equations for the three surfaces have the following forms

$$z_1 = f_1(r_1), z_2 = f_2(r_2), z_3 = f_3(r_3).$$

In this system design, the secondary and the tertiary mirrors are used to give the aplanatism. One assumes that the equation of the first surface is known and has the following form

$$z_1 = f_1(r_1, A_1, A_2, \dots, A_n) \quad (3)$$

where  $A_1, A_2, \dots, A_n$  are the parameters we choose to define the shape of the first surface. These parameters may include conic constant, radius of curvature, and aspherical coefficients.

From Fig.1, we can trace a ray passing through the whole system. Using the law of reflection at each mirror surface, imposing the constant optical path length condition Eq.(1) and the Abbe Sine condition Eq.(2), we can set up the differential equations for the secondary and tertiary mirrors in the following forms:

$$z'_2 = z'_2(r_1, r_2, z_1, z_2, z'_1, c, M), \quad (4)$$

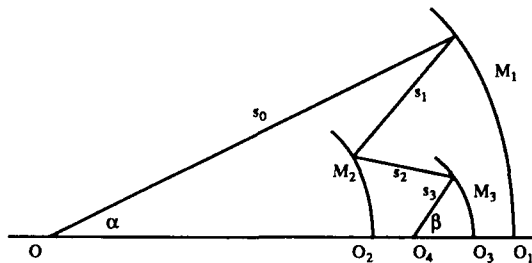


Figure 1. Basic configuration of a three-mirror projection system.

$$z'_3 = z'_3(r_1, r_3, z_1, z_3, z'_1, c, M). \quad (5)$$

Before solving these differential equations, one needs to find relations between parameters of the first mirror and the secondary and the tertiary mirrors. More details of this approach will appear [17].

The differential equations, Eqs.(4) and (5), for the secondary and tertiary mirrors normally cannot be solved analytically. Numerical methods, such as the Runge-Kutta method, have been used. Then, we can obtain numerical surface data for this three-mirror system. The surface data table of each mirror contains the radial coordinates, the sags, and the first order derivatives at those coordinates. This surface data will be used later for ray tracing and system analysis.

### Canon Three-mirror Systems

In 1987, Canon Inc. filed an European patent application [12] for the design of a three-mirror exposure system for use in x-ray projection lithography. The basic layout of this kind of system is shown in Fig.2 :

This reduction projection imaging system consists of a concave mirror  $M_1$ , a convex mirror  $M_2$  and a concave mirror  $M_3$ . This projection system is essentially a coaxial image system, and only half of each concave mirror  $M_1$  and  $M_3$  is used. The convex mirror  $M_2$  is given a function of an aperture stop.

In order to correct the system aberrations, the vertex radii of curvature of the three mirrors are determined so as to maintain a small Petzval sum, while the distances between each element are determined so that the distortion is corrected. The coma, astigmatism and spherical aberration are corrected by using non-spherical surfaces.

Canon reported two different versions of this type of system. In the first version, the concave mirrors  $M_1$  and  $M_3$  are substantially equi-distant from the convex mirror  $M_2$ . This system, like Canon Example 1-8, was reported to be able to achieve resolution of 0.35 microns over 28 mm x 14 mm image field size. In another version, the concave mirror  $M_3$  is spaced apart by approximately one half of the distance between the concave mirror  $M_1$  and the convex mirror  $M_2$ . This system, like Example 1-11, was reported to obtain resolution of 0.35 microns over 28 mm x 14 mm image field of view with lower distortion than Example 1-8.

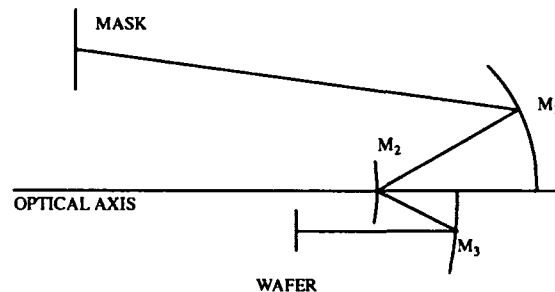


Figure 2. Basic Scheme of Canon three-mirror system

### Design and Optimization

Given configuration parameters of a system, such as, distances between elements, the parameters defining the shape of the first mirrors, e.g. radius of curvature and conic constant, the differential equation design method (DEDM) can generate appropriate surface data for the system configuration. After ray tracing and optical performance analysis using MTF and rms wavefront aberration values, we can determine if the system design at this stage has reached the desired performance. If not, we go back to the starting point, and change some system parameters, and then repeat DEDM. We continue this iteration procedure until specific requirements of the system have been achieved.

We have applied DEDM to some Canon three-mirror projection lithography systems. Using the original configuration parameters of those systems, we varied the parameters of the first mirror and obtained surface data for the optimized system. The systems are described in terms of numerical data. Multiple cubic spline fitting methods were used to fit the numerical data. Then, a ray trace and optical analysis were carried out on the systems described by multiple cubic spline functions.

Figure 3 shows the rms blur radius versus the numerical aperture, N.A., for Canon Example 1-11. Figure 3 indicates that the differential equation design method produces a system with improved optical performance.

Initially, the parameters of the first mirror were not varied, but the secondary and tertiary mirrors were adjusted following the solutions of the differential equations. This led to the results represented by the dotted curve. Then, we changed the value of the conic constant of the first mirror and followed the optimization procedure as mentioned above to minimize the residual aberration such as astigmatism. The results

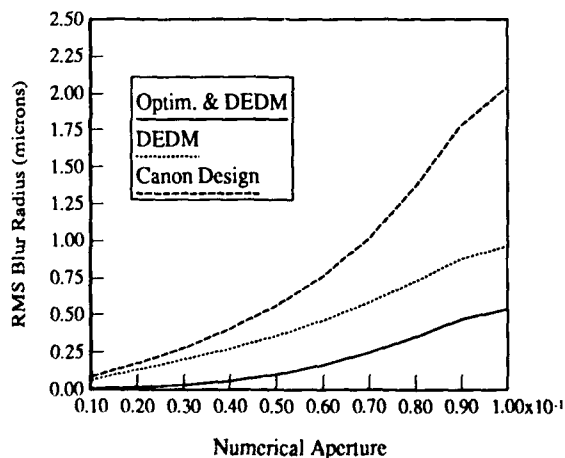


Figure 3. rms blur radius vs. numerical aperture. The object height is 135 mm.

for this optimized system are indicated by the solid line. Compared with the rms values for the original system indicated by the dashed curve, the rms values are improved significantly by the DEDM and optimization.

The rms blur radii versus the object height (field of view) for the original Canon system and the optimized Canon systems are shown in Fig.4.

It appears that the DEDM can increase the field of view or image field size while improving optical performance. A sine wave MTF analysis will be reported for incoherent light to provide more information on the system performance.

In projection lithography applications, the MTF is the optical performance function which has been used extensively in evaluating the projection lithography systems. The MTF values for the original Canon Example 1-11 are shown in Fig.5.

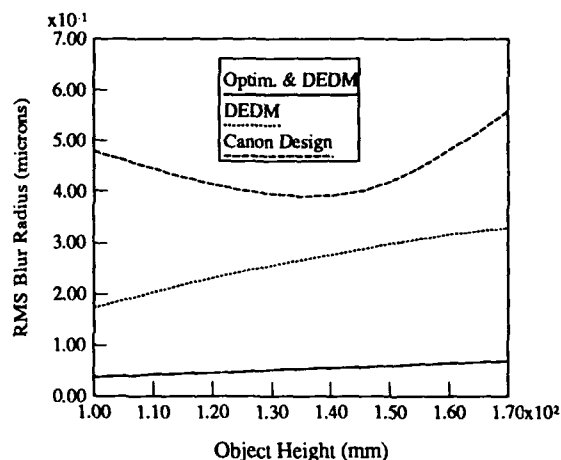


Figure 4. rms blur radius vs. object height. The numerical aperture is 0.0385.

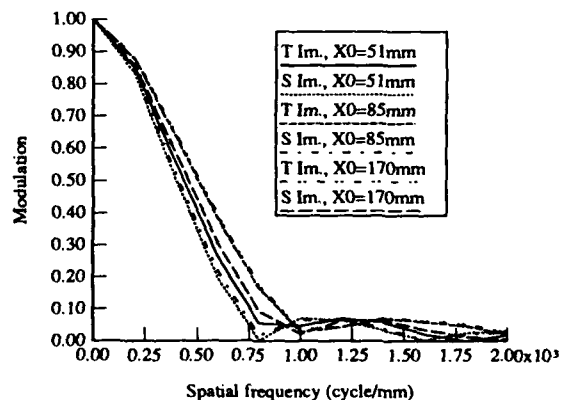


Figure 5. MTF for the sagittal(S) and tangential(T) rays of the original Canon Example 1-11 with numerical aperture 0.0385 and magnification 5x. The conic constant of the first mirror is -0.94278. The parameter



$X_0$  is the object height.

Since the MTF is less than ten percent at a spatial frequency of 1500 cycles/mm, the original Canon system Example 1-11 can not achieve the resolution reported.

After optimization by DEDM, the MTF values are improved significantly for all spatial frequencies. The MTF for the optimized Canon Example 1-11 is shown in Fig. 6.

For the optimized Canon system, the MTF values at a spatial frequency of 1500 cycles/mm reach as high as 0.70. This means that the Canon system Example 1-11, after DEDM optimization, can achieve a resolution of 0.35 microns over a large image field.

While continuing to vary the shape of the first mirror of the Canon system Example 1-11, we decentered some mirrors in the system. This gave an optimized three-mirror projection lithography system which achieves a resolution of 0.1 microns over 5 mm x 5 mm image field. The MTF values for this optimized Canon system are shown in Fig. 7.

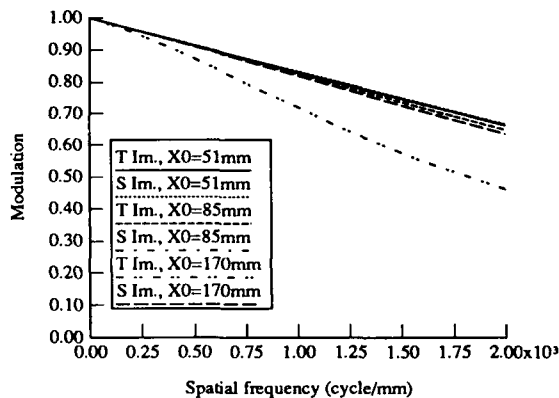


Figure 6. MTF for the optimized Canon Example 1-11 with numerical aperture 0.0385 and wavelength used is 10 nm. The conic constant of the first mirror is -0.94700. The parameter  $X_0$  is the object height.

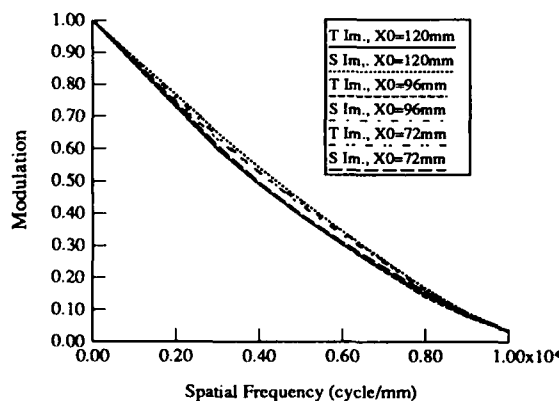


Figure 7. MTF for the optimized Canon system Example 1-11. The N.A. for this system is 0.055, and the wavelength is 10 nm.  $X_0$  is the object height.

From Figs. 3-7, it is clear that DEDM optimization of the Canon projection lithography systems has improved the systems performance significantly. The Canon systems have not been able to reach the performance level as reported. But after being optimized by our differential equation method, the optimized Canon systems can obtain the performance level or better than the reported level.

After using differential equation method on the Canon three-mirror systems and trying to obtain some system designs which have resolution of 0.1 microns over large image field, e.g., 10 mm x 10 mm, we found that the original layout design limited our differential equation method from further optimization. With better layout designs, the differential equation method may obtain better designs by optimizing the original systems.

### Differential Equation Method for Four-mirror System

The differential equation design method has been also applied to shaping two surfaces within four reflection projection systems. Preliminary results have shown that DEDM can significantly improve the optical performance of four reflection projection systems previously reported in the literature [10]. Additional work in this area is in progress and will be reported later [17].

### Conclusion

These results indicate that a significant improvement in the resolution and the field of view for projection systems (reflective) can be achieved when the Abbe Sine condition and the constant optical path length condition are satisfied. The differential equation design method (DEDM) provides a technique for determining numerical values of the sag and slope of two aspherical surfaces within a multi-mirror aplanatic projection system. Iterative application of DEDM and variation of the system variables appears to be a promising optimization method for design of high resolution, large field of view projection systems. Further work is required to evaluate and optimize the distortion and alignment tolerances for these systems.

In summary, this optimization technique should be applicable to a range of soft x-ray projection lithography configurations which may be fabricated and tested for practical applications.

### Acknowledgment

Authors would like to thank Los Alamos National Laboratory for supporting this work (Grant no. 9-XG8-8606Q-1) and acknowledge many stimulating conversations with Brian E. Newnam of Los Alamos National Laboratory about this research.

### References:

1. M.T. Silfast and O.R. Wood II, "Tenth-micron lithography with a 10-Hz, 37.2-nm sodium laser,"

Microelectron. Eng. **8**, 3-11 (1988).

2. A.M. Hawryluk and L.G. Seppala, "Soft x-ray projection lithography using an x-ray reduction camera," J. Vac. Sci. Technol. **B 6.6**, 2162-2165 (1988).

3. O.R. Wood II, W.T. Silfvast, and T.E. Jewell, "Short-wavelength annular-field optical system for imaging tenth-micron features," J. Vac. Sci. Technol. **B 7.6**, 1613-1616 (1989).

4. H. Kinoshita, K. Kurihara, Y. Ishii, and Y. Torii, "Soft x-ray reduction lithography using multilayer mirrors," J. Vac. Sci. Technol. **B 7.6**, 1648 (1989).

5. D. W. Berreman, J.E. Bjorkholm, M. Becker, L. Eichner, R.R. Freeman, T.E. Jewell, W.M. Mansfield, A.A. MacDowell, M.L. O'Malley, E.L. Raab, W.T. Silfvast, L.H. Szeto, D.M. Tennant, W.K. Waskiewicz, D.L. White, D.L. Windt, and O.R. Wood II, "Use of trilevel resist for high-resolution soft-x-ray projection lithography," Appl. Phys. Lett. **56.22**, 2180-2182 (1990).

6. D.W. Berreman, J.E. Bjorkholm, L. Eichner, R.R. Freeman, T.E. Jewell, W.M. Mansfield, A.A. MacDowell, M.L. O'Malley, E.L. Raab, W.T. Silfvast, L.H. Szeto, D.M. Tennant, W.K. Waskiewicz, D.L. White, D.L. Windt, and O.R. Wood II, "Soft-x-ray projection lithography: printing of 0.2 micron features using a 20:1 reduction," Optics Letters **15.10**, 529-531 (1990).

7. T.W. Barbee, Jr., "Multilayers for x-ray optical applications," in *X-Ray Microscopy*, Eds. G. Schmahl and D. Rudolph (Springer-Verlag, New York, 1984), 144-162.

8. E. Spiller, "Enhancement of the reflectivity of multilayer x-ray mirrors by ion-polishing," Proc. SPIE **1160**, 271-279 (1989).

9. D.L. White, J.E. Bjorkholm, J. Bokor, L. Eichner, R.R. Freeman, J.A. Greggs, T.E. Jewell, W.M. Mans-

field, A.A. MacDowell, E.L. Raab, W.T. Silfvast, L.H. Szeto, D.M. Tennant, W.K. Waskiewicz, D.L. Windt, O.R. Wood II, "Soft x-ray projection lithography: experiments and practical printers," Proc. SPIE **1343**, 204-213 (1990).

10. D.L. Shealy and V.K. Viswanathan, "Design survey of x-ray/XUV projection lithography systems," Proc. SPIE **1343**, 229-240 (1990).

11. J.M. Rodgers and T.E. Jewell, "Design of reflective relay for soft x-ray lithography," in *Technical Digest on lens Design, 1990* (Optical Society of America, Washington, DC, 1990), vol. 10, p. 85.

12. M. Suzuki, N. Mochizuki, S. Minami, S. Ogura, Y. Fukuda, Y. Watanabe, Y. Kawai, T. Kariya of Canon Kabushiki Kaisha, "X-ray reduction projection exposure system of reflection type," European Patent Application No. 87306037.0, Date of filing: 08.07.87, Publication no. 0 252 734.

13. I.M. Egdall, "Manufacture of a three-mirror wide-field optical system," Optical Engineering **24.2**, March/April (1985).

14. W.B. Wetherell, D.H. Schulte, and D.A. Womble, *Optical and infrared Telescopes for the 1990s* edited by A. Hewitt (Kitt Peak National Observatory, Tucson, 1980), p. 878.

15. I.R. Abel and M.R. Hatch, "The pursuit of symmetry in wide-angle reflective optical designs," Proc. SPIE **237**, 271-280 (1980).

16. D. Korsch, "Design and optimization technique for three-mirror telescopes," Applied Optics **19.21**, 3640-3645 (1980).

17. C. Wang and D.L. Shealy, "Differential equation method for design of multi-mirror projection lithography systems," to appear in Proc. SPIE Conf. 30 on Multilayer Optics for Advanced X-Ray Applications in San Diego, CA, July 21-26, 1991.



## Illumination Requirements for Optical Projectors and How to Think about Them

Douglas S. Goodman

*IBM Research, Yorktown Heights, New York 10598*

### Abstract

A fundamental requirement of chip lithography is that patterns be imaged identically everywhere in the field. The illumination should be arranged to achieve this end by compensating, insofar as possible, for variations caused by the rest of the system. These include variation of power/area, direction, polarization, and spectral distribution. The illumination should also be configured so that patterns are imaged the same way regardless of their orientations. Full telecentricity is achieved only if the illumination, as well as the imaging lens, is telecentric.

### Introduction

Illumination systems are often given too little thought, since the main lens in a projector is usually much more difficult, and because many of the effects of non-optimum illumination are too small to be noticed in many applications. For modern chip lithography, however, nothing can be assumed negligible.

### Terminology

The nomenclature of image formation is not standardized. Useful, non-standard terms are shown in italics, as well as other important terms.

### Aspects of illumination technology

There are two aspects of illumination technology, which should be distinguished. One is deciding what is wanted, which can be called *illumination design* or *illumination specification*. The other is figuring out how to get it, or *illumination engineering*. We are concerned here with the former.

### Projector terminology

An *optical projector* consists of an *illumination system*, an *object*, and an *imaging system*. *Imaging* refers here to what might be called *imaging per se*, i.e. what happens between the object and the aerial image. *Projection* refers to the entire process of illumination, interaction of light with the mask, and imaging. In chip lithography, the object is a *mask*. The projector output is an *aerial image*, which produces in the resist a re-

*corded image*, which is influenced by the interaction of the light with the resist and with the underlying structure.

### Basic fact

What we call "the image (of an object)" is not due to the object *per se*, but rather to the light leaving it. Since the object in a projector is not self-luminous, the properties of this light depend on both the physical structure of the object and on the light provided by the illuminator. Thus the aerial image depends *jointly* on the illumination system, the imaging system, and the object.

### Purpose of chip lithography

Chip lithography is an industrial process, whose purpose is to make as many good parts as fast and as inexpensively as possible. Illumination requirements should be considered in terms of their ultimate affect on such economic factors as throughput and process control.

### Determining illumination requirements

Take the imaging system and mask as given, and identify the requirements and desired attributes of the aerial image. Determine the illumination required to produce them.

### Where illumination matters

The *illumination* is incident on the mask and is thus usually specified in this plane. But it is really the *image* that matters, so the prescription in the mask plane should provide the desired result in the image plane.

### Description of illumination

A monochromatic plane wave is described classically by its irradiance, direction, wavelength, and polarization. A polychromatic plane wave has some spectral distribution and is, in general, partially polarized. Everything can vary with field position. Within a small region in the object plane, the illumination can be considered as an angular superposition of polychromatic, partially polarized plane waves, each with some irradiance. There is little coherence between the plane wave components. If it were otherwise, the components

would interfere so the irradiance would not be sufficiently uniform. We usually make the approximation that these plane wave components are mutually incoherent.

Instead of treating illumination in this detail, we usually consider its aggregate properties. Thus we describe the range of directions, the net irradiance, the net spectrum, and the net polarization—but not the variation with direction of irradiance, color, and polarization. Since very small effects may be significant in chip lithography, the validity of such a description should be verified.

#### Directions

In image formation, directions are properly described in direction cosines, rather than angles. Accordingly, such terms as *direction* and *average direction* always refer to cosines here. The *principal illumination direction*, is, roughly speaking, the average or central direction, by analogy to the principal ray of the imaging system. The *illumination numerical aperture* describes the extreme direction or the range of illumination directions. (This term is preferred to "condenser numerical aperture," which is ambiguous.)

Pupils should not be thought of as objects, but as ranges of direction, which vary, in general, over the field. Most important in image formation are the *relative illumination directions*, i.e. those with relation to the entrance pupil of the imaging system. For a transmitting mask, these directions derive from those incident; for a reflecting mask, those specularly reflected.

#### Compensation

Insofar as possible, illumination should compensate for systematic effects of the imaging system or the mask that would cause image variations across the field. For example, if mask reflectivity changes with the chief ray angle, and hence with field position for a non-telecentric imaging system, the illumination irradiance should vary to compensate. This particular compensation is demonstrated by uniformly imaging a featureless mask. Another example is that in which the entrance pupil direction varies across the field, in which case the absolute illumination directions should change, so that the relative ones do not.

#### Stationary projection

On the chip being fabricated, a given type of electronic device should be the same regardless of its location. Hence, the image irradiance of a given mask feature should be identical whatever its position in the field. This condition can be called *stationary projection*, where the stationarity is with respect to irradiance, as opposed to field, partial coherence, etc. Stationarity requires certain properties of the imaging system, of the illumination system, and of mask, as well as proper relationships between the them and with the image plane. The imaging system must have little variation with field position of aberrations, exit pupil directions, and transmission.

*Stationary illumination* is that which, in conjunction with a proper imaging system, gives stationary projection. One requirement is *uniform illumination*, which gives a uniform image irradiance with a featureless mask. Another requirement is *matched illumination*, in which the relative illumination directions are constant across the field. In this case, the

diffraction pattern in the pupil due to a given type of feature is the same, regardless of the feature location—at least in the scalar wave approximation. For example, for a grating object, the various orders from all parts of the field coincide in the imaging system aperture. Image uniformity with a featureless mask is a necessary, but not sufficient condition for stationarity, since irradiance uniformity can occur without proper directionality.

For a given illumination which is approximately stationary, the deviation from projection stationarity is pattern dependent. Computer simulations can be used to investigate the variation.

#### Isotropic imaging

Each electronic device should be the same regardless of its orientation on a chip. Hence, the image irradiance of a given feature should be the same regardless of its orientation, a condition that can be called *isotropic projection*, where the isotropy refers to irradiance and to azimuth. For complete isotropy, the pupil and illumination distribution must be concentric figures of revolution. In chip lithography, the number of device orientations is usually limited, so this condition is relaxed. Deviations from isotropy are pattern dependent. Polarization effects can degrade isotropy in a way that is pattern dependent.

#### Wavelength

The range of wavelengths must be limited to that over which the lens is corrected. In addition, for refractive systems there may be sharp imaging over some wavelength range, but a change of focal position exceeding the depth of focus. In this case, a variation of illumination color over the mask could look experimentally as if the lens did not have a flat field. In general, the spectrum should be as broad as the imaging system permits, to minimize standing wave effects in the resist. Non-actinic light should be filtered out, although it does not expose the resist, since it can heat the lens or the wafer, causing a variety of deleterious effects.

#### Polarization

In general, non-polarized illumination best minimizes feature-dependent effects. If the mask or lens has a systematic polarizing influence, then the illumination should be partially polarized to compensate.

#### Defocus and telecentricity

The aerial image should be as insensitive as possible to defocus, to maintain registration with wafer defocus. Imaging systems are telecentric in image space, or sufficiently so within their depth of focus. In order that the entire projector be telecentric, it is necessary also to have *telecentric illumination*, which is obtained if the principal illumination direction is normal to the wafer plane. If the entrance pupil direction varies with field position, the illumination direction must vary likewise to maintain telecentricity. This occurs, for instance, if the imaging system has pupil spherical aberration. Variation of telecentricity with field shows up as distortion that changes with focus. Non-telecentric illumination affects projection telecentricity in a way that is feature dependent. This can be understood by considering the diffraction pattern in the entrance pupil arising from different types of mask features. Telecentricity effects are minimum for very small features,

since the pupil is filled with light diffracted by them, regardless of the illumination direction. If the illumination is uniformly non-telecentric across the field, the relative positions of different sized features can change through focus, because of the pattern-dependence,

#### **Directional distribution**

Most aspects of illumination are mandated by stationarity, isotropy, telecentricity, and compensation. The main choice is that of angular distribution. The directional distribution need not be continuous. For example, stationarity can be obtained with a discrete set of directions, a situation that arises with lens arrays and kaleidoscope uniformizers. The directions may also be radially discontinuous, as is the case with a ring-shaped illumination directions, which can be both stationary and isotropic. This case may arise, for instance, when an illuminator mirror is wobbled during exposure, to average away coherence noise effects.

If the illumination is uniform across the angular range, then its directions are described by a single parameter, the ratio of the illumination numerical aperture to that of the imaging system. (As a consequence of the sine condition, this ratio is the same in both object and image space.) This parameter, usually denoted by  $\sigma$ , is given a number of names in the literature, e.g. "pupil filling factor," and "coherence factor." If the illumination is not uniform over the range of directions,  $\sigma$  is still

useful to indicate the extreme direction. Roughly speaking, illumination spatial coherence increases as  $\sigma$  decreases. In photolithography, the spatial coherence per se is not important; what matters is the image irradiance. The main effect is that edge slopes decrease as  $\sigma$  increases. If  $\sigma$  is than about 0.25, the irradiance tends to be bumpy and the constant irradiance contours wiggly. The optimum  $\sigma$  is pattern dependent. For instance, phase masks function best with small  $\sigma$ , and the imaging of mask defects may vary in importance with  $\sigma$ . The pupil is never overfilled in chip lithography, since the resulting stray light is unacceptable.

#### **Throughput**

Throughput depends mainly on illumination irradiance. For a source of given brightness, the irradiance varies as  $\sigma^2$  if the illumination is uniform over direction. With array uniformizers, this is not the case. In general, there is a trade-off between total power and uniformity. For a given source brightness, overfilling does not help throughput, since the light directed beyond the pupil gives rise to a weak image contribution.

#### **Collection efficiency**

The illumination system should collect the light from the source as efficiently as possible. Conservation of brightness limits what is possible. In general, there is a trade-off between uniformity and quantity of light.

92-19489



AD-P007 233



## Development of Reflective Optical Systems for XUV Projection Lithography

V. K. Viswanathan and Brian E. Newnam

*Chemical and Laser Sciences Division, Los Alamos National Laboratory,  
MS-J564, Los Alamos, New Mexico 87545*

### Abstract

We describe two full-field reflective reduction systems (1 cm<sup>2</sup> and 6.25 cm<sup>2</sup> image area) and one scanning system (25 mm x scan length image size) that meet the performance requirements for 0.1-μm resolution projection lithography using extreme-ultraviolet (XUV) wavelengths from 10 to 15 nm. These systems consist of two centered, symmetric, annular aspheric mirrors with 35-40% central obscuration, providing a reduction ratio of 3.3 x. Outstanding features include the remarkably low distortion ( $\leq 10$  nm) over the entire image field and the comparatively liberal tolerances on the mirror radii and alignment. While optimized annular illumination can improve the performance, the required performance can be met with full illumination, thereby allowing simpler system design.

### Introduction

Near the end of this century, 1-Gbit DRAM and SRAM integrated circuits will be needed with minimum features of 0.1-0.15 μm with  $\leq 0.01$ -μm distortion over a chip area of at least 6.25 cm<sup>2</sup>. XUV projection lithography using all-reflective optical elements has been proposed as a process that may achieve this result. The basic sub-systems are: 1) an XUV photon source with a beam-conditioning, illuminator system, 2) a reflective mask, 3) a reflective, reduction, projection system capable of producing a large, low-distortion image by scanning or full-field illumination, 4) a photoresist-coated silicon (or GaAs) wafer, and 5) a wafer/chip alignment system with precision of  $\sim 0.1$  of the minimum feature size. In this paper we describe a promising solution for the projection system.

Our major goals for designing XUV reflective, projection systems are: 1) a 3 to 5 x reduction ratio, 2) resolution  $\leq 0.1$  μm for  $\lambda = 10 - 20$  nm, 3) distortion  $< 0.01$  μm (10% of resolution) over the entire image

field and even less for scanning systems, 4) diffraction-limited image fields  $\geq 25$  mm x 25 mm (i.e.,  $\geq 6.25$  cm<sup>2</sup>), 5) telecentricity  $< 5$  mrad in the image space, and 6) depth of focus  $\geq 1$  μm at the operating XUV wavelength. In addition, a minimum number of surfaces with attainable manufacturing tolerances and with relatively easy alignment requirements is desired.

We have found that an aspherical version of the two-spherical mirror system conceived by Shafer (1-3) can meet these goals. As shown in Fig. 1, these systems require four reflections from two centered, partially obscured, symmetric mirrors. We have designed three optical reduction systems with a reduction factor of 3.3x and 35-40% obscuration. Systems with larger (up to 4.5 x) reduction factors were found to have smaller image fields for a fixed distortion allowance. In principle, all three of the systems to be described herein can be used in either full-field or scanning mode illumination, but one of them was designed specifically for scanning applications. These systems exhibit less severe tolerance requirements than four-mirror axial systems as well as four-mirror tilted and decentered systems, and the asphericity, in terms of departures from the best-fit spheres, also is not severe. They have been optimized for diffraction-limited, low-distortion optical performance with achievable fabrication and alignment tolerances. They do, however, tend to be long with relatively large mirrors, and it is hoped that further optimization will result in smaller-size systems.

### Description of the Proposed Reduction Systems

The three projection systems described in this paper produce image-field dimensions of:

- 1) 25 mm x 25 mm, full-field illumination
- 2) 25 mm x scanlength
- 3) 10 mm x 10 mm, full-field illumination.

\*Work supported by Los Alamos Program Development Funds and conducted under the auspices of the U.S. Department of Energy.

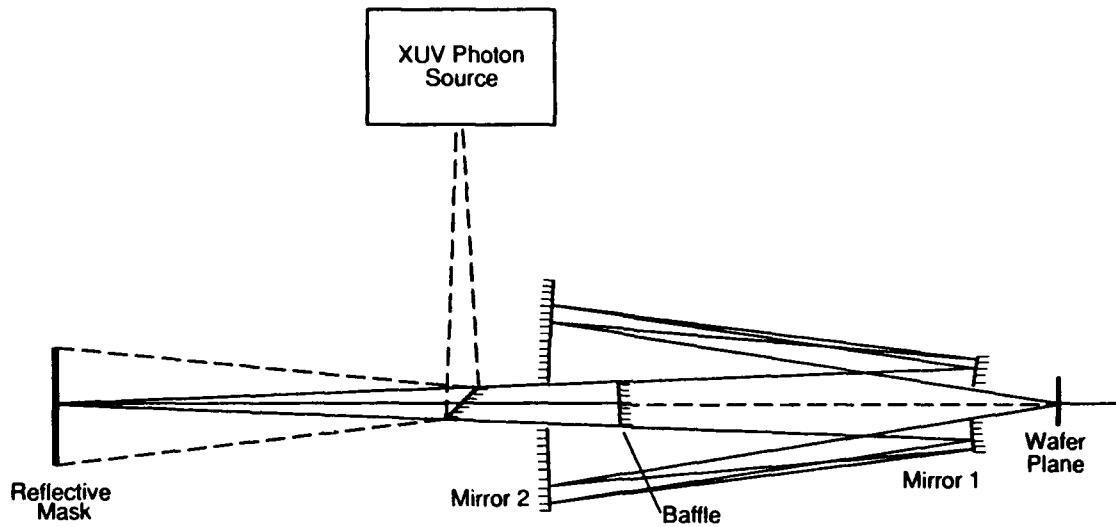


Figure 1. Schematic of a symmetric, centered, two-mirror, four-reflection xuv projection system.

The major advantages of these three systems include: 1) a minimum number of two surfaces is required which are centered and rotationally symmetric, 2) the image size, resolution, distortion and image-space telecentricity requirements are attained, 3) application in either scanning or non-scanning modes is possible, 4) the asphericity of the mirrors is not severe - they are not far from best-fit equivalent spheres, 5) the illumination does not need to be annular, though its use can further enhance the attainable performance, 6) the symmetry makes these systems intrinsically superior for ease of alignment, as well as tolerant to figure imperfections and thermal distortion due to absorbed power, and 7) the variations of the angles of incidence over the illuminated parts of the mirror surfaces are within  $\pm 5^\circ$  for the non-scanning examples and  $\pm 10^\circ$  for the scanning example, over which the reflectance of multilayer coatings will be nearly constant.

The possible disadvantages are that the mirrors are relatively large, the systems are long, and 35-40% of the incident energy is lost due to the obscuration. We expect that the dimensions of these systems can be reduced with further optimization. The obscuration loss can be totally prevented with increased performance by use of optimal annular illumination. Also, the obscured space can be used for mask-to-wafer alignment or for input of the XUV illumination as shown in Fig. 1.

The relevant optical properties of the three systems are presented in Table 1 (4). The rms wavefront-deviation is considerably less than  $0.071\lambda$ , the usual criterion for diffraction-limited correction level. This enables realistic tolerancing of the systems. The telecentricity level of 0.2 - 0.4 mr is far less than the 5 mr usually needed, and the distortion levels attained are

Table 1. Optical Characteristics of the Proposed Two-Mirror Reduction Systems

| System Image Size   | Resolution for $\lambda=10$ nm | Distortion (Maximum) | RMS Wavefront Deviation                            | Telecentricity | Mask-to-Wafer Distance |
|---------------------|--------------------------------|----------------------|--|----------------|------------------------|
| (mm x mm)           | ( $\mu\text{m}$ )              | ( $\mu\text{m}$ )    | ( $\lambda=10$ nm)                                 | (millirads.)   | (meters)               |
| 25 x 25             | 0.1                            | 0.002                | 0.015 $\lambda$ - center<br>0.031 $\lambda$ - edge | 0.22           | 4.1                    |
| 25 mm x scan length | 0.1                            | 0.002                | 0.009 $\lambda$ - center<br>0.009 $\lambda$ - edge | 0.39           | 2.3                    |
| 10 x 10             | 0.1                            | 0.001                | 0.006 $\lambda$ - center<br>0.012 $\lambda$ - edge | 0.22           | 1.7                    |

less than the required  $0.01\text{ }\mu\text{m}$  for the manufactured system.

The theoretical aerial image of  $0.1\text{-}\mu\text{m}$  equal lines and spaces in the wafer plane is shown in Fig. 2 at the edge of the field for the  $25\text{ mm} \times 25\text{ mm}$  system. For this case, partially coherent illumination with a numerical aperture ratio of 0.98 was used. It can be seen that the diffraction intensity profile for  $0.1\text{-}\mu\text{m}$  features can be resolved with good contrast. For this same system, Fig. 3 shows the depth of focus over which the incoherent modulation transfer function at 5000 line pairs/mm (corresponding to  $0.1\text{-}\mu\text{m}$  features) is at least 0.45. This value is the criterion also used by Jewell et al (5).

The diameters of the two aspheric mirrors for each of the three systems are given in Table 2, as well as the deviations from best-fit spheres. The reasonably small deviations are in the range to permit practical manufacture. Additional information revealing the relatively large fabrication tolerances is presented in Table 3. Comparison with the four aspheric-mirror system

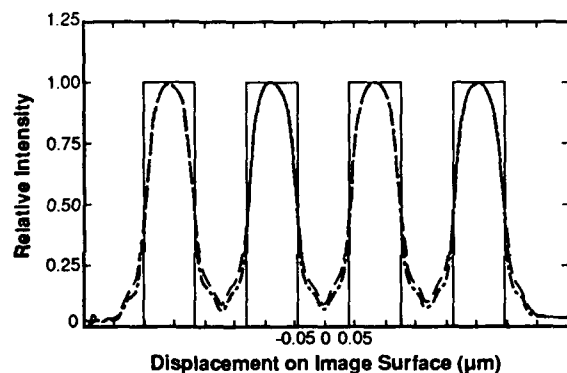


Figure 2. Projected  $0.1\text{-}\mu\text{m}$  aerial image of equal  $0.33\text{-}\mu\text{m}$  lines and spaces illuminated with  $10\text{-nm}$  radiation with 0.98 partial coherence factor for the  $25\text{ mm} \times 25\text{ mm}$ -image field of a two-mirror full-field illumination system. Image simulations are shown in the focal plane at the edge of the field; the on-axis image is nearly identical.

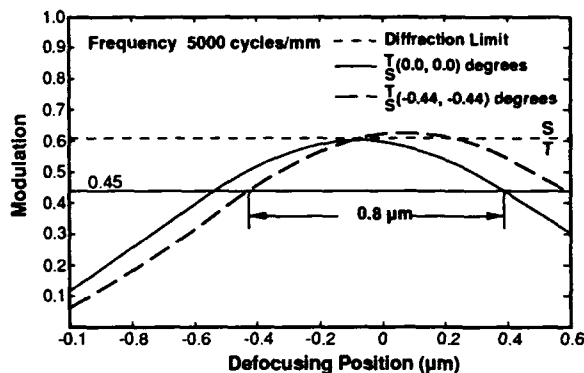


Figure 3. Depth of focus for 5000 line pairs/mm images with  $10\text{-nm}$  incoherent light. The square-wave modulation transfer function is shown as a function of defocus position. Tangential and sagittal curves are overlapping in this case.

Table 3. Distributed Fabrication Tolerances Producing a Net  $0.025\lambda$  Increase in RMS Wavefront Deviation

| System Image Size                       | Mirror Radii M1 / M2 | Spacing           | Tilt                |
|---|----------------------|-------------------|---------------------|
| (mm x mm)                               | (nm)                 | ( $\mu\text{m}$ ) | ( $\mu\text{rad}$ ) |
| 25 x 25                                 | $\pm 35 / \pm 10$    | $\pm 0.05$        | $\pm 1$             |
| 25 mm x scan length                     | $\pm 40 / \pm 10$    | $\pm 0.05$        | $\pm 0.3$           |
| 10 x 10                                 | $\pm 35 / \pm 10$    | $\pm 0.05$        | $\pm 1$             |
| -----                                   |                      |                   |                     |
| 4-Aspheric mirrors, decentered, tilted; | $\pm 1$ each         | $\pm 0.001$       | $\pm 0.01$          |
| 10 x 10 image                           |                      |                   |                     |

Table 2. Aspheric Mirror Sizes and Deviations From Best-Fit Spheres

| System Image Size   | Mirror 1 |                                     | Mirror 2 |                                     |
|---------------------|----------|-------------------------------------|----------|-------------------------------------|
|                     | Diameter | Max. Deviation from Best-Fit Sphere | Diameter | Max. Deviation from Best-Fit Sphere |
| (mm x mm)           | (cm)     | ( $\mu\text{m}$ )                   | (cm)     | ( $\mu\text{m}$ )                   |
| 25 x 25             | 45       | +6                                  | 70       | -4                                  |
| 25 mm x scan length | 30       | +1.7                                | 50       | -1.7                                |
| 10 x 10             | 20       | +2.5                                | 30       | -1.7                                |



(decentered and tilted) shows dramatically how much more tolerant the proposed two-mirror systems are.

### **System Manufacturability**

The issue of system manufacturability cannot be overemphasized. Surface fabrication requirements for four-mirror systems (irrespective of configurations - co-axial or decentered four-mirror systems) have been discussed in detail by T.E. Jewell et al (5). They assumed all of the error budget (except the nominal design wavefront error of  $0.033\lambda$ ) to be used up by one mirror at the stop and concluded that at  $\lambda=546$  nm (using root-sum-square combination of errors to get the allowed  $0.071\lambda$  rms diffraction limit), the maximum tolerable surface figure error is  $\sim \lambda/300$  peak-to-valley (P-V). If this error is distributed among the four mirrors, the maximum tolerable figure error is  $\lambda/600$  P-V for each mirror. We suggest, however, that fabrication and alignment tolerances also must be included before a realistic figure error requirement can be assigned to individual mirrors.

For our three systems, using the same root-sum-squares technique (assuming individual tolerances are independent), we allocated the  $0.071\lambda$  deviation as follows:  $0.031\lambda$  rms for nominal design wavefront error [see Table 1],  $0.025\lambda$  rms for fabrication tolerance [see Table 3],  $0.035\lambda$  rms for surface irregularity error, and  $0.047\lambda$  rms allocation for alignment error. This alignment error is allowed for the total lithographic system. These tolerances were derived from detailed computations using Code V<sup>TM</sup>. With these allocations of the various errors that have to be accounted for in the manufacture of a practical system, we find that the surface irregularity error allowed per surface is  $\sim \lambda/125$  P-V at 546 nm. This is to be contrasted with the  $\lambda/600$  per surface required for the four-mirror systems even with all the tolerance taken up just by surface irregularity error. Clearly, the two-mirror centered systems proposed here are far more tolerant to mirror imperfections.

### **Conclusions**

The theoretical performance of the three reduction systems described in this paper meet the resolution, field size, distortion, and telecentricity requirements for 0.1- $\mu$ m lithography. These systems allow for relatively large fabrication and alignment tolerances. They are capable of operating in both full-field and scanning modes and should be much less sensitive to source-induced thermal distortion than tilted, decentered sys-

tems as well as co-axial systems with mirrors being used off-aperture.

### **Future Plans**

Development of these two-mirror systems for practical implementation will include optimization of the designs for size, manufacturability, ease of alignment, as well as location and size of the baffle for stray-light suppression. This will be followed by design integration of one of the systems with an XUV source, e.g. a free-electron laser (6), and optimal illumination optics. A structural-thermal-optical analysis of the reduction systems will indicate the limit on the incident source flux. Finally, it is our intention to build and test the most promising system for lithography in collaboration with semiconductor equipment manufacturers.

### **Acknowledgments**

We are indebted to David Shafer (consultant) whose two-spherical mirror design was the starting point for the large-field systems derived in this work.

### **References**

1. D. R. Shafer, Fairfield, Connecticut, consultant on optical design.
2. F. Zernike and F.Y. Wu, "Challenges in the Design and Fabrication of XUV Projection Lithographic Optics," in Free Electron Laser Applications in the Ultraviolet, 1988 Technical Digest Series, Vol. 4, (Optical Society of America, Washington, DC, 1988), pp. 106-108.
3. D.L. Shealy and V.K. Viswanathan, "Design Survey of X-Ray/XUV Projection Lithography Systems," in X-Ray/EUV Optics for Astronomy, Microscopy, Polarimetry, and Projection Lithography, R. Hoover and A. Walker, eds., Proc. Soc. Photo-Opt. Instrum. Eng. **1343**, 229-240 (1991).
4. The optical design and evaluations reported in this paper were performed using Code V<sup>TM</sup> available from Optical Research Associates, 550 North Rosemead Blvd., Pasadena, Calif. 91107.
5. T.E. Jewell, J.M. Rodgers, and K.P. Thompson, "Reflective Systems Design Study for Soft X-Ray Projection Lithography," J. Vac. Sci. Tech. **B8**, 1519-1523 (1990).
6. B.E. Newnam, "XUV Free-Electron Laser-Based Projection Lithography Systems," in X-Ray/EUV Optics for Astronomy, Microscopy, Polarimetry, and Projection Lithography, op. cit., pp. 214-228.

# Specifying Optical Fabrication Tolerances for Soft X-ray Projection Lithography Systems

James E. Harvey  
CREOL/UCF

12424 Research Parkway  
Orlando, Florida 32826  
(407) 658-6818

AD-P007 234



## SUMMARY

The rapidly emerging technology of soft X-ray projection microlithography requires very stringent tolerances upon the residual surface errors inherent with any optical fabrication process. The scattering effects of these optical fabrication errors can severely degrade system performance. These optical fabrication errors must therefore be controlled over the entire range of relevant spatial frequencies, including "mid" spatial frequency surface irregularities that bridge the gap between the traditional "figure" and "finish" errors. The surface power spectral density (PSD) function thus becomes the natural quantity to monitor during the optical fabrication process.

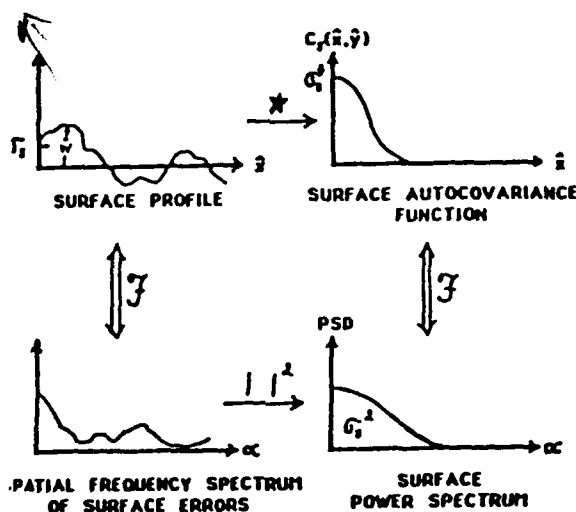


Figure 1. Relationship between the surface profile and surface PSD

A procedure will be outlined for making parametric optical performance predictions from assumed or measured metrology data for both grazing incidence X-ray imaging systems and normal incidence X-ray multilayer coated optical systems. This procedure is quite straightforward for those wavelengths where the smooth surface approximation is valid since the resulting scattering function is directly proportional to the surface PSD function.

For those wavelengths and surfaces where the smooth surface approximation is not valid, the generalized point spread function (PSF) which includes the effects of scattering can be calculated by Fourier transforming the surface transfer function given by

$$H(x, y) = H_c(x, y) \exp\{-(4\pi \sin\phi \sigma_s / \lambda)^2 [1 - C(x/l, y/l \sin\phi) / \sigma_s^2]\} \quad (1)$$

where  $H_c(x, y)$  is the transfer function of the image core,  $\phi$  is the grazing angle,  $\sigma_s$  is the rms surface roughness, and  $C(x/l, y/l \sin\phi)$  is the surface autocovariance function.<sup>1</sup>

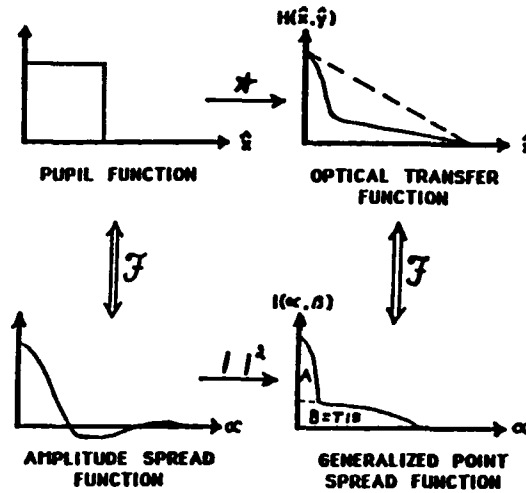


Figure 2. Relationship between the complex pupil function, the surface transfer function, and the generalized point spread function.

Surface scatter phenomena has been shown to exhibit shift-invariant behavior with respect to incident angle, thus justifying this linear systems approach to predicting the performance of X-ray imaging systems as degraded by optical fabrication errors over the entire range of relevant spatial frequencies.<sup>2</sup> By assuming that the surface PSD function obeys an inverse power law as illustrated in Figure 3, parametric performance prediction curves can be generated which allow the optical fabrication tolerances necessary to satisfy a given image quality requirement to be specified.

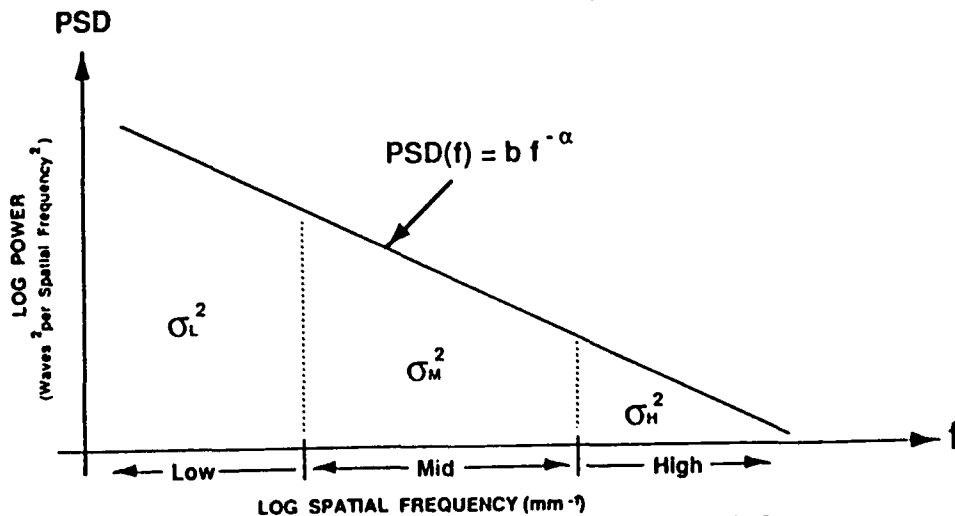


Figure 3. Surface power spectral density (PSD) function.

It is widely recognized that "supersmooth" substrates are required for X-ray multilayers since microroughness can decimate the reflectance of the multilayer. However, small angle scatter from correlated mid spatial frequency surface irregularities will limit the resolution attainable without any significant effect upon the reflectance. If we assume that the interfaces making up a multilayer are uncorrelated at the high spatial frequencies (microroughness) and perfectly correlated at the low and mid spatial frequencies, then the multilayer can be thought of as a surface PSD filter function, as shown in Figure 4. The exact location and shape of the cut-off is material and process dependent.

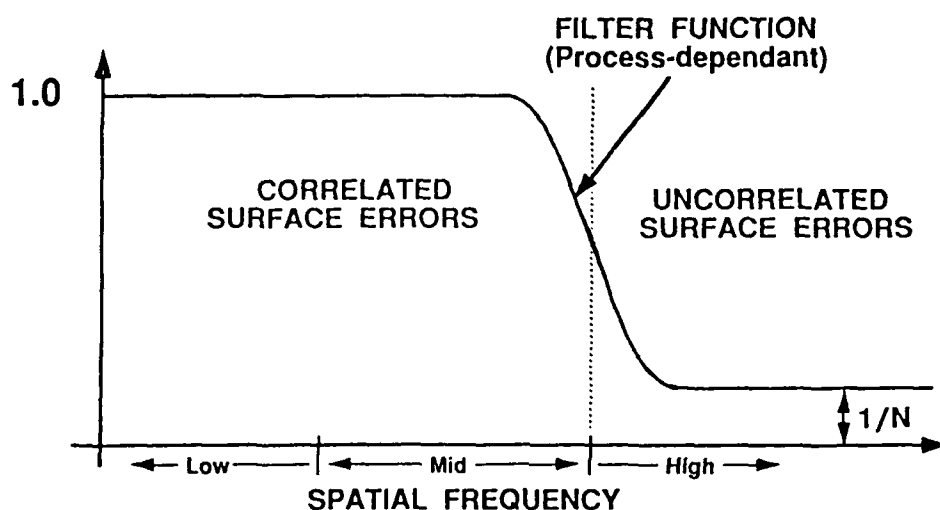


Figure 4. X-ray multilayers behave as a low-pass spatial frequency filter acting upon the interface PSD.

By multiplying the PSD of a typical interface in a multilayer by this PSD filter function, the effective PSD of the multilayer is obtained. This effective PSD can be Fourier transformed to obtain the effective surface autocovariance function. This quantity is then substituted into Eq. (1) to describe the effective surface transfer function, which is then Fourier transformed to yield the generalized point spread function. The appropriate image quality criterion (fractional encircled energy for X-ray telescopes, characteristics of three-bar target images for microlithography) for a given application can now be evaluated as a function of the optical fabrication parameters and compared to optical performance requirements. This process will allow optical fabrication tolerances to be specified. Examples of parametric performance predictions for both X-ray astronomical telescopes and soft X-ray projection microlithography systems will be presented.

1. J. E. Harvey, E. C. Moran and W. P. Zmek, "Transfer function characterization of grazing incidence optical systems", *Appl. Opt.* **27** (8), 1527-1533 (1988).
2. J. E. Harvey, "Surface scatter phenomena: a linear, shift-invariant process", *Proc. SPIE* **1165** (1989).



## Analysis of Thermally Induced Distortion of Optics for Soft-X-Ray Projection Lithography

R. D. Watson

Sandia National Laboratories, P.O. Box 5800,  
Albuquerque, New Mexico 87185

AD-P007 235



R. H. Stulen

Sandia National Laboratories, P.O. Box 969,  
Livermore, California 94551-0969

### Introduction

The development of lens systems for soft x-ray projection lithography presents significant challenges associated with the fabrication and testing of ultra-precise optical surfaces. Once assembled, these projection lenses must further be dimensionally stable to tolerances determined by the wavelength of the soft x-rays used for illumination, typically between 100 Å and 300 Å. Lens systems capable of printing over large areas will contain a number of mirrors with reflectivities in the range of  $60 \pm 10\%$ . For these systems, the first element will be subjected to a significant incident x-ray flux, of which about 40% will be absorbed in the multilayer coating. This absorbed power causes differential thermal expansion from temperature gradients and, hence, distortion of the optical surface. These thermal distortions should be less than about 10 Angstroms in order to preserve accuracy.

In any lens system, each element will be mounted on a substrate which serves both to hold the optic and to provide a thermal sink. This latter function is important since the overall lens assembly will be mounted in vacuum to avoid absorption of soft x-rays by the ambient gas. Assuming that the substrate is metallic with a reasonable thermal conductivity  $k$  (on the order of 100 W/m-K), it is likely that the lens itself will become a significant barrier for heat extraction. It is therefore desirable to use lens materials that have large  $k$  and small coefficients of thermal expansion (CTE). We present here the results of finite element calculations of the heating and physical distortions caused by the absorption of soft x-rays at the surface of a mirror.

A number of materials and boundary conditions have been examined in this study. The five materials are: Corning ULE (Ultra Low

Expansion), Corning 9600, Shott Zerodur, Silicon, and Silicon Carbide. A special grade of SiC was selected, "Hitacram SC-101", (made by Hitachi) because of its very high thermal conductivity (270 W/m-K) at room temperature. The materials properties used in this analysis are shown in Table 1. All of the glasses have low thermal conductivity. The lowest thermal expansion coefficient belongs to Corning ULE, and the highest to silicon carbide. We expect that low values of the figure of merit,  $CTE/k$ , are desirable in order to minimize thermal distortions.

### Finite Element Model

The thermal model of the first mirror is shown in Fig. 1. The mirror is a flat disk with dimensions: 150 mm in diameter and 37.5 mm in thickness. A uniform heat flux of 10 milliwatts/cm<sup>2</sup> is applied to a circular area 50 mm in diameter and is centered on the axis of the disk. In reality, the surface heat loading is pulsed with a pulse length of 30 nanoseconds, frequency of 10-100 Hz, and heat flux of 3000-30,000 W/cm<sup>2</sup>. This is equivalent to a steady-state heat flux of 0.01 W/cm<sup>2</sup> when averaged over time. We will demonstrate later on that the effects of pulsing can be neglected.

There are three thermal boundary conditions in this analysis: (1) conductively cooled on the backside to 20 C, (2) conductivity cooled on the edge to 20 C, and radiatively cooled from the backside to a sink of 20 C. A surface emissivity of 0.8 was assumed for the backside of the mirror. Correspondingly, there are three mechanical boundary conditions: (1) unconstrained, (2) rigidly constrained on the backside, and (3) constrained on the outer edge. The finite element mesh used by the ABAQUS code consists of 294 axisymmetric, 8-noded, bi-quadratic elements and 982 node points.

## Results

First, we will determine if the effects of pulsing the heat source are significant. A transient thermal analysis was performed using ABAQUS to determine the time constant of the mirror using the average heat flux of 10 milliwatts/cm<sup>2</sup>. For Corning ULE it was found that a steady-state temperature profile was achieved in about 30 minutes. This is many orders of magnitude longer than the pulse length of the actual heat load, e.g. 30 nanoseconds. Hence, the bulk temperature rise of the mirror is not affected by the pulsing, only by the time-averaged heat load. However, the instantaneous surface heat flux is still large, 3000-30,000 W/cm<sup>2</sup>, and causes a surface temperature rise of 4-40 °C for 100-10 Hz, respectively. The physical distortions will depend on the thickness of the heated layer. This can be estimated by noting that the thermal diffusion depth is only 3000 Angstroms for a pulse length of 30 nanoseconds. For the worst case 40 °C rise, we estimate that the thermal distortion will be less than 0.005 Angstroms, and can be reasonably neglected. Consequently, the time-averaged heat flux can be used.

Fig. 2 shows the steady-state temperature profile for Corning ULE glass exposed to 10 milliwatts/cm<sup>2</sup> and cooled on its backside to 20 °C. In this case, the maximum surface temperature is 21.5 °C, resulting in a front-to-back temperature difference of only 1.5 °C. Fig. 3 shows the circumferential stress (e.g. hoop stress) distribution caused by the thermal gradient shown in Fig. 2. There are compressive stresses of -390 Pascals in the center of the mirror where the glass is expanding the most, and tensile stresses of 174 Pascals on the outer edge. These stresses are very small compared to the strength of the glass, e.g. 10<sup>7</sup> Pascals. Fig. 4 shows the elastic distortions (magnified by 50 x 10<sup>6</sup>) that are caused by this stress distribution. The largest vertical displacements, 5.5 Angstroms, occur when the mirror is totally free to expand and bend (see Fig. 4-a). When the mirror is rigidly constrained around its edge, the deflection decreases to 3.9 Angstroms, as shown in Fig. 4-b. Finally, constraining the mirror on the backside reduces the distortion to 3.2 Angstroms, as shown in Fig. 4-c.

Table 2 summarizes the results of the ABAQUS finite element analyses. The front-to-back temperature difference ranges from 1 to 2 °C for the glasses, and is very small, 0.01 °C, for Silicon Carbide because of its high thermal conductivity. Edge cooling causes a larger temperature difference because the heat sink is at a greater distance than with backside cooling. The results for radiation cooling are in-between edge and backside cooling. The maximum surface temperature for ULE glass with radiation

cooling is only 23.9 °C. This indicates that water cooling of the mirror may be unnecessary, and thermal radiation may be sufficient to cool the mirrors.

The maximum vertical displacements are largest for the unconstrained models, and smallest for backside constraint. In all cases, the thermal distortions of both Corning ULE, Silicon Carbide, and Corning 9600 are less than the limit of 10 Angstroms. However, Shott Zerodur exceeds the limit by about a factor of 2, and Silicon is borderline acceptable.

It is interesting to note that Invar, an alloy iron and nickel, has a thermal distortion of only 0.6 Angstroms under the same conditions for the unconstrained case because of the very favorable combination of high thermal conductivity (12.9 W/m-K) and low CTE at room temperature, 0.01 E-6 1/K. This is expected because the figure of merit, CTE/k, for Invar (0.8 E-9 m/W) is nearly a factor of 10 smaller than Corning ULE glass. If Invar can be adequately polished, it would make an excellent mirror material.

Fig. 5 plots the maximum vertical displacement as a function of the figure of merit, CTE/k, for three materials, ULE, SiC, and Shott Zerodur. As can be seen, the displacement is linearly proportional to CTE/k. Knowing this, we can predict the performance at temperatures other than room temperature. Fig. 6 shows the temperature dependence of the CTE for Corning ULE glass. We can see that the best operating temperature would be at a bulk average temperature of 21 °C. However, for the case of backside constraint, it would be acceptable to operate the mirror as high as 42 °C, or as low as 7 °C, and still not exceed the allowed displacement limit of 10 Angstroms. Production quality control will be important because the temperature where CTE=0 can vary from batch-to-batch as much as 20-30 °C.

## Conclusions

A detailed finite element analysis of the physical distortions due to surface heating of optical elements of soft x-ray projection lithography systems has been performed. Acceptable mirror materials were found to include: Corning ULE, Silicon Carbide, and Corning 9600. The thermal deflections due to a steady-state heat flux of 10 milliwatts/cm<sup>2</sup> were determined to be less than the maximum allowed limit of 10 Angstroms. It was found that the distortions could be minimized by constraining the mirror on its backside or edge. Shott Zerodur exceeded the limit by about a factor of 2, and pure silicon was marginally acceptable. Radiation cooling alone was shown to be an acceptable alternative to conduction cooling. Finally, it was shown that Corning ULE could operate within a wide range of bulk temperatures, from 7-42 °C, without exceeding the limits.

### Acknowledgments

This work was performed at Sandia National Laboratories and was supported by the U.S. Department of Energy under contract #DEAC04-76DP00789.

Table 1 Material's Properties

| Mirror Material | Thermal Conductivity (W/m-K) | Thermal Expansion Coefficient CTE (1/K) | Young's Modulus (MPa) | Poisson's Ratio | Figure of Merit CTE/k (m/K) |
|-----------------|------------------------------|---|-----------------------|-----------------|-----------------------------|
| Corning ULE     | 1.31                         | 0.01 E-6                                | 67.6 E3               | 0.17            | 7.9 E-9                     |
| Hitacram SiC    | 270.                         | 3.7 E-6                                 | 4.8 E5                | 0.19            | 13.7 E-9                    |
| Corning 9600    | 1.52                         | -0.02 E-6                               | 9.5 E4                | 0.25            | 13.2 E-9                    |
| Shott Zerodur   | 1.64                         | 0.5 E-6                                 | 1.9 E5                | 0.24            | 30.5 E-9                    |
| Silicon         | 123                          | 2.33 E-6                                | 1.9 E5                | 0.25            | 18.9 E-9                    |

Table 2 Summary of ABAQUS Finite Element Results

| Mirror Material | Front-to-Back Temperature Difference (C) |             |                  | Maximum Vertical Displacement (Angstroms) |                  |                      |
|-----------------|--|-------------|------------------|---|------------------|----------------------|
|                 | Backside Cooled                          | Edge Cooled | Radiation Cooled | Free                                      | Edge Constrained | Backside Constrained |
| Corning ULE     | 1.49                                     | 1.81        | 1.64             | 5.45                                      | 3.92             | 3.22                 |
| Silicon Carbide | 0.01                                     | 0.01        | 0.01             | 9.88                                      | 7.2              | 5.87                 |
| Corning 9600    | 1.29                                     | 1.56        | 1.42             | -9.76                                     | -7.4             | -5.92                |
| Shott Zerodur   | 1.19                                     | 1.45        | 1.32             | 22.5                                      | 16.9             | 13.6                 |
| Silicon         | 0.02                                     | 0.02        | 0.02             | 14.1                                      | 10.7             | 8.5                  |

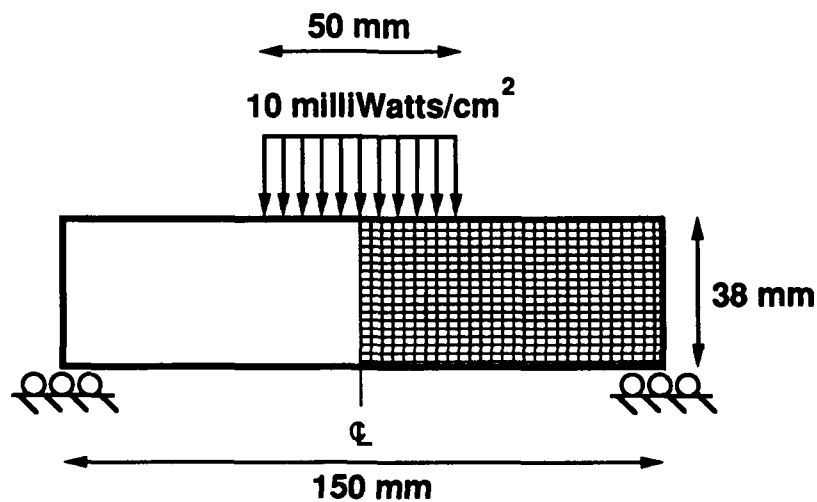


Fig. 1 Simplified model of first mirror of projection system with 2-D axisymmetric ABAQUS finite element mesh.

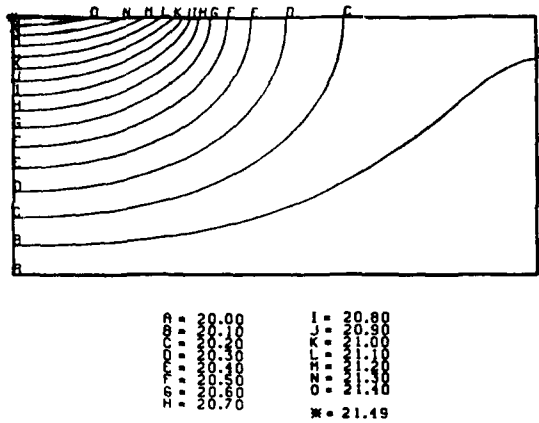


Fig. 2 Steady-state temperature distribution (C) for Corning ULE glass at 10 milliwatts/cm<sup>2</sup> with backside cooled at 20 C.

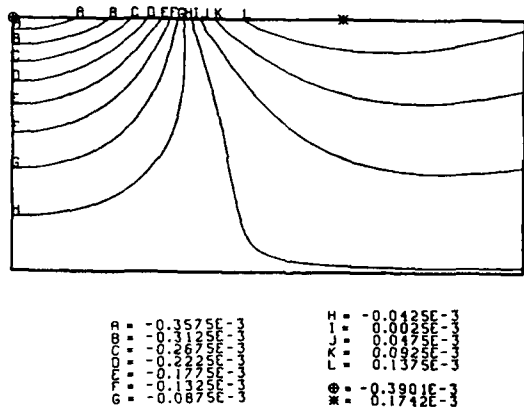


Fig. 3 Thermal stress profile (MPa) showing the circumferential (hoop) stress distribution for temperature gradients in Fig. 2.

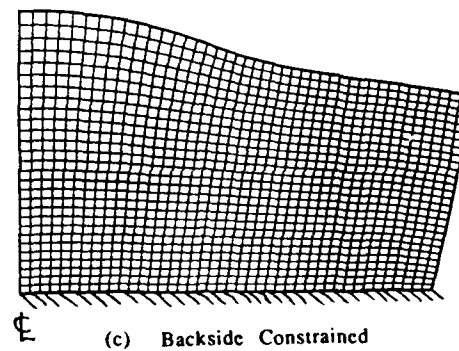
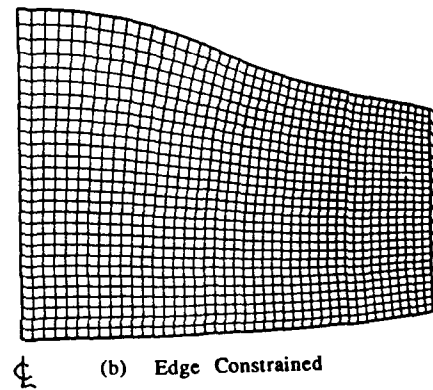
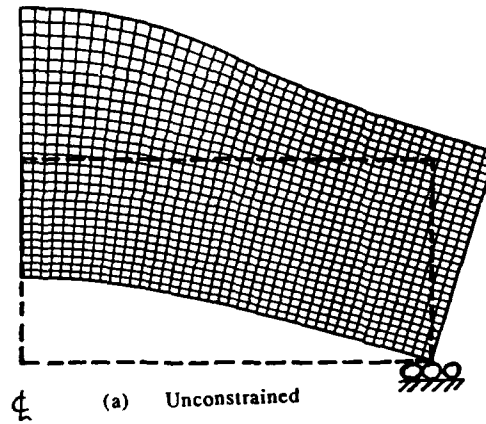


Fig. 4 Thermal distortions magnified by 50 million. (a) unconstrained, (b) edge constrained, (c) backside constrained. Dotted line shows undeformed original shape.



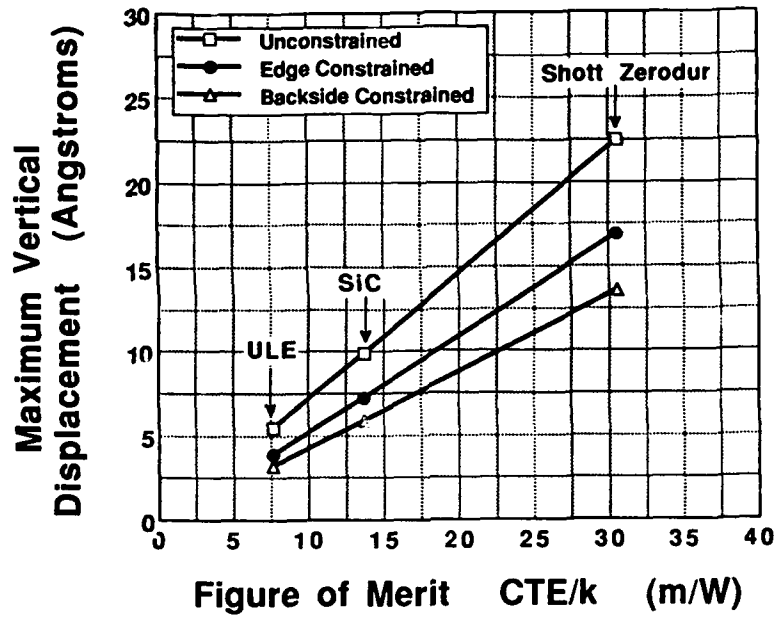


Fig. 5 ABAQUS finite element results of maximum vertical displacement plotted as a function of the figure of merit, CTE/k.

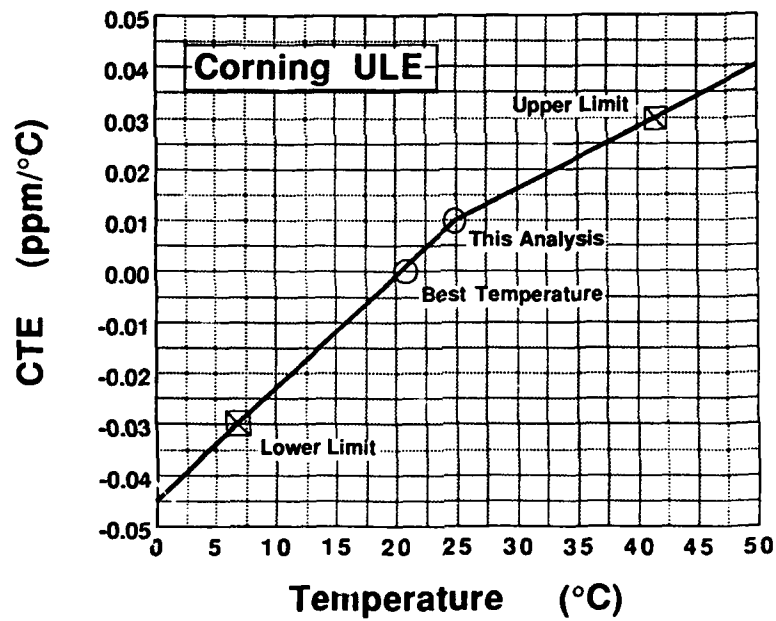


Fig. 6 Coefficient of thermal expansion for Corning ULE v.s. temperature.



## Optical Alignment for Lithography

Norman Bobroff and Alan E. Rosenbluth

IBM Thomas J. Watson Research Center, P.O. Box 218,  
Yorktown Heights, New York 10598

The total overlay budget in semiconductor lithography has many components, including mask dimensional accuracy, tool-to-tool printing distortion, and process bias, but historically alignment registration has been the most critical. Yet progress in alignment has not kept pace with the exponential increases in printing resolution achieved during the last 10 years. In manufacturing, it is difficult to overlay lithography levels better than 200 nm at the  $3\sigma$  confidence level. Registration accuracy is limited by the complex interaction of the alignment optics with wafer registration marks at different process levels. Recent experimental and analytical work has led to an understanding of how to design optical alignment systems with reduced sensitivity to mark structure, coatings and processing. However, it is possible that no single alignment system can be optimized for all process layers encountered in the fabrication of DRAMS or bipolar logic.

Alignment optics are usually categorized as either brightfield or darkfield. Brightfield systems derive an optical alignment signature from a combination of specularly reflected and scattered or diffracted illumination radiation. In darkfield systems specularly reflected light is not collected. Properly engineered darkfield systems show consistently better results than brightfield when performance is averaged over all process levels.

This result is elucidated by a comparison study of brightfield and darkfield systems incorporating asymmetric non-planar, thick film objects [1]. Performance criteria are sensitivity to asymmetric coating processes, and the statistical uncertainty in location of the alignment mark per incident illumination photon. Non-planar mark structure is modeled by computing a complex scattering matrix for the substrate. Each column of the matrix contains the phase and amplitude for a single input Fourier component of the illumination to be scattered into a spectrum of outgoing components. The scattering matrix is evaluated for a given geometry by eigenfunction expansion in each thin film layer of the solution to Maxwell's equations. Boundary conditions are applied at each interface to solve for the complex

amplitudes of the eigenfunctions. The problem is tractable in two dimensions for the TE and TM illumination modes allowing polarization effects to be studied. The scattering matrix is incorporated in an image formation program which can vary the partial coherence of the illumination. Although the model converges mathematically for a wide range of topographies, the primary demonstration of accuracy is agreement with image scan data from prepared sample marks.

Alignment signals parameterized by a range of resist coating thickness and coating asymmetries clearly show darkfield systems to be less sensitive to asymmetric process coatings than brightfield systems. Underlying this result is diminished interference between light scattered by the wafer mark and light originating at the process coating interfaces. Of course, some degree of thin film interference coupling is unavoidable and ultimately limits alignment performance. Broadband illumination also reduces interference between light from different coating interfaces by decreasing the coherence length of the source and is essential to construction of high performance brightfield aligners. However, because wafer coating structures are of the order of the wavelength of alignment radiation, incoherent illumination is difficult to achieve. Also, partially coherent illumination can enhance modulation of the signal. Registration improvement accrued from darkfield alignment is of much greater significance than that realized from broadband illumination. This central result is illustrated in the success of the ASM [2] and Nikon [3] alignment systems which both use monochromatic laser illumination.

Another significant feature of darkfield alignment is the consistent signal profile presented to the processing electronics. Positioning algorithms for brightfield systems, such as Canon's aligner, must accommodate a variety of signal profiles in which reflectivity from a mark may be diminished or enhanced according to coating thickness. Although this can be done by signal correlation with a library of profiles it increases the number of system parameters which must be evaluated and optimized at each process

level. In practice, brightfield systems always encounter signal variations that require frequent adjustment of the alignment algorithm, often within each individual wafer. While this adjustment can be automated, there is no known algorithm which, even in principle, can accurately infer the location of underlying mark edges when presented with signals exhibiting the dramatic variety of profiles that are obtained with brightfield systems, even in the broadband case. Darkfield signals usually show a much smaller variation in shape.

Darkfield systems can have difficulty aligning to grainy metal levels which have pronounced scattering at large angles. SNR is enhanced for these cases by choosing a suitable deadband between illumination and collection apertures to remove light scattered at small angles from the signal. Additional spatial filtering can be tailored around the detailed angular distribution of the diffracted alignment signal from the marks.

Confocal systems offer some immunity to thin film interference by reducing the vertical dimension over which light from the object can reach the detector. However, brightfield confocal alignment does not outperform darkfield optics, and requires a more complex optical system. Combination of darkfield illumination with confocal optics may provide the ultimate insensitivity to mark topography. Conventional darkfield systems offer SNR which usually equal or exceed brightfield systems despite the much lower overall light levels. This is an intrinsic result [1] (the strong specular background in brightfield signals conveys no information about edge position), but requires that the detection system provide a near-shot-noise limited signal. This and other engineering requirements are more difficult to achieve with darkfield confocal optics.

Darkfield optics for lithography were developed during the 1970's, initially for direct mask to wafer registration through the lens (TTL). A system developed by Wilczynski [4] images a narrow, subresolution mask fiducial onto the wafer through the central 0.5 of the available NA of the projection lens. An alignment signal is formed from scattered light collected through the outer NA as the fiducial image scans the edge of the wafer mark. SNR is increased by simultaneous scanning of an extended pattern of alignment marks. This type of system is used with broadband radiation in proximity x-ray lithography [5], and for both on-axis and off-axis alignment on GCA steppers [6]. The role of illumination and collection apertures can be reversed so that the mask fiducial is imaged through the outer NA, and signal collection occurs through a small portion of the center of the pupil. This latter system, conceived by Hershel [7] and Ultratech Stepper, incorporates spatial filtering to block light scattered perpendicular to the alignment scan direction. Tailoring the wafer mark design to illumination-collection deadband and directional spatial filtering greatly improves SNR. A direct mask to wafer system developed by Philips [2] for ASM lithography illuminates a grating feature on the wafer by a laser beam introduced at the lens pupil. Coherent interaction of the grating features concentrates diffracted light into  $\pm 1$  orders which are passed through the lens pupil by spatial filters. The interfering orders are correlated to a reticle

grating. Correlation is accomplished by modulation of the fringe pattern relative to the mask by an electro-optic polarization plate and synchronous detection.

The systems above use TTL optics to directly align the mask to the wafer, or to register the wafer to an intermediate fiducial whose relation to the mask is calibrated in a separate procedure. The latter approach, referred to as TTL alignment with baseline correction, is often used in projection optics which are not corrected for imaging at both the exposure and alignment wavelengths. Resists always have significant absorption at the exposure wavelength, and this absorption has tended to increase as wavelengths have decreased. In practice, it has proved difficult to obtain useful alignment signals at exposure wavelengths of 365nm or below, even if exposure of the resist by the alignment system is allowed. Alignment must then be carried out at longer wavelengths. Due to the index dispersion of optical materials, auxiliary correction optics are often required to achieve direct TTL alignment in the visible when the exposure wavelength is below 400nm. X-ray scanning projection printers, though achromatic in principle, may have unsatisfactory TTL optical alignment performance because of coating phase shifts, low coating reflectivity, and packaging constraints which limit the NA. The ASM wafer grating technique is a candidate for direct TTL mask-wafer registration in soft x-ray lithography because of the high illumination radiance of the laser. The system is also suited to low NA optics because the resolution of interfering  $\pm 1$  orders of a grating is  $\lambda/2NA$ , compared to  $\lambda/NA$  for imaging which includes the DC or zero order diffraction. TTL systems with baseline correction require long term dimensional stability because calibration of the intermediary fiducial to the mask and alignment system is time consuming. Recalibration at mask changes is avoided over the short term by registering the mask to a set of markers on the optical column. Although this indirect method is useful at 0.5 to 1.0  $\mu\text{m}$  geometries, the extra alignments and dimensional drift may use a substantial portion of the error budget for lithography below 0.3  $\mu\text{m}$ .

One step removed from TTL with baseline correction, is non-TTL alignment with baseline correction in which the alignment optics do not use the projection lens. In the best scenario, the auxiliary alignment optics are located near the center of the projection field and alignment marks in the chip kerf. In practice, packaging constraints usually require marks to be placed in outlying chipsites, making the system more sensitive to wafer distortions. Alternatively, the stage can move off axis to view the alignment marks accepting a performance degradation from inplane geometric and interferometric metrology errors. One possible configuration uses soft x-ray projection imaging to register the mask alignment aids to a fiducial on the wafer stage by transmission x-ray detection, or photo-emission. The same fiducial is registered to the off axis optical alignment system transferring the mask location to the TTL system.

There are no physical limitations to achieving alignment accuracies below 50nm in alignment times of 500 mS or less. Considerable progress has been made in improving the planarization and uniformity of mark coatings. However,

registration and printing integrity is a system problem as well as a mark registration problem. Dimensional stability of the order of 10 nm in a few hundred millimeters is required, and must be maintained for a day or more. The system must have sufficient mechanical stiffness and

damping to remove self-induced vibrations originating from stage motions. Self vibration is a particular problem for scanners which have a very limited settling time after each acceleration.

1. N. Bobroff and A. Rosenbluth, "Alignment errors from resist coating topography," *J. Vac. Sci. Tech.* **B6**, 403-408 (1988).
2. G. Bouwhuis and S. Wittekoek, "Automatic alignment system for optical projection printing," *IEEE Trans. Elec. Devices*, **ED26**, 723-728 (1979).
3. N. Magome, K. Ota, and K. Nishi, "New alignment sensors for optical lithography," *JJAP* **29**, 2577-2583 (1990).
4. J. Wilezynski, "Optical step and repeat camera with dark field automatic alignment," *J. Vac. Sci. Tech.* **16**, 1929-1933 (1980).
5. N. Bobroff, "An optical alignment microscope for x-ray lithography," *J. Vac. Sci. Tech.* **B4**, 285-289 (1986).
6. D. Beaulieu and P. Hellebrekers, "Dark field technology - a practical approach to local alignment," *Proc. Soc. Photo-Instrum. Eng.* **772**, 142 (1987).
7. R. Herschel, "Autoalignment in step and repeat wafer printing," *Proc. Soc. Photo-Instrum. Eng.* **174**, 54 (1979).



AD-P007 237



## Reflection Mask Technology for Soft-X-Ray Projection Lithography

A. M. Hawryluk, N. M. Ceglio, D. W. Phillion, and D. P. Gaines\*  
*University of California, Lawrence Livermore National Laboratory,  
P.O. Box 5508, Livermore, California 94550*

R. Browning and R. F. Pease  
*Center for Integrated Systems, Stanford University, Palo Alto, California  
94305*

D. Stewart and N. Economou  
*Micrion Corporation, Peabody, Massachusetts 09160*

### ABSTRACT

Soft X-ray Projection Lithography (SXPL) may be used to fabricate high resolution structures for future integrated circuits. This technique will use a reflection mask which is a substrate coated with an x-ray multilayer mirror and patterned with a thin (~50 nm) layer of x-ray absorber. Mask patterning processes must not degrade the reflectivity of the x-ray mirror and mask repair techniques must be developed.

The technical challenges of conventional reflecting optical imaging system designs are severe and mask technology can have a significant impact on this issue. Specifically, innovative mask designs can reduce the complexity of the optical system by decreasing the number of mirrors and replacing aspheric optical surfaces with spherical surfaces. We have developed a technique, called Encoded Mask Lithography, with which we have designed an optical system which uses only two (spherical) imaging mirrors and has < 100 nm spatial resolution, negligible distortion and > 30 mm diameter field of view.

### Introduction

Soft X-ray Projection Lithography (SXPL) is a promising new technique for the replication of high resolution patterns suitable for the fabrication of ultra-high density circuits (1-3). One key element in SXPL is the x-ray reflecting mask which typically is a thin (~50-100nm) gold pattern on an x-ray reflecting multilayer mirror, figure 1. A successful SXPL capability will require the development of mask patterning, inspection and repair technologies. We will report on current work in SXPL mask patterning and repair.

It has long been appreciated that the mask is an integral part of any lithographic system and a properly configured mask can improve resolution (for example: "phase shifting" masks in optical lithography) or reduce improper line placement (for example: reduce "runout" in x-ray proximity print lithography). Using the mask as an integral component of the optical system, we report on a new approach to lithography, called Encoded Mask Lithography, which can reduce the severe demands on projection imaging optics and still achieve < 100 nm spatial resolution with negligible distortion over a large (~30 mm diameter) field of view.

\*Visiting Scientist from Department of Physics, Brigham Young University, Salt Lake City, Utah.

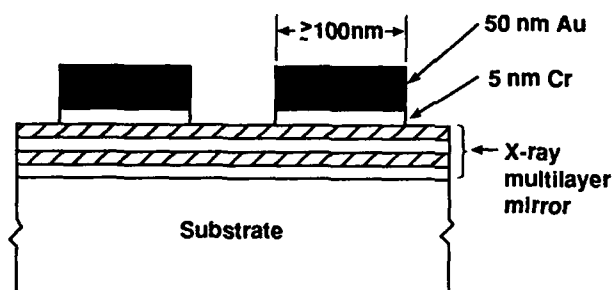


**Figure 1** A Soft x-ray Projection Lithography mask will consist of a thin Cr/Au pattern on top of an x-ray multilayer mirror.

#### Mask Patterning

We have patterned SXPL masks with both optical and e-beam lithography. Optical lithography has been used (4) to pattern 100 nm thick gold on a substrate coated with an x-ray multilayer mirror designed for normal incidence operation at  $\lambda=13\text{nm}$ , figure 2. The x-ray mirror was composed of 30 layer pairs of molybdenum and silicon, with a period ("d spacing") of 6.7 nm. X-ray reflectivity measurements were made on the mask and the reflectivity was similar to the reflectivity measured from (unpatterned) monitor mirrors. The contrast on these masks (i.e. the ratio of measured intensity reflected from the mirror relative to the measured intensity reflected from the gold coated areas) was greater than 500:1.

For high resolution SXPL, it may be necessary to use electron beam lithography to pattern the SXPL mask. However, the effect of an electron beam on a multilayer mirror has never been studied. We exposed an x-ray multilayer mirror to varying dosages (1-400  $\mu\text{C}/\text{cm}^2$ ) of a 10 KeV electron beam, figure 3, measured the normal incidence x-ray reflectivity from multilayer regions exposed to the electron beam and compared this to the reflectivity from unexposed multilayer mirror regions, figure 4. Within the accuracy of the measurement, the electron beam had no effect on the multilayer mirror x-ray reflectivity.

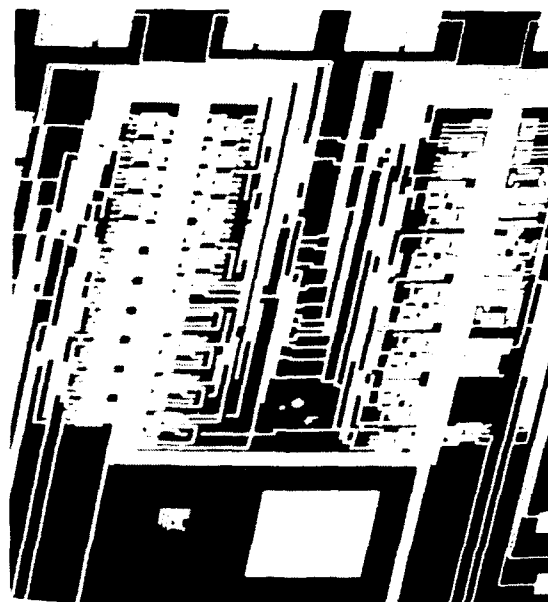


**Figure 2** A scanning electron micrograph of a Soft X-ray Projection Lithography Mask, consisting of a 100 nm thick gold pattern on a x-ray multilayer mirror. The minimum linewidth in this pattern is 8 microns.

From these two experiments, we conclude that both optical and electron beam lithography (and subsequent resist processing) can be safely used to pattern a SXPL mask without degrading the reflectivity of a molybdenum/silicon multilayer mirror.

#### Mask Repair

A successful SXPL mask technology will require the capability to repair mask defects which can arise during the fabrication process. In general, there are two types of mask defects: a region on the mask which is highly reflecting when it should be non-reflecting, and a region on the mask which is non-reflecting when it should be reflecting. The first type of defect is relatively easy to repair; it requires the local degradation of the multilayer mirror reflectivity. This can be accomplished by locally depositing a thin layer of absorbing metal (5), by removing the multilayer mirror (using a local etch), or by disrupting the coherence between the multilayer mirror layers (using ion bombardment). The possible processes required for this defect repair utilize

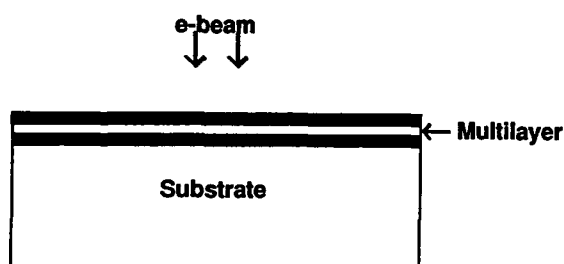


**Figure 3** An x-ray mirror was exposed to a 10 KeV electron beam with dosages ranging from 1-400  $\mu\text{C}/\text{cm}^2$ .

technologies developed for other applications within the integrated circuit industry.

The second type of defect repair (transforming a non-reflecting region to a reflecting region) requires the local improvement of mirror reflectivity. A likely cause of this defect is residual gold in a region where gold is not required. Similar defects are seen in proximity print x-ray lithography masks and have been successfully repaired using focused ion beam etching (6).

We simulated SXPL mask repair by first depositing a thin layer of chromium and gold (5 and 50 nm) onto a 40 layer pair, molybdenum/silicon x-ray multilayer mirror ( $d \sim 6.7$  nm). Subsequently, we removed the Cr/Au from two areas using focused ion beam etching (25 KeV Ga ions, 4 namp current), figure 5. An endpoint detector was used to determine when the process was completed. Optical microscopy did not indicate any obvious damage to the ion beam etched regions. We measured the normal incidence x-ray reflectivity from the etched regions and compared these to the reflectivity from unprocessed multilayer regions, figure 6.

The x-ray reflectivity data shows reduced reflectivity from the ion beam etched regions. The cause of this degradation in reflectivity is currently under investigation. It could result from residual Cr/Au on top of the multilayer or ion-beam induced mixing within the multilayer. We plan to examine

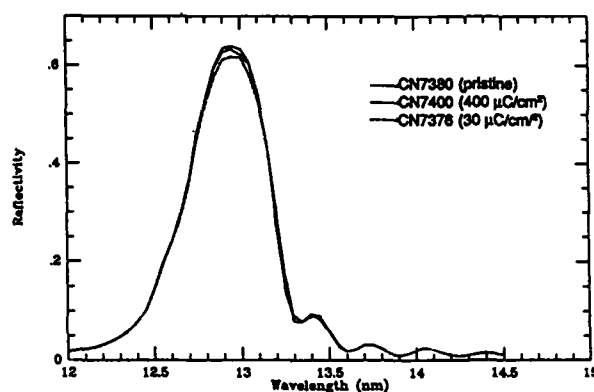


**Figure 4** The x-ray reflectivity from multilayer mirrors exposed to varying electron beam dosages. The e-beam had no measurable effect on the x-ray mirror reflectivity.

these samples in a transmission electron microscope. If the degradation is a result of ion beam induced multilayer mixing, future experiments will use lower energy and possibly lower atomic mass ion beams for Cr/Au etching.

#### The Mask As Part of the Optical System

The development of SXPL into a practical tool for lithography will depend critically upon the design and fabrication of a practical, high resolution ( $<100$  nm), low distortion ( $<10$  nm) optical imaging system. Two different strategies for optical systems have been proposed: "Step and Repeat" optical systems, which image the entire chip but require large aspheric optics, versus "Step and Scan" optical systems which image a small annular segment of a chip, requiring smaller aspheric optics but also dynamic alignment between the moving mask and wafer. Many simple, high resolution imaging systems using spherical optics exist but do not meet the distortion requirement for lithography. To date, several optical designs that meet the resolution and distortion requirements for lithography have been suggested (7-10). However, the optic figure requirements for even the smallest aspheric optic in the above designs exceeds

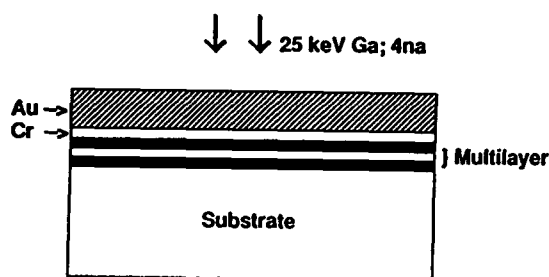


**Figure 5** An x-ray multilayer mirror was coated with 5 nm Cr/50 nm Au and this metalization layer was then etched with a 25 KeV Ga ion beam. This simulated ion-beam repair of a non-reflecting mirror region.

present state-of-the-art metrological and fabrication techniques. Using spherical optics with a curved mask has been suggested (1,11) but is considered impractical because of the anticipated difficulties in writing the mask and aligning the optical axis of the curved mask to the optical axis of the imaging system.

We have found a solution to the twin problems of writing and aligning curved reflection masks. In an imaging system which is free of point aberrations, each point in the object maps to a unique, diffraction limited point in the image. If such an optical system produces a high resolution, but distorted, image of a reticle, then a pattern made from the distorted image will produce an undistorted image of the original reticle when viewed through the same optical system in the reverse direction, figure 7. There is no significant loss in resolution provided the spherical aberration, coma and astigmatism are small. We call the pattern created from the distorted image an "Encoded Mask" because this mask contains the information of the original reticle, encoded with the distortions of the imaging system. If the imaging system has both field distortion and field curvature, then the surface of the Encoded Mask must follow the surface of the field curvature, to within the depth of focus of the imaging system. The Encoded Mask is recorded only once and can be used many times to replicate the original reticle onto many wafers, figure 8.

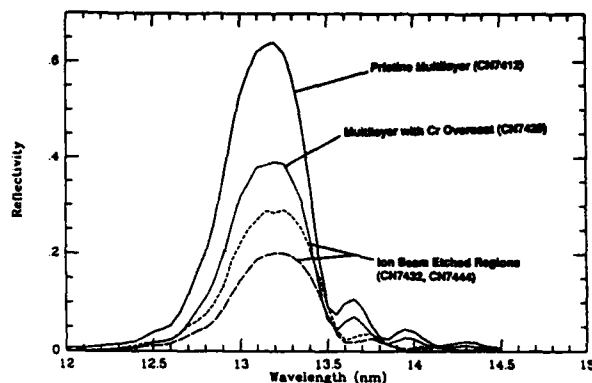


**Figure 6** The x-ray reflectivity of ion beam "repaired" regions (using 25 KeV Ga ions) was significantly reduced from the reflectivity of unprocessed mirror regions. The x-ray reflectivity from a multilayer coated with 5 nm Cr is shown for comparison.

#### A High Resolution Optical System With Field Distortion And Field Curvature

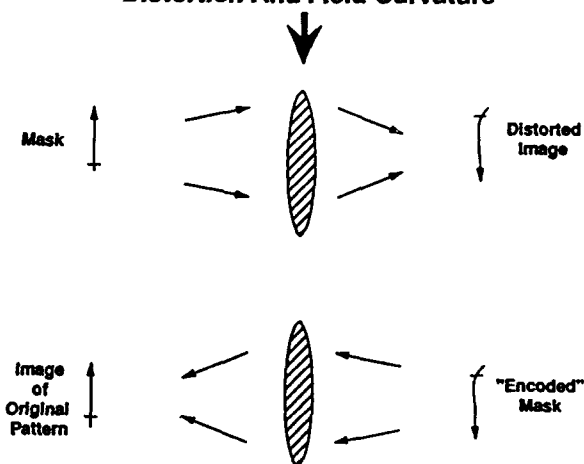


**Figure 7** In an optical system, there exists a unique mapping between each point in the object plane and each point in the image plane. Therefore, a replica of a distorted image can recreate the original pattern with no distortions when imaged through the optical system in the reverse direction.



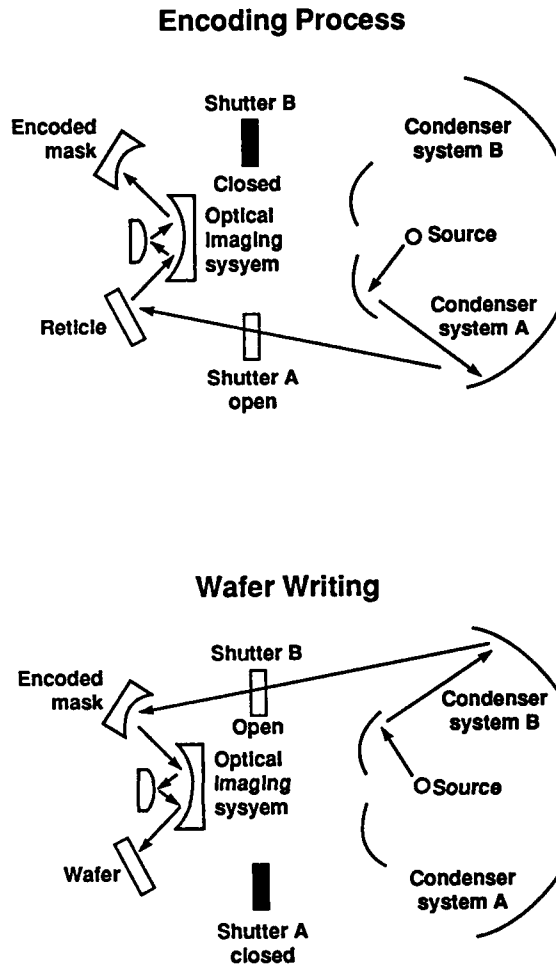


**Figure 8** (Top) An Encoded Mask is generated from a reticle using a high resolution optical system with arbitrary distortion. All the information in the reticle, along with the distortion of the optical system, are recorded in the Encoded Mask. (Bottom) The Encoded Mask can now be used to pattern wafers. By imaging the Encoded Mask through the optical system in the reverse direction, the distortions in the optical system are exactly canceled.

The major benefit of Encoded Mask Lithography is that one can use simple optical systems with a small number of spherical mirrors and still perform high resolution, low distortion lithography. In particular, a high resolution imaging system using two spherical mirrors can be used regardless of its intrinsic distortion. Alignment of the Encoded Mask to the optical system can be achieved by aligning the Encoded Mask to the original reticle first.

The major difficulty with Encoded Mask Lithography is the need to fabricate a 1X reticle, although the optical system can have arbitrary magnification between the reticle and the Encoded Mask.

We have analyzed several spherical mirror optical designs which use either two or three bounces between the reticle (or wafer) and the encoded mask. One attractive design is shown in figure 9. This design uses two spherical mirrors (100 and 300 mm in diameter with radii of curvature ~560 and 1400 mm respectively) and three bounces between the reticle and the Encoded Mask. The Encoded Mask itself is spherical, but its radius of curvature is very large (1.6 meters). Using Encoded Mask Lithography, this spherical optical imaging system with modest mirror sizes is capable of < 100 nm resolution with negligible distortion over a 30 mm diameter field of view.

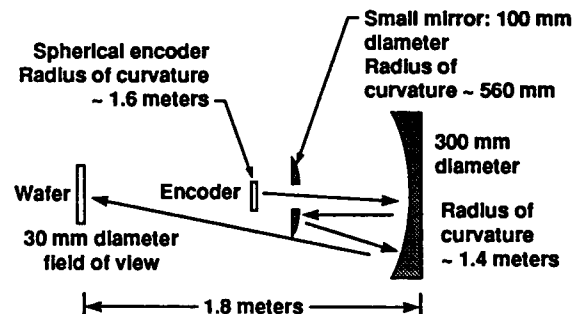


**Figure 9** An example of Encoded Mask Lithography using a simple, all spherical optical system design. This system has <100 nm spatial resolution with zero distortion over a 30 mm diameter field of view.

### Conclusions

We have reviewed the current status of SXPL mask patterning and mask repair. Both optical and electron beam lithography (and subsequent processing) can be used to pattern thin gold on x-ray multilayer mirrors to produce a SXPL mask. The investigation of ion beams for SXPL mask repair has just begun and preliminary results indicate that the ion beam degrades the reflectivity from the multilayer mirror. Future work in this area will include damage identification (using transmission electron microscopy) and damage reduction (possibly using lower energy and lower mass ion beams).

We have presented an innovative optical design, Encoded Mask Lithography for high resolution, low distortion lithography. In Encoded Mask Lithography, a simple optical system is used to record the image of a reticle onto an "Encoded Mask". This image is "played-back" through the same optical system, canceling both field distortion and field curvature and producing a distortion-

free replication of the original reticle. We have shown a simple, two spherical mirror optical system which is capable of  $< 100$  nm spatial resolution with negligible distortion over a 30 mm diameter field of view.

### Acknowledgments

The authors would like to acknowledge the contributions from the Advanced X-ray Optics Program at the Lawrence Livermore National Laboratory, in particular: D. Stearns, R. Rosen, S. Vernon, R. Hostetler, S. Hill, J. Hayes and W. Cook. The x-ray reflectivity measurements were made in a collaborative association with P. Müller, M. Krumrey and

M. Kühne of the VUV Radiometric Laboratory of the Physikalisch Technische Bundesanstalt at BESSY. In addition, this Projection Lithography work would not be possible without the active support of J. I. Davis, E. M. Campbell and E. Storm of LLNL. This work was performed under the auspices of the U.S. Department of Energy by the Lawrence Livermore National Laboratory under contract number W-7405-Eng-48.

### References

- 1) A.M. Hawryluk, et al; J. Vac Sci Tech B; Vol. 6, No. 6, p 2162, 1988
- 2) J. Bjorkholm, et al; J. Vac Sci Tech B; Vol 8, No. 6, 1990
- 3) H. Kinoshita, et al; J. Vac Sci Tech B; Vol 7, No. 6, p 1648, 1989
- 4) A. Hawryluk, et al; J. Vac Sci Tech B; Vol 7, No. 6, p 1702, 1989
- 5) D. Stewart, et al; SPIE, Vol 1089, p 18, 1989
- 6) H. Petzol, et al; SPIE, Vol 1089, p 45, 1989
- 7) T. Jewel, et al; Conference Proceedings of the OSA Annual Meeting; Boston, Ma, Nov. 1990
- 8) D. Shafer; Conference Proceedings of the OSA Meeting on Soft X-ray Projection Lithography; April 1991
- 9) V. Viswanathan, et al; Conference Proceedings of the OSA Meeting on Soft X-ray Projection Lithography; April, 1991
- 10) D. Shealy, et al; Conference Proceedings of the OSA Meeting on Soft X-ray Projection Lithography; April, 1991
- 11) F. Bijkerk, et al; Conference proceedings of the OSA Meeting on Soft X-ray Projection Lithography; April, 1991



## Design of an Extended Image Field Soft-X-Ray Projection System

F. Bijkerk, H. -J. Voorma, E. J. Puik, E. Louis, G. E. van Dorssen, and M. J. van der Wiel  
FOM-Institute for Plasma Physics Rijnhuizen, P.O. Box 1207, 3430 BE Nieuwegein,  
The Netherlands

J. Verhoeven  
FOM-Institute for Atomic and Molecular Physics, Amsterdam, The Netherlands

E. W. J. M. van der Drift, J. Romijn, and B. A. C. Roussecuw  
DIMES, Delft, The Netherlands

### Abstract

A soft-X-ray projection system has been designed, consisting of all-reflective multilayer optics. The design enables 0.1  $\mu\text{m}$  resolution over a wide circular image field of 12.5  $\text{mm}^2$ .

### Introduction

Optical systems for X-ray projection lithography use various normal-incidence geometries to realize sub-0.1  $\mu\text{m}$  resolution with a depth of focus of  $\sim 0.5 \mu\text{m}$ . To meet all other lithography imaging requirements, with respect to telecentricity, distortion, and image field size, the number of components in such a design can be as high as five, often including aspherical elements. Since the reflectivity of the applied multilayer mirrors in the XUV wavelength range ( $\lambda < 15 \text{ nm}$ ) used for this application is limited to 50 to 70 % per mirror, multi-component designs have a limited throughput. The complexity of the alignment of the optics also scales with the total number of components. Schwarzschild-like designs<sup>1</sup> use only two optical components, but have an image field which is too small ( $\sim 10^{-2} \text{ mm}^2$ ) for practical application of chip manufacture. A solution to achieve significantly larger image fields using two-component optics, is to allow a spherically curved object field.

### Results

The optical system for projection lithography designed in this study is a con-focal two-mirror system and a concave reflection mask (Fig. 1). All components are spherical. The system uses a reduction factor of 10; it is optimized to yield a resolution of better than 50 nm over a large, flat circular image field of  $\sim 12.5 \text{ mm}^2$ . The system is free of third order aberrations and coma over this image field. Data of the components are given in Tab. 1. Tab. 2 gives the inter-component distances.

The image field curvature resulting from imaging flat objects with a two-component system, can be compensated by applying curved objects. For this purpose we approximated the exact object figure by a spherical surface with a radius of 73.4 mm. This surface figure results in a flat image field of  $\sim 12.5 \text{ mm}^2$ . Larger fields require aspheric

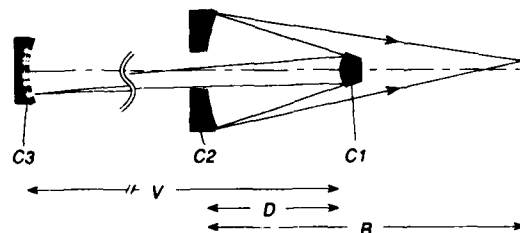


Fig. 1. Outline of the design.

|   | $C_1$ (mm) | $C_2$ (mm) | $C_3$ (mm) |
|---|------------|------------|------------|
| R | -100       | 316        | 73.4       |
| A | 22         | 120        | 40         |
| P | -          | 55         | -          |

Tab. 1. R are the radii of curvature of the mirrors ( $C_1$ ,  $C_2$ , and  $C_3$ ), A the outer diameters and P the diameter of the central hole.

| V (mm)   | B (mm)   | D (mm)   |
|----------|----------|----------|
| 698.6062 | 396.3637 | 216.0700 |

Tab. 2. Distances between the components. The notation refers to the symbols in Fig. 1.

object surfaces. Fig. 2 gives the curvature of the image field for different radii of the object. We note that the required surface accuracy of the object amounts to 200 nm. This is two orders of magnitude less than the accuracy required for components  $C_1$  and  $C_2$ . By avoiding the use of aspherical components, this design relaxes the requirements on the substrate fabrication technique.

The system is optimized with respect to depth of focus (DOF) and throughput. The resulting diameters of the mirrors are given in Tab. 1. According to the Rayleigh criterion ( $\text{DOF} = \pm \lambda/2(\text{Na})^2$ ), the DOF amounts to 440 nm for a wavelength of 10 nm. The geometrical resolution is plotted in Fig. 3. Curve c) shows that a resolution of 50 nm can be achieved over an image field with a diameter of 4 mm.

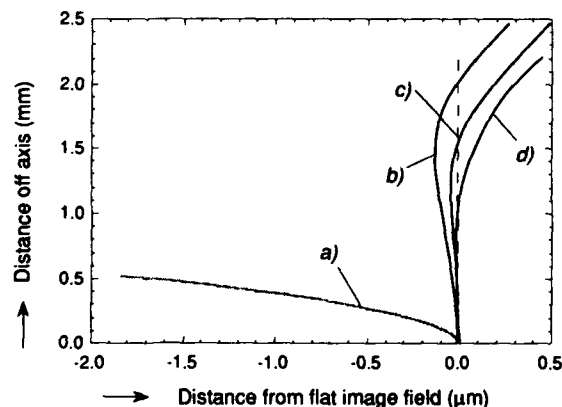


Fig. 2. Curvature of the image field for different curvatures of the object: a) flat object; b), c), and d) spherical objects with radii of resp. 73.8 mm, 73.4 mm, and 73.0 mm.

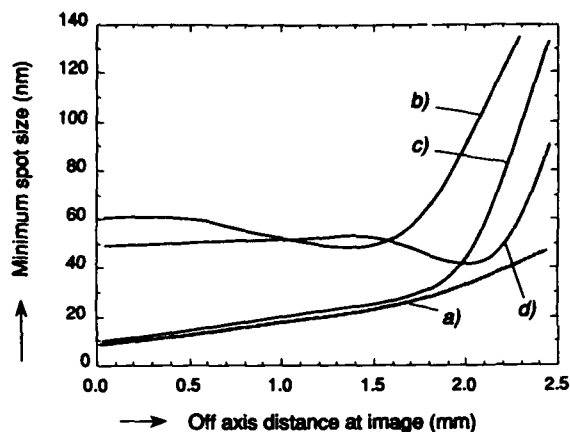


Fig. 3. Resolution at the image field versus distance off axis. Curve a) is in the case of a curved image field; b), c), and d) are for flat image fields, resp. -0.25  $\mu\text{m}$  out focus, in focus, and +0.25  $\mu\text{m}$  out focus.

A novel coating-facility will be used for production of the multilayer coatings on the curved substrates. It is suitable for coating of highly curved or large mirror substrates. The dual vacuum chamber set-up uses the electron-beam deposition technique and allows ion-beam assisted deposition.<sup>2</sup>

Mask patterning of Ni/C multilayer structures is done by electron-beam writing in multilayer resist structures spun on a Ni/C stack. Using subsequent low-pressure plasma etching the structures are transferred into the Ni/C multilayer. Fig. 4 is a micrograph of a 0.5  $\mu\text{m}$  line-and-space pattern. For the patterning process of curved masks, analogues approaches will be studied.

## Conclusion

To investigate the feasibility of simple, demagnifying optical systems for X-ray projection lithography, a three component system has been designed, consisting of two spherical elements and a spherical reflection mask. The system uses a reduction factor of 10 and it is optimized to yield a resolution of better than 50 nm over a large, flat circular image field of  $\sim 12.5 \text{ mm}^2$ .



Fig. 4. SEM micrograph of 0.5  $\mu\text{m}$  line-and-space pattern transferred into a Ni/C multilayer structure.

### Acknowledgments

These investigations in the research programme of FOM, the Foundation for Fundamental Research on Matter, have been supported by the STW, the Netherlands Technology Foundation, and the Netherlands Government in the framework of EUREKA.

### References

- <sup>1</sup> A.K. Head, Proc. Phys. Soc. LXX 10 B (1957) pp.944-949
- <sup>2</sup> E.J. Pulk, M.J. van der Wiel, H. Zijllemaker and J. Verhoeven, Appl. Surf. Sc. 47 (1991) 251-260



## Soft-X-Ray Projection Imaging Using a Laser Plasma Source

D. A. Tichenor, G. D. Kubiak, M. E. Malinowski, R. H. Stulen, S. J. Haney, K. W. Berger,  
and L. A. Brown

*Sandia National Laboratories, P.O. Box 969, Livermore, California 94551-0969*

R. R. Freeman, W. M. Mansfield, O. R. Wood II, D. M. Tennant, and J. E. Bjorkholm  
*AT&T Bell Laboratories, Crawfords Corner Road, Holmdel, New Jersey 07733-1988*

T. E. Jewell, D. L. White, D. L. Windt, and W. K. Waskiewicz  
*AT&T Bell Laboratories, 600 Mountain Avenue, Murray Hill, New Jersey 07974-2070*

### Abstract

Printing of 0.1  $\mu\text{m}$  features is demonstrated using a Mo/Si multilayer coated Schwarzschild objective and 140  $\text{\AA}$  illumination from a laser plasma source.

### Introduction

The feasibility of producing small feature sizes in resists using soft x-ray projection lithography has been demonstrated [1]. Experiments by AT&T Bell Laboratories [2] have achieved features small as 0.05 microns using a Schwarzschild objective and 140  $\text{\AA}$  radiation from an undulator at the National Synchrotron Light Source. We describe here a similar imaging system in which the illumination is derived from a high-fluence laser plasma source (LPS) of soft x-rays instead of a synchrotron radiation source. The laser plasma source has been shown to be a useful illumination source for soft x-ray microscopy [3]. It offers significant advantages of size and cost over synchrotron sources but with some trade-offs. The intent of the work described in this paper is to

determine the viability of the LPS for future implementation of soft x-ray projection lithography (SXPL).

### Experimental Arrangement

Figure 1 shows a schematic of the imaging apparatus. The Schwarzschild design is similar to the one used previously [2] by AT&T Bell Laboratories. It is a 14.265 mm focal length objective, fabricated and aligned by GCA Corporation/Tropel Division. Total figure and alignment error is estimated at  $\lambda/4$  at 140  $\text{\AA}$ . Both surfaces were multilayer coated with 20 layer pairs of Mo/Si to provide a reflectivity of  $\sim 40\%$  at 140  $\text{\AA}$ . A decentered entrance pupil, 1.78 mm in diameter, placed between the mask and the objective, reduces the numerical aperture to 0.08 and provides a 1  $\mu\text{m}$  depth of field at the wafer. The diffraction limited image field is approximately 25  $\mu\text{m}$  by 50  $\mu\text{m}$ .

The Sandia high-fluence laser plasma source [4] uses an excimer laser (KrF) running at 100 Hz with  $\sim 1.5$  J/pulse. The laser light is focused onto a rotating, gold coated, target drum producing a 15 eV plasma



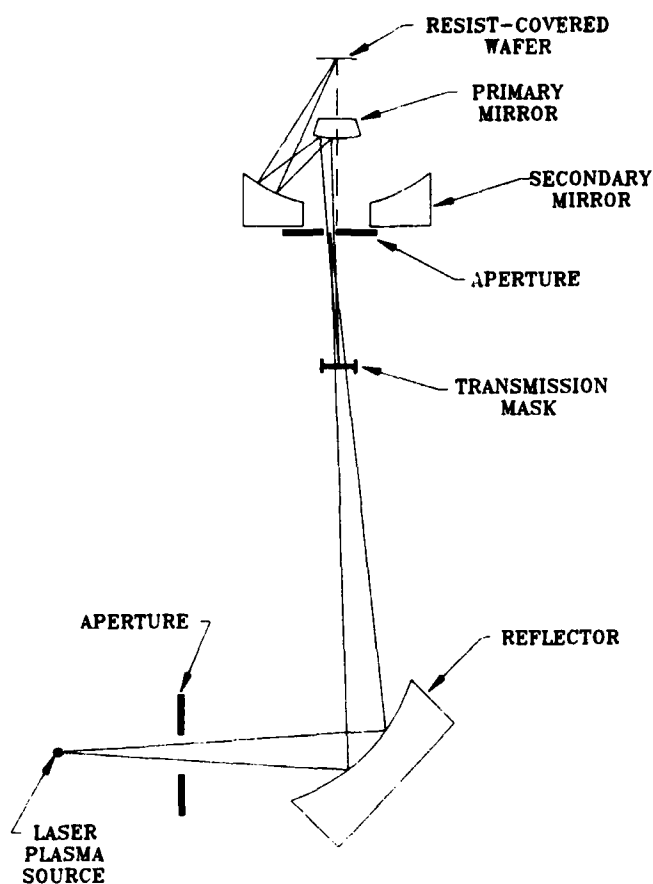


Figure 1. Soft x-ray projection imaging system

which emits an intense burst of soft x-rays from a spot having a variable diameter from  $150\ \mu\text{m}$  to  $300\ \mu\text{m}$ . The flux from this source has been calibrated and, in the spectral region around  $120\ \text{\AA}$ , is found to be competitive with that obtained from bending magnet beamlines at synchrotron radiation sources. Figure 2 compares the spectrum of a 15 eV black body, approximating that of the laser plasma source, to the spectral reflectance of a Mo/Si multilayer coating and the spectral transmittance of a silicon membrane. The LPS spectrum is a good match to the multilayer coatings and membranes which comprise the optical elements available in the soft x-ray region.

Soft x-rays from the laser plasma source are collected by a multilayer mirror and reflected upward into the entrance pupil of the Schwarzschild objective. The system is designed for an ellipsoidal illuminator with

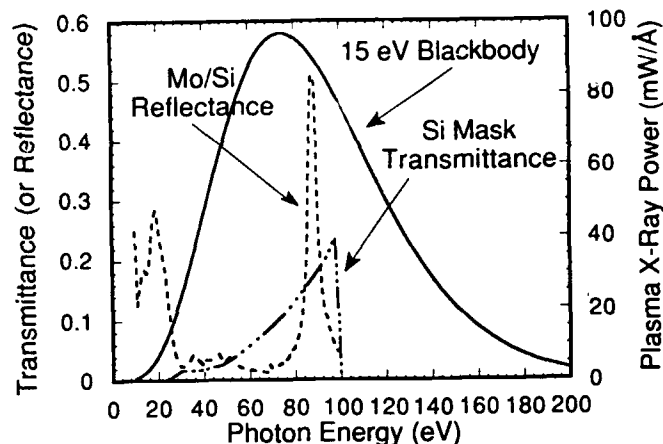


Figure 2. 15 eV blackbody spectrum compared to silicon mask transmittance and Mo/Si multilayer reflectance.

foci at 250 mm and 1500 mm from the center of the mirror. An image, magnified 6x, of the laser plasma source is projected into the entrance pupil of the Schwarzschild, providing Kohler illumination with under fill ratio varying from 0.5 to 1.0 depending on the selected source size.

### Condensing Optics

Pending delivery of the ellipsoidal mirror, imaging experiments were conducted using a spherical mirror having a radius of 600 mm as the condensing system. This mirror was multilayer coated for  $45^\circ$  incidence at  $140\ \text{\AA}$  achieving a reflectivity of about 30%. X-rays from the laser plasma source illuminate the spherical mirror through a rectangular aperture 10 mm in y (in the plane of Figure 1) by 3 mm in x (out of plane). The aperture is placed over the mirror to protect the unused part from gold deposition which is suppressed using a helium overpressure. Gold deposition degrades the reflectivity of the condensing reflector by 30% after one million laser pulses. When properly aligned the condenser forms a line focus at the aperture plane having the narrow (focused) dimension in the y direction. In the x direction the beam continues to expand.

There are two consequences of using the spherical condenser. First, since the x-rays

are not focused in the x direction, the mask illumination is of much lower intensity than that expected from the ellipsoid. An estimated 20 times longer exposure is required to compensate. Second, the under fill factor is different in the two directions. Using a source size of  $150\text{ }\mu\text{m}$  the under fill factor determined by tracing rays from the perimeter of the source through the center of the mask plane to the aperture plane is 0.52 in y. This value provides nearly the optimum partial coherence for lithography. In the x direction, however, the under fill factor is 0.025 resulting in nearly spatially coherent illumination in x. Furthermore, illumination is nonstationary as a function of x. Approximate stationarity is achieved for x much less than the entrance pupil radius. Imaging experiments using the spherical illuminator concentrate on features in the y direction where the desired illumination is achieved.

### Imaging results

Images of a transmission mask were recorded on silicon wafers coated with PMMA resist 400 to  $600\text{ }\text{\AA}$  in thickness. The transmission mask consists of a  $7000\text{ }\text{\AA}$  silicon membrane containing a germanium template created by e-beam lithography and reactive-ion etching. Lines and spaces included on the mask are: 10, 7.5, 5, 4, 3, 2 and  $1\text{ }\mu\text{m}$  in width, which image at 20:1 reduction to 0.5, 0.375, 0.25, 0.2, 0.15, 0.1 and  $0.05\text{ }\mu\text{m}$  lines and spaces, respectively. The overall dimension of the mask is  $1/2\text{ mm}$  square. Wafers were placed on three ball bearings which locate the image plane and exposed for about 7 to 10 minutes. The estimated exposure time for the ellipsoid illuminator is 20 seconds.

X-ray images were recorded using an numerical aperture of 0.08. The  $0.1\text{ }\mu\text{m}$  lines were completely cleared in the resist as were larger features. In the diffraction-limited incoherent limit the modulation is 0.44 at this frequency (5000 line pairs/mm). No modulation is observed in finer features which approach the cut off frequency for this numerical aperture.

The NA was increased to 0.12. Although aberrations begin to increase at this aperture,

$0.1\text{ }\mu\text{m}$  features are again recorded with high contrast and a slight modulation is observed at  $0.05\text{ }\mu\text{m}$  lines and spaces (10,000 line pairs/mm). An atomic force micrograph of a soft x-ray image in PMMA is shown in Figure 3. At 10,000 line pairs/mm the diffraction-limited modulation transfer function for this aperture is less than 0.3.

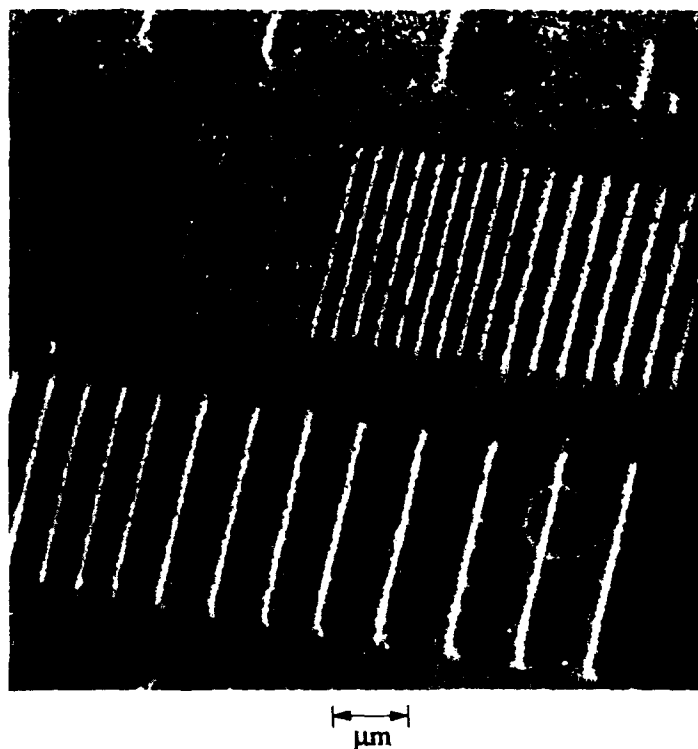


Figure 3. Atomic force micrograph of soft x-ray image at NA 0.12 in PMMA showing high contrast recording of features down to  $0.1\text{ }\mu\text{m}$  and low contrast recording of  $0.05\text{ }\mu\text{m}$  lines and spaces.

### Conclusion

We have demonstrated soft x-ray projection imaging at  $140\text{ }\text{\AA}$  wavelength with diffraction-limited performance using a laser plasma source. Features as small as  $0.1\text{ }\mu\text{m}$  have been recorded with high contrast in PMMA resist. These results were obtained using a non-ideal illuminator. Improvement in the 2-D image quality and exposure time is expected with correct illumination optics.



\* Work at Sandia National Laboratories has been supported by the U.S. Department of Energy under contract #DEACO4-76DP00789.

W. T. Silfvast, L. H. Szeto, D. M. Tennant, W. K. Waskiewicz, D. L. White, D. L. Windt, O. R. Wood, II, and J. H. Bruning, "20:1 projection soft x-ray lithography using tri-level resist," Proceedings of the SPIE Symposium on Microlithography, paper 1263-34, March, 1990, San Jose.

Reference:

1. H. Kinoshita, K. Kurihara, Y. Ishii and Y. Torii, "Soft x-ray reduction lithography using multilayer mirrors," J. Vac. Sci. Technol. **B7** (6), 1648 (1989)
2. T. E. Jewell, M. M. Becker, J. E. Bjorkholm, J. Bokor, L. Eichner, R. R. Freeman, W. M. Mansfield, A. A. MacDowell, M. L. O'Malley, E. L. Raab, W. T. Silfvast, L. H. Szeto, D. M. Tennant, W. K. Waskiewicz, D. L. White, D. L. Windt, O. R. Wood, II, and J. H. Bruning, "20:1 projection soft x-ray lithography using tri-level resist," Proceedings of the SPIE Symposium on Microlithography, paper 1263-34, March, 1990, San Jose.
3. J. A. Trail, and R. L. Byer, "Compact scanning soft-x-ray microscope using laser-produced plasma source and normal-incidence multilayer mirrors," Opt. Lett. **14**, 539 (1989)
4. G. D. Kubiak, D. A. Outka, and J. M. Zeigler, Proc. of the SPIE **1263**, 272 (1990); G. D. Kubiak, D. A. Outka, C. M. Rohlfing, J. M. Zeigler, W. K. Waskiewicz, and D. L. Windt, J. Vac. Sci. Technol. **B8**, 1643 (1990).

Schwarzschild microscope at  $\lambda = 7$  nm

K. A. Tanaka, M. Kado, H. Daido, T. Yamanaka, and S. Nakai

Institute of Laser Engineering, Osaka University, 2-6 Yamada-oka, Suita, Osaka, 565, Japan  
(Tel. 06-877-5111, Fax. 06-877-4799)

K. Yamashita, and S. Kitamoto

Department of Physics, Faculty of Science, Osaka University, 1-1 Machikaneyama-cho,  
Toyonaka, Osaka, 560, Japan

X-ray imaging optics have been essential diagnostics in inertial confinement fusion (ICF) research. A micro pellet ( $<1$ mm dia.) is irradiated by a giant multi-beam laser system. This pellet is imploded to create a thermonuclear fusion condition, making use of the inertia of the imploding pellet wall. It is of critical importance for ICF to measure nonuniformities at the implosion core ( $\sim 100\mu\text{m}$ ) or the laser spot in order to drive the pellet to a very high density. Such measurements require a spatial resolution of less than  $1\mu\text{m}$ . We have chosen to build a Schwarzschild type x-ray microscope with a magnification of 15. This x-ray microscope can be applied to fields other than laser fusion, such as lithography, biology and medicine. This can be a powerful tool when coupled with laser plasma x rays (LAPLAX), since the high brightness and temporal resolution ( $<1$ ns) of LAPLAX is added to the high spatial resolution.

There have been several attempts to develop Schwarzschild x-ray microscopes. Some of these works presented the spatial resolution higher than  $0.2\mu\text{m}$  and diffraction limited performance<sup>(1)</sup>. But most of the instruments use wavelengths exceeding  $10\text{nm}$ , exhibiting demagnified images<sup>(1), (2), (3)</sup> and using synchrotrons as x-ray sources<sup>(2), (3)</sup>. For a case of LAPLAX, multiple pulses were needed to obtain an image<sup>(2)</sup>. In biology and medicine it is important to use a single pulse of LAPLAX, since a high temporal resolution and a minimum radiation damage are necessary. In addition the shorter wavelength (at least less than  $10\text{nm}$ ) is desirable in x-ray lithography.

92-19496



We present the development of a Schwarzschild type x-ray microscope. This microscope images with a magnification of  $15^{(4)}$  at an x-ray wavelength of 7nm. Using a bright LAPLAX, an exposure time of less than 1ns can be obtained.

Ray traces have been calculated for a working distance (the separation between the object point and the image point) of 1500mm and a magnification of 15. These values were determined taking into account our implosion experimental conditions. The ray trace calculation showed that the spatial resolution had almost linear dependence on the mirror surface rms height. Best spatial resolutions were calculated for both rms height of 0.3nm and 0.6nm. The value of 0.3nm corresponds to the surface roughness of the quartz mirror substrates. The value of 0.6nm corresponds to an estimated value of the interfacial roughness of the multi-coated layers for the Schwarzschild type x-ray microscope. In case of the 0.3nm the best spatial resolution was 80 nm within a  $\pm 100\mu\text{m}$  field of view. In case of the 0.6nm the spatial resolution was 300 nm.

To produce the x-ray mirrors, Ni and C layers were deposited onto quartz substrates using an electron beam evaporation method. Using this method it is possible to form large uniform layers ( $\sim 150\text{mm}\phi$ ). The surface roughness of the substrate was measured to be 0.3nm by a WYKO optical heterodyne profilometer. The thickness of Ni and C layers are 1.2nm and 2.3nm respectively, which correspond to the x-ray wavelength of 0.7nm. A peak value was obtained with 30 layer pairs. For example the reflectivity was 6% at the Al-Ka line x ray (0.834nm).

The resolution test was conducted using LAPLAX. The fourth harmonic light (263nm) of a Nd:glass laser was used to irradiate 0.2 $\mu\text{m}$  thick Au foil. The beam energy was 3 to 6J, with a pulse width of 400ps and a focal spot diameter of 200 $\mu\text{m}$ . Under these laser conditions a high x-ray conversion efficiency ( $\sim 80\%$ ) can be obtained<sup>(5)</sup>, providing a bright source of soft x rays.

A 1 $\mu\text{m}$  CH filter coated with 0.1 $\mu\text{m}$  Mo and 0.1 $\mu\text{m}$  Ag was placed in front of the microscope in order to block plasma particles and strong scattered light. The soft x-ray

transmission of the filter was estimated to be 15% at 170eV. Four filters were set on a rotating filter holder and could be selected without opening the vacuum chamber.

In this experiment a 0.2 $\mu$ m thick free standing Au foil was used as an x-ray target. The incident angle of the laser beam was 45° with an *f*/10 focus lens. Cu meshes of 500(lines/inch) and 1000(lines/inch) were attached on the rear side of Au foil. The 500(lines/inch) mesh has a opening of 30 $\mu$ m and a bar width of 20 $\mu$ m. The 1000(lines/inch) mesh has a opening of 15 $\mu$ m and a bar width of 10 $\mu$ m. The 263nm laser irradiated the gold side, producing and transmitting an x-ray flux on the mesh. In this manner backlit mesh images were taken with the Schwarzschild type x-ray microscope. The x-ray images were recorded on Kodak 101-07 type x-ray films. From the 1000 mesh image the best resolution was determined to be 500 nm taking the 25-75 % contrast of the image.

## References

- (1) D. W. Berreman, J. E. Bjorkholm, L. Eichner, R. R. Freeman, T. E. Jewell, W. M. Mansfield, A. A. MacDowell, M. L. O'Malley, E. L. Raab, W. T. Silfvast, L. H. Szeto, D. M. Tennat, W. K. Waskiewicz, D. L. White, D. L. Windt, O. R. Wood II, and J. H. Bruning, *Optics Lett.* **15**, 529 (1990).
- (2) J. A. Trail and R. L. Byer, *Optics Lett.* **14**, 539 (1989).
- (3) H. Kinoshita, T. Kaneko, H. Takei, N. Takeuchi, and N. Ishihara, In *Conf. of Appl. Phys.*, ( 28p-ZF-15, Jpn. Soc. Appl. Phys. 1986).
- (4) M. Kado, K. A. Tanaka, R. Kodama, A. Yamauchi, T. Mochizuki, K. Yamashita, T. Yamanaka, S. Nakai, and C. Yamanaka, *Jpn. J. Opt.* **17**, 234 (1988) in Japanese.
- (5) R. Kodama, K. Okada, N. Ikeda, M. Mineo, K. A. Tanaka, T. Mochizuki, and C. Yamanaka, *J. Appl. Phys.* **59**, 3050 (1986).

## Soft-X-Ray Sources



## Source Issues Relevant to X-Ray Lithography

Khanh Nguyen,\* David Attwood, and T. K. Gustafson\*

*Electrical Engineering and Computer Sciences,\* Center for X-Ray Optics,  
Lawrence Berkeley Laboratory, University of California, Berkeley,  
Berkeley, California 94720*

92-19497



### **Abstract**

Considerations of the various issues relating to radiation sources for x-ray lithography are presented, focusing on two leading candidates - laser-produced plasma and synchrotron radiation sources. Issues to be addressed include power requirements of an x-ray source, deliverable power to wafer for both synchrotrons and laser plasma sources, and the requirement for collection solid angle and conversion efficiency for laser plasma sources. In our analysis, we attempt to bring out the relative merits of the sources and the advances necessary to make them viable for future x-ray lithographic systems.

### **Introduction**

X-ray projection lithography requires an x-ray source capable of delivering high power to the wafer to maintain high wafer throughput. We will assume that the new x-ray process must achieve throughput comparable to today's process - approximately 20 wafers per hour [1]. With 8" wafers, this corresponds to exposing approximately 2 cm<sup>2</sup> per second.

Measurements show that sensitivity of current resists in the wavelength range of interest for

projection printing ranges from 600-1000 mJ/cm<sup>2</sup> [2]. Chemically amplified resists have shown sensitivity of 5 to 40 mJ/cm<sup>2</sup> for x-ray proximity printing [3, 4]. Assuming continued advances in resist technology or the use of surface imaging with multilayer resist, sensitivity of ~10 mJ/cm<sup>2</sup> with high resolution and good etch resistance may be achievable. Therefore, incident power of 10-20 mW/cm<sup>2</sup> is required at the wafer to obtain a throughput of 20 wafers/hr. As a result, assuming an optical system with several reflective optics [5, 6] (condensors, masks and imaging optics) with 70% reflectivity per surface, the source power requirement is 100-200 mW in the nominal 3% bandwidth imposed by multilayer coatings.

Since the highest normal incidence reflectivity for multilayer-coated mirrors has been obtained at 130 Å, high power output at this wavelength is desired. In the future, interest will shift to shorter wavelengths as coating technology improves since shorter wavelengths, with correspondingly reduced absorption, result in deeper resist penetration and greater process latitude [7].

Synchrotrons and laser plasma x-ray sources (LPS) are leading candidates for providing the desired power output, and work is in progress to evaluate the feasibility of using them for as sources for x-ray lithography [8-19].

**Table 1. Characteristics of synchrotron sources and laser plasma sources**

|   | SYNCHROTRONS  | LASER PLASMA  |
|---|---|---|
| <b>COST</b>                                 | ~\$20 million for storage ring, plus \$1 million per beamline | Unknown<br>(Depends on pump laser, collection optics, etc...)                             |
| <b>NO. OF PRINTERS SUPPORTED</b>            | 15 - 25 per synchrotron                                       | 1 per laser   |
| <b>POWER OUTPUT AT 130 Å<br/>(mW/3% BW)</b> | 25 - 100 mW<br>(20 mrad hor. coll. angle)                     | $1.2 \times 10^{-3}$ mW<br>( $10^{-4}$ sterad. coll. solid angle and 150 W average power) |

At the present time, only synchrotrons are capable of providing the desired power for high wafer throughput. Advances in many aspects of LPS — average laser power, collection optics, and conversion efficiency — are necessary for it to become a viable alternative to synchrotrons.

### Synchrotron Source

The characteristics of synchrotron sources and LPS are summarized in Table 1. Synchrotrons involve well-understood processes, provide high photon flux into a broad band of wavelengths, and can simultaneously drive many wafer printers. Arguments against them, however, are their large footprints and buy-in costs. Their footprint ranges from 25 m<sup>2</sup> to 200 m<sup>2</sup> for normally conducting rings, and 0.8 m<sup>2</sup> to 20 m<sup>2</sup> for superconducting rings [13]. LPS are smaller and could fit more easily into existing facilities.

As a basis for cost comparison with LPS, a storage ring capable of driving up to 25 printers will cost approximately \$20 million [20, 21]. The costs are roughly the same for either normally conducting or superconducting rings. Each beamline will cost approximately \$1 million, resulting in a total cost of \$40 million for 25 printing stations. Twenty-five laser plasma sources would be needed to drive the same number of printers. Hence, to be competitive, each LPS system must cost about \$1.8 million. Additional issues would then include true

footprint for both sources, reliability and operating costs.

Many synchrotrons are being built for x-ray lithography around the world [9, 13]. Four of them are presented here as comparison to laser-plasma sources — Helios at IBM East Fishkill, CAMD at Louisiana State University (LSU), the Advanced Light Source at Lawrence Berkeley Laboratory (LBL), and Aurora by Sumitomo Heavy Industries in Japan. Helios and Aurora use superconducting magnets, while ALS and CAMD use normally conducting magnets. Using the parameters provided in Table 2, power output from bending magnets in these storage rings were calculated using well-established formulas [22, 23].

Power output was calculated assuming a 3% collection bandwidth and 20 milliradians horizontal collection angle. The result tabulated in Table 2 show power output at wavelengths suitable for both proximity printing at 8 Å and projection printing at 45 Å, 70 Å, and 130 Å. Due to its broadband output, the same synchrotron can be a source for both proximity and projection lithography. Since Helios, Aurora and CAMD were built with proximity printing in mind, power outputs are much higher at 8 Å. Even so, they are still capable of 25 mW to 84 mW at 130 Å. Increasing the horizontal collection solid angle from 20 milliradians might be possible with appropriate condensing optics and would make it possible to obtain the desired 100 mW. In addition, if high reflectivity multilayers can be

**Table 2. Power output and parameters of four representative synchrotrons**

|  | HELIOS<br>(IBM) | AURORA<br>(Sumitomo) | CAMD<br>(LSU) | ALS<br>(LBL) |
|--|-----------------|----------------------|---------------|--------------|
| <b>ELECTRON ENERGY (GeV)</b>                 | 0.70            | 0.65                 | 1.20          | 1.50         |
| <b>CURRENT (mA)</b>                          | 200             | 300                  | 400           | 400          |
| <b>MAGNETIC FIELD (T)</b>                    | 4.5             | 4.3                  | 1.37          | 1.04         |
| <b>POWER OUTPUT<br/>(mW/3% BW - 20 mrad)</b> |                 |                      |               |              |
| 8 Å  | 320             | 390                  | 1000          | 1450         |
| 45 Å   | 84              | 120                  | 290           | 370          |
| 70 Å   | 56              | 80                   | 200           | 204          |
| 130 Å  | 25              | 33                   | 84            | 105          |

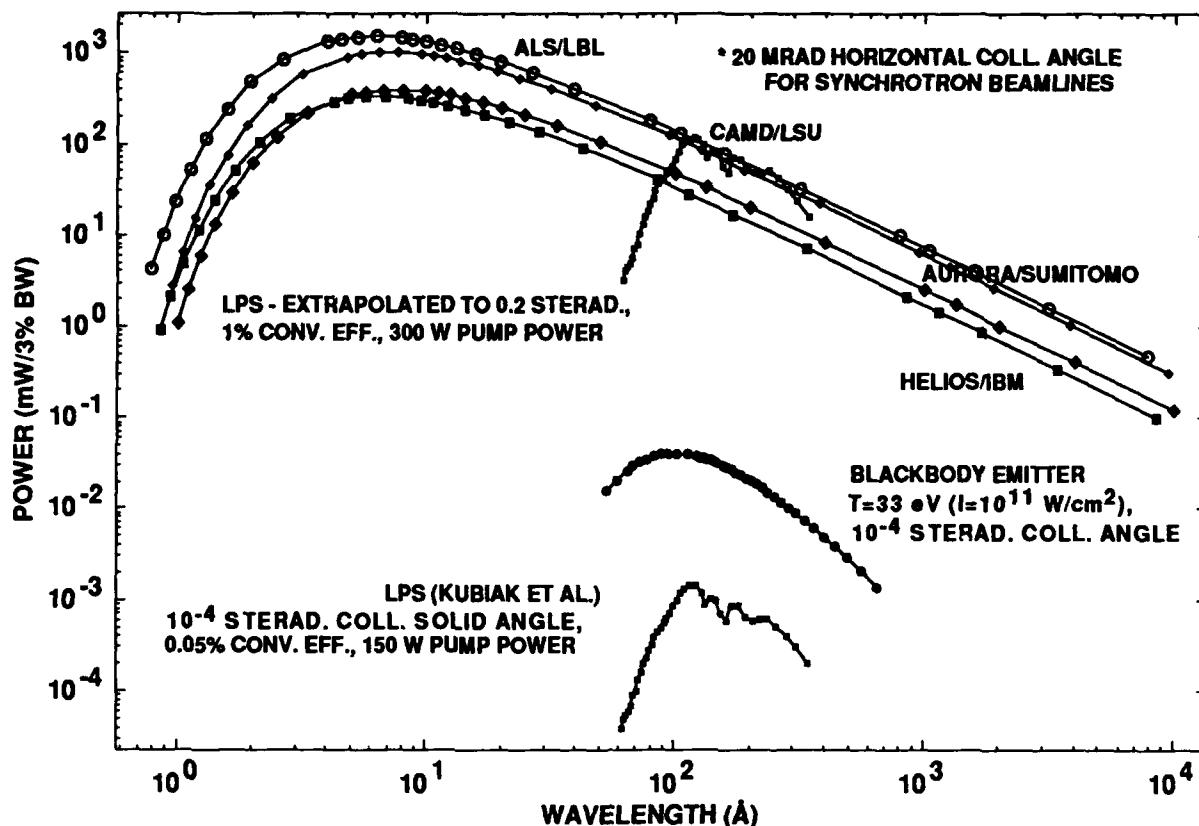


Figure 1. Power output for synchrotrons and laser plasmas. LPS power output is shown as obtained experimentally, as would be obtained with increases in collection solid angle, laser power and conversion efficiency, and as modeled by a blackbody emitter.

made at 70 Å, more power would be available from synchrotrons because power output for a bending magnet increases with decreasing wavelength in the wavelength region of interest.

### Laser Plasma Source

The advantages of laser-plasma x-ray sources are their low-initial investment cost and modularity, both important to the acceptance of X-ray lithography by the IC industry. Low initial investment makes it easier for more companies to invest in x-ray lithography on a trial basis, to obtain a few steppers to evaluate their performance and to ease the introduction of the new technology. Modularity means each printer has its own source, and when the source needs to be refurbished, only one printer must be taken off production so that wafer throughput is reduced by only a fraction of the total output. If

a synchrotron, with 15 to 25 printers connected to it, needs to be refurbished, wafer printing would be temporarily halted. While the reliability of the next generation of high average power laser and superconducting storage rings are unknown, however, the reliability of normally conducting synchrotrons have been demonstrated to be quite high at present facilities such as NSLS in Brookhaven and BESSY in Berlin. These storage rings need only be turned off for two to three weeks a year for major maintenance and perhaps one or two shifts per week for routine maintenance.

For the time being, 130 Å is the wavelength of choice for x-ray projection lithography because it is the shortest wavelength at which high normal incidence reflectivity can be obtained. Consequently, the emission of LPS should peak in that region. An interesting model with which to understand radiation scaling is that of black-



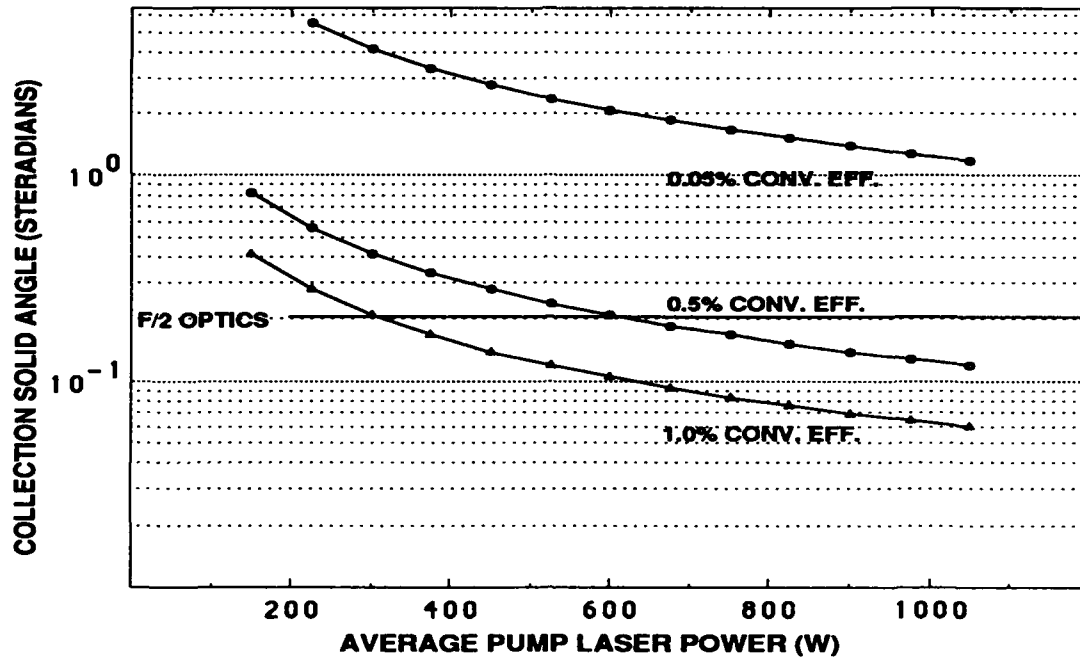


Figure 2. Collection solid angle and average laser power necessary to obtain 100 mW power output with 0.05%, 0.5% and 1.0% conversion efficiency into a 3% bandwidth.

body emission. Although simplistic considering the complicated physics of laser-plasma emission processes, it provides an easy-to-understand upper limit for near equilibrium processes. Of course experiments in the proper intensity and wavelength range will contribute to our best understanding and optimization of this process.

Using blackbody emission as a first-order model for x-ray emission from a laser-plasma, the desired intensity on target for high conversion efficiency at 130 Å can be estimated.

The relationship between the radiated intensity and characteristic temperature for a blackbody is given by the Stefan-Boltzman equation:

$$I = \sigma T^4, \quad (1)$$

where  $I$  is the radiated laser intensity ( $\text{W}/\text{cm}^2$ ),  $\sigma$  is the Stefan-Boltzman constant equal to  $1.027 \times 10^5 \text{ W-cm}^{-2}\text{-eV}^4$ , and  $T$  is the plasma temperature in eV. Hence, the plasma plume is modeled as an optically thick blackbody emitter in local thermodynamic equilibrium with peak emission at photon energy  $h\nu = 2.82 \kappa T$ .

Assuming further that the plasma absorbs a fraction  $\eta_{\text{abs}}$  of the incident laser intensity  $I_L$ , and effectively radiates a fraction  $\eta_{\text{rad}}$  into the broad

blackbody spectrum, the anticipated characteristic temperature  $\kappa T$  in this simplified (upper-limit) model is,

$$\kappa T = (\eta_{\text{abs}} \eta_{\text{rad}} I_L / \sigma)^{1/4} \quad (2)$$

where again the spectral peak is at  $2.82 \kappa T$ .

Assuming 80% absorption and 50% re-radiation into x-rays, the desired intensity for peak emission at 95 eV is  $3 \times 10^{11} \text{ W}/\text{cm}^2$  [24].

Though many experiments have been performed on laser-plasmas, only a few have been performed at intensities less than  $10^{13} \text{ W}/\text{cm}^2$  [2, 14, 15, 19] with sufficient spectral resolution to evaluate conversion efficiency into the desired bandwidth. Kubiak et al. used an excimer laser at 248 nm with 25-30 ns. pulse width, 150 W average laser power, and  $10^{11} \text{ W}/\text{cm}^2$  intensity on a gold target to achieve ~0.05% conversion efficiency into 3% bandwidth. Kauffman et al. used a frequency doubled YAG at 0.53 micron with 10 ns. pulse width and intensity ranging from  $2 \times 10^{10}$  to  $2 \times 10^{12} \text{ W}/\text{cm}^2$  to achieve 0.5% conversion efficiency into 3% bandwidth, using high Z elements such as gold, lead and tantalum as targets.

As seen in Table 1 and Fig. 1, at the present

time, power output at 130 Å from laser plasma source is about four orders of magnitude smaller than that from synchrotrons. Also plotted in Fig. 1 is the power output from a blackbody at 33 eV, with 250 μm diameter source size, 25 nsec. pulse width, 100 Hz repetition rate, and  $10^{-4}$  sterad. collection solid angle. As can be seen, larger collection solid angle, higher conversion efficiency and higher average laser power are all necessary for LPS to achieve the same output power as synchrotrons. To generate x-rays efficiently, the laser driver for plasma x-ray source must have both high average power and moderately high peak power.

The effects of conversion efficiency on the required collection solid angle and average laser power is shown in Fig. 2. The plot shows the collection solid angle and average laser power necessary to obtain 100 mW of output power from a laser-plasma x-ray source for conversion efficiencies of 0.05%, 0.5% and 1.0%. At 1% conversion efficiency and 0.2 sterad. collection angle, to provide 100 mW of X-ray, a 300 W average power laser is required. If conversion efficiency is reduced to 0.5% and collection solid angle to 0.1 sterad., a 1200 W laser is required - a much more difficult task for laser makers.

## **Conclusion**

X-ray projection lithography for integrated circuits applications requires high average x-ray power that only synchrotrons can provide at the present time. In addition, one synchrotron can drive many lithography stations, while one LPS can only drive one station. The laser plasma source is desirable because of its low initial investment cost and its modularity. However, LPS power output must increase by four orders of magnitude to be comparable to that of synchrotrons. This increase could come about through higher conversion efficiency, higher average laser power and larger collection solid angle. For the foreseeable future, synchrotrons are capable of higher power output and are the more suitable tool for high volume IC production.

LPS, with lower power, may provide satisfactory throughput for device development and IC pilot line.

## **Acknowledgments**

Helpful discussions with James Underwood, Jeff Kortright and Tai Nguyen are gratefully acknowledged. We thank Tony Warwick for the URGENT tutorial. This work is supported by the Director, Office of Energy Research, Office of Basic Energy Sciences, Materials Science Division, of the Department of Energy under contract No. DE-AC03-76SF00098 and by the Air Force Office of Scientific Research of the Department of Defense under contract No. F49620-87-K-001.

## **References**

1. C. W. T. Knight, "The future of manufacturing with optical microlithography," *Optics & Photonics News*, pg. 11-17, (Oct 1990)
2. G. Kubiak et al., "Extreme Ultraviolet Resist and Mirror Characterization: Studies with a Laser Plasma Source," *J. Vac. Sci. Technol. B* **8**, pg. 1643-1647 (1987)
3. S. M. Preston, D. W. Peters, D. N. Tomes, "Preliminary testing results for a new x-ray stepper," *SPIE Proceedings* **1089**, pg. 164-177 (1989)
4. J. W. Taylor et al., "Sensitivity/resolution variables in x-ray chemically amplified resists exposed to synchrotron radiation," *J. Vac. Sci. Technol. B* **8**, pg. 1547-1550 (1990).
5. N. M. Ceglio et al., "Soft X-ray Projection Lithography," *J. Vac. Sci. Technol. B* **8**, pg. 1325-1328 (1990)
6. T. Jewell, J. M. Rodgers, K. P. Thompson, "Reflective Systems Design Study for Soft X-ray Projection Lithography," *J. Vac. Sci. Technol. B* **8**, pg. 1519-1523 (1990)

7. T. D. Nguyen, E. Gullikson, J. B. Kortright, "Normal incidence multilayer reflector for sub-10 nm region," presented at the Topical Meeting on Soft-X-ray Projection Lithography, Monterey, April 10-12, 1991.
8. D. E. Andrews and M. N. Wilson, "High energy lithography illumination by Oxford's synchrotron: A compact superconducting synchrotron x-ray source," *J. Vac. Sci. Technol. B* **7**, 1696-1701 (1989)
9. J.B. Murphy, "Electron Storage Rings as X-ray Lithography Sources: An Overview," *SPIE Proceedings* **1263**, pg. 116-123 (1990)
10. D. E. Andrews et al., "Helios: A Compact Superconducting X-ray Source for Production Lithography," *SPIE Proceedings* **1263**, pg. 124-130, (1990)
11. J. Nishino et al., "Development of Centrally Controlled Synchrotron Radiation Lithography Beamline System," *J. Vac. Sci. Technol. B* **8**, pg. 1514-1518 (1990)
12. H. Yamada, "Commissioning of Aurora: The smallest Synchrotron Light Source," *J. Vac. Sci. Technol. B* **8**, pg. 1628-1632 (1990)
13. J. B. Murphy and G.P. Williams, "Electron Storage Rings as X-ray Lithography Sources: an update," *Synchrotron Radiation News* **3**, pg. 18-21 (1990)
14. R. Kauffman, D. Phillon, "X-ray Production Efficiency at 130 Å from Laser-Produced Plasmas," this proceedings.
15. H. Pepin et al., "X-ray Sources for Microlithography created by Laser Radiation at  $\lambda = 0.26$  mm," *J. Vac. Sci. Technol. B* **5**, pg. 27-32 (1987)
16. F. O'Neill et al., "Plasma X-ray Sources for Lithography Generated by a 0.5 J KrF Laser," *SPIE Proceedings* **831**, pg. 230-236 (1987)
17. I. Toubans et al., "X-ray Lithography with Laser-Plasma Sources," *Microelectronic Engineering* **6**, pg. 281-286 (1987)
18. E. Turcu et al., "X-ray Lithography using a KrF Laser-Plasma Source at  $h\nu \sim 1$  keV," *Microelectronic Engineering* **6**, pg. 287-292 (1987)
19. M. Chaker et al., "Laser plasma x-ray sources for microlithography," *J. Appl. Phys* **63**, pg. 892-899 (1988).
20. G. Dahlbacka, Maxwell/Brobeck division, private communications.
21. H. Nakabushi, Sumitomo Heavy Industries, private communications.
22. K. J. Kim, "X-ray Sources: Characteristic of Synchrotron Radiation," X-ray Data Booklet, LBL Center for X-ray Optics, PUB-490.
23. K. J. Kim, "Characteristics of Synchrotron Radiation," *Proceedings of U. S. Particle Accelerator Summer School* (1987)
24. Higher temperature blackbody radiate more strongly at 95 eV, but conversion efficiency into the desired 3% bandwidth would be reduced.



## X-Ray Production Efficiency at 130 Å from Laser-Produced Plasmas

Robert L. Kauffman and Donald W. Phillion

Lawrence Livermore National Laboratory, Livermore, California 94550

### Abstract

X-ray production at 130 Å is measured from laser-produced plasmas using sub-Joule energies. Dependence of efficiency on target material and intensity are presented.

Projection x-ray lithography systems require high brightness, narrow band sources in the soft x-ray region. Source requirements are set by the multilayer x-ray imaging optics and these typically have a bandpass of a few per cent below 200 eV. We have begun investigating laser-produced plasmas as a potential x-ray source for projection lithography. Although these are typically broadband sources they can be efficient radiators in the sub-kilovolt region. By proper choice of laser wavelength, pulse length, irradiation intensity, and target material, emission in the bandpass of interest can be optimized.

Although much work has been done in measuring x-ray production from laser-produced plasmas, most experiments have been done at intensities greater than  $10^{13}$  W/cm<sup>2</sup> primarily measuring total x-ray production for understanding energy balance. Only limited experiments have been done at intensities less than  $10^{13}$  W/cm<sup>2</sup> with sufficient spectral resolution required for a relatively narrow band application [1-3]. We report preliminary measurements of x-ray production for various Z targets using a 0.53 μm laser in a 10 ns pulse at intensities from  $2 \times 10^{10}$  W/cm<sup>2</sup> to  $2 \times 10^{12}$  W/cm<sup>2</sup>. Both absolute x-ray production around 95 eV (130 Å) and continuous spectra from 50 to 500 eV are measured. The spectral region at 95 eV is of interest for projection systems using Mo-Si multilayer mirror technology. Preliminary results indicate that production efficiencies greater than 0.2% into a 1 eV bandwidth are achievable for high Z targets for intensities above  $10^{11}$  W/cm<sup>2</sup>. These efficiencies are within a factor of two of

the projected efficiency goal [4]. Better control and optimization of the laser parameters offer promise that laser-produced plasmas can be developed as a source for projection x-ray lithography.

For these initial experiments, 0.53 μm light from a frequency doubled Nd(YAG) laser [5] irradiates thick targets of various Z materials. The incident laser pulse has been measured to be about 10 ns FWHM in a quasi-Gaussian pulse using a 50 ps diode and a Tek 7250 oscilloscope. Intensity fluctuations of a factor of two or greater are observed on time scales of 100 ps, or less. The incident laser energy is measured on each shot with a calorimeter viewing an uncoated beam splitter placed before the beam enters the interaction chamber. Intensity scans are done by inserting neutral density filters before the energy monitors. Errors in beam calorimetry are estimated to be about 5% for most of the data. For the lowest energy data the errors may be as large as 20%.

The beam, approximately 2 cm in diameter, is focussed on target at normal incidence using a 20 cm focal length lens. The target is placed at best focus by maximizing x-ray production above about 500 eV. Best focus has been measured to be 40 μm diameter using an

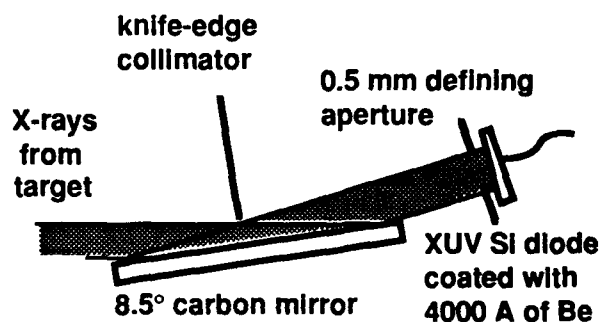


Figure 1. Schematic of the detection system for measuring absolute yields around 95 eV.

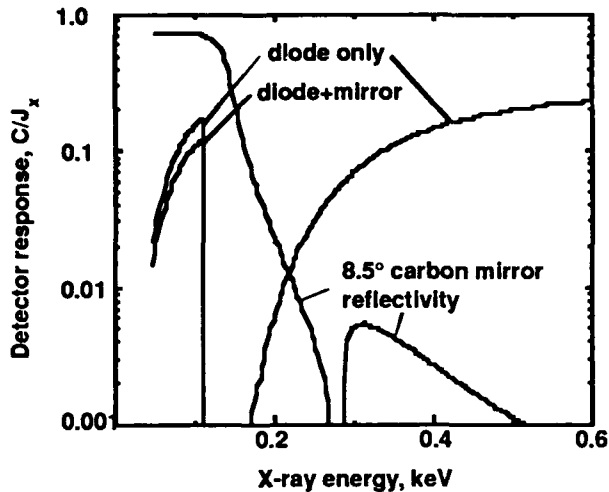


Figure 2. Calculated response for the Si diode detector system.

equivalent lens imaging the beam onto a frosted glass reticle which is viewed by a CCD camera. This is consistent with the expected spherical aberrations in the lens.

The absolute x-ray intensity around 95 eV is measured using a VUV Si diode coupled with a grazing incidence carbon mirror viewing the target at 45° to the target normal. A schematic of the detector system is shown in Fig. 1. For our energy range of interest, the Si diode is linear with x-ray energy [6]. The diode has

been coated with approximately 4000 Å of Be to make it sensitive only in the region of interest. The calculated response of the diode including transmission through the Be is shown in Fig. 2. A similar Be-coated diode has recently been calibrated [7] and the sensitivity is slightly less than calculated. This difference is probably due to variations in coating thickness and the purity in the Be. The curves are calculated including this calibration. A grazing incidence carbon mirror is placed in front of the diode to attenuate x rays above 200 eV where the Be becomes transparent. The mirror response is also shown in Fig. 2. The mirror diode combination results in a detector sensitive in the region from 75 eV to 110 eV with little contributions to the signal from other regions of the spectra.

The absolute x-ray intensity dependence has been measured for solid targets of different Z materials. The results are shown in Fig. 3. The angular distribution has been assumed to be Lambertian to obtain the total flux. Experiments are presently planned to measure the angular distribution, but the Lambertian assumption usually under estimates the x-ray production for these small plasmas at this observation angle. In addition the spectrum is assumed to be constant over the range of sensitivity of the detector. Spectral measurements discussed later suggest that this underestimates the x-ray production at 95 eV. Because of these uncertainties the absolute errors in the flux are probably as large as 50%, but the relative errors are much smaller.

The intensity scaling data in Fig. 3 show that x-ray production efficiency at 95 eV is highest for high Z

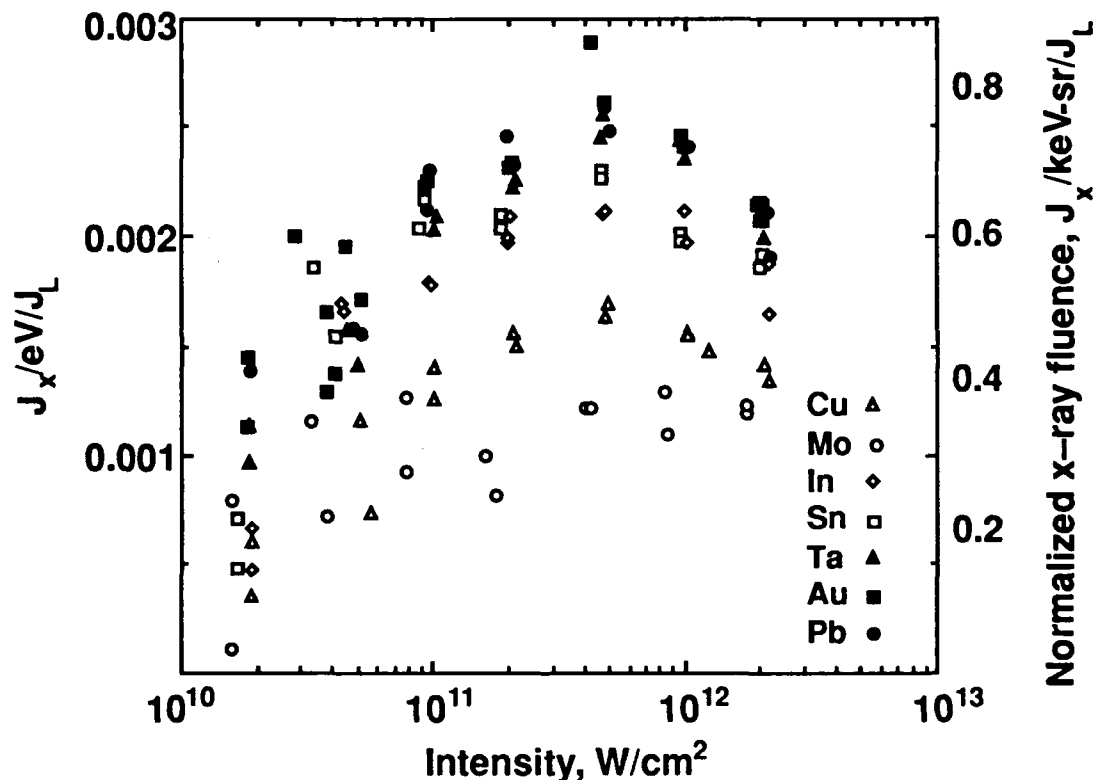


Figure 3. intensity dependence of x-ray production at 95 eV for 0.53 μm light in a 10 ns pulse.

material ( $Z > 72$ ) although In ( $Z=49$ ) and Sn ( $Z=50$ ) are nearly as bright. All data show a threshold around  $2 \times 10^{10}$  W/cm<sup>2</sup> increasing with increasing intensity. Although the high  $Z$  targets are the brightest, the production efficiency does not increase monotonically with  $Z$ . For example, Cu ( $Z=29$ ) is higher than Mo ( $Z=42$ ) for much of the data range. X-ray production efficiency is above 0.22% per eV for high  $Z$  targets between  $10^{11}$  W/cm<sup>2</sup> and  $10^{12}$  W/cm<sup>2</sup>. For a projection system having a  $2^\circ$  bandpass at 130 Å this implies a conversion efficiency of 0.5% into the bandpass. When final analysis including angular distribution and spectral effects are included this value may be even higher.

Continuous spectral measurements are made using a transmission grating [8] coupled with a microchannel plate (MCP) detector shown schematically in Fig. 4. The transmission grating is a free standing Au grating having a 3000 Å period. The grating is placed about 17.8 cm before the MCP for a dispersion of 16.9 Å/mm at the detector plane. The grating is masked by a 100 μm slit resulting in a resolution of about 4.5 Å for a 40 μm source size. The MCP is a single stage plate coated with Inconel. Output from the phosphor is coupled through the vacuum by a fiberoptic face plate and spectra are recorded on a single shot using Kodak 2484 film.

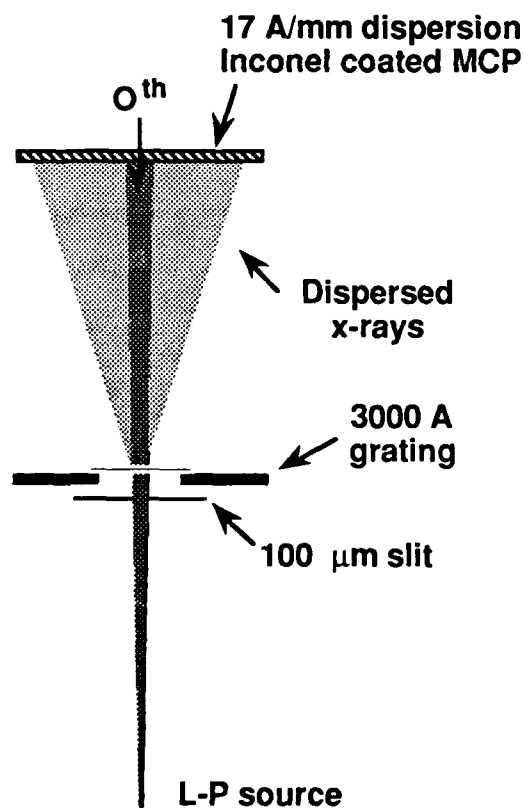


Figure 4. Schematic of the transmission grating-microchannel plate detector used for continuous spectral measurements from 50 eV to 500 eV.

The film data is analyzed to obtain time integrated spectra from 50 eV to 500 eV. The film data is digitized and converted to intensity using an optical calibration wedge developed at the same time as the data to reduce processing variations. The dispersed spectra on both sides of zeroth order are analyzed. The present MCP has a significant non-uniformity across the dispersion direction. This non-uniformity can distort the spectral shape as much as a factor of two. Also the bright central image is usually saturated and the wings of the image can extend into the diffracted spectrum. This effects mostly the higher energy portion of the spectrum. The energy response of the MCP is deconvolved assuming its energy dependence is similar to a Ni x-ray photocathode [9]. Absolute spectra are obtained by normalizing the spectra to the absolute diode measurement.

Spectra are shown in Fig. 5 from a Au target at a number of intensities. No sharp features are observed in Au, but the spectra do exhibit considerable structure. A few isolated Au lines have been identified in higher resolution spectra of laser-plasmas at higher irradiation intensities [10], but these do not dominate the spectrum. Broad structure in this region has been identified as  $n=4$  to  $n=4$  and  $n=3$  to  $n=3$  transitions [11]. For the present experiment the structure is probably from similar transitions but with lower ionization states. The major change in the spectra with intensity is that the spectrum increases at higher energy for increasing intensity. In the region of interest the structure is nearly independent of intensity and is consistent with the absolute diode results. The signal was too low to obtain useful spectra at lower laser intensity. Absolute x-ray production at 95 eV is about 20% higher inferred from the spectrum than derived from the diode assuming a constant spectrum. This difference demonstrates the uncertainty in the present data analysis technique. Presently the uniformity in the MCP is being improved and characterized in order to better measure the x-ray production at 95 eV.

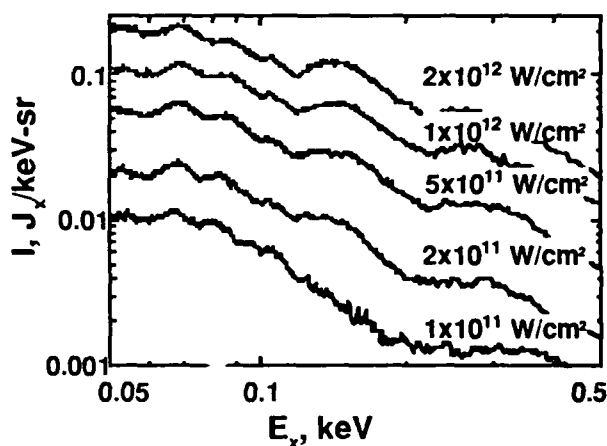


Figure 5. Intensity dependence of Au spectra from laser-produced plasmas.

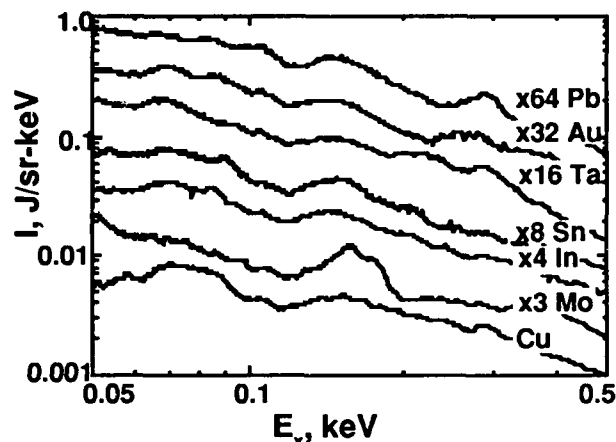


Figure 6. Dependence of soft x-ray spectrum on target material. The spectra are produced with  $0.53 \mu\text{m}$  light in a 10 ns pulse at an intensity of  $2 \times 10^{12} \text{ W/cm}^2$ .

The dependence of the spectrum on target material is shown in Fig. 6. All spectra show generally similar shapes although some structure due to bound-bound emission is observed. In principle x-ray production in the region of interest can be enhanced by selecting an element with bound-bound emission at that energy. For the present selection of targets, most of this structure is outside the x-ray region of interest although Sn does show a slight increase in x-ray intensity at 95 eV. A larger target search is planned to determine if there is a better choice of target material.

In summary, we have begun characterizing laser-produced plasmas as a potential source for projection x-ray lithography. Present experiments are concentrating on absolute x-ray production around 95 eV consistent with planned systems using Mo-Si multilayer technology. We have developed diagnostics that can absolutely measure the x-ray production in the region of interest as well as measure the spectra from 50 eV to 500 eV from a single laser pulse. We have made preliminary measurements of the intensity dependence of the absolute x-ray production at 95 eV from a number of target materials irradiated with  $0.53 \mu\text{m}$  light in a 10 ns pulse. Absolute intensities greater than 0.2% into a 1 eV band have been measured from high Z targets for intensities. Presently efforts are underway to improve the accuracy of the measurements and uncertainties in the spectral shape. Future experiments are planned to measure the dependence of x-ray production on laser spot size, wavelength, and pulse length in order to provide a data base for evaluating overall system performance of planned projection x-ray lithography systems.

This work was performed under the auspices of the U. S. Department of Energy under contract W-7405-ENG-48.

## References

1. H. Pépin, P. Alaterre, M. Chaker, R. Fabbro, B. Faral, I. Toubhans, D. J. Nagel, and M. Peckerar, "X-ray sources for microlithography created by laser radiation at  $\lambda=0.26 \mu\text{m}$ ," *J. Vac. Sci. Technol. B* **5**, 27-32 (1987).
2. M. Chaker, H. Pépin, V. Bareau, B. Lafontaine, I. Toubhans, R. Fabbro, and B. Faral, "Laser plasma x-ray sources for microlithography," *J. Appl. Phys.* **63**, 892-899 (1988).
3. G. D. Kubiak, D. A. Outka, C. M. Rohlffing, J. M. Zeigler, D. L. Windt, and W. K. Waskiewicz, "Extreme ultraviolet resist and mirror characterization: Studies with a laser plasma source," *J. Vac. Sci. Technol. B* **8**, 1643-1647 (1990).
4. N. M. Ceglio, "Soft x-ray projection lithography technology," this conference.
5. Model YG661S, Continuum, Santa Clara, Ca.
6. L. R. Canfield, J. Kerner, and R. Korde, "Stability and quantum efficiency performance, of silicon photodiode detectors in the far ultraviolet," *Applied Optics* **28**, 3940-3943 (1989).
7. L. R. Canfield, National Institute of Standards and Technology, Gaithersburg, Md. (personal communication).
8. N. M. Ceglio, R. L. Kauffman, A. M. Hawryluk, and H. Medeck, "Time-resolved x-ray transmission grating spectrometer for studying laser-produced plasmas," *Applied Optics* **22**, 318-327 (1983).
9. R. H. Day, P. Lee, E. B. Saloman, and D. J. Nagel, "Photoelectric quantum efficiencies and filter window absorption coefficients from 20 eV to 10 keV," *J. Appl. Phys.* **52**, 6965-6973 (1981).
10. J. F. Seely, J. O. Ekberg, C. M. Brown, U. Feldman, W. E. Behring, J. Reader, and M. C. Richardson, "Laser-produced spectra and QED effects for Fe-, Co-, Cu-, and Zn-like ions of Au, Pb, Bi, Th, and U," *Phys. Rev. Lett.* **57**, 2924-2926 (1986).
11. J. F. Seely, U. Feldman, C. M. Brown, W. E. Behring, and M. C. Richardson, "High-resolution XUV spectroscopy using the OMEGA laser," *SPIE Vol. 831 X-Rays from Laser Plasmas*, 25-29 (1987).



## Laser-Produced Plasma Soft-X-Ray Generation

C. Cerjan and M. D. Rosen

Lawrence Livermore National Laboratory, P.O. Box 808, L-296,  
Livermore, California 94550

# 92-19499



### Abstract

The efficiency of soft x-ray production from laser-irradiated plasmas is simulated for two different spectral regions. These two regions,  $14\text{\AA} \pm 15\%$  and  $130\text{\AA} \pm 1\%$ , were chosen for proximity mask or point-projection technological applications. Relatively large conversion efficiencies were obtained from irradiation of a stainless steel target using the conditions suggested by recent Hampshire Instruments' experiments for proximity masking. Pulse-width and laser frequency parameter studies were performed for point-projection applications which suggest that the conversion efficiency is sensitive to pulse-width but not to laser frequency.

One of the critical components of any x-ray lithographic scheme is of course the x-ray laser source. There are two primary contenders for a reliable, efficient source currently: synchrotron radiation and spectral emission from laser-produced plasmas. The dominant issue for laser-plasma emission is the conversion efficiency -- output in the intended operating spectral region relative to the required incident laser energy. Simulations are described in the following for both high and low energy spectral regions which have been suggested by either the proximity masking or point-projection technology.

### Proximity Masking Simulations

The primary radiation-hydrodynamic simulation computer code used for the Inertial Confinement Fusion (ICF) program at LLNL is LASNEX. This calculational tool is widely used to interpret data from various laser experiments including the modeling of x-ray conversion efficiencies at high laser intensities, so that a significant amount of experimental verification

of the code has been performed. The code assumes a three-fluid description (ions, electrons, and photons) using a cylindrical Lagrangean mesh which can of course be suitably restricted to planar or spherical one-dimensional geometries. There are several options for the radiation field treatment, but in the calculations below only a multi-group diffusive approximation is invoked, avoiding any major re-coupling of the radiation field to the opacity determination required for self-consistency. Another important feature of LASNEX is the flexibility permitted in the choice of atomic database for the opacity calculation. Since narrow atomic spectral emission features are determined by the bound-bound and bound-free radiative rates, this capability is important.

Several simulations were performed using a prototypical set of parameters which mimic an experiment performed recently at Hampshire Instruments. These experiments characterized the x-ray conversion efficiency in the spectral region  $14\text{\AA} \pm 15\%$  (752 eV to 1018 eV) for laser irradiation of a solid slab target. The energy on target was assumed to be 16.0 Joules, delivered in 8.0 nsec within a 220 micron diameter focal spot using  $1.053\text{ }\mu\text{m}$  ( $1\text{ }\omega$ ) light. The slab target was taken to be a  $2.0\text{ }\mu\text{m}$  thick stainless steel solid with a  $2.0\text{ }\mu\text{m}$  plastic substrate. The temporal pulse of the incident light was chosen to be Gaussian with a full-width-at-half-maximum of 8.0 nsec. The intensity derived from these parameters is  $5.26 \times 10^{12}\text{ Watts/cm}^2$ . Three different geometrical constraints were considered which correspond roughly to the amount of allowed hydrodynamic expansion allowed in the direction transverse to the incident laser light: "straight" one-dimensional, "diverging" one-dimensional, one-dimensional spherical, and two-dimensional cylindrically symmetric. "Straight" one-dimensional flow is defined as flow with no transverse expansion allowed. "Diverging" one-dimensional flow permits the rectangular flow at a fixed angle. Spherical



one-dimensional flow assumes that the expansion occurs in a spherical wedge with a fixed opening angle. Additionally, two different sets of atomic rates were used: XSN -- an average-atom model which ignores fine structure splitting -- and DCA -- a detailed atomic rate database. The XSN rates are essentially modified hydrogenic rates while those of DCA arise from detailed atomic physics calculations. In this case, the only element considered in detail was Iron whose properties were calculated using multi-configuration Dirac-Fock states up to the Neon-like ionization stage ( $\text{Fe}^{+16}$ ). Since the Neon-like shell is closed, there is a large energy requirement to open it, consequently there will be a relatively broad electron temperature range over which emission from this ionization stage will dominate the spectral output.

A comparison of the dimensional effects simulated under these conditions is presented in Table 1. The first column of results lists the expected conversion efficiency in the range  $14\text{\AA} \pm 15\%$ ; the second column lists the conversion efficiency in the range  $10 - 14\text{\AA}$ ; the last column lists the total conversion efficiency from the entire spectral range. For these relatively simple ablating plasmas, the energy is almost strictly partitioned into mass motion and radiative output. In all cases the sum of these two effects accounted for more than 90% of the incident applied energy in the one-dimensional calculations. The XSN and DCA two-dimensional runs had significantly more conductive losses; the sum of radiative loss and hydrodynamic expansion contributions was 80.4% and 86.9% respectively.

TABLE 1. Comparison of geometrical and atomic rate effects in x-ray production

|                       | CE( $14\text{\AA} \pm 15\%$ ) | CE( $10 - 14\text{\AA}$ ) | CE(total) |
|-----------------------|-------------------------------|---------------------------|-----------|
| <b>"Straight" 1D</b>  |                               |                           |           |
| 1 $\omega$ (XSN)      | 0.175                         | 0.184                     | 0.468     |
| 2 $\omega$ (XSN)      | 0.233                         | 0.172                     | 0.525     |
| 1 $\omega$ (DCA)      | 0.327                         | 0.151                     | 0.713     |
| <b>"Diverging" 1D</b> |                               |                           |           |
| 1 $\omega$ (XSN)      | 0.262                         | 0.100                     | 0.654     |
| 2 $\omega$ (XSN)      | 0.213                         | 0.049                     | 0.758     |
| <b>Spherical 1D</b>   |                               |                           |           |
| 1 $\omega$ (DCA)      | 0.226                         | 0.064                     | 0.784     |
| <b>Cylindrical 2D</b> |                               |                           |           |
| 1 $\omega$ (XSN)      | 0.107                         | 0.039                     | 0.465     |
| 1 $\omega$ (DCA)      | 0.167                         | 0.049                     | 0.586     |

Several general points can be quickly discerned from these calculations. First, the total conversion efficiency is relatively high with a significant fraction of the radiated energy appearing in the desired band about  $14\text{\AA}$ . There is a profound dependence on the dimensionality of the calculation since the various one-dimensional simulations systematically over-estimate the electron temperature because of the restricted expansion into transverse hydrodynamic motion. The higher electron temperatures are of course more favorable the production of the desired x-rays. Furthermore, the x-ray output is strongly skewed toward the lower end of the studied energy range -- the conversion efficiencies in the higher range  $10 - 14\text{\AA}$  are substantially lower than those including the energy range below  $14\text{\AA}$ . In broad terms, the one-dimensional calculations are not reliable since these experimental conditions have significant two-dimensional effects. Finally, a slight sensitivity to laser light frequency can be noted; a similar sensitivity appears in the choice of atomic database. The more realistic detailed rates indicate higher total and narrow-band conversion efficiencies.

The x-ray yield in Joules/keV over a large photon energy range is plotted in Figures 1 and 2 for the two-dimensional XSN and DCA simulations on a logarithmic scale. The average nature of the XSN calculation is clearly observed with qualitatively accurate features occurring in the yield distribution. A more detailed comparison of the output spectra is provided by Figures 3 and 4, in which the relevant output band is isolated from the total output spectrum. Most of the features above 900 eV are due to the Fluorine-like ionization stage. As noted above, the Neon-like stage dominates the ionization balance in this energy range. In summary, the average-atom atomic rates provide a fairly accurate description of the integrated x-ray yields. It is obvious from these

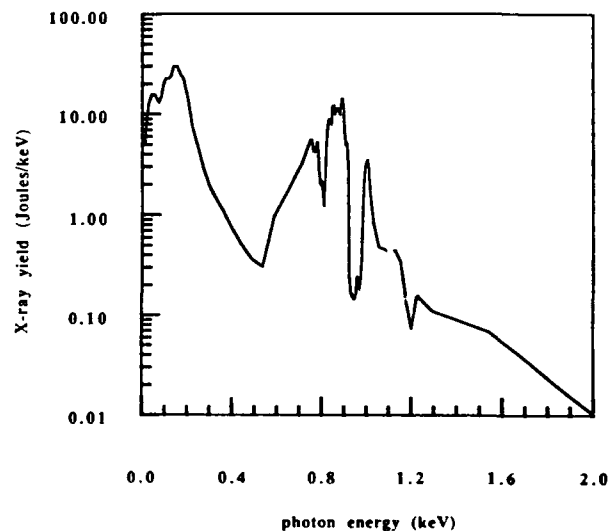


Figure 1. X-ray yield predicted by XSN for the total spectral output range.

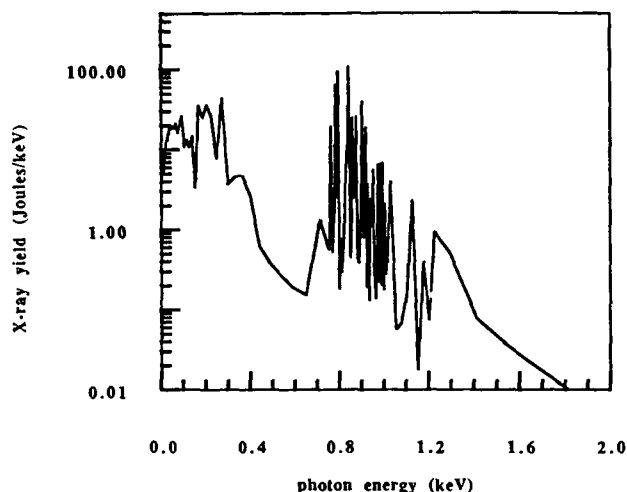


Figure 2. X-ray yield predicted by DCA for the total spectral output range.

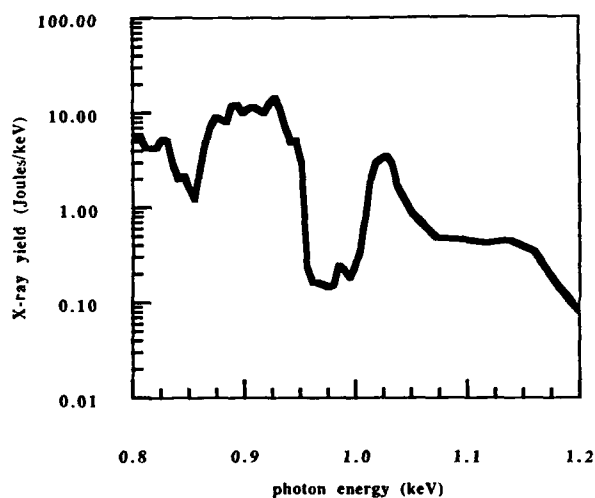


Figure 3. X-ray yield predicted by XSN about 14 Å.

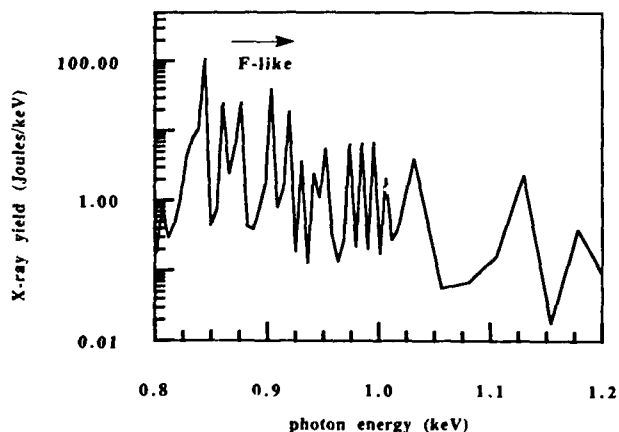


Figure 4. X-ray yield predicted by DCA about 14 Å.

Figures, though, that a restriction to narrow output bands will depend critically on the choice of detailed rates included.

### Point Projection Simulations

A preliminary parameter study was performed to examine x-ray conversion efficiency at more modest laser energies. Since the x-ray mirror reflectivity is very sharply peaked about 130 Å, it is necessary to optimize the x-ray yield in this energy band without excessive expenditure of incident laser energy. Two general studies were undertaken: the variance of conversion efficiency with respect to laser-light frequency and with respect to laser pulse length. The laser frequency range was varied from  $1\omega$  to  $4\omega$ , where the largest frequency was actually that of a typical KrF laser, 0.248  $\mu\text{m}$ . The energy on target was assumed to be 0.30 Joules delivered in 5.0 nsec with a 50  $\mu\text{m}$  focal spot giving a derived intensity of  $3.06 \times 10^{12}$  Watts/cm<sup>2</sup>. The target was assumed to be a solid slab of Gold. The two-dimensional XSN simulation results are detailed in Table 2. The first column of results lists the expected conversion efficiency within the narrow band  $95.0 \pm 1.1$  eV; the second lists the total conversion efficiency. The same general trends noted above hold for these lower energy calculations: the total conversion efficiency is high, about 60%, and there is a slight dependence on the frequency. In these simulations, almost all of the energy is accounted by summing radiative losses and hydrodynamic expansion, typically only a few percent remains for conductive losses. It appears that  $1\omega$  laser light is the best choice, though  $4\omega$  light is also quite good.

TABLE 2. Frequency and pulse length effects on x-ray production

|                           | CE(95 eV $\pm$ 1.1) | CE(total) |
|---------------------------|---------------------|-----------|
| $1\omega$                 | 0.0096              | 0.679     |
| $2\omega$                 | 0.0082              | 0.635     |
| $3\omega$                 | 0.0077              | 0.632     |
| $4\omega(248 \text{ nm})$ | 0.0090              | 0.632     |
| 2.0 ns                    | 0.0060              | 0.588     |
| 5.0 ns                    | 0.0121              | 0.630     |
| 10.0 ns                   | 0.0166              | 0.616     |
| 30.0 ns                   | 0.0060              | 0.551     |

Table 2 also contains the results of the pulse length study which was performed for a laser energy of 0.33 Joules focused on a 100  $\mu\text{m}$  diameter spot using  $2\omega$  laser light. Four pulse lengths ranging from 2.0 nsec to

30.0 nsec were used with the spectral output monitored in the desired narrow band. The respective derived intensities are  $2.12 \times 10^{12}$ ,  $8.50 \times 10^{11}$ ,  $4.24 \times 10^{11}$ , and  $1.41 \times 10^{11}$  Watts/cm<sup>2</sup>. The total conversion efficiency is again quite large with a peak efficiency at 10.0 nsec for the 95 eV band. In all cases, radiative loss and hydrodynamic expansion accounted for the energy balance to within a few percent.

### Conclusions

Summarizing these preliminary results, then, the simulations generally indicate high total conversion efficiencies with most of the incident energy partitioned into radiative output and mass (ion) motion. Only at the higher energies is there any other significant energy loss mechanism. The corresponding physical effects

which dominate are the dimensionality of the plasma flow which directly influences the achievable electron temperature and the choice of atomic rate description. The obvious experimental optimization scheme would thus involve a minimization of expansion cooling by making the target conditions as "one-dimensional" as possible and to choose a material which emits in closed-shell ionic stages within the desired bandwidth.

### Acknowledgments

The authors would like to thank Drs. A. Osterheld and J. Scofield of LLNL for a valuable discussion of the reliability of the atomic data employed above. Work performed at Lawrence Livermore National Laboratory is performed under the auspices of the U. S. Department of Energy under contract No. W-7405-Eng-48.



92-19500



## XUV Conversion Efficiency in a Low-Intensity KrF Laser Plasma for Projection Lithography

Paul D. Rockett, John A. Hunter, Ron Kensek, and Richard E. Olson  
Sandia National Laboratories, Albuquerque, New Mexico 87185

Glenn D. Kubiak and Kurt W. Berger  
Sandia National Laboratories, Livermore, California 94550

### Abstract

Measurements of XUV conversion efficiency in the 20-280eV range were made on a low intensity ( $7 \times 10^{10}$  W/cm<sup>2</sup>) KrF laser-produced plasma with seven targets of varying Z. Novel mass-limited targets were studied to develop ultra-low debris laser-targets for projection lithography.

### Introduction

The efficiency of XUV production from a laser-plasma directly relates to the cost of fielding such a source for projection lithography (PXRL). Measurements of the radiated conversion efficiency were made on the Sandia National Laboratories Laser Plasma Source (LPS), a bright reliable point x-ray source. The LPS was designed for use as a prototype XUV source for PXRL and included a Lambda Physik KrF laser focused weakly onto a rotating drum target. The laser produced 1.1J pulses at 248nm in 30ns and could be operated up to 100Hz. Focal intensities on target were controlled to be either  $7 \times 10^{10}$  W/cm<sup>2</sup> or  $3.5 \times 10^{10}$  W/cm<sup>2</sup>.

Radiation in the 20-280eV range was measured with an array of absolutely calibrated aluminum photocathode x-ray diodes, from which XUV conversion efficiency was inferred. Seven different targets provided data upon Z-scaling phenomena (Fig. 1) and upon the effects of limited target mass on x-ray yields. Typically 0.5% of the incident laser energy was converted into a 4.5% band about 13.9nm. (This corresponded to the passband of the Schwarzschild optic that was later used for diffraction-limited imaging onto a photoresist.) The total radiated yield was 50% of the incident laser radiation.

Additionally, ultrathin, low mass targets were designed and fielded for debris mitigation.

### Background

In spite of the wealth of data on soft x-ray conversion efficiency from high-intensity laser plasmas<sup>1-5</sup>, there is a dearth of such data for intensities below  $10^{12}$  W/cm<sup>2</sup>.<sup>6-9</sup> This lack of data is especially true for long pulse laser-plasmas of 20ns or longer.<sup>10</sup>

Laser Fusion experiments developed the use of absolute detectors for soft x-ray measurements, including x-ray diodes, transmission grating spectrographs, varied line-space reflection gratings, and compact Rowland mount gratings. These instruments all permitted the recording of extended spectra with fine time resolution.

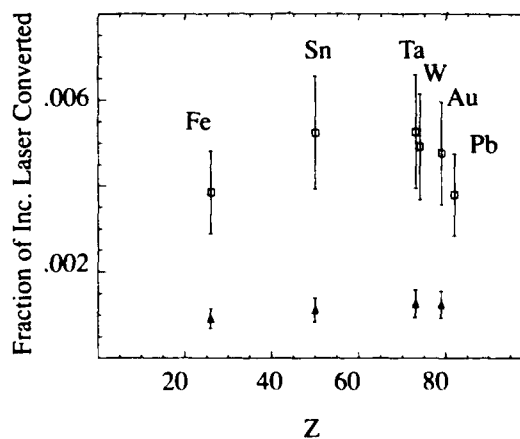


Figure 1.

Conversion Efficiency as a Function of Target Z into a 4.5% Band about 13.9nm

The calibrated aluminum photocathode x-ray diode (XRD) was the easiest of these to field and characterize, although it required equal care in handling. Diamond turning of the aluminum 100 detecting surface assured stable operation for three to six months. Several broad-band channels could be used to unfold a spectrum, whose shape was roughly known a priori.

Data on gold targets with .53 $\mu$ m and .26 $\mu$ m lasers showed total conversion efficiencies of 40-80% above  $10^{13}$  W/cm<sup>2</sup>. Radiation temperatures, assuming a black-body, ranged from 60eV to 200eV with said temperatures scaling weakly with laser intensity to the .11-.13 power.<sup>1</sup> These, however, were all for pulselengths of 1.8ns or shorter.<sup>6</sup>

Laser wavelength proved to be important in the  $>10^{13}$  W/cm<sup>2</sup> intensity regime due to differences in the absorption mechanism between short visible wavelengths and long IR wavelengths. At very low intensities, however, absorption should be entirely inverse bremsstrahlung. Heating along the path and the length of that path will now affect the level of plasma heating and concomitant soft x-ray production. Early calculations indicate that 1.06 $\mu$ m light will work as well as .26 $\mu$ m light in producing VUV radiation.

Finally, laser studies at high intensities produced valuable data on mass ablation rates in laser-target interactions. During a low intensity KrF pulse with the Sandia LPS, very little material may actually be directly ablated. The history of debris production in a laser-target only begins with the laser pulse itself. X-ray production occurs solely during the laser pulse, when heated material is ablated from the target surface. Using the data of Tarvin et al.<sup>11</sup> and Goldsack et al.<sup>12</sup> one can estimate the depth of penetration of this electron conduction wave driven by the laser. At  $7 \times 10^{10}$  W/cm<sup>2</sup> one would expect that in 30ns the burnthrough depth for gold would be a mere 30nm. This suggested that extremely thin target layers could be used for a PXRL laser-plasma source, significantly reducing the debris problem.

Following the laser pulse a shock wave is driven into the bulk of the target material, causing substantial release of particulate matter. It was this material that we intended to eliminate--by thinning the target down so that virtually no bulk existed. The results of x-ray yields as a function of gold thickness on a 1.3 $\mu$ m plastic backing are shown in Figure 2. The asterisk indicates the predicted burnthrough depth based upon refs. 11 and 12.

## Experimental Configuration

These experiments consisted of three parts: laser beam characterization, variation of conversion efficiency as

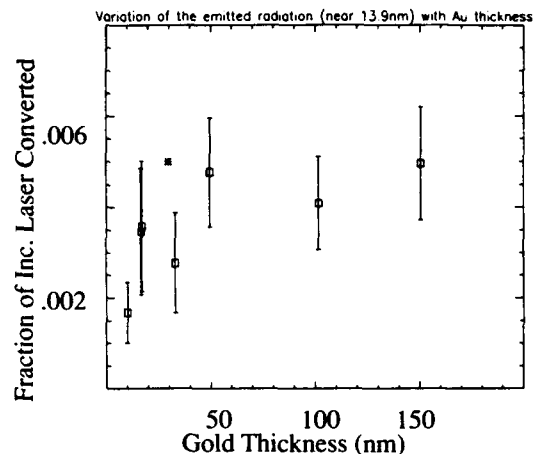


Figure 2

a function of material atomic number, and variation of conversion efficiency with gold thickness.

Initially, measurements were made of the time-integrated far-field pattern of the incident KrF beam. An equivalent plane lens imaged an attenuated full power beam onto high resolution Kodak SA-1 UV sensitive photographic plates. These were digitized and folded back through H&D curves to infer incident laser intensity. Scans taken at several focal positions appear in Figure 3, demonstrating a depth of field of greater than 5mm. The hot radiating diameter was 270 $\mu$ m, confirming past x-ray pinhole photos taken at right angles to the beam. These same UV images revealed long, very low intensity wings going out to 1100 $\mu$ m diameter.

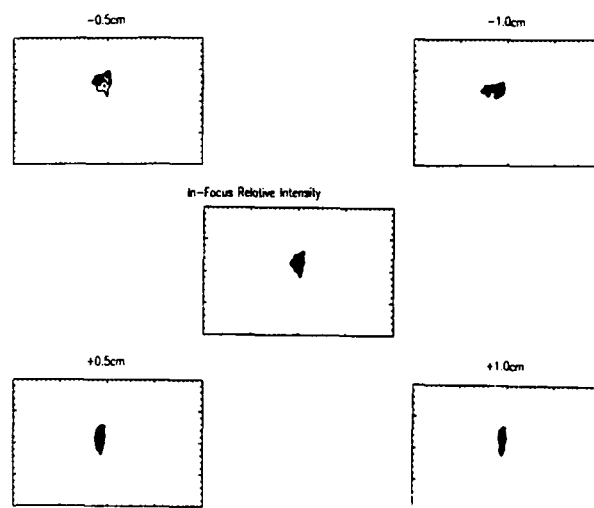


Figure 3

KrF laser beam intensity as a function of position along the optical axis

Figure 4 shows a schematic of the laser and vacuum chamber geometry. The laser was normally incident on a drum, upon which target materials were mounted.

Measurements of conversion efficiency were made at 45° to the laser axis and were performed with four channels of a six channel x-ray diode built by KMS Fusion Inc. Diamond-turned aluminum photocathodes were filtered by beryllium (75-108eV), aluminum (20-80eV), parylene N (90-280eV), and parylene D (90-206eV), providing broad coverage around the 89eV (13.9nm) energy of interest. The XRD's sat 396mm from the target; incident laser energy was monitored on each shot.

Target Z was varied to take advantage of characteristic manifolds of line in the wavelength region of interest.

## Results

The mean conversion efficiency into a 4.5% band about 13.9nm was .5% of the incident laser energy at an intensity of  $7 \times 10^{10}$  W/cm<sup>2</sup>. Figure 1 shows the slight variation of this efficiency as target Z was changed. Tin and tantalum gave the highest yields, however, uncertainties in the XRD calibrations and the broadband nature of these diodes renders the experimental differences between tin, tantalum, tungsten, and gold negligible. What is striking is the significant reduction in conversion efficiency with a 2x reduction in laser intensity. As indicated by R. Kauffman et al. elsewhere in these proceedings, a clear threshold in conversion to the VUV exists between  $10^{10}$  and  $10^{11}$  W/cm<sup>2</sup>.

Our experiments with mass-limited targets confirmed our estimates of burnthrough depths on the order of a few tens of nanometers. Targets were designed to be varying thicknesses of gold laid upon a 1.3μm plastic

substrate. Gold thickness ranged from 10.2nm to 150nm and showed a clear threshold of XUV yield between 10nm and 50nm. After the gold thickness reached 50nm no significant change in yield was observed, all the way up to 250μm thick targets. Thus a low debris target may be fabricated for a laser-plasma projection lithography source that consists of a mere 50nm of gold on an ultrathin plastic substrate.

Measurements of total x-ray yield were approximately 50% at  $7 \times 10^{10}$  W/cm<sup>2</sup>.

## Discussion

The values of conversion efficiency we have measured are consistent with those observed by Chaker et al.<sup>10</sup> and Popil et al.<sup>9</sup> for long pulse, short wavelength radiation. Improvements in laser intensity are not likely to buy more than a factor of two increase in fractional XUV yield, unless clever target design can take advantage of specific, high probability atomic transitions.

Debris, on the other hand, can be reduced even farther than our mass-limited targets will produce. Gas back-grounds, mechanical devices, and others will be developed in the coming year.

Hydrodynamic calculations have begun to help in future target design, using LASNEX in a 1-D and 2-D version. This code was developed for use in the design of laser-driven inertial fusion targets at intensities greater than  $10^{13}$  W/cm<sup>2</sup>. Our lower intensities should present a simpler more classical problem that will yield detailed information on energy transport in long pulse, long gradient length plasmas and on radiated yield into the spectral region of interest in the extreme ultraviolet.

The expansion of the plasma in 1-D was calculated to identify the regions in which laser energy was being absorbed. A long laser pulse could permit the plasma to expand to large dimensions, creating a relatively large source of radiation. This is undesirable from an optical point of view, where a singular point source is most useful for creating uniform lithographic illumination. Figure 5 shows the results of such a calculation. It demonstrates that at early times (up to 20ns), the laser is absorbed over a 150μm length. Most of the laser energy is delivered during this period, creating a small radiating region. At late times, however, the delivered energy extends over a 400-500μm length, suggesting that one cannot continue to gain in conversion efficiency by simply extending the KrF pulselength.

## Conclusions

We have designed an efficient, low debris target for use with soft x-ray projection lithography at 13.9nm. The target consists of 50nm of gold deposited upon an

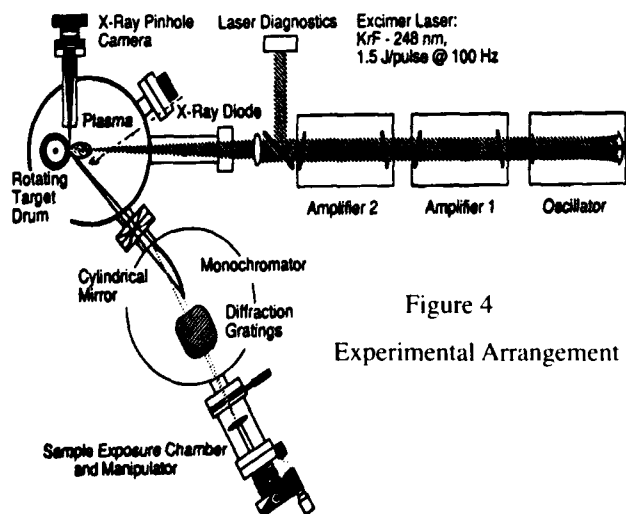


Figure 4  
Experimental Arrangement

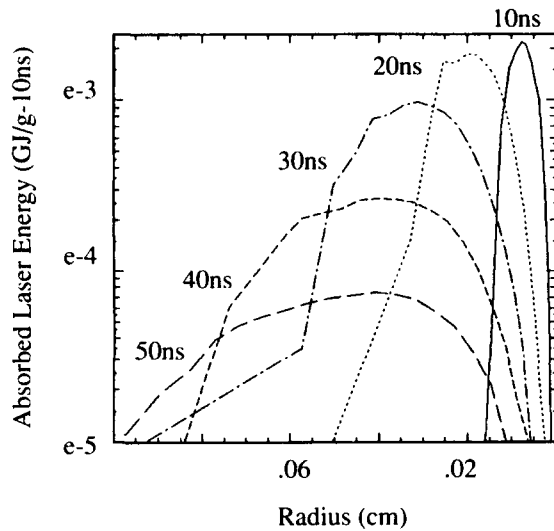


Figure 5

1-D Simulation of the Absorption of 248nm light as a function of time and space

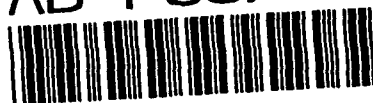
ultrathin plastic substrate. A conversion efficiency of .5% of the incident laser energy from a 30ns KrF laser at 248nm is typical for tin, tantalum, tungsten, and gold.

## References

1. H. Nishimura, et al., "Studies of Radiation Conversion and Transport in a 0.53 $\mu$ m Laser Produced Gold Plasma," AIP Conf. Proc. No. 75, Low Energy X-ray Diagnostics-1981, D. Attwood and B. Henke ed., Monterey, CA, 261 (1981).
2. B. Yaakobi, et al., "High x-ray conversion efficiency with target irradiation by a frequency tripled Nd:Glass laser," Opt. Commun. **38**, 196 (1981).
3. P. Rockett, W. Friedhorsky, and D. Giovanielli, "Radiation losses from high Z, 10.6 $\mu$ m laser-irradiated microballoons," Phys. Fluids **25**, 1286 (1982).
4. D. L. Matthews, et al., "Characterization of Laser-Produced Plasma X-ray Sources for Use in X-ray Radiography," J. Appl. Phys. **54**, 4260 (1983).
5. P. Alaterre, H. Pepin, R. Fabbro, and B. Faral, "X-ray conversion efficiency as a function of atomic number for 0.26 $\mu$ m-laser-irradiated targets," Phys. Rev. A **34**, 4184 (1986).
6. M. Chaker, et al., "Laser plasma x-ray sources for microlithography," J. Appl. Phys. **63**, 892 (1988).
7. D. J. Nagel, et al., "Repetitively pulsed-plasma soft x-ray source," Appl. Opt. **23**, 1428 (1984).
8. J. M. Bridges, C. L. Cromer, and T. J. McIlrath, "Investigation of a laser-produced plasma VUV light source," Appl. Opt. **25**, 2208 (1986).
9. R. Popil, P. D. Gupta, R. Fedosejevs, and A. A. Offenberger, "Measurement of KrF-laser-plasma x-ray radiation from targets with various atomic numbers," Phys. Rev. A **35**, 3874 (1987).
10. M. Chaker, et al., "Study and application of soft x-ray emission from laser-produced plasmas," SPIE Conf. Proc. Vol. 831, X-rays from Laser Plasmas, San Diego, CA, 237 (1987).
11. J. A. Tarvin, et al., "Mass Ablation Rates in a Spherical Laser-Produced Plasma," Phys. Rev. Lett. **51**, 1355 (1983).
12. T. J. Goldsack, et al., "Evidence for large heat fluxes from the mass ablation rate of laser-irradiated spherical targets," Phys. Fluids **25**, 1634 (1982).

# Multilayer Optics





## Interface Imperfections in Metal/Si X-Ray Multilayer Structures

David L. Windt, R. Hull, and W. K. Waskiewicz

*AT&T Bell Laboratories, Murray Hill, New Jersey 07974*

### Abstract

The structural and optical properties of optimized Mo/Si and Ru/Si X-ray multilayers prepared by sputter deposition have been examined using high-resolution TEM, optical profilometry, and X-ray and soft X-ray reflectance. In addition, the effect of sputter gas pressure on the structure and performance of Ru/Si multilayers has been investigated using the same techniques. We find that, similar to previous results for Mo/Si, lower pressure results in smoother layers. For optimized multilayers, interfacial roughness is negligible compared to interfacial diffuseness; the presence of amorphous interlayer regions in both of these systems is the major cause of reduced reflectance. The growth mechanism associated with these interlayers is unclear, though it seems likely that it is a diffusion process rather than the result of a ballistic effect.

### 1 Introduction

The development of multilayer coatings for soft X-ray optics has matured in the last decade, resulting in numerous high-resolution imaging applications in various research areas. Most recently, Mo/Si multilayer coated optics were used to demonstrate the feasibility of Soft X-ray Projection Lithography at  $\lambda = 140$  Å [1]. Indeed the highest reflectance multilayer coatings developed thus far are those consisting of M/Si bilayers (where M is a metal such as Mo, Rh, or Ru), which exploit the low absorption of Si just below the L-edge near  $\lambda = 125$  Å. Multilayer combinations designed for normal incidence reflectance at shorter wavelengths similarly exploit the absorption features of other light elements such as Be, B and C, though the peak reflectance of these systems is at present significantly lower than for M/Si multilayers.

The outstanding physics issues related to X-ray multilayer structures for high-resolution imaging applications include the limits to optical performance (e.g. normal incidence reflectance) and stability to thermal and radiative loading. Central to these issues is understanding the structure and growth of the layers and interfaces. It is by now clear that the role of interface imperfections (i.e. roughness and diffuseness) is critical to the optical performance of X-ray multilayer structures. However a number

of issues remain uncertain, including how these interface imperfections are formed, the precise way in which they affect the X-ray optical performance, and how they may be eliminated in order to improve performance.

In this paper, we have used a variety of characterization techniques to examine the nature of both Mo/Si and Ru/Si X-ray multilayer structures. From soft X-ray reflectance measurements, we have related the measured structural properties to the optical properties, and conclude that for optimized structures, the dominant interface imperfection is interdiffusion with interfacial roughness playing a much less important role. These results are discussed in terms of possible growth mechanisms for the amorphous interface regions, and how these interlayers may be eliminated.

### 2 Experimental

All multilayer samples examined were prepared by DC magnetron sputtering in argon, using a deposition system that is described elsewhere [2]. A variety of Mo/Si and Ru/Si samples were investigated, all with either 20 or 40 bilayers, with bilayer spacings  $d$  ranging from 68 to 75 Å, appropriate for use as reflectors in the range  $\lambda \sim 130$ -160 Å. All samples were deposited onto 3-inch-diameter, electronic grade Si (100) wafers.

The affect of argon gas pressure on layer formation in metal/metal and metal/silicon multilayers has been investigated by a number of authors [3]. For the case of Mo/Si, it has been found that lower argon pressure during deposition results in smoother layers. In this work we have similarly investigated this effect for Ru/Si multilayers; multilayer samples were prepared with Ar pressures of 2, 5 and 8 mTorr. The Mo/Si multilayer samples were all deposited with 2 mTorr Ar pressure.

High resolution transmission electron microscopy (HRTEM) was performed on each of the samples using a JEOL 2000FX operating at 200 keV, having a practical resolution limit of  $\sim 3$  Å. Cross sectional samples were prepared using the now conventional technique of mechanical polishing followed by ion milling, in this case using 3 keV Ar ions incident at 15 degrees to the surface, with the samples held at LN2 temperature. In order to extract quantitative information from the HRTEM measurements, the images were digitized, and interface widths and topography profiles were measured using techniques which have

been described previously [4].

Surface topography measurements were made using a WYKO TOPO-3D optical profilometer, with both 20X and 200X magnification objectives. These magnifications can resolve spatial wavelengths ranging from 2.5  $\mu\text{m}$  to 500  $\mu\text{m}$ , and .25  $\mu\text{m}$  to 50  $\mu\text{m}$ , respectively, with surface height sensitivities of  $\sim 2$  Å. From these topography measurements, and also from the interface topography profiles measured using HRTEM, Power Spectral Density (PSD) functions were computed for each of the samples studied, thus covering the range of spatial wavelengths from  $\sim 2$  Å to 500  $\mu\text{m}$  (albeit with some gaps in coverage.)

Absolute X-ray reflectance measurements were made using a Rigaku four-circle, rotating anode X-ray diffractometer ( $\lambda = 1.542$  Å) in the  $\theta - 2\theta$  geometry. The reflectance was measured from  $0^\circ$  to  $8^\circ$  grazing, which resulted in the observation of 12 Bragg peaks, with reflected intensities ranging over 8 orders of magnitude.

Soft X-ray reflectance measurements were made near normal incidence ( $5^\circ$ ) versus wavelength, and at fixed wavelengths versus incidence angle (from  $5^\circ$  to  $90^\circ$ ) using a new high-resolution laser-plasma-based reflectometer. This instrument will be described in detail elsewhere. We note, however, that the spectral resolution for the present measurements is approximately 0.1 Å, angular resolution is  $\sim 0.003^\circ$ , and absolute reflectance values are uncertain to approximately  $\pm 5\%$ .

The X-ray and soft X-ray reflectance data were compared with theoretical values, as computed from a dynamical model based on recursive application of the Fresnel equations. Interface imperfections are included in the model as a perturbation, where we have adopted the method described by Stearns [5]. In this method, to account for the decrease in specular reflectance due to scattering at an imperfect interface, the ordinary Fresnel reflection coefficient characterizing the amplitude of the reflected field at an abrupt interface between two optically dissimilar materials is multiplied by a factor which depends on the detailed nature of the interface. In particular, if the change in the dielectric function across an interface is described by the interface profile function  $p(z)$ , then the 1st order correction to the Fresnel reflection coefficient is the multiplicative factor  $\tilde{w}$ , which is the Fourier transform of the derivative of  $p(z)$ . For example, if the interface profile is described by an error function,  $p(z) = \frac{1}{\sqrt{\pi}} \int_{-\infty}^z e^{-t^2/2\sigma^2} dt$ , where  $\sigma$  is the interface width, the modified Fresnel reflection coefficient takes the form  $r = r_0 \cdot e^{-2(\frac{\lambda}{2\sigma} \cos \theta)^2}$ . Other analytical forms for  $p(z)$  can be used as well, as will be described below. We note that since  $p(z)$  is defined as the normalized, averaged value of the dielectric function along the direction normal to the surface, the modified Fresnel coefficient does not distinguish between a diffuse and a rough interface. Consequently, for the case of an interface which is both rough and diffuse, the interface width  $\sigma$  will be the sum of contributions from both interfacial roughness and diffuseness:  $\sigma_{\text{total}} = \sigma_{\text{rough}} + \sigma_{\text{diffuse}}$ .

### 3 Results

#### 3.1 Mo/Si Multilayers

Our results for Mo/Si multilayers are consistent with those reported by a number of authors [6], [7], [8]. We find that the Mo layers are polycrystalline, and the Si layers amorphous, with slightly asymmetric amorphous interlayer regions. The thicknesses of these interlayers are measured from HRTEM to be  $\sim 10$  and 12 Å for the Si/Mo and Mo/Si interfaces, respectively. These thicknesses correspond to  $\sigma$ -values of 6 - 7 Å. No indication of

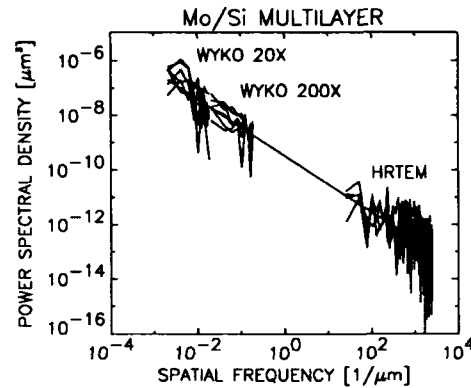


Figure 1: Power-spectral-density function for a Mo/Si multilayer.

crystalline silicide phases is evident in any of the HRTEM images.

The measured PSD functions for the Mo/Si samples were all approximately the same; as an example, Figure 1 shows the measured PSD for one such sample. The observation that the PSD functions measured using the optical profilometer (which refers to the surface of the multilayer), and those measured from the digitized HRTEM images (which refer to the interfaces) all lie on a straight line in the log-log plot of Figure 1 supports the assumption that the measured interface and surface topographies are meaningful.

The measured PSD functions  $S(f)$  were compared with power-law expressions of the form  $S(f) = K_n/f^n$ , where  $f$  is the spatial frequency,  $n$  is the (possibly fractional) exponent, and  $K_n$  is a constant. For all Mo/Si samples, the best fit values were found to be  $n \sim 1.0$ , and  $K_n \sim 5 \times 10^{-10}$ . As discussed by Church [9], power law PSD functions of this form represent a surface which is fractal in nature; the surface topography has no inherent scale, which is to be expected for a high quality optical surface. Thus the common description of a surface in terms of an autocorrelation function having an inherent correlation length does not apply for surfaces of this type. Furthermore, for fractal surface finish the rms surface roughness parameter  $\sigma$ , will depend on the range of spatial wavelengths considered. In terms of the PSD function,  $\sigma$  is given by

$$\sigma^2 = \int_{f_{\min}}^{f_{\max}} S(f) df \quad (1)$$

From the fractal fits to the measured PSD functions we can estimate the  $\sigma_{\text{rough}}$  values relevant to both X-ray and soft X-ray specular reflectance measurements using equation 1. For the case that  $n=1$ , equation 1 yields  $\sigma^2 = K_n \ln(f_{\max}/f_{\min})$ . The estimated ( $f_{\min}$ ,  $f_{\max}$ ) values are (1.5 Å, .5  $\mu\text{m}$ ) for reflectance measurements at  $\lambda = 1.542$  Å and  $\theta \sim 85^\circ$ , and (120 Å, 4  $\mu\text{m}$ ) for near-normal incidence soft X-ray reflectance measurements. We thus find that the  $\sigma_{\text{rough}}$  values are less than 1 Å, using  $K_n \sim 5 \times 10^{-10} \mu\text{m}^2$ . This implies that for these high-quality multilayers, interfacial roughness is negligible compared with interdiffuseness, as the  $\sigma_{\text{diffuse}}$  values (determined from HRTEM) are of order 6-7 Å.

The peak normal incidence reflectances of the Mo/Si multilayer coatings were measured to be  $61 \pm 2\%$  for a 40 layer pair sample (shown in Figure 2), and  $40 \pm 2\%$  for 20 layer pair samples at  $\lambda \sim 135$  Å. These values are consistent with theoretical values assuming interface widths of  $\sigma \sim 7 - 8$  Å, using the model described in the preceding section.

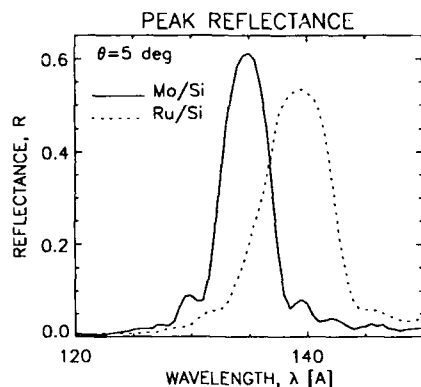


Figure 2: Measured normal-incidence reflectance of 40 layer-pair Mo/Si and Ru/Si multilayers.

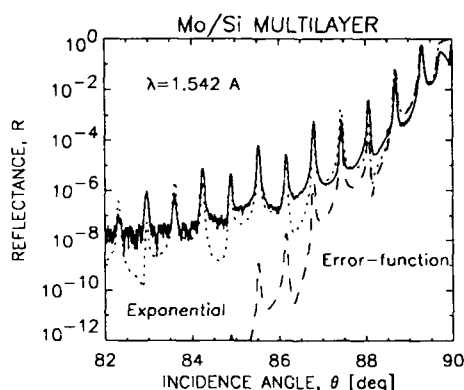


Figure 3: Measured (solid line) X-ray reflectance of a 20 layer-pair Mo/Si multilayer. The dotted line is a fit assuming an exponential interface profile function; the dashed line assumes an error-function interface profile.

The X-ray (1.542 Å) reflectance measurements were also fit using the modified Fresnel coefficient model. Assuming an error-function interface profile function, the  $\sigma$ -values obtained from these measurements were much lower (e.g.  $\sigma \sim 2$  Å) than those measured from both HRTEM and from normal-incidence reflectance. However, if an exponential interface profile function is used instead (as described in [5]), the derived  $\sigma$ -values were found to be  $\sim 6$  Å, which are more consistent with those measured from the other techniques. This is illustrated in Figure 3, where we show the measured X-ray reflectance of a Mo/Si multilayer along with the theoretical values assuming both error-function and exponential interface profile functions, with  $\sigma=6$  Å in each case.

### 3.2 Ru/Si Multilayers

HRTEM indicates much less crystallinity in the Ru layers and, as in Mo/Si multilayers, amorphous Si layers for the Ru/Si multilayers studied here. Analysis of the digitized images indicates that the contrast of the Ru layers is not constant, but varies continuously across the layers with a maximum near the center. The interface widths were found to be  $\sim 10$  and  $12$  Å for the Si/Ru and Ru/Si interfaces ( $\sigma=6-7$  Å). The thickness of the Ru-rich layers is  $\sim 50$  Å, while the Si layers are  $\sim 20$  Å-thick. Based on the estimated deposition rates for Ru and Si in our sputtering

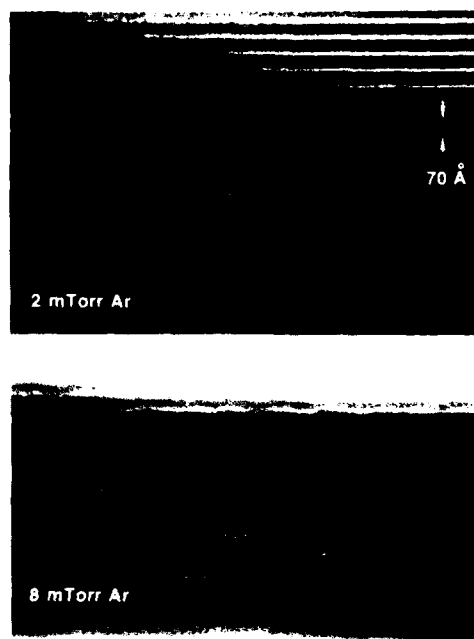


Figure 4: Low-magnification TEM images of Ru/Si multilayers grown at 2 and 8 mTorr Ar pressure. Note: Interface widths discussed in the text were measured from digitized high-magnification images, with pixel resolution of  $\sim 5$  Å.

system, the expected layer thicknesses for Ru and Si were 28 Å and 42 Å, respectively, indicating that significant intermixing of Ru and Si has occurred.

Similar to previous results for Mo/Si multilayers, we find that the effect of increased Ar pressure during deposition is increased layer roughness, as is evident in Figure 3.2 which shows the HRTEM results for Ru/Si samples prepared at 2 mTorr and 8 mTorr Ar pressure. The effect of this roughness on the measured optical properties is described below.

The PSD functions for the Ru/Si multilayers prepared at low Ar pressure are essentially identical to those for the Mo/Si samples. Again, power law fits were obtained with  $K_n \sim 5 \times 10^{-10}$  and  $n \sim 1.0$ . For the samples prepared at 5 and 8 mTorr Ar pressure, the long-wavelength PSD functions remained the same, yet the short-wavelength PSD functions (computed from the HRTEM interface topography profiles) increased in magnitude, corresponding to the  $\sim 100$  Å-spatial wavelength roughness observed in the HRTEM images.

The effects of increased layer roughness in the 5 and 8 mTorr Ru/Si samples is evident in the X-ray reflectance results. Shown in Figure 5 are the measured X-ray reflectance along with the theoretical fits for the 2 and 8 mTorr samples, revealing that the absolute reflectance and the number of observed Bragg peaks decreases rapidly with increasing Ar pressure.

For all Ru/Si multilayers, we find that acceptable fits to the measured X-ray data require a model using graded interfaces. That is the reflectance is computed from a multilayer stack consisting of not 2 but 5 layers per period: a pure Si layer and a pure Ru layer, plus mixed Ru/Si interlayers. This model is consistent with the varying composition of the Ru-rich layers observed from HRTEM. The measured reflectance is fit using this graded

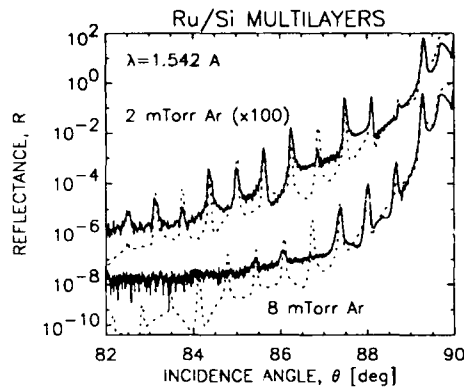


Figure 5: Measured (solid lines) and theoretical (dotted lines) X-ray reflectance of Ru/Si multilayers grown at 2 and 8 mTorr Ar pressure.

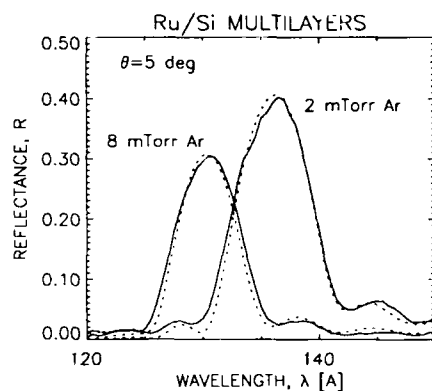


Figure 6: Measured (solid lines) and theoretical (dotted lines) normal incidence soft X-ray reflectance of Ru/Si multilayers grown at 2 and 8 mTorr Ar pressure.

interface model for each of the curves shown in Figure 5, with increasing  $\sigma$ -values to account for the decreasing reflectance with Ar pressure due to roughness. The best-fit  $\sigma$  values ranged from 6 to 16 Å, consistent with the HRTEM observations.

The normal-incidence reflectance for these Ru/Si multilayers is shown in Figure 6, along with fits to the data using the same graded-interface model just described. The decrease in reflectance with increasing Ar pressure here is not as dramatic: the peak reflectance decreased from ~40% to 30%, and the corresponding  $\sigma$ -values increased from 9 to 12 Å. The peak reflectance measured for a 40 layer pair Ru/Si multilayer prepared at 2 mTorr Ar pressure was  $53 \pm 2\%$  (shown in Figure 2.)

## 4 Discussion

The improved layer smoothness with decreasing gas pressure during sputtering has been explained previously for Mo/Si as well as other metal/metal multilayers in terms of the surface mobility of the deposited atoms [3]. Simply, the decreased gas pressure results in fewer collisions between the deposited atoms and the sputtering gas (so the deposited atoms are more energetic,) resulting in increased surface mobility and therefore films which are closer to their thermodynamic equilibrium condition. For the case of Mo-on-Si and Ru-on-Si this equilibrium condition is evidently one in which the layers have decreased roughness.

Nonetheless, even the Mo/Si and Ru/Si multilayers grown under optimized sputtering conditions (where layer roughness plays a negligible role) still show amorphous interlayer regions which result in decreased optical performance.

The growth mechanism for these asymmetric, amorphous interlayers is still unclear. A ballistic argument has been proposed [6], though this does not explain the observation of amorphous interlayers present in Mo/Si samples grown using MBE techniques onto room temperature substrates [10], where the energy of the deposited atoms is much lower than for sputter deposition. Anneal studies [7], [8] have shown that solid-state amorphization reactions (SSAR) which have been observed in other multilayer systems, apparently do not occur in Mo/Si. What is observed is crystallization of the amorphous regions upon thermal anneal, rather than an increased-thickness amorphous interlayer typical of a SSAR. These results may indicate that the initial formation of the amorphous interlayer is due to a diffusion process, most likely one in which the Si atoms tend to migrate to the surface as the Mo atoms are deposited, which would be consistent with the observed asymmetric interlayer widths. It is not clear if a similar situation exists for Ru/Si; an anneal study is presently underway in order to further elucidate the nature of the interlayer formation in this system.

## 5 Conclusions

We have shown that for Mo/Si and Ru/Si X-ray multilayer structures grown under optimized sputtering conditions, the dominant contribution to interface imperfections is interdiffusion, with interfacial roughness playing a negligible role. The amorphous interlayer regions present in both of these systems results in reduced reflectance. The growth mechanism of this interlayer is unclear, though it seems likely that it is a diffusion process rather than the result of a ballistic effect. If this is the case, it may be possible to inhibit the growth of this interlayer region using a diffusion barrier, or possibly a surfactant during growth. The possibility of growing heteroepitaxial X-ray multilayers still exists, and may in fact be the only way to produce truly abrupt interfaces, though the difficulty remains in finding suitable lattice-matched material combinations.

## 6 Acknowledgments

The authors gratefully acknowledge D. Bahnck for HRTEM sample preparation, and D. Grier for assistance in digitizing the HRTEM images. The authors also thank D. G. Stearns of Lawrence Livermore National Laboratories and M. Grabow of AT&T Bell Laboratories for many enlightening discussions and useful suggestions relating to this work.

## References

- [1] J. E. Bjorkholm, *et al.*, *J. Vac. Sci. Technol. B*, **8**, 1509 (1990)
- [2] W. K. Waskiewicz, *et al.*, *these proceedings*
- [3] See, for example, D. G. Stearns, *these proceedings*; B. M. Clemens, *J. Appl. Phys.*, **61**, 4525 (1987)
- [4] P. L. Windt, R. Hull, and W. K. Waskiewicz, *Proc. SPIE*, **1343**, 292 (1990)
- [5] D. G. Stearns, *J. Appl. Phys.*, **65**, 491 (1988)

- [6] A. K. Petford-Long, *et al.*, *J. Appl. Phys.*, **61**, 1422 (1987)
- [7] K. Holloway, K. B. Do, and R. Sinclair, *J. Appl. Phys.*, **65**, 474 (1989)
- [8] D. G. Stearns, *et al.*, *J. Appl. Phys.*, **67**, 2415 (1990)
- [9] E. L. Church, *App. Opt.*, **27**, 1518 (1988)
- [10] J. Slaughter, *et al.*, *Proc. SPIE*, **1343**, 73 (1990)



## Multilayers for Soft-X-Ray Optics

Takeshi Namioka, Masaki Yamamoto, and Mihiro Yanagihara

Research Institute for Scientific Measurements, Tohoku University,  
2-1-1 Katahira, Aoba-ku, Sendai 980, Japan

Masato Koike

Center for X-Ray Optics, Lawrence Berkeley Laboratory,  
University of California, 1 Cyclotron Road, MS 2-400,  
Berkeley, California 94720

### Abstract

Some problems fundamental to the design of soft-x-ray (SXR) multilayers are discussed. This includes an optical criterion for selecting proper material pairs and the critical film thickness needed for a film to become optically isotropic. A laboratory-type spectro-reflectometer useful for the evaluation of SXR multilayers is presented with experimental results. For practical interest in SXR projection lithography, preliminary results are also presented on irradiation tests of SXR multilayers and design of a demagnifying Schwarzschild optics for use with synchrotron radiation.

### 1. Introduction

Soft-x-ray (SXR) multilayers have been successfully applied to various optical elements and systems, and their technology seems to have been nearly perfected. However, various fundamental problems associated with the design, evaluation, and application of SXR multilayers have to be solved for further development. They are, for example, accumulation of data on the physical nature of very thin films and on irradiation damage of SXR multilayers, a convenient testing facility for SXR multilayers, and an effective method of designing SXR multilayer optics to be used on a synchrotron beamline. The present paper describes the results of our studies on some of these problems.

### 2. Optical criterion for selecting proper material pairs

Based on the Berning's formula [1] for the complex amplitude reflectance of a multilayer, we proposed an optical criterion for the selection of a proper material pair needed to produce an SXR multilayer that shows a high reflectance at given wavelength and angle of incidence [2].

Our optical criterion is stated as follows: when plotted in a complex plane, Fresnel reflection coefficients

(FRCs)  $r_A$  and  $r_B$  of two materials A and B in respect to a vacuum should lie in the immediate vicinity of the real axis and as far apart as possible from each other.

To show the usefulness and the correctness of our criterion, we consider, as an example, several multilayers designed for SXR of 12.4 nm at normal incidence. Figure 1 shows plots of the FRCs of various elements calculated, under the given conditions, with the optical constants,  $\tilde{n} = n - ik$ , of Henke et al. [3]. According to our criterion, the best pair should be Rh/Si, whereas it should be Ag/Si if we adopt Spiller's criterion [4], i.e., the spacer material should have the smallest possible  $k$  and two materials should have the largest possible difference in  $|\tilde{n}|$ . In addition to the pairs Rh/Si and Ag/Si, we take Mo/Si, a popular pair in this wavelength region.

We calculated for SXR of 12.4 nm the normal incidence reflectance of the optimized non-periodic multilayers of Rh/Si, Ag/Si, and Mo/Si formed on glass substrate. The optical constants ( $n, k$ ) used are (0.9070, 0.0066) for Rh [3], (0.8917, 0.038) for Ag [3], (0.4319, 0.0089) for Mo [3], (1.0319, 0.0015) for Si [3], and (0.9813, 0.0070) for glass [5]. The results obtained are shown in Fig. 2 as a function of the number of layers. The figure clearly illustrates the validity of our proposed criterion.

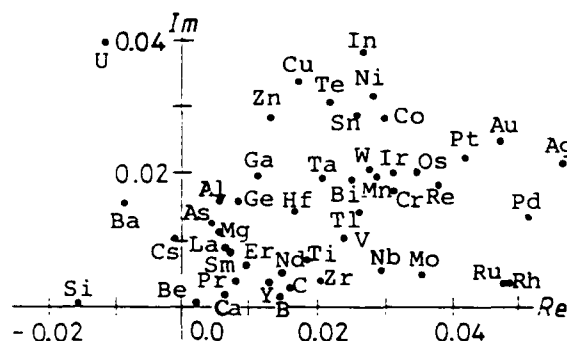


Figure 1. Complex plane plot of FRCs of various elements for SXR of 12.4nm at normal incidence.

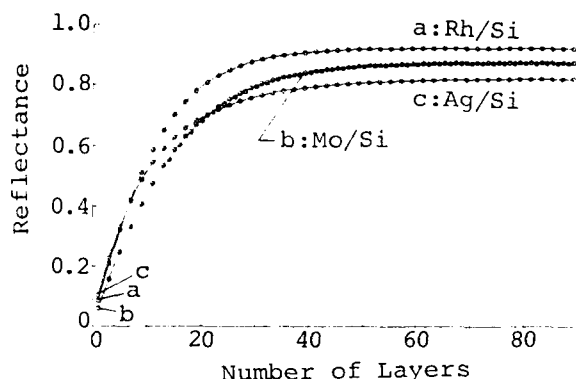


Figure 2. Calculated reflectances of multilayers vs number of layers (normal incidence, SXR of 12.4nm).

### 3. Critical film thickness

At early stages of deposition the film undergoes a transition from an island or an anisotropic state to an optically isotropic and continuous state at a certain film thickness  $d_c$  which we call critical film thickness. Information on  $d_c$ 's is of practical importance in the design and fabrication of SXR multilayers. It can be obtained through in-situ ellipsometric measurements of  $\rho$ , the ratio of complex amplitude reflectances of the film for p- and s-components.

A series of  $\rho$  plots in the Gaussian plane illustrates the growth process of the film as the change in  $\rho$ . We call this  $\rho$  plot a growth curve in the following. In Fig. 3 are shown the growth curves of various materials deposited on BK7 substrate. For reference the point corresponding to a film thickness of 10 nm is indicated by an open circle on each curve. The optical constants,  $n$  and  $k$ , and the thickness,  $d$ , of a growing film at various stages of its deposition process can be determined by analyzing the observed growth curve on the basis of a homogeneous, isotropic plane-parallel film model. Since the process of determining  $n$ ,  $k$ , and  $d$  is involved, only a few examples of the results will be presented here. (For the details refer to ref. 6).

The results obtained for tungsten, silicon, and gold are shown in Fig. 4 as examples. As the deposition proceeds,  $n$  and  $k$  start from those of the substrate and

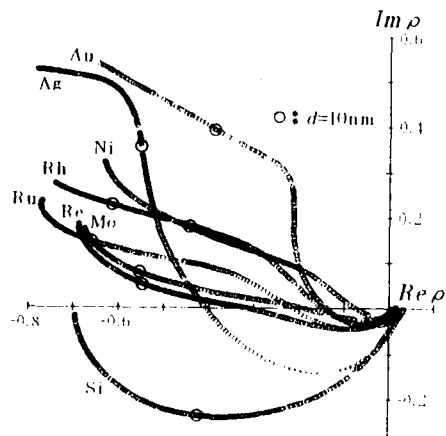


Figure 3. Growth curves of various films (ref. 6).

in most cases monotonically increase toward the values for the bulk. On the other hand,  $d$  goes through an anomalous peak. At around a certain deposition time  $t_c$ , the film parameters  $n$ ,  $k$ , and  $d$  begin to show the behavior that is expected from the isotropic model: the values of  $n$  and  $k$  become nearly constant and  $d$  begins to increase linearly with  $t$ . This suggests that at  $t \approx t_c$

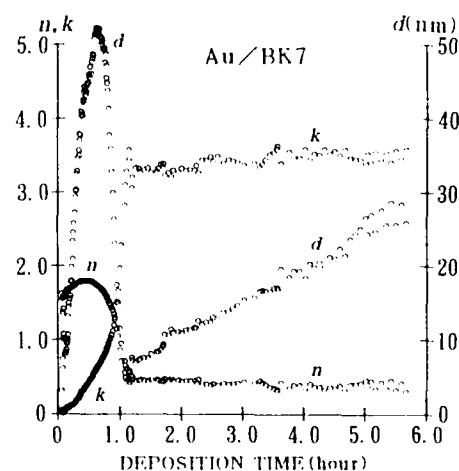
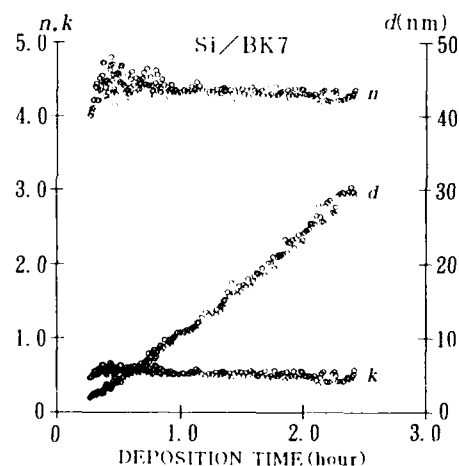
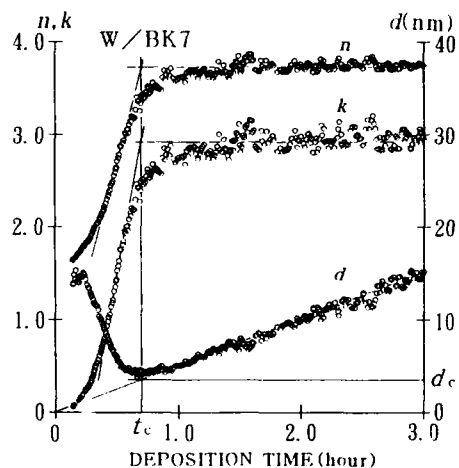


Figure 4. Plots of  $n$ ,  $k$  and  $d$  against deposition time for films of W, Si, and Au (ref. 6).

the film undergoes a transition from an optically anisotropic (including island) stage to an optically isotropic state. The values of  $n$  and  $k$  obtained at  $t \leq t_c$  are apparent values resulted from regarding the anisotropic state as an isotropic one.

Since the transition takes place gradually in most cases, we define  $t_c$  as the deposition time that corresponds to the intersecting point of tangents to the  $n$ - $t$  curves (and  $k$ - $t$  curves) on both sides of  $t \sim t_c$  (see Fig. 4). The critical film thickness  $d_c$  is defined as the film thickness that corresponds to the intersecting point of the straight line  $t = t_c$  and the one passing through the origin and the data points at  $t > t_c$  (see Fig. 4). The values of  $d_c$  thus obtained are listed in Table 1.

Table 1. Critical film thickness  $d_c$  of various films prepared by ion-beam sputtering (ref. 6).

| Material | $d_c$ (nm) | Material | $d_c$ (nm) | Material | $d_c$ (nm) |
|----------|------------|----------|------------|----------|------------|
| C        | 2.8        | Mo       | 3.3        | Ag       | 17.0       |
| Si       | <2.8       | Ru       | 2.8        | W        | 3.7        |
| Ni       | 4.2        | Rh       | 3.9        | Re       | 4.0        |
| Nb       | 3.2        | Pd       | 4.2        | Au       | 5.8        |

#### 4. SXR spectroreflectometer

Performance tests of SXR multilayers at their designed wavelengths and angles of incidence have been carried out almost exclusively by using synchrotron radiation (SR). A lack of sufficient machine time is, however, the drawback in utilizing SR for evaluation.

To ease the situation we designed and constructed a laboratory-type SXR spectroreflectometer with a laser-produced plasma (LPP) source [7]. This facility, called JUNE (JUNior Evaluator), consists of a laser-produced plasma source driven by a Nd:YAG laser (800 mJ/pulse, 12 ns FWHM, 10Hz), a focusing mirror with a radius of curvature of 4 m, a  $166^\circ$  constant-deviation monochromator equipped with a 3-m, 600-grooves/mm concave grating, and a reflectometer.

The center portion of monochromatized pulse beam is allowed to pass through the center hole (3 mm in diam) of a microchannel plate (MCP) placed behind the exit slit of the monochromator, while its outer portion is detected by the MCP. This provision made it possible to carry out intensity measurements with a reproducibility of  $\pm 1\%$  or better. With a samarium target we can obtain with the present system a fairly clean continuum over the working wavelength range of  $\sim 7$ – $40$  nm. We examined the performance of JUNE by measuring the spectral reflectance curve of a Mo/Si which had been evaluated with SR at the Photon Factory. Figure 5 compares the results of two sets of measurements, one with SR and the other with LPP. Two sets of the curves taken at angles of incidence of 40, 45, and 48 degrees are almost identical, if the reflectance measured with JUNE is doubled. It should be noted here that (1) SXR emerging from the monochromator is almost unpolarized in the case of JUNE, whereas SR is linearly polarized to a high degree and (2) at angles of incidence near  $45^\circ$  the multilayer has practically no reflectance for p-component. With this in mind, we can conclude that the

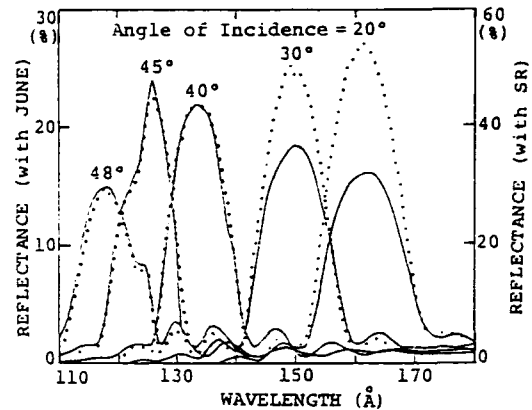


Figure 5. Reflectance of a Mo/Si multilayer measured with SR (—) and LPP (----).

agreement between the two data taken at  $\sim 45^\circ$  angles of incidence is excellent: JUNE is proved to have high reliability and performance.

JUNE is fully automated and takes about 5 minutes to cover a spectral range of 7–31 nm at intervals of 0.08 nm. JUNE has been extremely useful in evaluating multilayers right after their fabrications. Only shortcoming JUNE has at present is that reflectance measurements cannot be made with linearly polarized SXR over an extended wavelength region. SXR multilayers have been used as efficient SXR polarizers [8, 9], but they are effective only for SXR of wavelengths in the immediate vicinity of their respective peak wavelengths at an angle of incidence of  $\sim 45^\circ$ .

We have adopted a scheme of a double crystal monochromator to realize wide-band SXR multilayer polarizers. Figure 6 shows preliminary results obtained for a double multilayer polarizer (DMP) consisting of two Ru/Si multilayers. The measurement was made with JUNE, and the degree of linear polarization of monochromatic SXR passed through DMP was found to be better than 99% at 97 eV and 95% or better at other photon energies. Recently, a DMP equipped with Ru/C has shown very good polarization characteristics over a range of 80–160 eV. We plan to install a DMP in JUNE in the very near future to expand JUNE's capability.

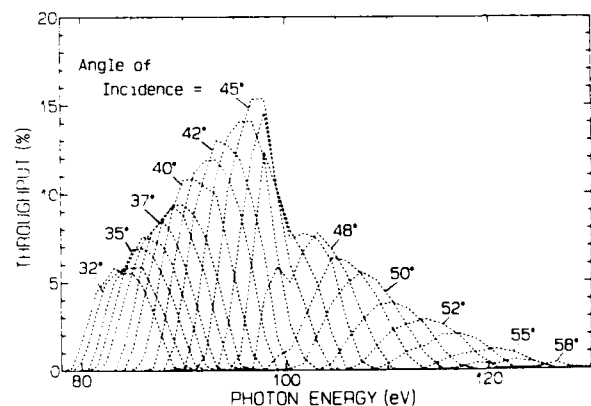


Figure 6. Throughput of a Ru/Si DMP.



## 5. Irradiation tests

Utilization of next-generation SR sources in highly sophisticated experiments, such as SXR projection lithography, requires the development of SXR multilayers that can withstand the unprecedented power load. It is therefore very pressing to conduct SR irradiation tests of multilayers.

To this end, several investigators [10,11] have studied SR irradiation effects on SXR multilayers. In these studies, the stability of SXR multilayers was evaluated in terms of changes in the reflectance and wide-angle x-ray diffraction patterns measured only before and after the irradiation test. Such data are valuable, but they do not reveal any information on how the degradation proceeded with exposure time. Furthermore, reflectances were measured almost exclusively for  $\text{CuK}\alpha$  radiation (0.154 nm) regardless of their design wavelengths and angles of incidence.

We have made a preliminary study on the stability of Mo/Si, Rh/Si, and Ru/Si multilayers against white SR (a power density of  $\sim 0.14\text{W/mm}^2$  on the sample surface) from a bending magnet at the Photon Factory [12]. The samples were designed to have high reflectance for SXR of  $\sim 13\text{ nm}$  ( $\sim 97\text{eV}$ ) at an angle of incidence of  $45^\circ$  and were fabricated by ion-beam sputtering (IBS) and magnetron sputtering (MS). We adopted a detector unit consisting of a carbon filter (150nm thick) and an aluminum cathode (1 mm thick, 30mm in diam) and monitored the intensity of reflected beam from the sample in terms of photoelectric current (see Fig. 7). To protect the cathode from irradiation damage, we placed an aluminum shutter in front of the detector and measured the current by opening the shutter intermittently. In this way, the detector unit functioned properly as a high-power-resistant detector for SXR of 73-105eV. The samples were exposed to white SR beam for 13-15 hours in a vacuum better than  $1 \times 10^{-8}$  Torr, so that no contamination footprint of the incident beam was noticed on the sample surface. The results are summarized in Fig. 8. The ordinate is the measured photoelectric current, which is normalized to its initial value after being corrected for changes in ring current. The figure clearly shows that the Mo/Si and Rh/Si multilayers are stable against continuous irradiation, whereas the Ru/Si exhibits a definite degradation at a steady rate of  $\sim 1.5$  per hour.

This method can be applied to other wavelengths by choosing a proper pair of materials for the filter and cathode. If needed, we can also apply active cooling to the detector unit without sacrificing its performance.

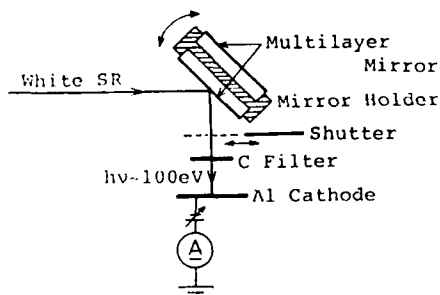


Figure 7. Schematic of SR irradiation test.

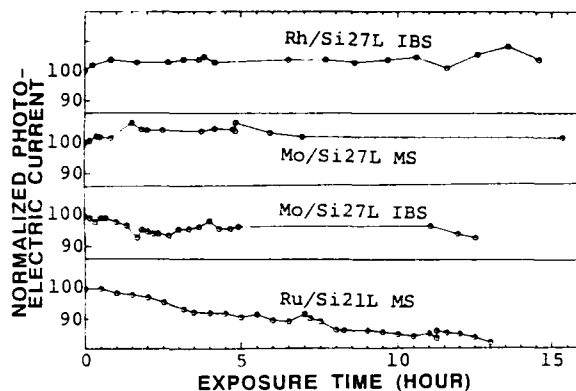


Figure 8. Results of SR irradiation test.

## 6. Design and simulation of demagnifying optics

A two-mirror system, such as the Schwarzschild optics, and a multi-mirror system are of current interest in the field of SXR projection lithography and SXR microscopy. In spite of this, no definite design principle is available at present even for a two-mirror system, although some studies [13] have been made on a concentric Schwarzschild optics. It is, therefore, of practical interest to establish a solid theoretical basis for the Schwarzschild optics.

To this end, we have made a preliminary study on a non-concentric Schwarzschild optics (Fig. 9). The necessary conditions for the best focusing in the meridional and the sagittal plane and for coma elimination in the meridional plane are, respectively, given [14] by

$$\cos^2\alpha/r' - 2\cos\alpha/R - \cos\alpha(2-\rho\cos\theta/r)/a\rho = 0, \quad (1)$$

$$1/r' - 2\cos\alpha/R - (2 - \rho/r\cos\theta)/b\rho = 0, \quad (2)$$

$$-2\sin\theta(1-\rho\cos\theta/r)/a^3\rho^2 + 2\sin\alpha[1/R + (2-\rho\cos\theta/r)/a\rho]^2 = 0, \quad (3)$$

$$\text{where } a = [\rho\cos\theta - D(2 - \rho\cos\theta/r)]/\rho\cos\alpha, \quad (4)$$

$$b = [\rho/\cos\theta - D(2 - \rho/r\cos\theta)]/\rho. \quad (5)$$

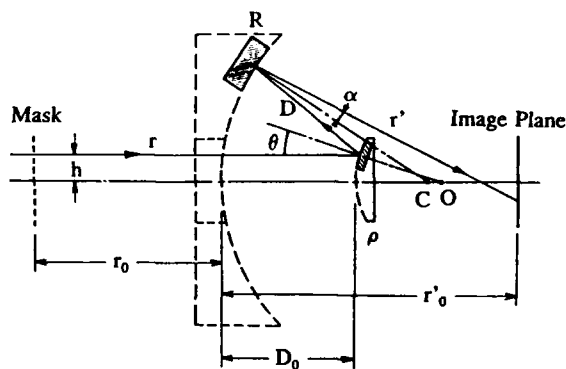


Figure 9. Non-concentric Schwarzschild optics.

We consider two small mirrors which are portions of the Schwarzschild optics and optimize this two-mirror system so as to satisfy Eqs. (1)-(3) for given values of  $\rho$ ,  $h$ , and magnification  $M$ . The design parameters thus determined are used to trace rays through the system consisting of an undulator (or a bending magnet), a foremirror, a mask (a mesh of  $2.5\mu\text{m}$  pitch and 25% transmission), and the Schwarzschild optics. The mask and the image plane are assumed to be perpendicular to the optical axis. For example, we obtain the following design parameters for  $\rho = -18\text{mm}$ ,  $h = 5\text{mm}$ , and  $M = 9.5$ :  $R = 59.783\text{mm}$ ,  $r_0 = 110.678\text{mm}$ ,  $D_0 = 41.624\text{mm}$ ,  $r'_0 = 74.425\text{mm}$ ,  $M_m = 9.500$ ,  $M_s = 8.929$ , where subscripts  $m$  and  $s$  stand for the meridional and the sagittal plane, respectively.

With these parameters, we obtained a spot diagram shown in Fig. 10. In this case we generated about one million rays from an undulator (13nm, fundamental) [15] and made a spot diagram for 2000 rays transmitted through a portion of the mesh whose diameter was  $50\mu\text{m}$ . It is clearly seen in the figure that the system has a spatial resolution of  $\sim 0.13\mu\text{m}$  on the image plane. However, the image has a small distortion, and the spatial resolution is reduced rather rapidly with increase in the amount of deviation from the designed height,  $h = 5\text{mm}$ : the usable height of the mask is limited to  $4\text{mm} \leq h \leq 5.5\text{mm}$  in this case. The spatial resolution and the usable mask area can be increased only by increasing  $\rho$ , if the magnification is retained constant. Thus, the performance and the overall length of the Schwarzschild optics should be compromised.

#### Acknowledgment

This work was supported in part by Grant-in-Aid for Scientific Research on Priority Areas, "X-Ray Imaging Optics", No.01651002 from the Ministry of Education, Science and Culture, Japan and by the U.S.Department of Energy under Contract No. DE-AC03-76SF00098.

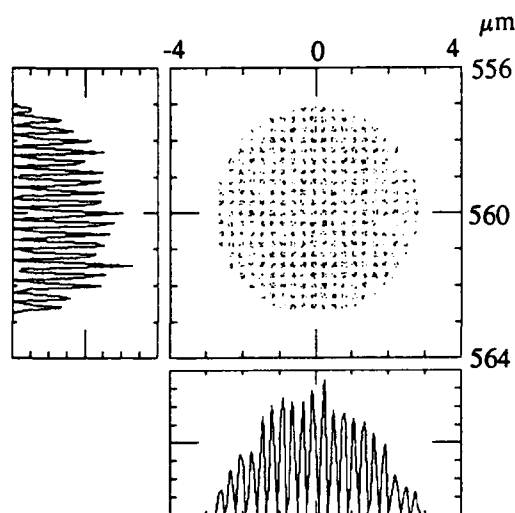


Figure 10. Spot diagram of the demagnified image of a mesh of  $2.5\mu\text{m}$  pitch and 25% transmission.

#### References

1. P. H. Berning, "Theory and Calculations of Optical Thin Films," in *Physics of thin films*, J. Hass, ed. (Academic, New York, 1963), p.100, Eq.(140).
2. M. Yamamoto and T. Namioka, "Layer-by-layer design method for soft x-ray multilayers," Submitted to Appl. Opt.
3. B. L. Henke, P. Lee, T. J. Tanaka, R. L. Shimabukuro, and B. K. Fujikawa, "Low energy x-ray interaction coefficients: photoabsorption, scattering and reflection  $E=100\text{-}200\text{eV}$   $Z=1\text{-}94$ ," *At. Data Nucl. Data Tables* **27**, No. 1, 1-144 (1982).
4. E. Spiller, "Evaporated multilayer dispersion elements for soft x-rays," *Am. Inst. Phys. Conf. Proc.* No. 75, 124-130 (1981).
5. H. R. Philipp, "Silicon dioxide (glass)," in *Handbook of Optical Constants of Solids*, E. D. Palik, ed. (Academic, New York, 1985), pp.749-763.
6. M. Yamamoto and T. Namioka, "In-situ ellipsometric study of optical properties of ultrathin films," submitted to Appl. Opt.
7. S. Nakayama, M. Yanagihara, M. Yamamoto, H. Kimura, and T. Namioka, "Soft x-ray reflectometer with a laser-produced plasma source," *Phys. Scr.* **41**, 54-757 (1990).
8. P. Dhez, "Polarizers and polarimeters in the X-UV range," *Nucl. Instr. Meth.* **A261**, 66-71 (1987).
9. H. Kimura, T. Inoue, T. Maehara, M. Yamamoto, M. Yanagihara, and T. Namioka, "Polarization measurement in the soft x-ray region," in *Book of Abstracts of the 15th International Conference on X-rays and Inner-Shell Processes* (Knoxville, 1990), paper B08.
10. E. Ziegler, Y. Lepetre, S. Joksche, V. Saile, S. Mourikis, P. J. Viccaro, G. Rolland, and F. Laugier, "Performance of multilayers in intense synchrotron x-ray beams," *Rev. Sci. Instrum.* **60**, 1999-2002 (1989) and the references therein.
11. J. B. Kortright, S. Joksche, and E. Ziegler, "Stability of tungsten/carbon and tungsten/silicon multilayer x-ray mirrors under thermal annealing and x-radiation exposure," *J. Appl. Phys.* **69**, 168-174 (1991) and the references therein.
12. M. Yanagihara, T. Maehara, S. Gunadi, M. Asano, and T. Namioka, "In-situ performance tests of soft x-ray multilayer mirrors exposed to synchrotron radiation from a bending magnet," submitted to Appl. Optics.
13. For example, D. L. Shealy, R. B. Hoover, T. W. Barbee, Jr., and A. B. C. Walker, Jr., "Design and analysis of a Schwarzschild imaging multilayer x-ray microscope," *Opt. Eng.* **29**, 721-727 (1990).
14. T. Namioka and M. Seya, "Optical properties of a system consisting of a mirror and a grating," *Appl. Opt.* **9**, 459-464 (1970).
15. M. Koike, "An efficient subroutine for simulating undulator radiation in ray tracing program," in *Book of Abstracts of the 15th International Conference on X-rays and Inner-Shell Processes* (Knoxville, 1990), paper B07.



## Multilayer Uniformity and Performance of Soft-X-Ray Imaging Optics

J. B. Kortright

*Center for X-Ray Optics, Lawrence Berkeley Laboratory, University of California,  
Berkeley, California 94720*

R. N. Watts

*Physics Laboratory, National Institute of Standards and Technology,  
Gaithersburg, Maryland 20899*

### ABSTRACT

A Schwarzschild objective coated with Mo/Si multilayers is used as an example to discuss issues of multilayer uniformity on soft x-ray reflective optics for imaging applications. Ray-tracing dictates the ideal multilayer period variation across the curved surfaces of these optics. Deposition system dependent factors are used to predict the expected variation. Measurements yield the actual variation obtained in practice. The multilayer bandwidth sets the tolerance scale for acceptable deviations from the ideal period variation. For Mo/Si multilayers for use at  $\lambda > 124 \text{ \AA}$  this bandwidth is relatively large, easing the tolerance for period variation control. At shorter wavelengths, high reflectance multilayer bandwidths are narrower, requiring more effort to obtain acceptable period variation.

### Introduction

Utilization of high reflectance multilayer coatings in soft x-ray focussing applications demands consideration of issues relating to the uniformity of the multilayer coatings across the surfaces of these reflective optics. This paper discusses these issues as they relate to the 20 times demagnification Schwarzschild objective in Figure 1 coated with Mo/Si multilayers for operation at 76 eV. The considerations made here for this Schwarzschild objective are generally applicable to all multilayer-coated reflective imaging systems of interest for projection lithography and other applications.

The Schwarzschild objective is a relatively simple reflective system for soft x-ray imaging, consisting of two spherical mirrors centered on an optic axis as in Figure 1. The primary (small) mirror obscures the central rays, so that only an annular

region exists with which to form a clear aperture. Symmetry about the optic axis of this system allows us consider rays defined by the numerical aperture of the incident light defined here as  $NA = \sin U$  where  $U$  is the off-axis angle of the incident ray on the primary as in Fig. 1.

Most of the analysis of the problem of multilayer period variation rests on the multilayer interference condition and on the width of the multilayer Bragg peak. The Bragg equation uncorrected for refraction is  $\lambda = 2d \cos \theta$ , where  $\lambda$  is the x-ray wavelength,  $d$  is the multilayer period, and  $\theta$  is the incident angle (from normal). For simplicity, we assume that the bandwidth of light illuminating the Schwarzschild is narrow compared to the bandwidth of the multilayer coating on the Schwarzschild. The multilayer bandwidth  $\Delta E/E$  scales as  $1/N$  where  $N$  is the number of periods contributing to the constructive interference. Because absorption is significant in the soft x-ray range, bandwidths tend to be somewhat larger than  $1/N$ , which would give the bandwidth in the limit of no absorption. For the 20 period Mo/Si multilayer considered here  $\Delta E/E = 0.076$ .

Both the performance implications of imperfect multilayer period variation, and the tolerance criteria for acceptable deviations from the optimum

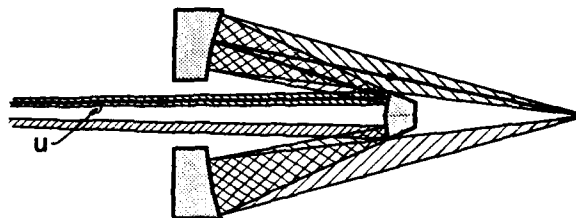


Figure 1. Cross section including the optic axis of a 20 times demagnification Schwarzschild objective.



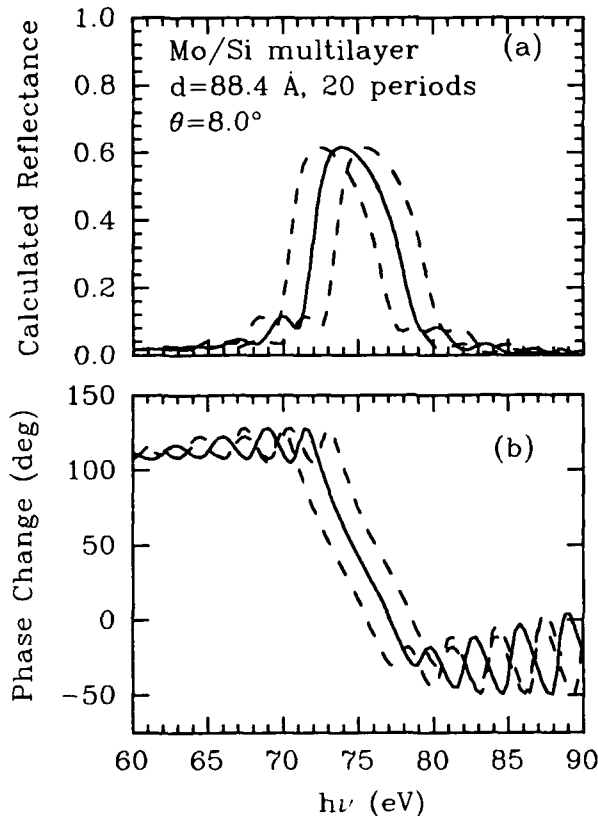


Figure 2. Calculated reflectance (a) and phase change on reflection (b) of Mo/Si multilayers.

period variation, are obtained from the multilayer Bragg peak as illustrated in Figure 2. Of primary importance to performance is that each ray passing through the clear aperture fall within the multilayer reflectance bandwidth at each mirror. Figure 2a shows the calculated reflectance profiles for several Mo/Si multilayers designed to peak near 75 eV. The dashed curves are offset from the solid curve by  $\pm 1/4(\Delta E/E)$ , illustrating that roughly this amount of multilayer period error can be tolerated without significant loss of reflected intensity in a narrow illumination bandwidth. Thus, to first order, the multilayer period variation across a given mirror, and the matching of multilayer periods on the primary and secondary mirrors, must be accurate to roughly  $\pm 1/4(\Delta E/E)$  for all rays to pass through the system without significantly decreased intensity.

The variation in phase change on reflection across the multilayer Bragg peak is a second issue relating the multilayer period variation to performance of imaging optics. This is illustrated in Fig. 2b, which shows the calculated phase change on reflection for the same multilayers shown in Fig. 2a. The phase change on reflection varies by roughly  $180^\circ$  across the Bragg peak. Such large phase shifts have implications for diffraction-limited imaging that have

received little investigation. To avoid unwanted phase change differences on reflection of more than  $\pm 45^\circ$  for all rays reflected by a single mirror requires that the  $d$  variation across that mirror deviate from the ideal variation by no more than roughly  $\pm 1/4(\Delta E/E)$ . Similar tolerances exist at the other mirror, and the total phase error for each ray passing through the system is the sum of errors accumulated at each reflection. The effect of these phase change errors on image formation is to blur the image, and the magnitude of this effect can be studied by full image simulations which include these multilayer phase effects [1]. These phase effects may be important in actual systems only when the optical figure and alignment are perfect enough that phase errors introduced by imperfections in these properties are less than some fraction of  $\lambda$ .

The multilayer bandwidth sets the tolerance scale for acceptable deviations from ideal multilayer period variation, and roughly  $\pm 1/4$  of this bandwidth is a reasonable allowance for deviations from the ideal variation. The bandwidth of the Mo/Si multilayer used here is large, allowing deviations in period of roughly  $\pm 2\%$  to be considered acceptable. This relatively large tolerance eases considerably the difficulty of depositing multilayers with acceptable period variation.

#### Ideal Multilayer Period Variation

To first order, geometrical ray-tracing dictates the ideal period variation of the multilayers across each mirror, as shown in Figure 3. The incidence angle  $\theta$  for each ray at each mirror is plotted vs. NA in Fig. 3a. The ideal  $d$  variation across each mirror is plotted in Fig 3b, and is calculated using the Bragg equation for fixed  $\lambda = 163 \text{ Å}$ . Aside from a small (and essentially constant with NA) correction for refraction, the  $d$  variation prescribed in Fig. 3b ensures a flat wavelength response across each optic, and minimizes the intensity and phase errors discussed in the previous section.

Thus, ideal multilayer coatings on focusing optics do not have constant or uniform period across the surfaces of the optics. Rather, they have a specific variation of the period across the surface of each mirror which is dictated by the varying incidence angles and by the Bragg interference condition. The problem of coating focussing optics with multilayers then becomes that of obtaining multilayers with acceptable period variation compared to the ideal variation, given the tolerances for acceptable deviations from this ideal.

This ideal variation in  $d$  across the surface of each optic has the effect of modifying the optical figure of that mirror, defined by the multilayer sur-

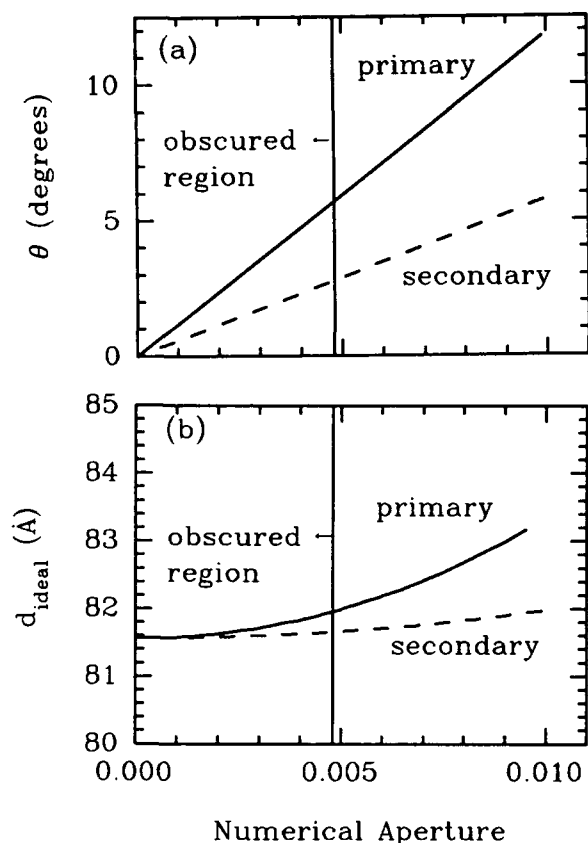


**Figure 3.** Incidence angles (a) and ideal multilayer period (b) are plotted as a function of numerical aperture.

face, by  $N$  times that variation. This in turn introduces additional phase errors in the imaging process, which again may be important only if substrate figure and alignment are perfect. The blurring introduced by these effects can be simulated by full image formation calculations.

#### Predicted Multilayer Period Variation

Our approach to date to the problem of obtaining acceptable multilayer period variations has been to characterize our sputter deposition system well enough to predict the expected period variation and to verify that it is acceptable. Then, the Schwarzschild mirrors are coated, followed by measurement of the obtained variation. Practical considerations regarding multilayer deposition are specific to a given deposition system. Many different approaches to multilayer deposition can lead to acceptable results.

Here, planar magnetron sputtering is used to deposit multilayers. Our sputtering system consists of three 10 cm diameter sputtering targets on a circle of radius 17.8 cm in the base plate of the vacuum chamber. 10 cm above the target surfaces rotate the substrates on the same circle. No planetary motion of

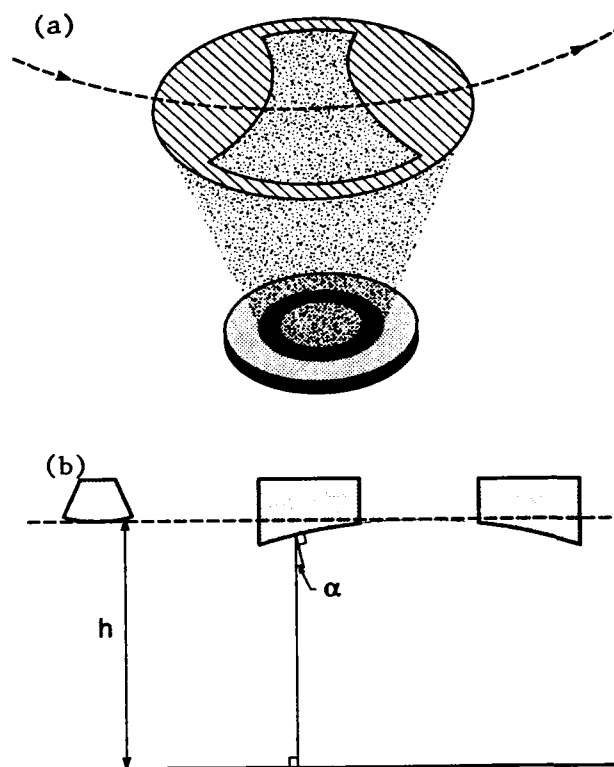


**Figure 4.** (a) shows an aperture the sputtered beam to improve uniformity on flat substrates. (b) shows deposition distance and angle dependencies

the substrates was used for the results presented here. Our major concerns in deposition are dealing with the relatively large coated areas (7.5 cm diameter) and the curved mirrors of the Schwarzschild objective. Our approach has been to deposit multilayers on flat substrates with good uniformity, and then to consider the effects of substrate curvature on the multilayer period variation on the Schwarzschild mirrors.

Placing an aperture in the sputtered beam allows us to achieve good uniformity on a flat area the size of the large, secondary mirror. This is illustrated in Fig. 4a, which shows an aperture just below the plane of the substrate in the sputtered beam. This aperture effectively equalizes the integrated deposition on the substrate as a function of radius from the center of the substrate table. Planetary rotation of the substrates with this aperture improves the uniformity on flat substrates to much better than this  $\pm 1\%$  level.

The spherical mirror surfaces introduce additional factors which affect the period  $d$ . These are illustrated in Figure 4b, which shows that different points on the mirror surfaces have different distances from and make different angles with respect to the planar sputtering target. Our analysis assumes that the deposition distance and angle dependencies

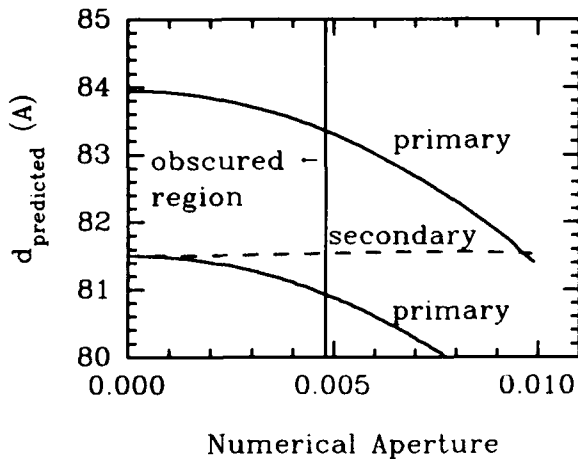


Figure 5. Predicted  $d$  variation on the Schwarzschild mirrors.

are separable, so that the period can be expressed as  $d = d_0 \cdot f(h) \cdot g(\alpha)$ , where  $f(h)$  and  $g(\alpha)$  represent the individual dependencies and  $d_0$  is the period at the mirror apex. Characterization of  $f(h)$  and  $g(\alpha)$  show that  $f(h)$  is linear in  $h$ , and  $g(\alpha)$  is roughly proportional to  $\cos(\alpha)$  over the range of these variables of interest [2].

From these characterizations we predict the variation in  $d$  across the two mirrors of the Schwarzschild pair, as shown in Figure 5. For the secondary mirror the  $f(h)$  and  $g(\alpha)$  factors tend to cancel, leading to the relatively flat predicted  $d$  vs. NA which is very close the ideal variation. Two separate curves are shown for the primary mirror, corresponding to two different heights in the sputtering system. The lower curve is the predicted  $d$  variation when the primary and secondary apexes have the same  $h$  as in Fig. 4b. The upper curve is the prediction when the primary is moved closer to the sputtering targets. This shift in the primary mirror height brings the range of the predicted  $d$  variation for that mirror into better agreement with the ideal  $d$  variation shown in Fig. 3b. For the primary, the  $f(h)$  and  $g(\alpha)$  factors yield variations in  $d$  in the same direction, resulting in a negative slope with NA. The ideal  $d$  variation for the primary in Fig. 3b has a positive slope. The shifted primary curve, while maintaining the negative slope, has a better overlap with the ideal curve in the unobscured region. Even with the difference in slope of the predicted and ideal  $d$  variation, the total deviation of the predicted from the ideal is just within the  $\pm 2\%$  criteria. The agreement for the secondary is much better. This analysis thus suggests that the period variation of the multilayers deposited onto the optics are just within the tolerance criteria set by the multilayer bandwidth.

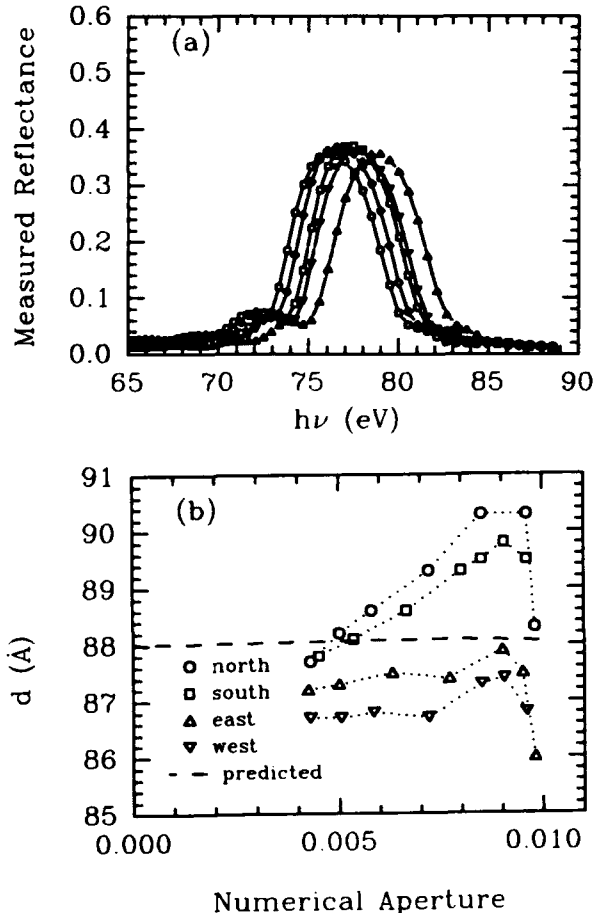


Figure 6. (a) shows the measured reflectance at different positions along a radius of the secondary mirror. (b) shows the measured  $d$  variation together with the refraction corrected predicted variation (dashed line).

#### Measured Multilayer Period Variation

Following deposition of multilayer coatings on the Schwarzschild objectives, soft x-ray reflectance measurements were made to determine the actual multilayer period variation on the secondary mirror. Using soft x-rays at near normal incidence facilitates such characterizations, whereas it is very difficult to use short wavelength x-rays near grazing incidence to measure multilayer reflectance from curved mirrors. The measurements reported here were made at the SURF facility at NIST [3] with the 2 mm<sup>2</sup> incident beam parallel to the optic axis of the secondary mirror and the detector at a fixed angle. The wavelength was scanned to measure the reflectance peak, and these data were fit to calculated multilayer reflectance curves to determine  $d$  at the point of illumination on the mirror. The mirror was then translated to measure the reflectance from another position. Measurements were made as a function of radial position at 4 different azimuths offset by 90°. A set of reflectance

profiles at one azimuth is illustrated in Figure 6a.

The measured  $d$  variation on the secondary mirror is in reasonable agreement with the predicted variation, as seen in Fig. 6b. The measurements show an asymmetry in the deposition, with north/south and east/west data clustering together. The dashed line is the predicted  $d$  variation on this mirror. (The inclusion of refractive effects yields a different position for this predicted variation than that in Fig. 5.) The deviation of the measured  $d$  variation from that predicted is mostly within the  $\pm 2\%$  tolerance, and since predicted variation for the secondary is less than 1% from the ideal variation, the  $d$  variation on the secondary mirror can be considered as just adequate for application in this Schwarzschild objective application. Planetary rotation of the substrates, which is now used in our sputtering system, will yield much improved uniformity in the azimuthal direction, and provides various options for actively grading the period in the radial direction from the planetary rotation axis.

#### Other Considerations

Many other considerations can be made in the analysis of the problem of multilayer period uniformity on focussing optics, some of which are mentioned here.

If the bandwidth of the incident spectrum is comparable to or greater than the multilayer bandwidth, the same analysis applies leading to the same ideal multilayer period variation. Throughput is optimized with the incident spectrum's bandwidth matched to that of the multilayer, and with this ideal  $d$  variation.

Tighter control of the  $d$  variation on focusing optics will be required by various deviations from the example presented here. Multilayers with high reflectance at shorter wavelengths generally have much narrower bandwidths than that of the Mo/Si multilayer discussed here. For example a Ru/B multilayer for use near  $\lambda = 70 \text{ \AA}$  would have  $\Delta E/E = 0.012$  yielding an acceptable deviation from the ideal  $d$  variation of only  $\pm 0.3\%$ , an order of magnitude smaller than that required in the example here. Optical systems with larger or more strongly curved surfaces will require more care in achieving acceptable  $d$  variations. Progress in these areas will require development of means to control and measure the  $d$  variation to a higher degree of precision than the current state of the art.

The optical systems of interest for projection lithography are more complicated than the Schwarzschild objective considered here. Larger mirrors of various shapes complicate the achievement of optimal multilayer deposition. The larger field sizes in these systems require consideration of the required angular

acceptance of the multilayer coated optics, and may introduce additional phase errors of the type mentioned above. Imperfections in the multilayers or substrates yield non-specular scattering [4,5], which together with other possible sources of stray light will degrade the point spread function of these systems. The magnitude and implications for high resolution imaging of these and other issues can be studied by further experiment and image simulation calculations.

#### Conclusions

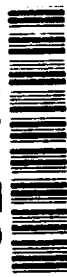
Reflected intensity and phase considerations, together with limited multilayer bandwidth, link multilayer period variations to performance of multilayer coated reflective imaging optics in the soft x-ray. The reflected intensity is of primary importance, and the phase issues may become important if substrate figure and alignment are nearly perfect. Ideal multilayer coatings would have specific variations across each focussing mirror surface. They would not be uniform. The multilayer period obtained in practice can and should be predicted and measured. Mo/Si multilayers for use at  $h\nu < 100 \text{ eV}$  have relatively large bandwidths, easing the requirements on  $d$  variation control considerably. Multilayers having high normal incidence reflectance at higher energies have much narrower bandwidths, and will make the achievement of acceptable  $d$  variations over large areas more difficult.

#### Acknowledgments

This work was supported by the Director, Office of Energy Research, Office of Basic Energy Sciences, Materials Sciences Division, of the U.S. Department of Energy under contract No. AC03-76SF00098.

#### References

1. B. Lai, F. Cerrina, and J.H. Underwood, "Image formation in multilayer optics: the Schwarzschild Objective," *Proc. Int. Soc. Opt. Eng.*, **563**, 174-179 (1985).
2. J.B. Kortright and J.H. Underwood, "Design considerations for multilayer coated Schwarzschild objectives for the XUV," *Proc. Int. Soc. Opt. Eng.*, **1343**, 95-103.
3. R.N. Watts, D.L. Ederer, T.B. Lucatorto, and M. Isaacson, "NIST metrology for soft x-ray multilayer optics," this volume.
4. J.B. Kortright, "Non-specular scattering from x-ray multilayer structures," this volume.
5. J.E. Harvey, "Specifying optical fabrication tolerances for soft x-ray projection lithography systems," this volume.



## Achieving Uniform Multilayer Coatings on Figured Optics

W. K. Waskiewicz, D. L. Windt, J. E. Bjorkholm, L. Eichner,  
R. R. Freeman, T. E. Jewell, W. M. Mansfield, A. A. MacDowell,  
L. H. Szeto, D. M. Tennant, D. L. White, and O. R. Wood II

*AT&T Bell Laboratories, Murray Hill, New Jersey 07974*

### Abstract

We discuss design considerations for high-reflectance multilayer coatings for use in soft X-ray projection lithography optical systems. Techniques used to control and characterize coating uniformity on figured optics are described. Recent results are presented.

### 1 Introduction

The spatial uniformity of multilayer coatings deposited onto figured optics for soft X-ray projection lithography (SXPL) optical systems must be accurately controlled in order to maximize throughput and to preserve the imaging quality of the substrate [1]. Throughput issues gain critical importance as the number of optical elements in a system increases and production uses are contemplated.

Practical SXPL systems will consist of multiple-mirror cameras, reflective masks, and various turning, collimating, and collecting optics. With each reflective surface some light is lost, so there are many considerations in designing the multilayer coatings for these systems. Uniform illumination in the focal plane is critical. For example, a light ray will, in general, experience different incidence angles on each figured surface in a system. Additionally, different rays will have different incidence angles on the same mirror. Since multilayer coatings reflect efficiently over a limited bandwidth, coating design must optimally overlap the spectral bandpass from each optical element so that all rays are reflected uniformly. Another consideration involves the trade-off between high reflectance and bandpass. The normal incidence reflectance of a multilayer stack increases with more layers but at the same time the bandpass decreases. Coating design, therefore, should maximize throughput by optimizing the number of bilayers.

For these reasons the spatial uniformity of the multilayer coating on figured surfaces must be precisely controlled during the deposition process. Due to the nature of physical vapor deposition processes and the range of possible substrate figures and sizes, this can be quite challenging. Various uniformity control techniques are employed world-wide: baffles or apertures [2],

collimating slits [3] or moving shutters [4] placed between source and substrate; large area or arrays [5] of sources; geometric fixturing (distance between and orientation of source and substrate) [6]; chemical or other non-physical vapor deposition schemes [7].

In this paper we present an approach to multilayer uniformity control using the baffled source technique, which we have successfully used to coat figured optics for SXPL. First, our sputter deposition system is described, followed by a discussion of the uniformity control technique. Several methods of coating uniformity characterization are then presented, followed by two examples of the successful application of this baffled source approach.

### 2 Deposition System

We have adapted a commercial sputter deposition system to the production of multilayer coatings for both general research and SXPL optical systems. The sources and a simple sample transport system are housed in an 18-inch-diameter O-ring sealed vacuum chamber (Figure 1) which is turbomolecularly pumped to a base pressure of  $10^{-7}$  torr. Multilayers are deposited using DC magnetron sputtering in argon. A 'sputter-up' geometry is used with two sources (one for each material) located 180 degrees apart on an 8-inch-diameter circle, concentric to both the sample transport and the chamber. Source to substrate distance, depending upon substrate geometry, can be adjusted from 80 mm to 150 mm.

Multilayer coatings are deposited by sequentially passing a sample over each source in turn. Samples move along an arc defined by the sources; position and velocity are computer controlled with stepping motors so that the rate of passage over and between each source can be separately determined. This allows for precise control of individual layer thicknesses independent of deposition rates. Additionally, for small substrates ( $\sim 5$  inch diameter by  $\sim 1.5$  inch thick), the sample can be spun (at a few Hz) about its own axis as it passes over the center of each sputter source.

Magnetron sputter sources (Research S-Guns) with 1.5-inch-diameter targets are used. These compact, cylindrically symmetric sources utilize a magnetically confined plasma to provide a wide range of deposition rates. Deposition rates remain stable over the course of a run, so real-time rate monitors are not



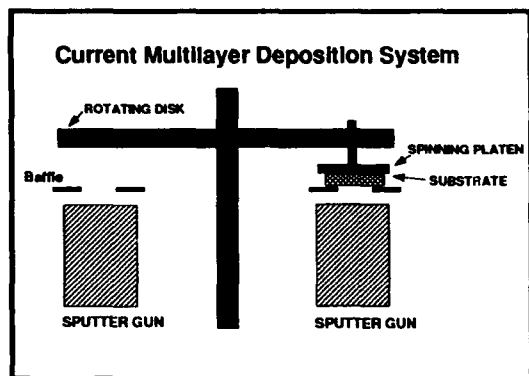


Figure 1: Magnetron sputtering system used to fabricate X-ray multilayer coatings.

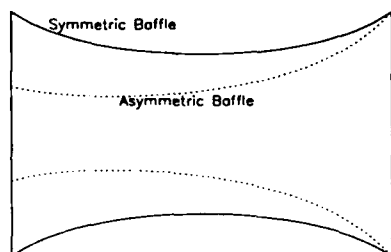


Figure 2: Example of baffles used during magnetron deposition to control coating uniformity.

needed. As with most physical vapor deposition processes however, the deposition rate emitted from sputter sources approximately follows a cosine spatial distribution [8]. That is, rates will be highest directly over the center of the gun and fall off as a function of distance from the gun center, though the details of this profile depend upon target materials and source design. It is this inherent nonuniformity that has driven our development of the baffled source technique.

### 3 Baffled Source Technique

We control coating uniformity by using specially designed baffles placed between the source and the substrate, coupled with sample motion. The baffles define the footprint of the source on the substrate, so that as the sample passes over the source the integrated deposition rate for the area being coated is uniform. In general, baffles are hour-glass shaped, tapered closed towards the source's center, as shown in Figure 2. This increases deposition where rates are lowest while decreasing deposition where rates are higher.

Substrate motion is a vital consideration in baffle design. Holding a flat substrate stationary over the center of a gun results in a film which is thickest at the center and follows a cosine drop-off radially. Rotating a substrate from source to source integrates the baffle-shaped source deposition profile along the tangential direction. By additionally spinning a substrate about its own axis as it moves from source to source, the deposition profile is

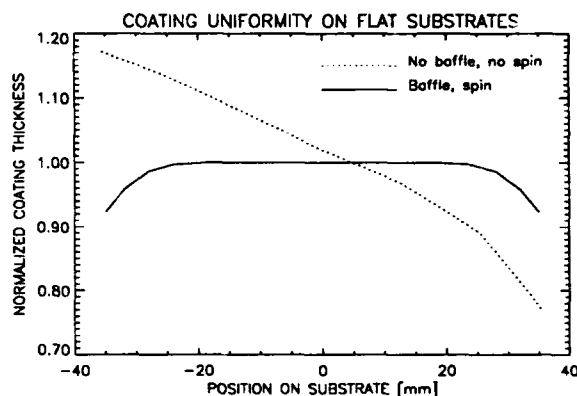


Figure 3: Comparison of measured coating uniformities on flat substrates illustrating that baffles and substrate motion can be used to produce highly uniform coatings over limited areas.

averaged over the whole substrate yielding increased uniformity, as shown in Figure 3. This effect is exploited to simplify baffle design. However, for large substrates where spin is impractical, the baffle shape is asymmetrical (Figure 2).

An additional complication in baffle design is due to the sensitive dependence of the deposition rate on the figure of the substrate. The deposited film thickness depends on both the source to substrate distance and the angle between the source and the substrate surface normals. It is this last point which forces us to design baffles through an iterative process. In this process, a trial baffle is used to deposit onto an inexpensive test substrate having the correct curvature and size. The resulting uniformity is used to design the next baffle. The process is then repeated until the desired uniformity is obtained. Typically, several such iterations are necessary for any given substrate geometry.

### 4 Uniformity

Several characterization tools have been developed to measure spatial uniformity. The fastest results are generated by measuring a step height using an optical profilometer. Application of a thin stripe of photoresist across a test substrate before deposition, and removal of it afterwards, leaves a step height equal to the total film thickness. Though the measurement lacks structural information about the multilayers and is necessarily destructive, this approach allows rapid determination of film thickness uniformity.

A much more time consuming technique uses glancing incidence (0 to 10 degrees) X-rays ( $\lambda=1.54\text{\AA}$ ) to measure multilayer reflectance. This technique reveals detailed information about the average bilayer spacing of the coating, though the time duration (due to typical flux rates from lab-sized rotating anode sources) limits the usefulness of this approach. Additionally, concave optics require sectioning in order to probe the surface at glancing incidence.

The most effective technique is the measurement of normal incidence reflectance. Not only can the multilayer bilayer spacing be (nondestructively) mapped over the surface of an optic but absolute reflectances can be accurately measured. Clearly this is our most powerful characterization tool. A new laser-plasma based soft x-ray reflectometer has been developed to facilitate these measurements and will be described elsewhere.

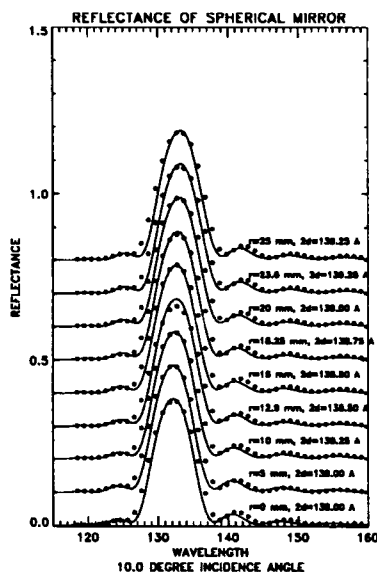


Figure 4: Measured and theoretical reflectance versus wavelength curves for a spherical witness sample with the same radius of curvature as the primary mirror of the Schwarzschild camera used to demonstrate SXPL imaging. The labels indicate the radial substrate position and the multilayer period (2d), showing excellent coating uniformity.

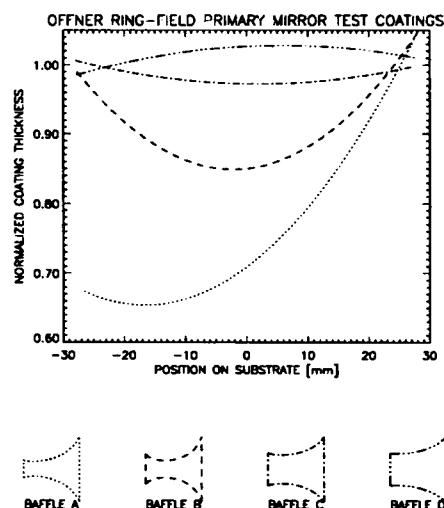


Figure 5: Measured multilayer coating uniformity on a 350 mm radius-of-curvature concave spherical test mirror deposited using the various baffles indicated. The uniformity is less than 1% with baffles C and D, though better uniformity is anticipated with the final baffle, which has not yet been tested.

## 5 Applications

AT&T Bell Labs' first demonstration of SXPL was performed using a Schwarzschild objective camera. This imaging system has been used to print features as small as  $0.05\mu\text{m}$  at  $\lambda=140\text{\AA}$ [9]. The Mo/Si (20 layer pairs) multilayer-coated optics were measured to have normal incidence reflectances of  $\sim 40\%$  and the coating uniformity over the relevant 10 mm-wide annular region of the concave secondary mirror (50 mm radius of curvature) was better than  $\pm 0.5\%$  (Figure 4).

Presently, we are coating an Offner annular-field system [10] for 1:1 imaging at  $130\text{\AA}$ . This system consists of three multilayer reflective surfaces and a multilayer reflection mask. The concave primary mirror (radius of curvature of 350 mm) is 10 inches in diameter, which is roughly the largest size substrate our deposition system can accommodate. Although we cannot control uniformity over the entire surface, it is only necessary to coat two 61 mm diameter regions due to the nature of the optical design. Figure 5 illustrates our progress in designing an appropriate baffle for the primary mirror. Uniformity of 0.1% has been achieved on the secondary mirror.

## 6 Summary

We use a baffled source technique to deposit uniform multilayer coatings on figured optics for SXPL. This technique utilizes apertures placed between the sputter sources and the substrate and sample motion to overcome the inherent nonuniformity of magnetron sources. The range of substrate surface figures and sizes force an iterative approach to baffle design. SXPL optical systems coated in this manner have shown excellent results.

Though the baffled source technique has proven effective, the limitations of our current system preclude its use for coating SXPL optics for practical printers. For one, the size of practical SXPL optics (larger than 10 inch) are beyond the capability of a

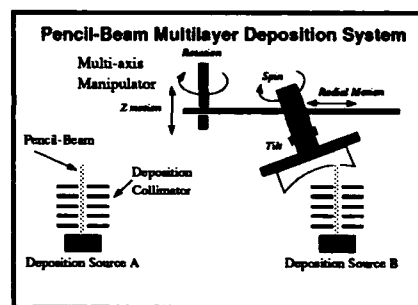


Figure 6: Schematic diagram of a proposed Pencil-Beam Deposition system.

small source and chamber. Secondly, practical SXPL optics will require graded multilayer coatings for optimum throughput. A larger version of the current system is not a solution, as controlling coating uniformity with the precision required for diffraction limited imaging becomes increasingly difficult with larger sources using the baffled source approach, and arbitrarily graded coatings are not feasible. Also, source and target costs increase roughly as the square of the surface area.

An intriguing alternative technique is the use of pencil-beam deposition. In such a system, as shown in Figure 6, the size and shape of various deposition source beams can be adjusted to less than 5 mm by using interchangeable beam collimators located over each source. Instead of tailoring unique baffles for each new optic, a computer-controlled, multi-axis manipulator transports the substrate and writes the coating onto the optical surface. Thus, once the system is calibrated, the computer can be programmed to deposit the desired coating profile onto any arbitrarily figured substrate.

## 7 Acknowledgments

We thank R. Watts at NIST for soft X-ray reflectance measurements made for our Schwarzschild camera.

## References

- [1] T.E. Jewell, *these proceedings*.
- [2] R.P. DiNardo, P.Z. Takacs, C.F. Majkrzak and P.M. Stefan, *Proc. SPIE*, **563**, 30 (1985); J.B. Kortright and J.H. Underwood, *Proc. SPIE*, **1343**, 95 (1990); H. Takenaka, Y. Ishii, H. Kinoshita and K. Kurihara, *Proc. SPIE*, **1345**, 213 (1990).
- [3] M.P. Bruijn, J. Verhoeven, E. Puik and M.J. van der Weil, *Proc. SPIE*, **984**, 54 (1988).
- [4] M.P. Bruin, P. Chakraborty, H.W. van Essen, J. Verhoeven and M.J. van der Weil, *Proc. SPIE*, **563**, 36 (1985); or *Opt. Eng.*, **25**, 916 (1986).
- [5] A.F. Jankowski, D.M. Makowiecki, M.A. McKernan, R.J. Foreman and R.G. Patterson, *Proc. SPIE*, **1343**, 32 (1990).
- [6] B. Vidal and P. Dhez, *Proc. SPIE*, **688**, 110 (1986); R. Philip, R. Rivoira, Y. Lepetre and G. Rasigni, *Appl. Opt.*, **27**, 1918 (1988); D.W. Schulze, J.M. Slaughter and C.M. Falco, *Proc. SPIE*, **984**, 75 (1988).
- [7] K. Mutoh, Y. Yamada, T. Iwabuchi and T. Miyata, *J. Appl. Phys.*, **68**, 1361 (1990); P. Boher, P. Houdy, L. Hennet, J.P. Delaboudiniere, M. Kuhne, P. Muller, Z.G. Li and D.J. Smith, *Proc. SPIE*, **1343**, 39 (1990).
- [8] G.K. Wehner and G.S. Anderson, *Handbook of Thin Film Technology*, edited by L.I. Maissel and R. Glang, Chapter 3 (McGraw-Hill, N.Y., 1970); D.B. Fraser and H.D. Cook, *J. Vac. Sci. Technol.*, **14**, 147 (1977).
- [9] J.E. Bjorkholm, J. Bokor, L. Eichner, R.R. Freeman, J. Gregus, T.E. Jewell, W.M. Mansfield, A.A. MacDowell, E.L. Raab, W.T. Silfvast, L.H. Szeto, D.M. Tennant, W.K. Waskiewicz, D.L. Windt, O.R. Wood II and J.H. Bruning, *J. Vac. Sci. Technol.*, **B8**, 1509 (1990).
- [10] O.R. Wood II, W.T. Silfvast and T.E. Jewell, *J. Vac. Sci. Technol.*, **B7**, 1613 (1989).



## Tungsten/Carbon Multilayers Prepared by Ion-Beam Sputtering

Katsuhiko Murakami, Hiroshi Nakamura, Tetsuya Oshino, and  
Hideo Nikaido

*Nikon Corporation, 1-6-3 Nishi-ohi, Shinagawa-ku, Tokyo 140, Japan*

### Abstract

Tungsten/carbon(W/C) multilayers were prepared by ion beam sputtering. The properties of the multilayers were studied by low-angle x-ray diffraction, transmission electron microscopy (TEM) observation of the cross section and Auger electron spectroscopy. It was found that carbon atoms diffused into the tungsten layers and formed carbide. The measured reflectivity was in good agreement with the calculation, considering the decrease in density and the interfacial roughness. The multilayers were deposited on a concave spherical mirror and x-rays were focused by the mirror on a line-shaped image.

### Introduction

X-ray multilayer mirrors are indispensable devices for the applications of soft x-ray optics such as x-ray microscopy and x-ray projection lithography. Several fabrication methods of the multilayers have been reported. We have selected ion beam sputtering for the following reasons. 1) The damage of films by fast ions or electrons is eliminated because the substrate is not exposed to plasma. 2) The optimum deposition conditions can be selected because the current and the voltage of the ion beam can be controlled separately. 3) The film thickness can be precisely controlled by deposition time because the deposition rate is relatively low and stable.

In this research, W/C multilayers, with a stable multilayer structure, were prepared and examined in detail. It was reported that the tungsten layers of the W/C multilayers contained carbon.[1] In our experiment, carbide formation in the tungsten layers

were clearly revealed by depth profiling with Auger electron spectroscopy and factor analysis of the data.

The reflectivity of the multilayers at a wavelength of  $1.54\text{\AA}$  was lower than the calculation obtained using Fresnel's formulae because of decrease of density and interfacial roughness. The calculated x-ray reflectivity curve was fitted to the measured one, with consideration given to the density of deposited films and interfacial roughness.

In confirmation of the usefulness of the multilayers, a simple focusing experiment was made using a concave spherical multilayer mirror.

### Sample preparation

Figure 1 shows the schematic diagram of the ion beam sputtering deposition system used in

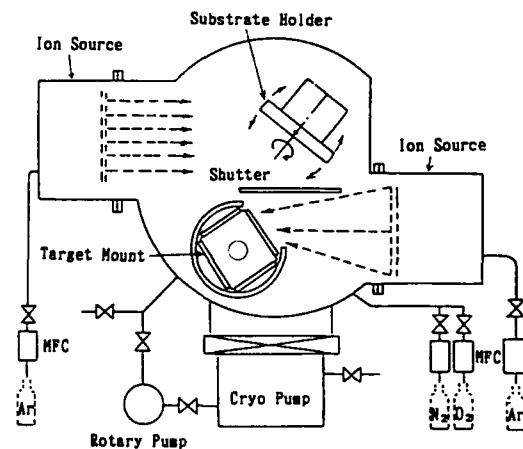


Figure 1. Schematic diagram of the ion beam sputtering system.

the research. The system is equipped with two ion sources, a target mount and a substrate holder. Four targets of 6 inches in diameter can be attached on the rotatable target mount. With concurrent ion bombardment of both the substrate and the target material to be sputtered, thin films are produced. But in this experiment, ion bombardment of the substrate was not performed. During deposition, the substrate was water cooled and kept at a constant temperature.

W/C multilayers with a period  $d$  of  $60\text{\AA}$ , layer thickness ratio  $d_W/d_C$  of  $1/2$  and 10 layer pairs were deposited on a Si substrate. The deposition conditions of the multilayers are shown in Table 1. Layer thickness was controlled by deposition time.

Table 1. Deposition conditions

|                      | W                             | C                             |
|----------------------|-------------------------------|-------------------------------|
| Acceleration voltage | 1000V                         | 1000V                         |
| Ion beam current     | 150mA                         | 100mA                         |
| Ar gas pressure      | $3.2 \times 10^{-3}\text{Pa}$ | $3.2 \times 10^{-3}\text{Pa}$ |
| Deposition rate      | $0.59\text{\AA/s}$            | $0.16\text{\AA/s}$            |

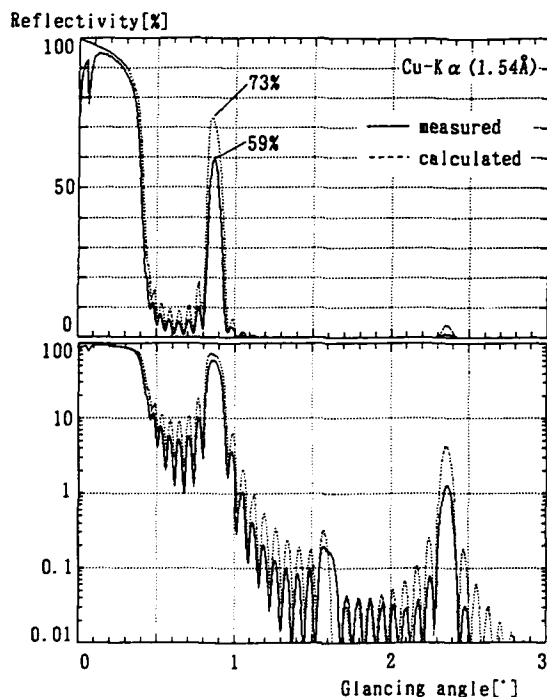


Figure 2. Reflectivity of W/C multilayers.

Solid line : measurement

Dashed line : calculation

The calculation was carried out using the optical constants as follows.

W :  $\delta$   $4.57 \times 10^{-5}$ ,  $\beta$   $3.75 \times 10^{-6}$

C :  $\delta$   $7.22 \times 10^{-6}$ ,  $\beta$   $1.08 \times 10^{-8}$

Si :  $\delta$   $7.59 \times 10^{-6}$ ,  $\beta$   $1.76 \times 10^{-7}$

### Characterization of the multilayers

The reflectivity curve of the multilayers measured with Cu K $\alpha$  radiation ( $1.54\text{\AA}$ ) using a low-angle diffractometer is shown by the solid line in Fig.2. The dashed line is the reflectivity curve calculated by Fresnel's formulae using the optical constants of the bulk. Measured reflectivity of the first-order main peak was 59%, while that of the calculated one was 73%. The shapes of subpeaks of the measured data agreed well with the calculated ones, suggesting that the layer thickness error is insignificant. The intensity of main peaks and subpeaks were lower than the calculated values; this point will be discussed later.

Figure 3 shows the cross section of the multilayers observed by TEM (JEOL JEM4000EX). Both tungsten and carbon formed continuous layer structures and smooth interfaces were formed. As no lattice fringes were observed in either the tungsten or carbon layer, both layers had almost amorphous structures.

Depth profiling of the multilayers was performed with Auger electron spectroscopy (Perkin Elmer PHI Model 4300). The experiment was performed with care in order to improve the depth-resolving power. The experimental conditions are shown in Table 2.



Figure 3. TEM image of the cross section of W/C multilayers.

Table 2. Auger analysis conditions

|                          |                         |
|--------------------------|-------------------------|
| Electron gun             |                         |
| Voltage                  | 1kV                     |
| Current                  | 200~500nA               |
| Beam size                | 0.5 $\mu$ m in diameter |
| Ar ion source            |                         |
| Voltage                  | 1kV                     |
| Current                  | 1 $\mu$ A               |
| Incident angle           | 75°                     |
| Sample rotation          | 1rpm                    |
| Crater size              |                         |
| 3 $\times$ 3 raster scan |                         |
| 3mm in diameter          |                         |

With the advance of etching, the shape of the carbon KLL Auger spectra was changed. As shown in Fig.4, the carbon KLL Auger peak was observed in the spectrum of the second tungsten layer, and the profile was different from that of the top carbon layer. This peak deformation is known as the chemical shift due to the carbide formation.[2] This means that carbon atoms diffused into the tungsten layers and formed carbide.

Using this profile deformation, carbide-like carbon can be distinguished from graphitelike carbon by the factor analysis.[3] Figure 5 shows the Auger depth profile of the W/C multilayers, separating carbide-like carbon from graphitelike carbon. It is thus clarified that carbide-like carbon exists in the tungsten layers.

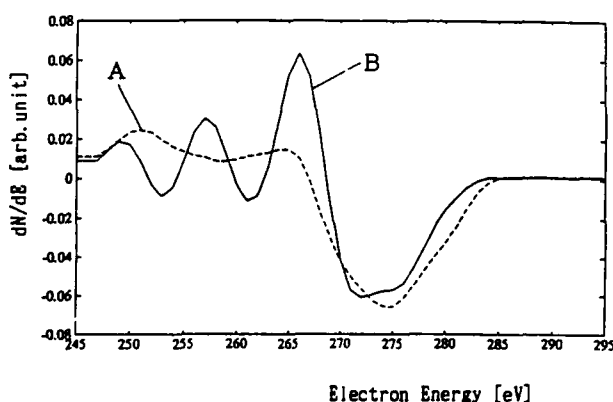


Figure 4. Carbon KLL Auger spectra.  
A : Graphitelike carbon found in the top carbon layer  
B : Carbide-like carbon found in the second tungsten layer

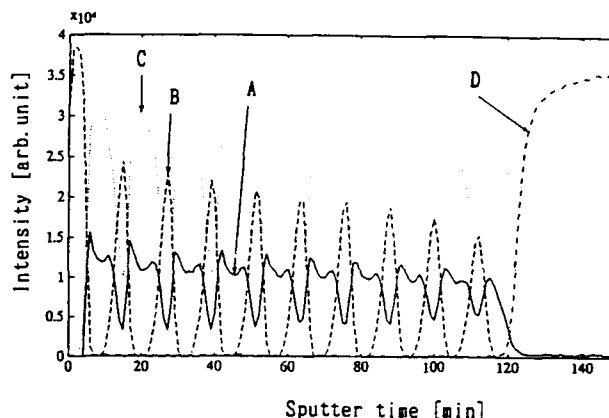


Figure 5. Auger depth profile of W/C multilayers.  
A : Carbide-like carbon, B : Graphitelike carbon,  
C : Tungsten, D : Silicon  
Carbide-like carbon was separated from graphitelike carbon by the factor analysis.

#### Curve fitting of the measured reflectivity

The calculated reflectivity of the first-order peak using the optical constants of the bulk was 73% and the measured reflectivity was 59%. The causes of this reduction were supposed to be the low density of the tungsten layers and the interfacial roughness.

The densities of tungsten and carbon thin films were determined through the measurement of weight using a precise microbalance (Sartorius S4) and the measurement of thickness by Talystep. The films were deposited on thin glass substrates (Corning 0211) in a thickness of about 500Å to 3000Å. These thicknesses were much larger than the thickness periods of the multilayers, but as is shown in Fig.3, each layer had continuous structure; therefore the difference of density was considered to be negligible. The density of the tungsten films was 15.8g/cm<sup>3</sup>, about 20% lower than the bulk density of 19.3g/cm<sup>3</sup>. The density of the carbon films was slightly higher than that of the bulk, but it hardly affected the reflectivity because the atomic scattering factor of carbon is very low.

The optical constants of tungsten and carbon were calculated using the reported atomic scattering factors[4] and the measured densities of thin films. The tungsten layers contained carbon, as was mentioned before, but this did not affect the reflectivity because the atomic scattering factor of carbon is much lower than that of tungsten. The reflectivity curve of the multilayers was calculated with these data by Fresnel's formulae, with the parameter of the interfacial

roughness considered to be the Debye-Waller factor of  $2\text{\AA}$ . The result is shown by the dashed line in Fig. 6, with the measured curve in the solid line. The calculated curve was in good agreement with the measured curve. If the curve fitting was made with the optical constants of the bulk without consideration of the decrease of density, the fitting parameter of the interfacial roughness was  $3.5\text{\AA}$ , but the intensity of subpeaks of the calculated curve did not agree with the measured curve.

### X-ray focusing experiment

The W/C multilayers were deposited on a concave spherical mirror and a simple focusing experiment with the mirror was performed. The experimental arrangement is shown in Fig. 7. The radius of curvature of the mirror was  $600\text{mm}$  and the diameter was  $80\text{mm}$ . Surface roughness of the mirror was less than  $1.5\text{\AA}$  rms measured with WYKO. The period of the thickness of the multilayers was  $26\text{\AA}$ .

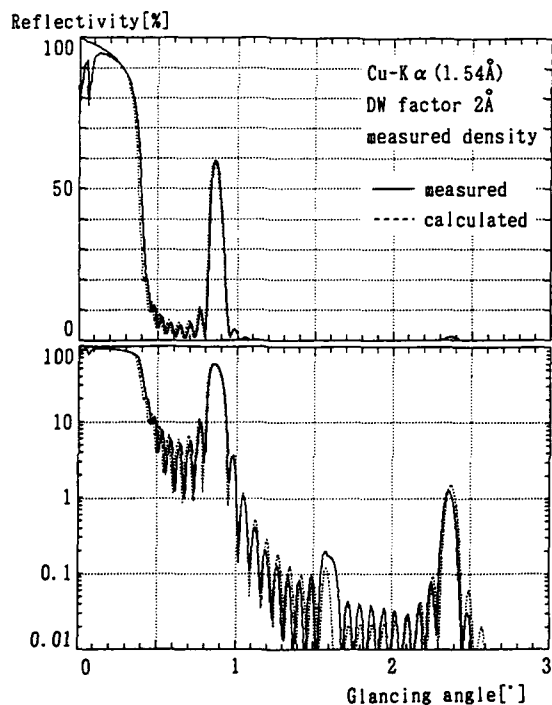


Figure 6. Curve fitting of the reflectivity of W/C multilayers.

Solid line : measurement  
Dashed line : calculation

The calculation was carried out using the optical constants as follows.

W :  $\delta$   $3.65 \times 10^{-5}$ ,  $\beta$   $2.99 \times 10^{-6}$   
C :  $\delta$   $8.05 \times 10^{-6}$ ,  $\beta$   $1.20 \times 10^{-8}$   
Si :  $\delta$   $7.59 \times 10^{-6}$ ,  $\beta$   $1.76 \times 10^{-7}$

This implied that the incident angle of the C K $\alpha$  line ( $44.7\text{\AA}$ ) was 30 degrees from the normal. The number of layer pairs was 50. The reflectivity of the multilayers was about 4% at this wave length.

A carbon film target was irradiated with a focused electron beam. X-rays emitted from the point source were reflected by this mirror. The focused images of the x-rays were recorded on photographic film, within the parameters of the distance between the mirror and the film.

The x-ray images obtained are shown in Fig. 8. As the distance was changed, two foci, sagittal and tangential, were observed, and x-rays were focused on narrow, line-shaped images. Because the whole area of the images was bright, it was confirmed that x-rays were reflected by the multilayers over the entire surface.

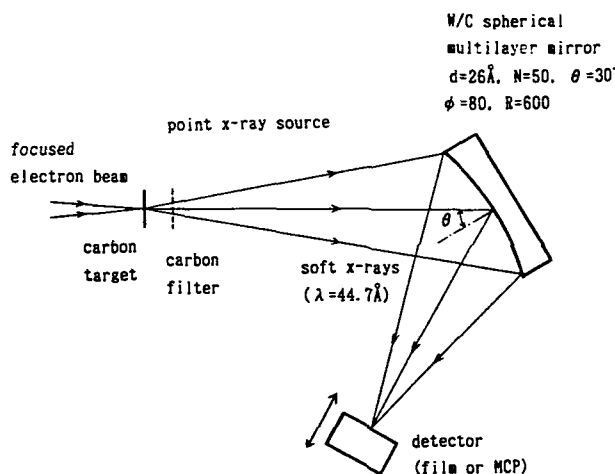


Figure 7. The arrangement of x-ray focusing experiment.

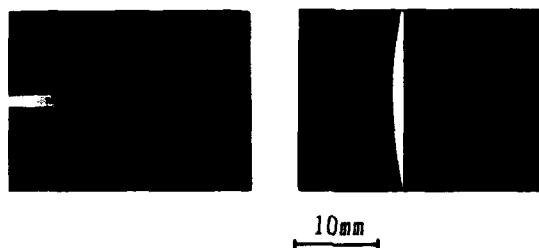


Figure 8. X-ray images recorded on film.

A : Sagittal focus  
B : Tangential focus

## Conclusions

The tungsten/carbon multilayers prepared by ion beam sputtering were investigated. Both tungsten and carbon layers had amorphous structures, and at a layer thickness period of 60Å; continuous layer structures and smooth interfaces were formed. It has become clear that the tungsten layers contained carbon, and carbide was formed.

The measured reflectivity curve was fitted to the calculated one with consideration of reduced thin film density and interfacial roughness. The measured curve was in good agreement with the calculated curve, using the measured density of the thin films and the Debye-Waller factor of 2Å.

A simple x-ray focusing experiment was conducted with a concave spherical multilayer mirror. The x-rays at a wavelength of 44.7Å

were reflected by this mirror and were focused on narrow, line-shaped images.

## References

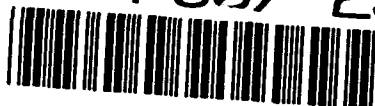
1. V. Dupuis, M. F. Ravet, M. Piecuch, and C. Tete, "Stability of multilayers for x-ray optics," SPIE Vol. 1140, 573-580 (1989).
2. C. C. Chang, Characterization of Solid Surfaces, P. F. Kane and G. B. Larrabee, eds. (Plenum Press, New York, 1974).
3. J. S. Solomon, "Factor analysis in surface spectroscopies," *Thin Solid Films*, 154, 11-20 (1987).
4. S. Sasaki, "Numerical tables of anomalous scattering factors calculated by the Cromer and Liberman's method," KEK Report, 88-14 (National Laboratory for High Energy Physics, Japan, 1989).



---

## **Holography and Phase Effects**

---



## Technique for Projection X-Ray Lithography Using Computer-Generated Holograms

Malcolm R. Howells

*Advanced Light Source, Lawrence Berkeley Laboratory, Berkeley, California 94720*

Chris Jacobsen

*Department of Physics, State University of New York, Stony Brook, New York 11794*

### Abstract

A method is described whereby projected lithographic images can be formed with x-rays by means of a transmission hologram. The form of the hologram is computed by an algorithm which eliminates all the unwanted signals normally present as systematic errors in holographic images. An example calculation is shown in which the form of a hologram is derived that is supposed to generate a diffraction image of a given test pattern. The holographic image is shown to have excellent fidelity with respect to both resolution and contrast. Such an approach to projection x-ray lithography requires an x-ray beam with very little coherence and is thus compatible with high wafer throughput schemes while at the same time being relatively immune to contamination.

### Introduction

Consideration of the possibilities of holographic projection as a means to print the image of a circuit pattern on to resist dates back to the late nineteen sixties [1, 2, 3]. While various ideas were studied, none of them prevailed as standard manufacturing techniques because there were better and easier alternatives based on the use of lenses for optical reduction. The characteristic of holographic imaging which led to its failure in competition with optical reduction was the presence in the image of various unwanted signals; some intrinsic to the holographic process, others derived from the recording medium. Although some of the difficulties can be mitigated or eliminated by the use of image-plane or near-image-plane recording geometry [4] and further benefits can be obtained by the use of computer-generated holograms, the apparent advantages of holographic projection [5] are not likely to be enough to impact the technological momentum of reduction techniques in optical lithography.

However, once one begins to consider soft x-ray lithography, for which refracting lenses cannot be used, the technology for reduction imaging is then exceedingly problematical and it becomes worthwhile to consider again the potential contribution of holographic techniques. The advantages of holographic projection schemes in general have been discussed by the present authors in an earlier paper [5] where a numerical example was presented for the use of a computer-generated hologram recorded on a flat, grazing-incidence reflector. The reflector was the only optical element in the scheme which (on paper) was able to realize many of the advantages of holographic projection imaging. Its

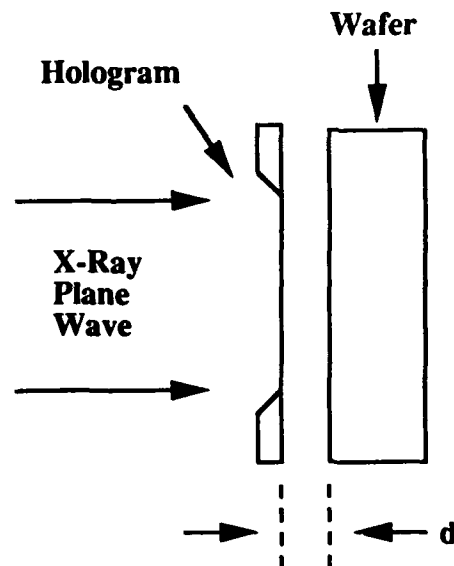


Figure 1. In-line holographic geometry

chief disadvantage was the need for an illumination beam of high spatial and temporal coherence and concomitant low intensity leading to limitations on the possible wafer throughput of the system. In this paper, we describe an alternative type of holographic projection system based on transmission through the hologram which would be free of these disadvantages. We consider the design of the (computer-generated) hologram, and we give examples of a binary test pattern, the hologram which "generates" it by diffraction of a plane wave, and the images which one would expect to be able to record in practice. We also consider a further advantage of this kind of holographic printing which may have very important practical implications, namely its relative immunity to contamination.

## Hologram Design

The holographic geometry we are now considering is in-line as shown in Fig 1 and is similar to the geometry for contact printing except that the hologram replaces the mask and is located at a slightly larger distance (0.2 mm in our examples) from the wafer. The requirement is to design a hologram which diffracts an incoming plane wave so as to form the desired image at the wafer plane. This is the inverse diffraction problem which is always involved in the design of computer-generated holograms and which has been discussed fairly extensively in the literature [6,7]. In our form of the problem we assume that the hologram is constructed

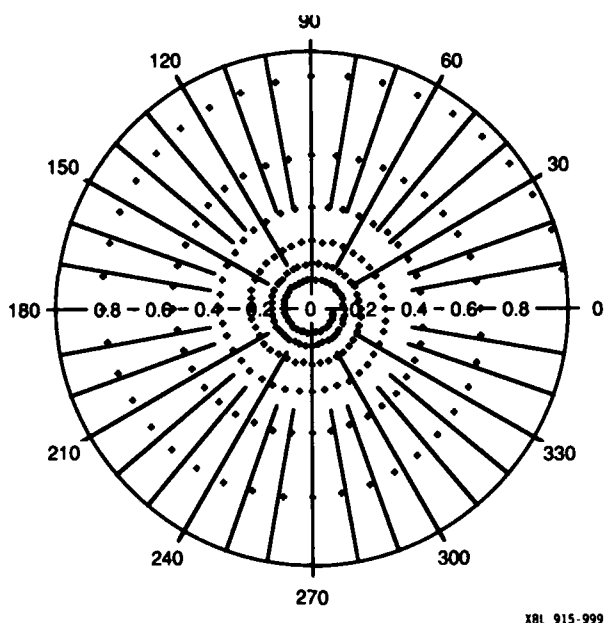


Figure 2. The logarithmic spiral  $r = \exp\{-\theta\delta/\beta\}$  in the complex plane representing the allowed values of the phase and amplitude of 50 Å x-rays transmitted through carbon.

from an optical medium whose thickness can be chosen by the algorithm and whose x-ray complex refractive index  $(1-\delta-i\beta)$  at the wavelength  $\lambda$  we know. If we choose the thickness ( $z$ ) at a certain location in the hologram to give a desired value for the phase change ( $\theta = 2\pi\delta z/\lambda$ ) then the amplitude attenuation factor ( $r$ ) must be  $\exp\{-2\pi\beta z/\lambda\}$ . Thus the only allowed combinations of amplitude and phase of the beam are those that lie on the logarithmic spiral  $r = \exp\{-\theta\delta/\beta\}$  in the Argand plane. An example of such a curve, for carbon at 50 Å, is shown in Fig 2.

The best materials for this exercise are those with a large value of  $\delta/\beta$ . This enables large phase changes to be achieved without a large attenuation. If large attenuation is desired then it can be approximated at least by adding a suitable number of  $2\pi$ 's to the phase angle. The best wavelengths for lithography are said to be [8, 9] either just above the carbon K edge at 44 Å or at about 10 Å. The use of 130 Å in many projection lithography schemes is driven by considerations of multilayer technology which is not involved here. Very good values of  $\delta/\beta$  at both 10 Å and 50 Å are available using standard microfabrication materials. Some examples of  $\delta/\beta$  for materials that have already been successfully used to make Fresnel zone plates (the archetypal holographic optical element) are shown in Fig 3.

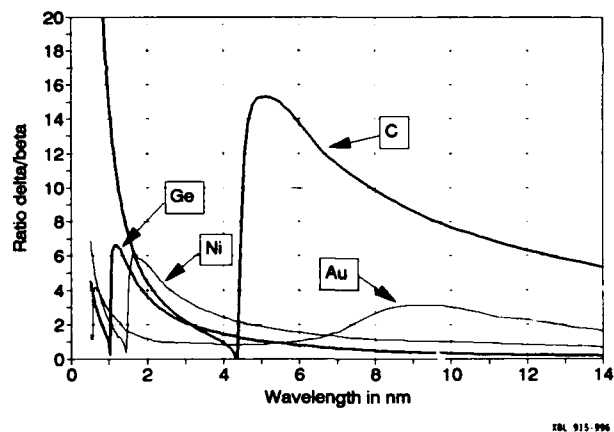


Figure 3.  $\delta/\beta$  values for some materials which have been used in manufacturing Fresnel zone plates.

The binary test-object for which specific calculations have been done is shown in Fig 4. It is represented by  $256 \times 256$   $0.063 \mu\text{m}^2$  pixels and has "black" (zero-exposure) features ranging in size from 0.063 to  $1.0 \mu\text{m}$  on a uniform "white" background of normalized intensity 1.0. We choose the very narrow linewidth to provide a severe test of the algorithm although in fact we have in mind the application of the procedure in the 0.1-0.25  $\mu\text{m}$  range of feature sizes which is why we later choose  $1 \mu\text{m}$  as the hologram thickness limit.

The intent is to design a carbon hologram which delivers the above illumination pattern to the wafer. As a first step we backpropagate a 50 Å wavefield whose

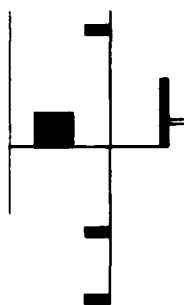


Figure 4. Test pattern shown with black= $(I=0)$ , white= $(I=0.7)$

initial phase and amplitude at the wafer plane are zero and the square root of the pattern intensity respectively.

This wavefield arrives at the hologram plane ( $200\mu\text{m}$  upstream of the wafer) with definite known values of the amplitude and phase at each pixel. We would like to design the hologram so that a unit plane wave transmitted through it would match these values. To do this with carbon we only have access to complex numbers lying on the spiral in Fig 2, but we proceed (within an upper limit of  $1\mu\text{m}$ ) to choose the correct value for the phase and add whatever number of  $2\pi$ 's

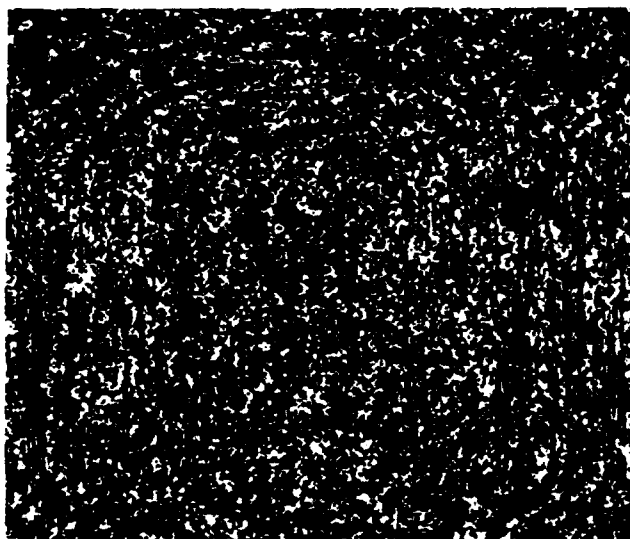


Figure 5. Hologram (carbon thickness map) generated by 100 iterations on a logarithmic, negative gray scale. black= $100\text{\AA}$ , white= $1\mu\text{m}$ .

gets us closest to the correct amplitude. This gives the zeroth order approximation to the hologram. Forward propagating the wavefield that would be transmitted by this hologram to the wafer plane and taking the magnitude squared produces the zeroth order approximation to the desired image at the wafer which turns out to be a surprisingly good approximation to the desired pattern. While we would like to produce a more accurate print of the desired *intensity* at the wafer plane we have no interest in controlling the phase. Thus for the next iteration we keep the current value of the phase and reimpose the correct value of the wafer-plane magnitude. We then backpropagate to the hologram plane, approximate the complex amplitude as before and forward propagate to the wafer plane and correct the magnitude only there as before and so on. The carbon thickness pattern calculated by 100 iterations of this procedure is shown in Fig 5 and the wafer plane intensity produced by this hologram is shown in Figs 6 and 7. As can be seen in Fig 7, if the pattern is overexposed by about 30% the desired dark features remain dark while the light features have an intensity mostly close to unity but with worst-case pixels at 0.7 and 1.6.

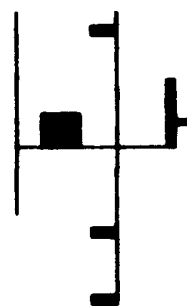


Figure 6. Image delivered by the hologram of Fig. 5 at the wafer showing full range of gray scales. black= $(I=0)$ , white= $(I=1.3)$

The good fidelity of this image is also illustrated in Fig 8 which shows the intensity pattern across a line of the wafer-plane image. It is noteworthy that the resolution of the image is essentially the same as that of the hologram. (This is true in general for in-line holograms of which the zone plate is an example). Thus the manufacturing tolerances and field size required in making the hologram would be essentially the same as in writing a proximity mask for the same test pattern. This result should be compared to the manufacturing

tolerances required to produce a similar resolution image by optical reduction. It is now accepted that the reflecting surfaces of the reduction optics in that case would need to be held within tolerances in the 5-10 Å range.

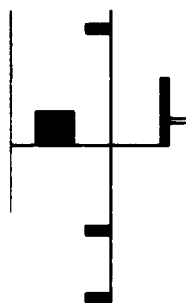


Figure 7. Same image as Fig 7, but overexposed by 30% ie black $\equiv$ ( $I=0$ ), white $\equiv$ ( $I=0.7$ ). Such an overexposure would be easy to do in practice. Note the high fidelity with respect to both resolution and contrast of the image formed in this way.

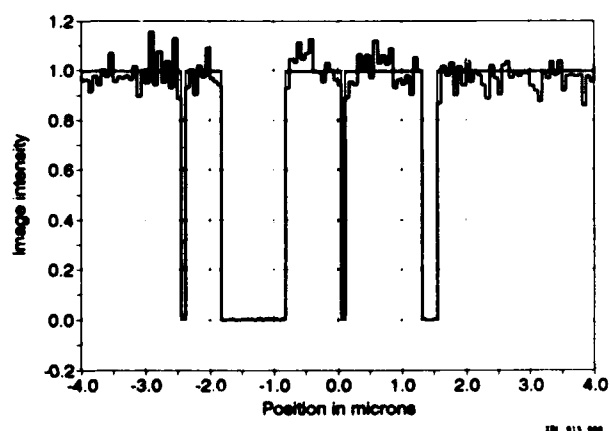


Figure 8. Line scan across the image of Fig. 7 showing the excellent contrast and resolution. The heavy lines represent the delivered intensity and the fine lines the ideal image as functions of position.

These calculations relate to a "mostly-white" type of test object. We have also tested the applicability of the method to "mostly-black" objects by utilizing the complement of the object in Fig. 4. The method works even better for this case. The overall image fidelity is very similar (see Fig 9) while the light intensity in the "white" regions is about 50 times higher showing that the holographic optical element is capable of concentrating the light in a manner analogous to a zone plate.

The carbon relief map that we have designed is a near-image-plane phase hologram [4] which has the remarkable property that the twin-image, intermodulation and zero-order terms are all suppressed. A general feature of this type of hologram is localization of the recorded information corresponding to each image pixel to a fairly small region of the hologram defined by the hologram-image distance and the numerical aperture. One consequence of this is a great reduction in the needed coherence in illuminating the hologram to make a reconstruction (projecting the image on to the wafer in our case). In the present example the coherence width would need to be 10  $\mu$ m and the coherence length, less than 20 waves both of which are easy to achieve and consistent with x-ray sources capable of illuminating high wafer throughput systems. Another consequence of the localization of information is that one can readily compute a large field by dividing it into computationally tractable parts and stitching the resulting holograms together afterwards.

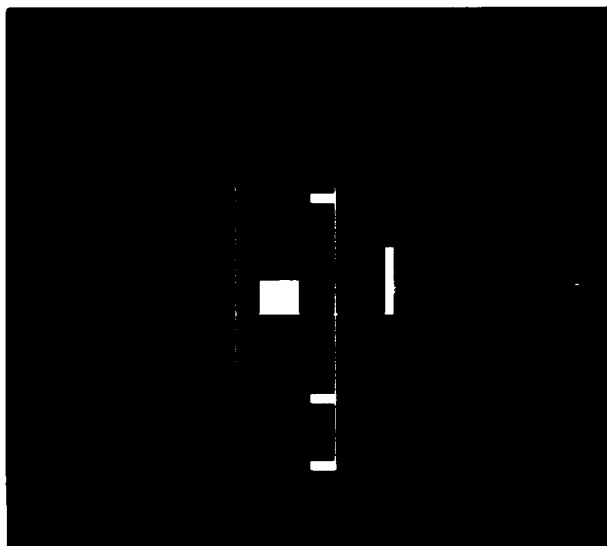


Figure 9. Image analogous to that of Fig 7 but using a test object which is the complement of the one in Fig 4.

## Holography as an approach to the contamination problem in lithography

As the line-width of optical lithography is reduced the problem of contamination becomes more and more serious. Proximity x-ray lithography at around 10Å offers some relief from the problem because some types of contaminant particles present on the mask or wafer will be transparent to the x-rays. This fact is considered one of the advantages of x-ray lithography. On the other hand the existence of contaminant particles between the mask and the wafer places limits on how small the mask-wafer gap can be made and this in turn leads to a corresponding limit on the diffraction-limited resolution. Furthermore the use of x-rays does not overcome defects in the mask resulting from contamination during its manufacture.

Holography provides a radical new approach to the contamination problem. Since the information relating to each point of the image is distributed over many pixels of the hologram, it does not matter if a small fraction of that area is blocked by a defect or a contaminant. Provided the change in image intensity due to the defect is less than some threshold it will have no effect and since circuit patterns are binary the intensity tolerances can be quite generous. If the wafer is in the far field of the defect, ie if the defect is less than about  $\sqrt{\lambda d}$  in size (where  $d$  is the hologram-mask distance) the defect's diffraction pattern will tend to be sufficiently spread to satisfy the condition. We have carried out the type of calculation described above with simulated contaminant particles deliberately introduced and have quantitatively verified these statements for some particular types of particle. Thus the possibility that a single defect of the mask could corrupt the image enough to make the devices printed from it rejects could be essentially eliminated. Moreover, the x-ray transparency advantage, where it applied, would still be maintained. The impact of these considerations on the economics of device manufacture could be considerable.

## Conclusions

- In-line carbon holograms for 50Å x-rays can be designed to project an extremely high-fidelity image of a binary test pattern with regard to both resolution and contrast. The pattern can be either mostly white or mostly black
- The needed hologram writing resolution and field size are essentially the same as those of a proximity mask for the same pattern. Moreover, the geometry for holographic projection is so similar to that of proximity printing that the two would be almost technologically compatible.

- The fabrication of the holograms would require a process whereby an electron beam writing machine could control the thickness of the optical material on a pixel-by-pixel basis.
- This kind of projection lithography has a high degree of immunity to contamination.
- The x-ray beam needed to illuminate the hologram is of low spatial and temporal coherence and thus would be easy to produce and compatible with high wafer throughput systems.

## Acknowledgments

The authors wish to acknowledge helpful conversations with Prof. H. I. Smith of MIT and Prof. J. Kirz of Stony Brook. We also wish to acknowledge the support of the NSF under grant DIR-9006893 (C. J. ) and of the Office of Health and Environmental Research of the Department of Energy under subcontract 431-3378A of grant DE-FG02-89ER60858 (M. H. ).

## References

1. M. J. Beesley, H. Foster, K. G. Hambleton, "Holographic Projection of Microcircuit Patterns", *Electronics Letters*, 4(3), 49-50 (1970).
2. E. B. Champayne, N. G. Massey, "Resolution in Holography", *Appl. Opt.*, 8(9), 1879-1885 (1969).
3. K. A. Stetson, "Holography with Totally Internally Reflected Light", *Appl. Phys. Lett.*, 12(11), 362-364 (1967).
4. G. Addiego, "Investigation of a Focussed-image Lens-hologram Projection System for Microlithography", Ph. D. Thesis, UCB/ERL M90/89 (Electronics Research Laboratory, College of Engineering, University of California at Berkeley, 1990).
5. M. R. Howells, C. Jacobsen, "Possibilities for Projection X-ray Lithography using Holographic Optical Elements", *Appl. Opt.*, 30(13) (1991).
6. Special Issue on Computer Generated Holograms, *Appl. Opt.*, S. H. Lee (ed), 26(20), 4350-4399 (1987).
7. J. R. Fienup, "Iterative Method Applied to Image Reconstruction and to Computer-generated Holograms", *Opt. Eng.*, 19(3), 297-305 (1980).
8. K. Early, M. L. Schattenburg, H. I. Smith, "Absence of Resolution Degradation in X-ray Lithography for  $\lambda$  from 4.5nm to 0.83nm", *Microelectronic Engineering*, 11, 317-321 (1990).
9. M. L. Schattenburg, I. Tanaka, H. I. Smith, "Microgap X-ray Nanolithography", *Microelectronic Engineering*, 6, 273-279 (1987).



## Effect of Amplitude and Phase Dispersion on Images in Multilayer-Coated Soft-X-Ray Projection Systems

Tanya E. Jewell

*AT&T Bell Laboratories, Murray Hill, New Jersey 07974*

92-19507



### Abstract

The effect of reflectance variation and phase dispersion introduced by multilayer coatings on the image quality for different types of soft x-ray projection systems is investigated.

### Introduction

The use of multilayer reflection coatings for soft x-ray projection lithography has been demonstrated.<sup>1-3</sup> Because these coatings have narrow reflectance stopbands, when introduced on curved surfaces, they generate amplitude and phase errors in the wavefront reflected from these surfaces. These errors depend on both wavelength and incident angle of the radiation going through the imaging system. Fig. 1 shows these dependencies for a multilayer coating containing 20 bilayers of Mo/Si. As can be seen from this figure, for a given wavelength the change in amplitude and phase due to incident angle variation can be significant.

Even a simple imaging system such as a single mirror has variation in angle of incidence across its aperture. Practical imaging systems will have several mirrors. Reflective systems designed for projection lithography, in order to avoid obscuration, are usually configured to be used either with decentered aperture or off-axis field. As a result, angles of incidence vary not only across each mirror but also are different for each mirror. By adjusting bilayer thickness of multilayers, coatings with maximum reflectance at a given wavelength for each mirror can be designed for a single incident angle (usually for a chief ray - the ray passing through the center of the aperture) and one point on the mask. The variation in incident angles of

other rays across the finite aperture in an imaging system introduces variation in reflectance and phase at each surface and, in turn, modifies the amplitude and phase of the wavefront passing through the system.

In this paper we investigate the effect of reflectance and phase errors on image for different types of projection systems. We start with a small field imaging system, the Schwarzschild system. Although, the total phase change across the multilayer bandwidth may be as large as  $\pi$ , the phase difference with respect to a chief ray is  $\pi/2$  and largely a linear function of incident angle (linear term in wavefront aberration function: does not degrade the image, but simply causes a lateral image shift). While small field imaging systems may have not much of a problem of image degradation due to multilayers, it may not be the case for systems with large image fields. In such system, every point on the mask will have different range of incident angles on every mirror. Thus, a uniform thickness multilayer coating designed for one point on the mask may introduce phase and reflectance variations for other mask points, degrading the image across the field and potentially making it impossible for the system to perform up to its designed specifications. Thus, before any practical soft x-ray projection system is built, it is crucial to understand the effect and limitations imposed by multilayer coatings. Knowledge of these effects may help in choosing one system over another and might lead to means for correcting the image degradations introduced by multilayer coatings.

### Polarization Ray Tracing

Normally the image is characterized by performing ray tracing and diffraction calculations assuming that

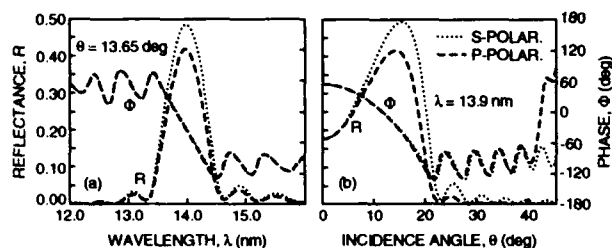


Figure 1. Calculated reflectance and phase versus wavelength (a) and angle of incidence (b) for a 20 bilayer Mo/Si multilayer coating.

rays represent scalar waves and the transmitted wavefront has uniform amplitude and constant polarization state across the exit pupil. In soft x-ray imaging systems, due to narrow bandwidth coatings, this assumption is inadequate and the polarization effects must be considered.

Conventional ray tracing calculates ray paths through an optical system and is used to determine the aberration function of transmitted wavefront, usually in the exit pupil of the system. Polarization ray tracing, assuming the vector nature of light, calculates the Jones matrix associated with an arbitrary ray path through an optical system.<sup>4,5</sup> The Jones matrix is the product of propagation and interface terms. For an isotropic medium, propagation terms are simply the optical path length calculations (conventional wavefront aberration contributions). Interface terms are thin-film calculations; they can be done separately and merged with conventional phase calculations.

We use polarization ray tracing to obtain the phase and amplitude data in the exit pupil of the imaging system for a large grid of rays. Using these data we perform diffraction calculations (point spread function, modulation transfer function, etc.) normally used to characterize the imaging properties of an optical system.

For these simulations we assumed that 100% linearly polarized light (s-polarization) illuminates the conventional amplitude transmission mask. Polarization ray tracing was performed using the Code V program.<sup>6</sup> In this program, rays with assigned vector properties are traced through an optical system. Polarization-dependent phase shifts at surfaces in the optical system alter these vector properties without changing the ray direction at each surface (the program calculates the amplitude, phase and state of polarization from thin-film calculations). After going through all surfaces, it determines the amplitude,

phase and polarization state of the wavefront at the exit pupil, and uses this information to compute several diffraction-based image quality metrics.

### Small Field Projection System

First we want to understand the effect of multilayer coatings on image for a single field point. For this purpose we have chosen a simple imaging system of two spherical mirrors known as Schwarzschild system and shown in Fig. 2. It is a 20 $\times$  reduction system and was used for imaging experiments at 14 nm wavelength.<sup>2,3</sup> Due to its field curvature the usable field is very small (25  $\mu\text{m} \times 50 \mu\text{m}$ ), so that a single field point well represents the entire field. Multilayer coatings designed for both mirrors in the system are shown in Fig. 3. The design provides maximum reflectance at each mirror for the chief ray angle of incidence and 13.9 nm wavelength. The variation in incident angles for other rays going through the system causes the reflectance peak to move as shown in Fig. 3, further reducing the total system bandpass.

With the appropriate coatings specified on all reflecting surfaces a 128  $\times$  128 grid of rays from a single field point was traced through the system. Fig. 4 shows their effect on the phase of the transmitted wavefront. Contour maps of the exit pupil wavefront are shown for two cases: first, when coatings are attached to surfaces and second, when there are no coatings on surfaces (ideal 100% reflectance). The effect of phase errors introduced by coated surfaces is not in change of the *shape* of the wavefront (Fig.

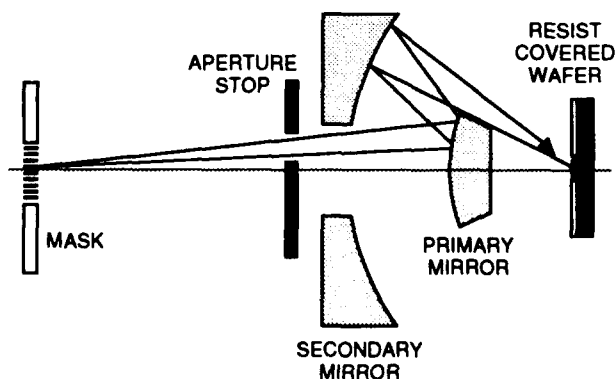


Figure 2. The Schwarzschild system used for imaging experiments at 14 nm wavelength.



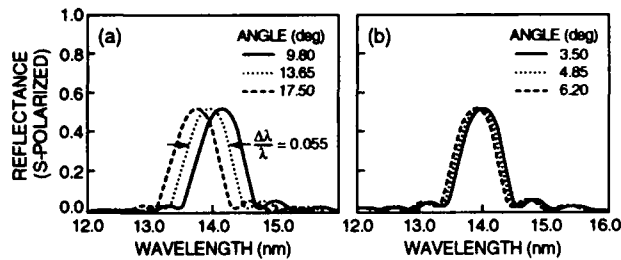


Figure 3. Calculated reflectance of 20 bilayer Mo/Si coatings designed for the primary (a) and secondary (b) mirrors of the Schwarzschild system. Curves are shown for the central (chief) ray and two extreme rays passing through the system.

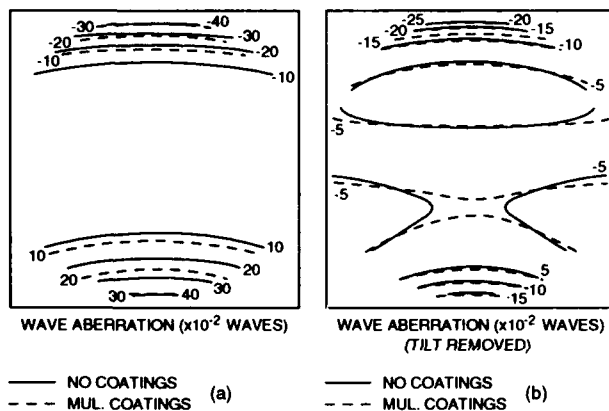


Figure 4. Contour maps of the exit pupil wavefront for two cases: first, when coatings are applied to surfaces and second, when there are no coatings. Actual wavefronts are shown in (a); in (b) are the same wavefronts with tilt terms removed.

4(b)), but mainly in some additional *tilt* of this wavefront as shown in Fig. 4(a). This is not surprising since the phase shift as a function of incident is nearly linear, with only slight curvature in the region of interest (Fig. 1).

When both wavefronts are fitted to Zernike polynomials and resulting coefficients are compared, we see that the largest difference is in the value of low order Zernike coefficients: tilt -  $0.110\lambda$ , and focus -  $0.008\lambda$ . These terms are not really aberrations, since they do not degrade the wavefront. They correspond to tilt and change in radius of the reference sphere which, in turn, generate lateral and longitudinal image shifts respectively. In this system the indicated

difference in aberration terms generate 20 nm of lateral and 35 nm of longitudinal shifts of the image point. The change in higher order terms such as spherical aberration, coma and astigmatism is less than  $0.001\lambda$ .

Fig. 5(a) shows the intensity reflectance map across the pupil, or the square of the amplitude variations in the exit pupil wavefront as the function of the pupil coordinates. (The amplitudes may be obtained by taking the square root of the intensity reflectance values). Because the system aperture is off-axis, the variation in incident angles for tangential rays is larger than for sagittal ones, resulting in larger variation of amplitude and phase.

Polarization ray tracing showed that multilayer coatings also cause a small change in polarization state across the pupil. For example, if the light is initially 100% s-polarized, then in the exit pupil of the system polarizations at opposite edges are elliptical with the major axes tipped slightly in opposite directions from the initial field vector direction. This implies that some amount of light is coupled into the orthogonal (p-polarization) state. However, the amount of this coupled light is very small: only 0.03% of the total reflected light; so its effect on the image is negligible.

When the wavefront information in terms of amplitude, phase and state of polarization is known, diffraction calculations may be performed. Fig. 6 shows the square wave modulation transfer function (MTF) for the Schwarzschild system as a function of spatial frequencies in the object for two different cases: when system contains coated and uncoated

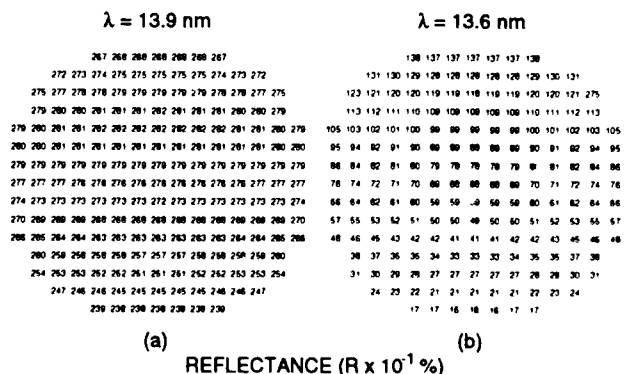


Figure 5. The intensity reflectance in the exit pupil as a function of pupil coordinates for the case of the ideal condition (a) and the case of mismatch between the source wavelength and thin-film design (b).

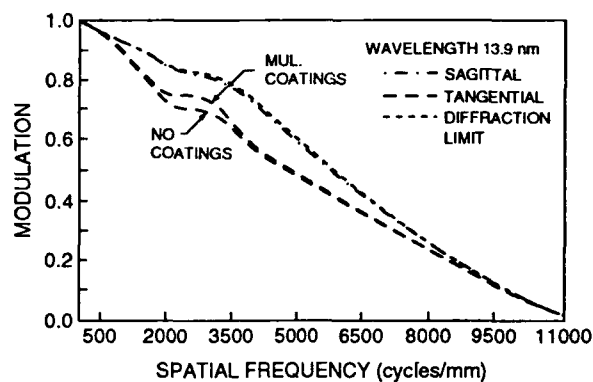


Figure 6. Square wave MTF as a function of spatial frequencies in the object for the Schwarzschild system containing coated and uncoated mirrors.

mirrors. The illumination is assumed to be incoherent (single wavelength, infinitely large source). The effect of coatings on image contrast for these conditions is very small and, as expected, is noticeable only for tangential features. The additional tilt of the wavefront caused by the coatings does not affect the shape of the point spread function and, therefore, does not change MTF.

#### Coating Thickness Errors

Next thing we want to know whether the image is affected when the illumination wavelength is different from the design value; or if the illumination wavelength is fixed, the bilayer thickness error in the coating shifts the reflectance maximum for the chief ray to a different wavelength value. Fig. 5(b) shows the intensity reflectance map in the exit pupil of the Schwarzschild system either when the illumination wavelength is shifted by one half width at half maximum (HWHM), or when the reflectance peak for primary mirror coating is shifted due to the bilayer thickness error of 2.7%. In this case, the same variation in incident angles on primary and secondary mirrors causes much larger variation in reflectance (about 88%) across the pupil. The phase error is about the same as in the case of ideal coatings: mostly linear function of incident angle with slightly larger quadratic term. This pupil apodization error (increased wavefront amplitude variation across the pupil) *does* affect the image contrast. Since the largest variation in the amplitude across the pupil is in one direction (direction of the aperture shift), the image of periodic structures in the same direction is going to be affected most severely. A 12% reduction in image

contrast for tangential features is shown in Fig. 7 which contains a plot of square wave MTF as a function of focus for 5000 l/mm spatial frequency (0.1  $\mu\text{m}$  features). Reduction in image contrast will reduce the system resolution and depth of focus. Some focus shift from the nominal position is also shown.

#### The Effect of Illumination on the Image Contrast

The above calculations were done for single wavelength, spatially incoherent illumination. The effect of the source bandwidth on the image in the multilayer coated system may be determined by performing similar calculations for several appropriately weighted (to represent the shape of the source linewidth) wavelengths. Overall MTF is obtained by summing individually weighted MTFs. We have performed calculations for a source of the same bandwidth as the reflectance bandwidth of 20 bilayer Mo/Si multilayer (5.4%) and a Gaussian shape beam profile. They show about 8% reduction in contrast for tangential periodic features in the frequency range from 3000 l/mm to 6000 l/mm (linewidth from 0.16  $\mu\text{m}$  to 0.08  $\mu\text{m}$ ). Obviously, reducing the source bandwidth reduces this problem.

In practice, partially coherent illumination is used in projection lithography with the entrance pupil of imaging system underfilled, i. e. the source image is smaller than the pupil. In this case, the same variation in reflectance across the pupil produces larger variation in intensity of interfering beams (which form the image) and, therefore, degrading it more severely than indicated by calculations done with incoherent illumination.

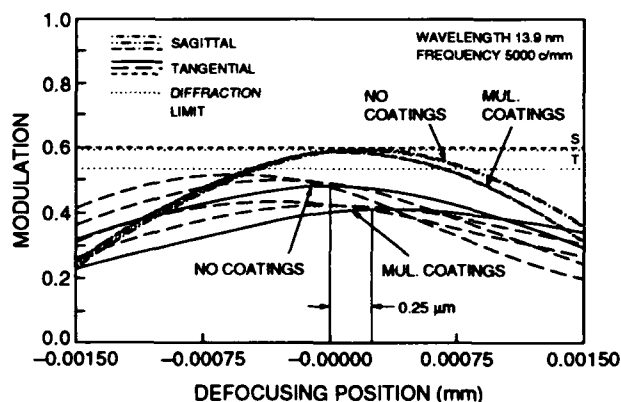


Figure 7. Square wave MTF as a function of focus for the Schwarzschild system containing coated and uncoated mirrors and the case of mismatch between the source wavelength and thin-film design.

### The Effect of Increasing the Number of Layers in the Coating

For the imaging system with multilayer coated surfaces, the sensitivity to wavelength and coating bilayer thickness errors increases as the number of layers increases, since a large number of periods in the coating reduces its bandwidth. To verify this, an image analysis for the Schwarzschild system having 40 Mo/Si bilayers was performed. When the illumination wavelength was shifted by HWHM (2.1% thickness error), a 20% reduction in image contrast for 0.1  $\mu\text{m}$  linewidth periodic pattern and incoherent illumination was observed as compared to 12% for the 20 bilayer case.

Therefore, there are certain limitations imposed by the multilayer coatings on the system design for higher resolution systems which intend to use shorter wavelengths. Shorter wavelengths require larger numbers of layers in the coatings resulting in very narrow bandpasses. Even if system designs with large numerical apertures and shorter wavelengths are possible, because of narrow coating bandpass, the reflectance of rays close to the edge of the pupil (high spatial frequencies) is very low (or zero), and the high resolution may not be achieved. Use of graded thickness coatings (which have thicknesses varying with respect to position on the mirror) reduce the problem of reflectance variation across the pupil and, therefore, should improve performance. Of course, in this case the surface shape change due to thickness variation in the coating should be taken into account during the imaging system design process. Use of alternative materials such as Be may inherently increase the stopband width ( $\sim 25\%$ ) and also improve system performance and tolerances.

### Large Field Systems

So far we have analyzed the system with the small image field. Because of its small size, the Schwarzschild system is not suitable for production lithography, since large chips can not be exposed. Fig. 8 shows one of the optical system designs which can cover a large field.<sup>7</sup> This 0.08 NA four-mirror design has good image quality over  $5 \times 10$  mm field (scaled up version has  $10 \times 15$  mm field size and still packaged in small size of about 800 mm object-image distance). In this system, because the field is large, every field point will have a set of rays which have different incident angles on each mirror in the system. Therefore, in addition to marginal ray incident angle variation for a single field point, there is variation in

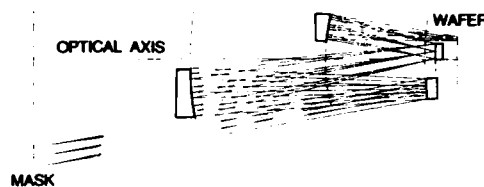


Figure 8. Layout of coaxial four-mirror design.

incident angle for a chief ray as well. Optimized 20 bilayer Mo/Si coatings have been designed for each mirror in this system and the image analysis was performed for several field points. The Bragg condition in each coating was satisfied for a single ray: the chief ray from the center of the object field.

One would expect that with more mirrors in the system and the larger image field, the problem of image degradation would be worsened. Fortunately, this is not the case. In four-mirror system the variation in marginal ray incident angle on each mirror is significantly reduced compared to the two mirror system (the power is distributed among four mirrors instead of two) and its maximum is less than half of that in the Schwarzschild system. Thus, the effect of amplitude and phase errors on the image is even smaller than in the system of two spherical mirrors. On the other hand, the variation in chief ray incident angle on mirror surfaces in the system produces intensity variation across the image plane. In this system a  $\pm 1.4^\circ$  variation in chief ray angle of incidence produces about 1.5% intensity variation in the image field of  $5 \times 10$  mm even for the ideal coatings (use of narrower bandwidth coatings will generate higher intensity variation across the image field). In addition, this system is more sensitive to errors in bilayer thickness of multilayers. For example, when illumination wavelength is shifted by HWHM relative to the reflectance peak of the entire system, the variation in intensity across the image field is as high as 68%.

A gradient thickness coating introduced on one or two mirrors in this system which have the largest variation in chief ray incidence angle may reduce the problem of nonuniform intensity in the image. The gradient profile may simply be a linear function across the mirror.

### Ring Field Systems

Ring field systems can cover large image fields. In this type of system, diffraction limited performance is

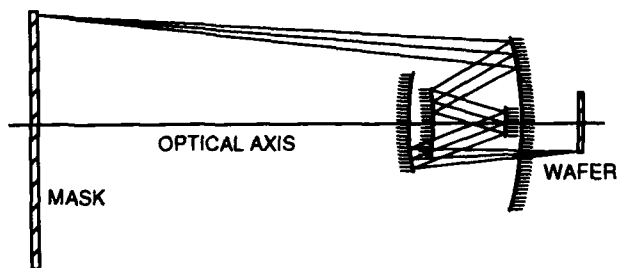


Figure 9. Layout of four-mirror ring field design.

obtained within a narrow annulus with its radius measured from the optical axis. Being a rotationally symmetric system with respect to an optical axis, it is used with an off-axis image field. To cover a large image field, both the mask and the wafer are scanned during the exposure.

A 5 $\times$  reduction ring field design shown in Fig. 9 has the diffraction limited performance over 2 mm ring width and 25 mm radius on the image side. Because of higher incident angles on mirrors in this design, relatively small variation of  $\pm 0.7^\circ$  in chief ray incident angle in radial direction generates  $\sim 3\%$  image intensity variation in the same direction for the case of ideal 20 bilayer Mo/Si coatings. It increases up to 91% for the case of mismatched thickness coatings. Due to rotational symmetry, there is no variation in chief ray angle of incidence for field points in the azimuth direction.

One advantage of ring field over a full field designs for photolithography is that in scanning systems the intensity nonuniformity in the image may be compensated by adjusting the slit width along the cross scan direction.

It is interesting to point out here that in the Offner 1 $\times$  ring field system, due to its almost complete symmetry, the variation in angle of incidence is very small:  $\pm 0.1^\circ$ . In this system the errors in the coating thickness may only reduce the throughput, but hardly affect the image.

### Conclusion

For a variety of realistic soft x-ray projection lithographic lens designs, the Mo/Si reflective coatings do *not* cause significant degradation in the system performance. Variation in the reflective phase shifts is nearly linear over incident angles of interest and thus, causes only a small tilt in the wavefront, which slightly displaces the image. This displacement

is constant enough such that its contribution to distortion is negligible. Variation in angles of incidence of chief ray across the field causes small (up to 3%) variation in the image intensity.

However, departures from the ideal condition e. g. finite source bandwidth, mismatch between thin-film design and source wavelength, can cause serious nonuniformity in the image intensity. This is particularly true for large field systems. Increasing the number of layers in the coating increases this problem.

Scanning ring field designs have an advantage over full field systems, since the nonuniformity in the image intensity may be compensated by adjusting the slit width along the cross scan direction. Gradient thickness coatings introduced on mirrors with largest variation in chief ray incident angle may reduce the image intensity variation.

### Acknowledgment

The author would like to thank Dave Windt for helpful discussions.

### References

1. H. Kinoshita, K. Kurihara, Y. Ishii, and Y. Torii, "Soft x-ray reduction lithography using multilayer mirrors," *J. Vac. Sci. Technol. B* **7** (6), 1648 (1989).
2. T. E. Jewell, *et al.*, "20:1 Projection soft x-ray lithography using tri-level resist," *Proc. SPIE*, **1263**, 90 (1990).
3. J. E. Bjorkholm, *et al.*, "Reduction imaging at 14 nm using multilayer-coated optics: Printing of features smaller than 0.1  $\mu\text{m}$ ," *J. Vac. Sci. Technol. B* **8** (6), 1509 (1990).
4. R. A. Chipman, "Polarization analysis of optical systems," *Opt. Eng.* **28** (2), 90 (1989).
5. E. Waluschka, "Polarization ray trace," *Opt. Eng.* **28** (2), 86 (1989).
6. Code V is a copyrighted lens design program developed by Optical Research Associates, 550 N. Rosemead Boulevard, Pasadena, California 91107.
7. T. E. Jewell, J. M. Rodgers, and K. P. Thompson, "Reflective systems design study for soft x-ray projection lithography," *J. Vac. Sci. Technol. B* **8** (6), 1519 (1990).

## Photoresists



## Surface-Imaging Lithography

Mark A. Hartney

Lincoln Laboratory, Massachusetts Institute of Technology,  
244 Wood Street, Lexington, Massachusetts 02173

Surface-imaging lithography is a technique which was first described by Taylor *et al.* [1] nearly ten years ago. In this approach, a pattern is defined at the surface or near-surface regions of a resist rather than throughout the entire resist thickness. Surface-imaging can eliminate problems such as reflectivity variations due to different substrates or topography in optical lithography and backscattering in electron-beam lithography [2]. The use of surface-imaging has also proven beneficial for deep-UV optical lithography, where the high absorbance of most resists necessitates such an approach. Resist absorption is also problematic for projection printing with soft x-ray radiation; the 1/e attenuation length ranges from 300 nm for 13.5-nm x-rays to less than 100 nm with 39-nm x-rays [3].

Of several surface-imaging schemes, silylation processes have been most extensively developed, and are being used in advanced processing lines [4]. A schematic of a positive-tone silylation process is shown in Fig. 1. The resist is patterned with an appropriate type of radiation, which in this example crosslinks the exposed areas. Next, the material is placed in an environment of a silicon-containing gas which diffuses into and reacts selectively with the uncrosslinked portions of the resist film. Development can then be carried out in an oxygen reactive ion etching (RIE) plasma, which selectively removes the unsilylated portions of the film. Areas in which the silylating agent has reacted with the film are converted to silicon oxide and are not etched in the plasma.

An example of a resist which would behave in the manner depicted in Fig. 1 is an acid-catalyzed resist which is designed to crosslink. Such materials were developed initially by Rohm and Haas [5], and are commercially available from Shipley as the resists SAL 601 and SNR 248. These resists function by generating an acid species in the exposed areas. A post-exposure baking step, typically around 120°C for a few minutes, causes a crosslinking reaction between a multifunctional melamine additive and the hydroxyl group of the resin polymer. Since the acid species is not consumed in the crosslinking reaction, it may trigger several crosslinking events, which leads to very high

resist sensitivity. This type of resist was designed for exposure with an electron-beam [5]. The acid generator is also sensitive however, to 248-nm [6] and 193-nm [7] optical exposure, synchrotron x-ray irradiation [8], and focused ion beams over a range from 20 to 240 keV [9]. SAL 601 has also been used recently as a resist for 13.5-nm soft x-ray exposure [10].

An alternative resist approach relies upon a site-generation process to achieve silylation selectivity rather than a diffusion limitation imposed by crosslinking. In these resists [11], a polymer containing a tertiary-butyloxycarbonyloxy (t-BOC) functionality is used with an acid-generating additive. Exposure produces the acid species, which reacts with the t-BOC group and leads to formation of a phenolic site on the polymer resin. Again, since the acid is not consumed in this reaction, several groups can be converted by one acid molecule and the resist shows high sensitivity. After the exposure and conversion, the phenolic sites produced are available for silylation, while the original t-BOC materials cannot be silylated. In this case the resist is silylated in the exposed areas, and a negative-tone image results after pattern transfer. Resists based on this approach have been used with some success for solution-based development with 248-nm [11] and hard x-ray (1.4 nm) exposure [12], and in one case as a silylation resist at 248 nm [13].

For resists based on crosslinking, the selectivity for silylation is determined by the relative diffusion rates in the exposed and unexposed areas. Since the silylating agent diffuses into the resist surface, only this portion of the film need be exposed and crosslinked to prevent silylation. Work in our laboratory has used this approach for 193-nm lithography [7], where the depth of light penetration, and hence crosslinking, is less than 100 nm, and for focused ion beam lithography [9], where ion ranges (which are a function of ion species and energy) as shallow as 20 nm have been used.

The amount of silicon required for etch selectivity is a function of the plasma conditions used for etching. In order to maintain adequate linewidth control for sub-0.5-μm

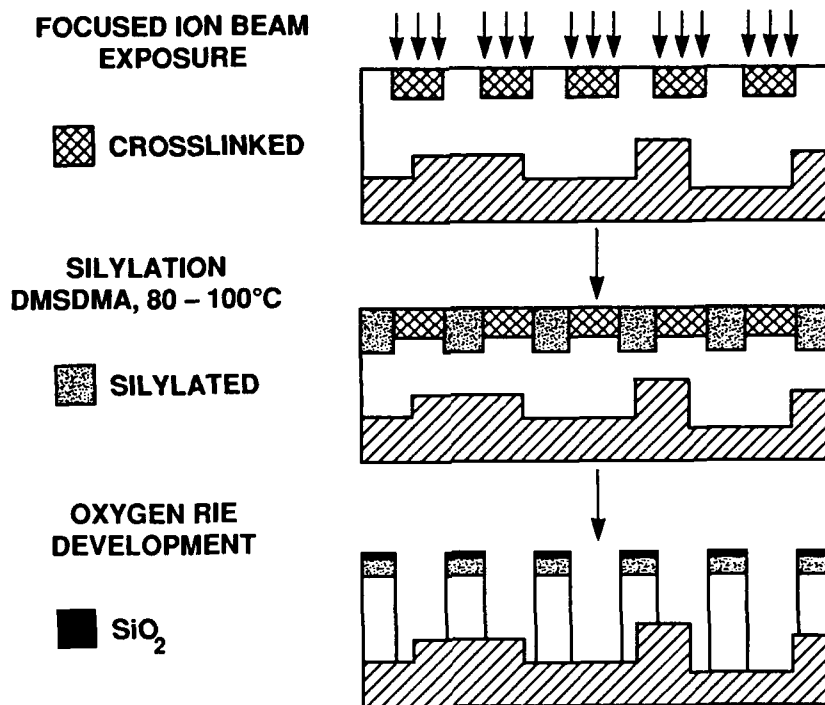


Figure 1. Schematic representation of a positive-tone silylation process.

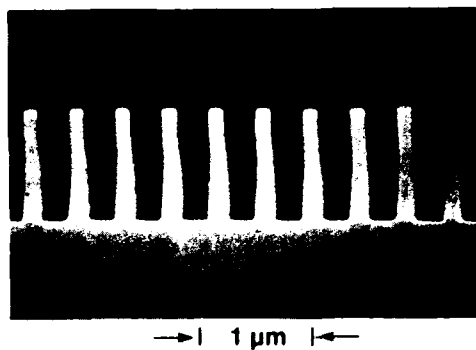


Figure 2. 0.2-μm resolution in polyvinylphenol resin, projection printed using a 193-nm excimer laser, silylated, and developed in an oxygen plasma.

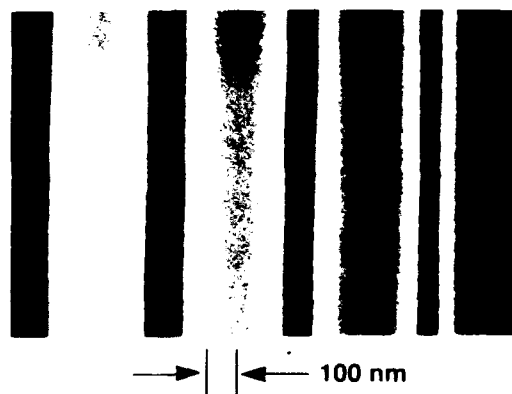


Figure 3. 100-nm resolution in SAL 601, exposed with at 30 keV Ga<sup>+</sup> ion beam, silylated and developed in an oxygen plasma.

features, RIE plasmas are typically used. These plasmas are characterized by low pressures ( $\sim 10$  mTorr) and relatively high ion bombardment energies ( $\sim 200$  eV). For a  $1.5\text{-}\mu\text{m}$ -thick resist film, and an etch selectivity of 15:1 between the silylated and unsilylated portions of the film, the silylated regions need to extend at least 100 nm into the film. Greater processing latitudes and throughput can be achieved in the etching step, however, with a greater depth of silylation.

A potential concern about the crosslinking based resists is that the depth of silylation often exceeds the depth of crosslinking, and the diffusion of silicon beneath the crosslinked regions seems likely. We have investigated this phenomenon for 193-nm lithography and it appears that underdiffusion does not occur under appropriately controlled silylating conditions [14]. The diffusion of silylating agent is controlled by the stress mismatch between the swollen silylated part of the film and the unreacted material beneath it. For a patterned film, the crosslinked regions do not silylate, and hence do not swell, thus minimizing the diffusion rate in the adjacent areas. We have found [14] that the diffusion is most rapid at the center of an unexposed feature, and the slower diffusion at the line edge prevents underdiffusion from occurring. For extreme cases, with more silylation than required to withstand etching, there can be some undercutting. However, optimal process control can prevent this.

The same phenomenon which prevents underdiffusion, however, can lead to a proximity effect, in which the amount of silicon diffusing into a feature size depends on the distance to the nearest crosslinked region. This can lead to thinner silylation depths for closely spaced gratings for example, when compared to a broad unexposed area [15]. At the feature sizes proposed for projection x-ray lithography this proximity effect may represent a significant challenge, and bears further investigation.

An example of patterning using silylation is shown in Fig. 2, which depicts  $0.2\text{-}\mu\text{m}$  line-and-space patterns projection printed with a 193-nm excimer laser using a polyvinylphenol resin. The depth of crosslinking in this case is estimated to be 75 nm, while the depth of silylation is approximately 150 nm. The equal line-to-space ratio indicates that the latent image in the resist was not distorted by underdiffusion of the silylating agent.

A more extreme case of shallow crosslinking is seen in Fig. 3, which shows features patterned with a 30 keV  $\text{Ga}^+$  ion beam in SAL 601 resist. In this case, the ion range is estimated to be 34 nm, while the depth of silylation is greater than 100 nm. Resolution of 100 nm lines is shown.

One report recently applied surface imaging to soft-x-ray projection lithography [3]. A series of novolac-based polymers were exposed and crosslinked using 13.5-nm x-rays, then flood exposed with UV light to prevent the photoactive compound from additional crosslinking in the unexposed areas during silylation. As mentioned earlier, the  $1/e$  attenuation length is approximately 300 nm at this x-ray wavelength, and film thicknesses of nearly  $2\text{ }\mu\text{m}$  were used. The resists were fairly insensitive, with doses between 500 and  $1000\text{ mJ/cm}^2$  required, and resolution capabilities were not described. With an acid-catalyzed resist, however, the sensitivity should improve, and the

examples given above demonstrate that sub- $0.25\text{-}\mu\text{m}$  resolution can be attained.

While silylation processes have shown considerable utility and are being considered for volume production, several questions persist about the benefits of using this technology. Compared to a standard single-layer lithography process, the additional capital equipment requirements for a silylation process are significant. This is not a strong impediment, however, if conventional processing cannot be used. Good process control has been reported [4] for  $0.5\text{-}\mu\text{m}$  minimum feature resolution, but has not been demonstrated for smaller features at this point. Appropriate etch processes to maintain vertical sidewalls, adequate linewidth control, and residue-free etching will be a challenging requirement.

In summary, surface imaging has shown strong potential for imaging below  $0.25\text{-}\mu\text{m}$  geometries. The absorption length of the imaging radiation does not present a limitation thus surface-imaging represents an attractive approach for projection soft x-ray lithography.

#### Acknowledgment

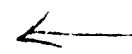
This work was sponsored by the Defense Advanced Research Projects Agency.

#### References

1. G.N. Taylor, L.E. Stillwagon, and T. Venkatesan, J. Electrochem. Soc. **131**, 1658 (1984).
2. B.J. Lin, in *Introduction to Microlithography*, edited by L.F. Thompson, C.G. Willson, and M.J. Bowden, ACS Symp. Ser. No. 219 (American Chemical Society, Washington, D.C., 1983).
3. G.N. Taylor, R.S. Hutton, D.L. Windt, and W.M. Mansfield, Proc. SPIE **1343**, 258 (1990).
4. C.M. Garza, G.R. Misium, R.R. Doering, B. Roland, and R. Lombaerts, Proc. SPIE **1086**, 229 (1989).
5. H.Y. Liu, M.P. deGrandpre, and W.E. Feely, J. Vac. Sci. Technol. B **6**, 379 (1988).
6. J.W. Thackeray, G.W. Orsula, E.K. Pavelchek, D.L. Canistro, L.E. Bogan, Jr., A.K. Berry, K.A. Graziano, Proc. SPIE **1086**, 34 (1989).
7. M.A. Hartney, R.R. Kunz, D.J. Ehrlich, and D.C. Shaver, Proc. SPIE **1262**, 119 (1990).
8. D. Seligson, S. Das, H. Gaw, and P. Pianetta, J. Vac. Sci. Technol. B **6**, 2303 (1988).
9. M.A. Hartney, D.C. Shaver, M.I. Shepard, J.S. Huh, and J. McIngvailis, Appl. Phys. Lett., in press.
10. H. Kinoshita, K. Kurihara, T. Mizota, T. Haga, Y. Torii, H. Takenaka, and Y. Ishii, to be published in these Proceedings.
11. H. Ito and C.G. Wilson, Polymer Eng. Sci. **23**, 1012 (1983).
12. A.E. Novembre, W.W. Tai, J.M. Komietani, J.E. Hanson, O. Nalamasu, G.N. Taylor, E. Reichmanis, and L.F. Thompson, Proc. SPIE **1466**, in press.
13. C.A. Spence, S.A. MacDonald, and H. Schlosser, Proc. SPIE **1262**, 344 (1990).



14. M.A. Hartney, M. Rothschild, R.R. Kunz, D.J. Ehrlich, and D.C. Shaver, *J. Vac. Sci. Technol. B* **8**, 1476 (1990).
15. E.K. Pavelchek, J.F. Bohland, J.W. Thackeray, G.W. Orsula, S.K. Jones, B.W. Dudley, S.M. Bobbio, and P.W. Freeman, *J. Vac. Sci. Technol. B* **8**, 1497 (1990).





## Resist Characterization at Soft-X-Ray Wavelengths

G. D. Kubiak, E. M. Kneeder,<sup>†</sup> K. W. Berger, and R. H. Stulen  
*Sandia National Laboratories, Livermore, California 94551-0969*

J. E. Bjorkholm and W. M. Mansfield  
*AT&T Bell Laboratories, Crawford's Corner Road, Holmdel, New Jersey 07733-1988*

H. Windischmann  
*BP America, 4440 Warrensville Center Road, Cleveland, Ohio 44128*

### Abstract

Sensitivities of the positive resists polymethylmethacrylate (PMMA) and diazonaphthoquinone sulfonate-novolac (Shipley System 9) have been determined at an exposure wavelength of 140 Å. Using thin transmissive support membranes of silicon and polycrystalline diamond, absorbance spectra have been measured over the wavelength range of 80 - 360 Å for several resist film thicknesses. The resulting linear absorption coefficients,  $\alpha$ , are found to agree with values calculated from published mass absorption coefficients only up to ~250 Å. At longer wavelengths, the experimentally measured  $\alpha$  values are larger than the calculated values for both resists. Combining the exposure sensitivity and absorbance results, the volumetric dose densities at 140 Å for PMMA and System 9 are 4600 J/cm<sup>3</sup> and 350 J/cm<sup>3</sup>, respectively.

### Introduction

The characterization of resist materials for soft X-ray projection lithography (SXPL) in the 75-350 Å spectral region is an important issue, although it has received little attention to date. With the recent demonstration of diffraction-limited SXPL at 140 Å [1], the need to optimize resists at specific exposure wavelengths for future SXPL commercialization has become acute. Near 300 Å resist absorbance is so large that a single-layer resist strategy does not

appear feasible, whereas near 80 Å it does. At intermediate wavelengths, for example where Mo/Si multilayer reflective coatings are efficient, it is not yet possible to determine whether a surface imaging or single-layer method is optimum. To estimate the maximum developed resist depth attainable at a given wavelength, the appropriate mass absorption coefficients may be used to calculate film absorbance. The accuracy of these estimates is questionable, however, especially at longer wavelengths where solid state effects can be pronounced. We have undertaken a study of single-layer resists in the spectral region relevant to SXPL and have characterized the sensitivity, contrast, and absolute absorbance of poly methylmethacrylate (PMMA), polysilane, and diazonaphthoquinone/novolac resists. In addition, we have evaluated the lithographic performance of these materials at an exposure wavelength of 140 Å using an SXPL instrument illuminated by a laser plasma source (LPS) of high average power.

### Experimental

Experiments were performed with an LPS having two distinct beamlines: one for performing resist spectroscopy and characterization with monochromatized extreme ultraviolet (XUV) beams and one for performing projection lithography. The monochromatized beamline has been described previously [2,3]. Resist sensitivity curves were determined for a range of exposure doses at

140 Å by exposing spin-cast films to the focused monochromator output flux, developing the exposed films, and then measuring the depth of the resulting depressions with a stylus profilometer. The development conditions for PMMA and System 9 exposures are tabulated in Table 1.

Resist transmittance spectra were recorded by spin-casting 0.075-0.50  $\mu\text{m}$  thick films onto  $\sim 3500$  Å-thick crystalline silicon[4] or  $\sim 2800$  Å-thick synthetic diamond[5] support membranes and then measuring the composite transmittance versus wavelength with an XUV diode. Film thickness was measured with a stylus profilometer along the margins of the membrane and is believed accurate to  $\pm 200$  Å. The resist film was then stripped from the support membrane and its transmittance spectrum measured. The spectral transmittance of the resist film was thus extracted from the composite transmittance by normalizing with the measured support membrane transmittance. Resist film densities were determined in order to compare experimental transmittance spectra with those calculated from published atomic scattering factors[6]. Densities were determined by measuring the mass increase of Si wafers of known surface area when spin-coated with resist films of selected, uniform thickness. Film thickness was subsequently established with a stylus profilometer. The resulting densities are listed in Table 1.

The lithography beamline will only be described briefly; a more detailed description can be found in refs. 7,8. A Mo/Si multilayer-coated spherical condenser optic, oriented at  $45^\circ$  incidence, was used to collect radiation from the plasma and focus it with 6x magnification (along one axis only) into the entrance pupil of a Schwarzschild objective having 20:1 demagnification ratio. The primary and secondary mirrors of the objective were

Table I. PMMA and System 9 Parameters

| Resist   | Density                 | Developer                               | Duration |
|----------|-------------------------|---|----------|
| PMMA     | 1.275 g/cm <sup>3</sup> | Cellosolve/<br>Methanol 3:7             | 60 sec.  |
| System 9 | 1.203 g/cm <sup>3</sup> | Shipley SAL660/<br>H <sub>2</sub> O 1:1 | 360 sec. |

coated with Mo/Si multilayers matched to that of the condenser. A transmissive Ge/Si mask was used to project test patterns onto the resist films.

## Results

### Exposure Sensitivities

Sensitivity curves of PMMA ( $M_n = 500,000$ ) and Shipley System 9 are shown in Fig. 1. At an exposure wavelength of 140 Å a dose of 22 mJ/cm<sup>2</sup> is required to clear a 0.45  $\mu\text{m}$  film of Shipley 9 and  $\sim 500$  mJ/cm<sup>2</sup> is required to clear a 0.55  $\mu\text{m}$  film of PMMA. The best contrast value obtained was 4.1, exhibited by the System 9 resist. PMMA exhibited a contrast of 1.8, in agreement with previous measurements[9].

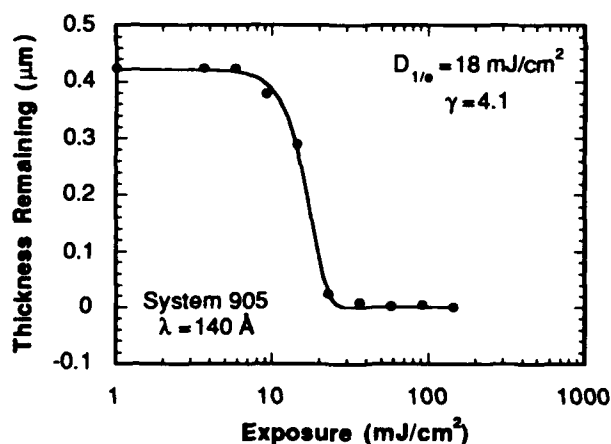
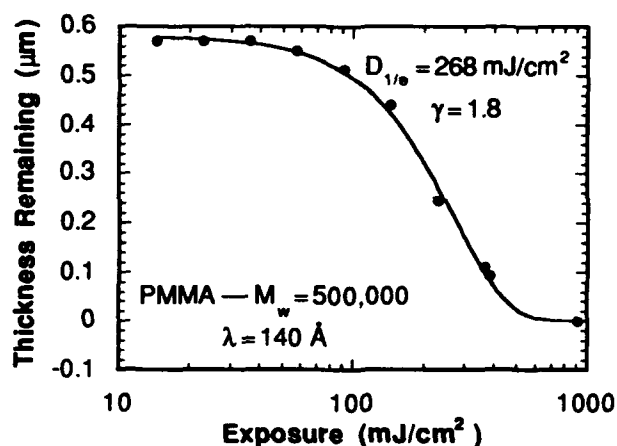


Figure 1. Exposure sensitivity curves for PMMA and System 9 positive resists at  $\lambda = 140$  Å.

### Spectral Transmittance

To determine resist absorbance, the absolute transmittance of each resist was measured for four film thicknesses between 125-360 Å using Si membranes. Diamond membranes were used to extend measurements to wavelengths below the Si L<sub>2,3</sub> edge. Figure 2 shows the measured transmittance of one such diamond film having a thickness of 2800 Å, comparing these data to the transmittance calculated from published mass absorption coefficients of carbon and assuming the bulk diamond density. For wavelengths below 100 Å these membranes may be useful as isolation windows in SXPL.

Figures 3 and 4 plot spectral transmittance and the derived linear absorption coefficients measured through the film thicknesses shown for PMMA and System 9, respectively. These data were obtained using Si support membranes. Also plotted in Figs. 3 and 4 are the values of film transmittance and linear absorption coefficient calculated using the mass absorption coefficients of Henke, et al.[6]. This comparison shows that the agreement between the data and the calculation is best for  $\lambda < 250$  Å; at longer  $\lambda$  the calculations yield systematically lower absorbance than is measured experimentally. Mass absorption coefficients are not expected to adequately account for the observed absorbance for  $\lambda > 250$  Å due to structured

absorption into the conduction bands of the resist. Since the band structure is sensitive to the bonding environment of the constituent atoms within a molecule, photoabsorption at long wavelengths may vary among molecules of identical atomic stoichiometry. Striking examples of this can be found in Ref. 10. Absorption coefficients were also determined for PMMA at 360 Å, although sensitivity problems due to low transmittance made measurements less precise; we find a value of  $\alpha = 33 \pm 4 \mu\text{m}^{-1}$ , slightly lower than that predicted.

The volumetric dose density (D) of PMMA and System 9 can be calculated by combining the exposure sensitivity values

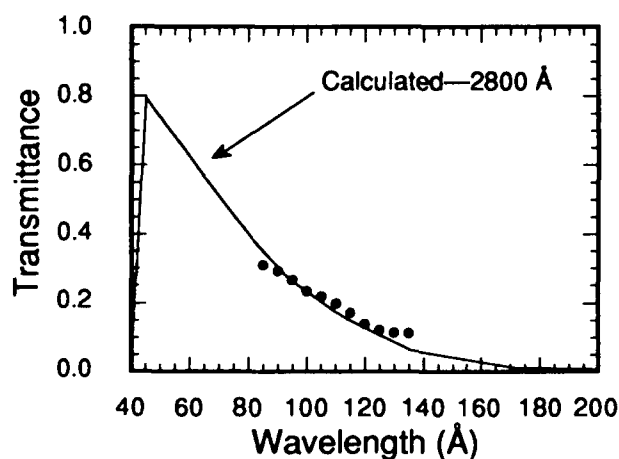


Figure 2. Comparison between measured and calculated spectral transmittance of CVD diamond film.

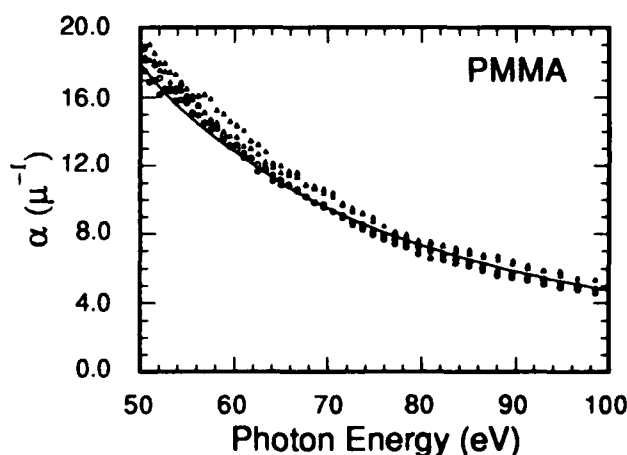
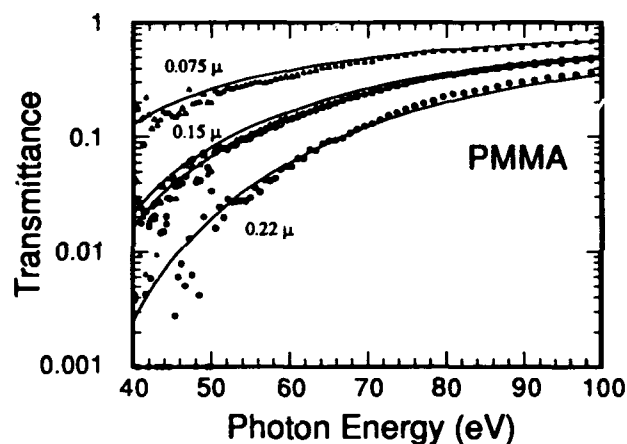


Figure 3. Comparison between measured and calculated spectral transmittance and linear absorption coefficients of PMMA.

plotted in Fig. 1 with the values of  $\alpha$  determined at 140 Å and shown in Figs. 3 and 4. For optically thin layers (i.e.  $\leq 500$  Å),  $D = 4600 \text{ J/cm}^3$  and  $350 \text{ J/cm}^3$  for PMMA and System 9, respectively. The value of  $D$  for PMMA is approximately twice the value obtained for e-beam exposures[11] and 50 % greater than recent values obtained at 140 Å using development conditions similar to those used in this work[12]. It is likely that this latter discrepancy represents the combined errors in the individual calibrations of the two XUV detectors used to measure exposure sensitivities.

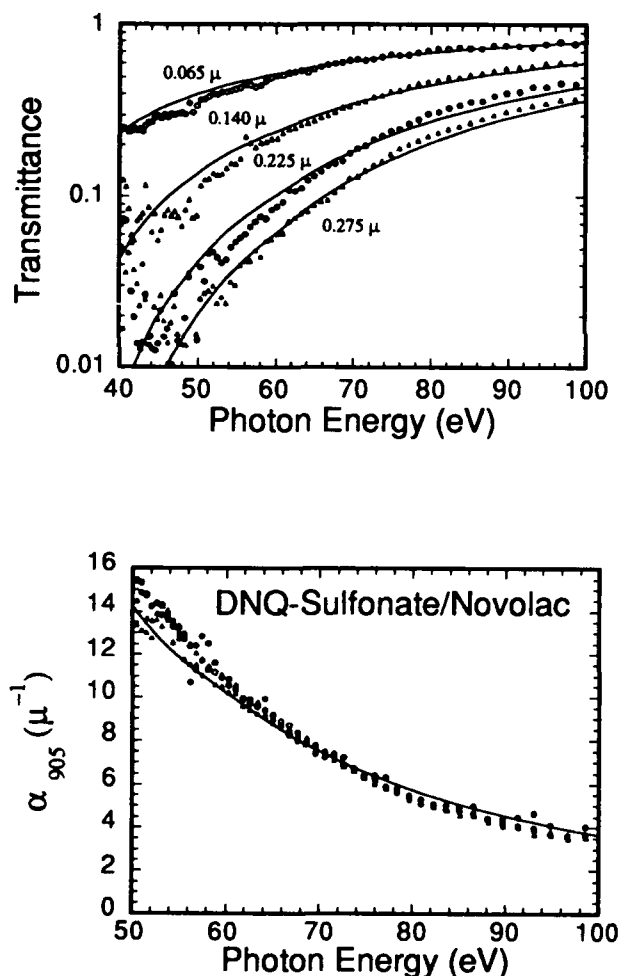


Figure 4. Comparison between measured and calculated spectral transmittance and linear absorption coefficients of System 9.

## Imaging

PMMA and System 9 resists were employed to record 20:1 demagnified images of the Si/Ge transmission mask in layer thicknesses of  $\sim 500$  Å and  $\sim 2500$  Å, respectively. The latent images were developed as described in Table 1 and then rinsed in methanol or water for 40 sec. to remove residue from the otherwise cleared surface of the wafer. Figure 5 shows two such images, recorded at 140 Å with an NA of 0.12, corresponding to a diffraction limited resolution of  $0.07 \mu\text{m}$ . The top panel shows that  $0.1 \mu\text{m}$  lines and spaces are well-resolved in PMMA with some modulation also present in the  $0.05 \mu\text{m}$  features, as previously observed using synchrotron exposures [1]. The System 9 layer, shown in the bottom panel of Fig. 5, exhibits more roughness overall than PMMA and resolves the  $0.15 \mu\text{m}$  features but does not fully resolve the  $0.1 \mu\text{m}$  ones. Exposure times were generally 3-5 times shorter to clear these layers than were required to clear the  $500$  Å thick PMMA layers, however. Electron beam exposures [13] have also demonstrated  $0.2 \mu\text{m}$  resolution in System 9. Studies are in progress to further assess the resolution capabilities of this material. At present, it appears that  $0.25 \mu\text{m}$  thick layers of System 9 may be useful for SXPL down to feature sizes of  $\sim 0.15$ - $0.20 \mu\text{m}$ .

## Acknowledgments

This work was supported by the U. S. Department of Energy under contract number DE-AC04-76DP00789. Daniel Tichenor, Steve Haney, and Les Brown (SNL,L) and Jeff Bokor, Richard R. Freeman, Tanya E. Jewell, Alistair A. MacDowell, Gary N. Taylor, Donald M. Tennant, Warren K. Waskiewicz, Donald L. White, David L. Windt, and Obert R. Wood, II, (AT&T) are gratefully acknowledged for contributions made to the imaging experiments.

§Permanent address: Department of Physics, University of Oregon, Eugene, OR 97403-1274

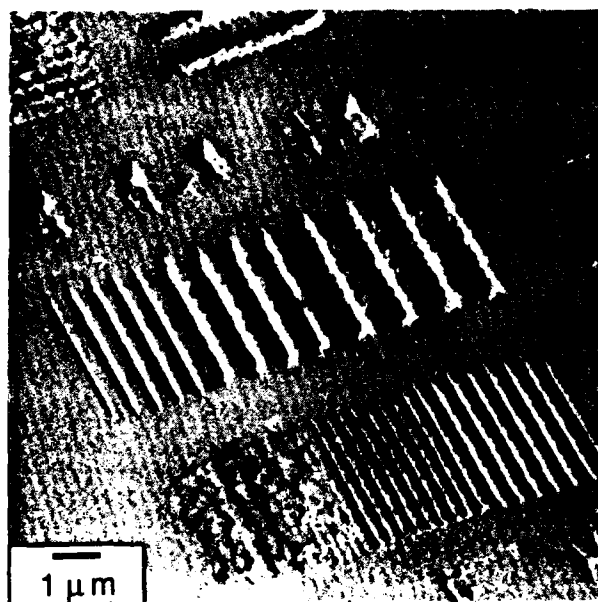
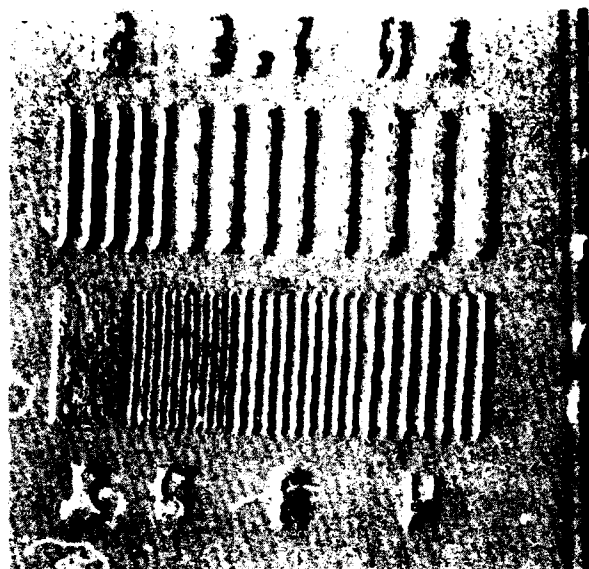


Figure 5 Atomic force micrographs of images recorded at  $\lambda = 140 \text{ \AA}$  with  $NA = 0.12$  in PMMA (top) and System 9 (bottom).

## References

1. D. W. Berreman, J. E. Bjorkholm, L. Eichner, R. R. Freeman, T. E. Jewell, W. M. Mansfield, A. A. MacDowell, M. L. O'Malley, E. L. Raab, W. T. Silfvast, L. H. Szeto, D. M. Tennant, W. K. Waskiewicz, D. L. White, D. L. Windt, and O. R. Wood, II, and J. H. Bruning, *Optics Lett.* **15**, 529 (1990); T. E. Jewell, M. M. Becker, J. E. Bjorkholm, J. Bokor, L. Eichner, R. R. Freeman, W. M. Mansfield, A. A. MacDowell, M. L. O'Malley, E. L. Raab, W. T. Silfvast, L. H. Szeto, D. M. Tennant, W. K. Waskiewicz, D. L. White, D. L. Windt, and O. R. Wood, II, and J. H. Bruning, *Proc. of the SPIE* **1263**, 90 (1990).
2. G. D. Kubiak, D. A. Outka, and J. M. Zeigler, *Proc. of the SPIE* **1263**, 272 (1990).
3. G. D. Kubiak, D. A. Outka, C. M. Rohlfing, J. M. Zeigler, W. K. Waskiewicz, and D. L. Windt, *J. Vac. Sci. Technol.* **B8**, 1643 (1990).
4. Prepared by boron diffusion doping of the silicon followed by ethylene diamine pyrocatechol etching and a final reactive ion etch to achieve the desired thickness.
5. H. Windischmann and G. F. Epps, *J. Appl. Phys.* **68**, 5665 (1990).
6. B. L. Henke, J. C. Davis, E. M. Gullikson, and R. C. C. Perera, LBL-26259, UC-411, (1988).
7. D. A. Tichenor, G. D. Kubiak, M. E. Malinowski, R. H. Stulen, S. J. Haney, K. W. Berger, L. A. Brown, J. Bokor, R. R. Freeman, T. E. Jewell, W. M. Mansfield, D. M. Tennant, W. K. Waskiewicz, D. L. White, D. L. Windt, and O. R. Wood, II, these proceedings, paper FC4.
8. D. A. Tichenor, G. D. Kubiak, M. E. Malinowski, R. H. Stulen, S. J. Haney, K. W. Berger, L. A. Brown, J. Bokor, R. R. Freeman, T. E. Jewell, W. M. Mansfield, D. M. Tennant, W. K. Waskiewicz, D. L. White, D. L. Windt, and O. R. Wood, II, *Optics Lett.*, submitted.
9. G. N. Taylor, R. S. Hutton, W. M. Mansfield, D. L. Windt, *Proc. of the SPIE* **1343**, 258 (1990).
10. F. R. Powell, P. W. Vedder, J. F. Lindblom, and S. F. Powell, *Opt. Engin.* **29**, 614 (1990).
11. R. J. Hawryluk, H. I. Smith, A. Soares and A. M. Hawryluk, *J. Appl. Phys.* **46**, 2528 (1975).
12. W. M. Mansfield, J. E. Bjorkholm, R. R. Freeman, A. A. MacDowell, L. H. Szeto, G. N. Taylor, D. M. Tennant, W. K. Waskiewicz, D. L. Windt, D. L. White, O. R. Wood, II, R. M. D'Souza, and A. R. Neureuther, these proceedings, paper ThD4-1.
13. A. H. Perera and J. P. Krusius, *Proc. of the SPIE* **1263**, 297 (1990).



## Effects of Absorption on Resist Performance in Soft-X-Ray Projection Lithography

W. M. Mansfield, J. E. Bjorkholm, A. A. MacDowell,  
R. R. Freeman, L. H. Szeto, G. N. Taylor, D. M. Tennant,  
W. K. Waskiewicz, D. L. Windt, D. L. White, and  
O. R. Wood II

AT&T Bell Laboratories, Holmdel, New Jersey 07733

AD-P007 254



R. M. D'Souza

University of Illinois, Urbana, Illinois 61801

A. R. Neureuther

University of California, Berkeley, California 94720

### ABSTRACT

We measure the lithographic parameters of the positive photoresist, PMMA (poly methyl methacrylate) at exposure wavelengths of 37.5 and 14 nm and use them in a modified version of SAMPLE (simulation and modeling of profiles in lithography and etching) to simulate resist profiles at these wavelengths. We conclude that the most important parameter in determining image quality is the exposure independent soft-x-ray absorption coefficient.

### INTRODUCTION

Soft-x-ray projection lithography (SXRPL) has been proposed as a possible printing technology for the delineation of integrated circuit features below  $0.25\ \mu\text{m}$  [1]. With this technique features as small as  $0.05\ \mu\text{m}$  have been printed in thin layers of PMMA using soft-x-ray radiation near 14 nm [2]. A number of problems arise when printing at any wavelength in the soft-x-ray region (5 to 40 nm) due to the high absorption of the radiation by resist materials. In practice, either resist layers must be thin to allow penetration through to the substrate, a tri-level resist scheme must be used to transfer features from a thin imaging top layer into a thick underlying layer or a surface imaging resist must be used.

In this paper we describe an experimental characterization of the positive photoresist PMMA at 37.5 and 14 nm and present measurements of thickness removed versus exposure dose, lithographic sensitivities, and exposure independent absorption coefficients. In addition, we model SXRPL using a modified version of the optical lithography routine of the SAMPLE simulation program [3]. We find that the smaller exposure independent absorption coefficient in PMMA at 14 nm causes the minimum image feature profile to be of significantly higher quality. We also find that the absorption coefficient of PMMA is the primary determinant of sensitivity and contrast in the soft-x-ray region.

### EXPERIMENTAL PROCEDURE AND RESULTS

The experimental arrangement for producing soft-x-ray exposures and measuring soft-x-ray absorption coefficients is similar to that described in Ref. 2. The source of soft-x-ray radiation was an undulator-equipped beamline at the National Synchrotron Light Source. Exposures at 37.5 nm were done through an  $0.8\ \mu\text{m}$  aluminum filter and an iridium coated Schwarzschild optic; those at 14 nm were done through a  $0.6\ \mu\text{m}$  silicon filter and a multilayer coated Schwarzschild optic. Silicon wafers were spin coated with 496,000 molecular weight PMMA of various thicknesses, ranging from 0.06 to  $0.5\ \mu\text{m}$ . Following exposure to soft-x-ray radiation at various doses the wafers were dip developed at room temperature for one minute in a 30:70 by volume mixture of cellosolve (propylene glycol monoethylether): methanol.

Measurements of thickness removed versus exposure dose at 37.5 nm (circles) and 14 nm (triangles) are shown in Fig. 1. By plotting the fraction of resist remaining in PMMA films of 60 nm initial thickness versus the log of the exposure dose, we explicitly obtained values for the sensitivity (the lowest dose at which the film was completely removed) of  $23\ \text{mJ}/\text{cm}^2$  at 37.5 nm and  $55\ \text{mJ}/\text{cm}^2$  at 14 nm. The corresponding volumetric sensitivity of PMMA was calculated by multiplying these values by the fraction of the incident radiation absorbed and dividing by the thickness of the PMMA layer. The volumetric sensitivity was found to be independent of wavelength and is approximately  $3 \times 10^3\ \text{J}/\text{cm}^3$ . This value is slightly higher than that for exposures by hard x-rays,  $1.8 \times 10^3\ \text{J}/\text{cm}^3$  [4], and that for exposures by 20 keV electrons,  $2.4 \times 10^3\ \text{J}/\text{cm}^3$  [5].

The absorption coefficient for a  $0.6\ \mu\text{m}$  thick silicon membrane at 14 nm was found to be  $1.84 \pm 0.08\ \mu\text{m}^{-1}$ . This value agrees to within 5% of the value calculated using data obtained by Henke [6]. The absorption coefficient for a thin film of PMMA at 14 nm was  $6.2 \pm 1\ \mu\text{m}^{-1}$  as determined by comparing the transmittance

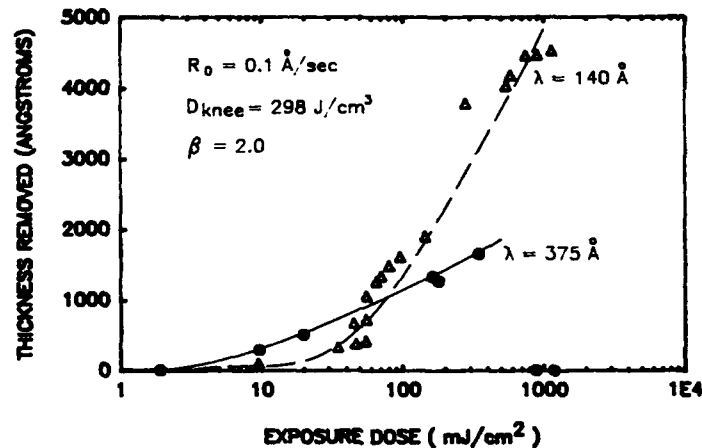


Figure 1. PMMA thickness removed versus exposure dose.

through the PMMA coated silicon membrane to that through a bare matched silicon membrane. This value agrees to within 4% of values calculated using Henke's data [6].

#### MODELING AND DISCUSSION

We have found that we can accurately model SXRPL using a slightly modified version of the SAMPLE simulation program for optical projection lithography, provided that the A, B and C Dill parameters [7] appropriate for PMMA in the soft-x-ray regime are used. The bleachable component of the absorption coefficient, A, is zero for all exposing wavelengths in the soft-x-ray region since absorption in this region is atomic in nature and would not be expected to change significantly as molecular bonds are broken or formed. The non-bleachable absorption coefficient, B, at 14 nm is  $6.2 \mu\text{m}^{-1}$  (calculated using Henke's data [6]). The optical sensitivity parameter, C, at 14 nm is  $0.01 \text{ cm}^2/\text{mJ}$ , as calculated from the experimental sensitivity data. The C parameter at 37.5 nm is  $0.042 \text{ cm}^2/\text{mJ}$  (calculated from the value at 14 nm keeping the ratio of B/C constant because the volumetric sensitivity is a constant).

We replaced the Dill resist dissolution model [7] which relates development rate, R, to inhibitor concentration, M,

with a model for PMMA developed by Neureuther, et al. [8]:  $R = R_0 [1 + D/D_{\text{knee}}]^\beta$  where  $R_0$  is the dissolution rate of unexposed resist in Å/sec., D is the exposing dose in  $\text{J}/\text{cm}^2$ ,  $D_{\text{knee}}$  is the dose at the intercept of the low- and high-dose asymptotes, and  $\beta$  is the asymptotic slope at extremely high doses. The Dill resist dissolution model is not applicable to soft-x-ray exposures in PMMA as there is no photoactive inhibitor present. In the soft-x-ray region dissolution of PMMA is a function of molecular weight changes caused by bond scission and crosslinking.

Our first application of the modified SAMPLE program was to simulate the resist thickness removed versus incident dose data shown in Fig. 1. The triangles (14 nm data) and solid circles (37.5 nm data) are the experimental measurements while the curves are the SAMPLE simulations. Although the functional dependence of thickness removed versus dose is strikingly different at 37.5 and 14 nm, an accurate simulation of the data required only a change in the value of the non-bleachable absorption coefficient, B, at the two wavelengths.

Using the above values for A, B, C,  $R_0$ ,  $D_{\text{knee}}$  and  $\beta$ , the SAMPLE program was then used to model the resist profiles shown in Fig. 2a and b in 60 nm thick layers of PMMA. The sidewall angles are significantly steeper in the resist exposed at 14 nm.

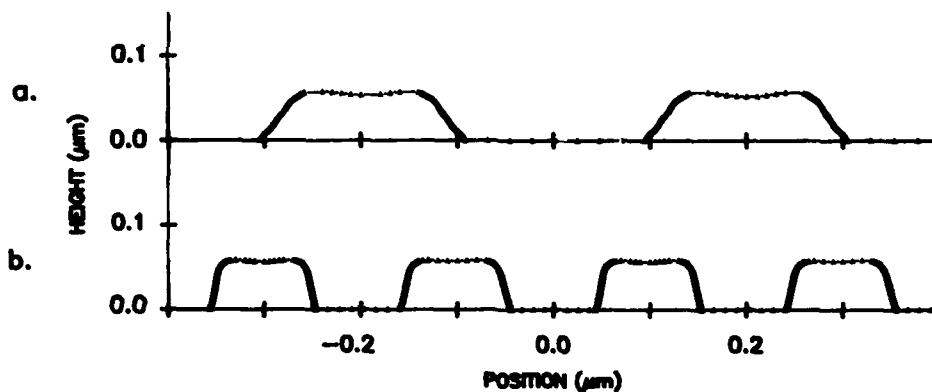


Figure 2. SAMPLE generated PMMA profile of a)  $0.2 \mu\text{m}$  lines and spaces exposed at 37.5 nm and b)  $0.1 \mu\text{m}$  lines and spaces exposed at 14 nm.



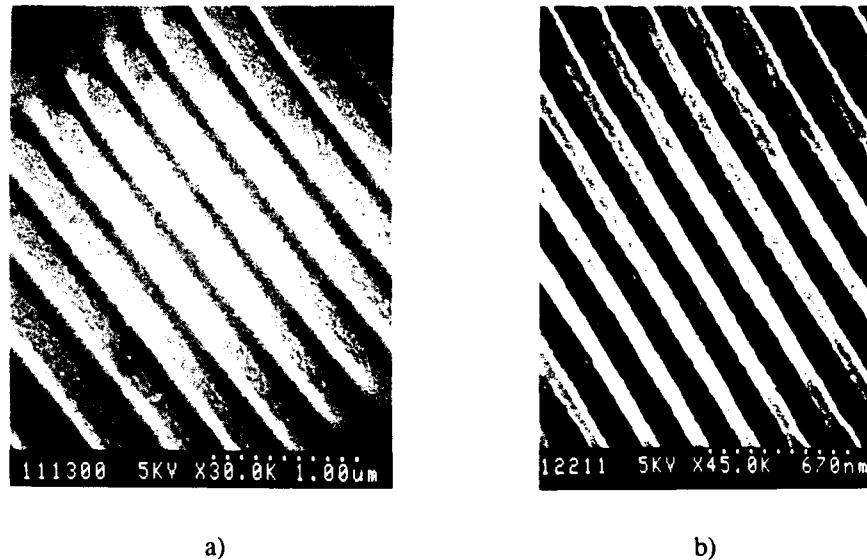


Figure 3. Scanning electron micrographs of 0.6  $\mu\text{m}$  thick films of PMMA for a) 0.2  $\mu\text{m}$  lines and spaces exposed at 37.5 nm and b) 0.1  $\mu\text{m}$  lines and spaces exposed at 14 nm.

We attribute the shallower sidewall slope at 37.5 nm to the higher x-ray absorption at the longer wavelength. The parameter which contributes most to this difference in sidewall slopes is the exposure independent absorption coefficient.

For comparison, scanning electron micrographs of a 0.2  $\mu\text{m}$  line and space pattern in 60 nm of PMMA produced using a 0.113 NA Schwarzschild optic coherently illuminated at 37.5 nm [9] is shown in Fig. 3a and of a 0.1  $\mu\text{m}$  line and space pattern in 60 nm of PMMA produced using a 0.08 NA Schwarzschild optic coherently illuminated at 14 nm [2] is shown in Fig. 3b. Just as in the SAMPLE simulation (Fig. 2a and b) the sidewall angles in resist exposed at 37.5 nm. Based on the excellent quantitative agreement between the SAMPLE simulation and the experimental data shown in Fig. 1 and the good qualitative agreement between the simulations of resist profiles shown in Fig. 3a and b, we claim that the SAMPLE program for optical projection lithography can provide an accurate simulation of the resist profiles produced by soft-x-ray projection lithography.

#### REFERENCES

1. W. T. Silfvast and O. R. Wood, II, *Microelectron. Engin.* 8, 3-11 (1988); A. M. Hawryluk and L. G. Seppala, *J. Vac. Sci. Technol. B* 6, 2162-2166 (1988).
2. J. E. Bjorkholm, et al., *J. Vac. Sci. Technol. B* 8, 1509-1513 (1990).
3. W. G. Oldham, S. N. Nandgaonkar, A. R. Neureuther and M. O. Toole, *IEEE Trans. Electron Devices* ED-26, 717-722 (1979).
4. S. E. Bernacki and H. I. Smith, in *Proc. 6th Int'l Symp. on Electron, Ion and Photo Beams*, ed. R. Bakish (The Electrochem. Soc., Pennington, 1974), pp. 34-46.
5. R. J. Hawryluk, H. I. Smith, A. Soares and A. M. Hawryluk, *J. Appl. Phys.* 46, 2528-2537 (1975).
6. B. L. Henke, J. C. Davis, E. M. Gullikson and R. C. C. Perera, "A preliminary report on x-ray photoabsorption coefficients and atomic scattering factors for 92 elements in the 10-10,000 eV region," Lawrence Berkeley Laboratory Report No. LBL-26259 (1988); G. N. Taylor, R. S. Hutton, D. L. Windt and W. M. Mansfield, *SPIE* 1343, 258-273 (1990).
7. F. H. Dill, W. B. Hornberger, P. S. Hauge and J. M. Shaw, *IEEE Trans. Electron Devices* 22, 445-452 (1975).
8. A. R. Neureuther, D. F. Kyser and C. H. Ting, *IEEE Trans. Electron Devices* ED-26, 686-693 (1979).
9. D. W. Berreman, et al., *Opt. Lett.* 15, 529-531 (1990).

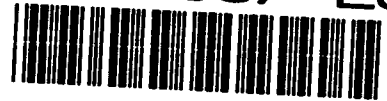
## **Metrology and Characterization**

→

Angstrom-level noncontact profiling of mirrors for soft x-ray lithography

Paul Glenn  
Bauer Associates, Inc.  
177 Worcester Road, Suite 101  
Wellesley, MA 02181  
617-235-8775

AD-P007 255



We have previously described a new noncontacting profilometer with Angstrom-level precision and accuracy<sup>1,2,3</sup>. We have used this instrument to measure a variety of profiles, from diametral scans of steep aspheres to axial and circumferential scans of cylindrical elements. Here we review the theory of operation, show some relevant measurement results, and discuss the upgrades underway that will make the instrument particularly well suited to the exotic mirrors needed for soft X-ray lithography.

Our technique is based on the measurement of test piece curvature along a line, and the double integration of the curvature to obtain a height profile. We measure curvature by differentially measuring the slope at two closely neighboring points. Because of its differential nature, the technique is self-referencing. But, it is self-referencing in a far more important respect than differential height measuring techniques. This is because slope, even when it is obtained differentially, is a relative quantity. Curvature, though, is unique because its value is intrinsic to the test piece. The measurement is thus immune to any drifts in position or angle during the measurement, since such drifts do not affect curvature. This gives accuracies orders of magnitude smaller than the accompanying drifts and scanning errors.

Figure 1 shows the differential measurement of slope. A calcite plate produces two parallel beams of opposite linear polarization. After being reflected by the test piece and focused by the lens, the beams are separated by a polarizing beam splitter, and focused onto separate detectors. The position of the focused spot on each detector is proportional to the slope of the corresponding incident beam. The difference between the sensed positions is thus proportional to the difference in test piece slopes, which is proportional to the test piece curvature. Two important design features incorporated in our design are a steering mirror inside the measurement arm, and a two axis micropositioning stage for one of the two detectors.

The steering mirror is the last optical element encountered by the beams before the test piece. It moves under closed loop electronic servo control so as to keep the focused spots centered on the detectors. This maintains a constant incidence angle on the test piece, and uses the detectors in their best characterized and most accurate regions. Since the steering mirror operates on both beams simultaneously, it maintains the intended viewing geometry, while not degrading (and in fact enhancing) the measurement accuracy. We have demonstrated



steering over a  $\pm 30$  degree range in both directions over a 30 Hz bandwidth. A further benefit of the steering mirror is that it can be used in an open loop mode to find the test piece - i.e., to perform automatic self alignment. We have demonstrated rapid automatic alignment over angles of several degrees.

The two-axis micropositioning stage on one of the detectors is used to accommodate test pieces with a wide range of base radii of curvature, by changing the effective separation between the detectors. The required detector displacement is proportional to the base curvature of the test piece. We can accommodate test piece radii from approximately 20 mm convex to approximately 20 mm concave

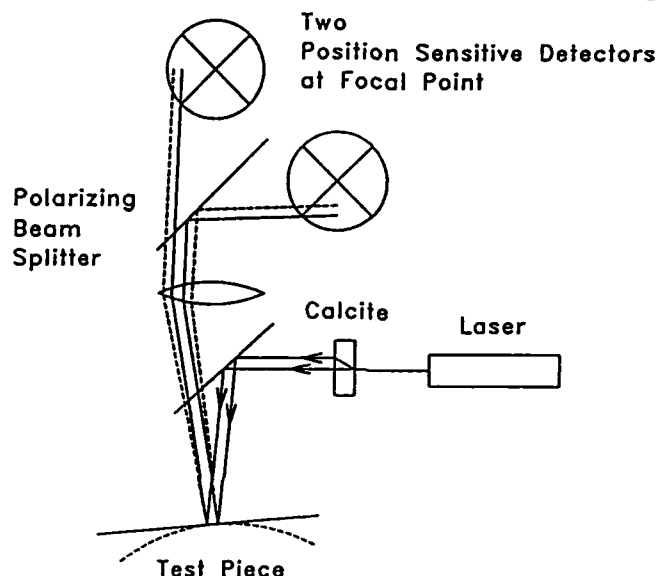


Figure 1. Optical schematic showing the differential measurement of slope at two neighboring points. The difference between spot positions on the detectors is proportional to the local test piece curvature.

An analysis<sup>2</sup> of the Power Spectral Density function (PSD) of the instrument's noise gives the following approximate formula for the band-limited RMS height measurement error for a scan of length  $L$ :

$$\sigma_{\text{height}} = ((h^{1/2} L^{3/2}) / (2 \pi^2 \epsilon^{1/2} d)) \sigma_{\text{slope}}$$

where  $\sigma_{\text{slope}}$  = RMS slope measurement error for each beam,  
 $h$  = spacing between successive curvature measurements,  
 and  $d$  = separation between the two beams on the test piece

A typical accuracy achievement is 6 Angstroms RMS for a scan length of 100 mm.

Figure 2 shows an excellent profile taken of a five inch F-1.4 parabola, typical of what might be required for a soft X-ray lithography application. Note that there are two independent but indistinguishable scans, with RMS surface height estimations of

41.10 and 42.27 Angstroms respectively (after removal of third order spherical aberration). The scan length is 80 mm.

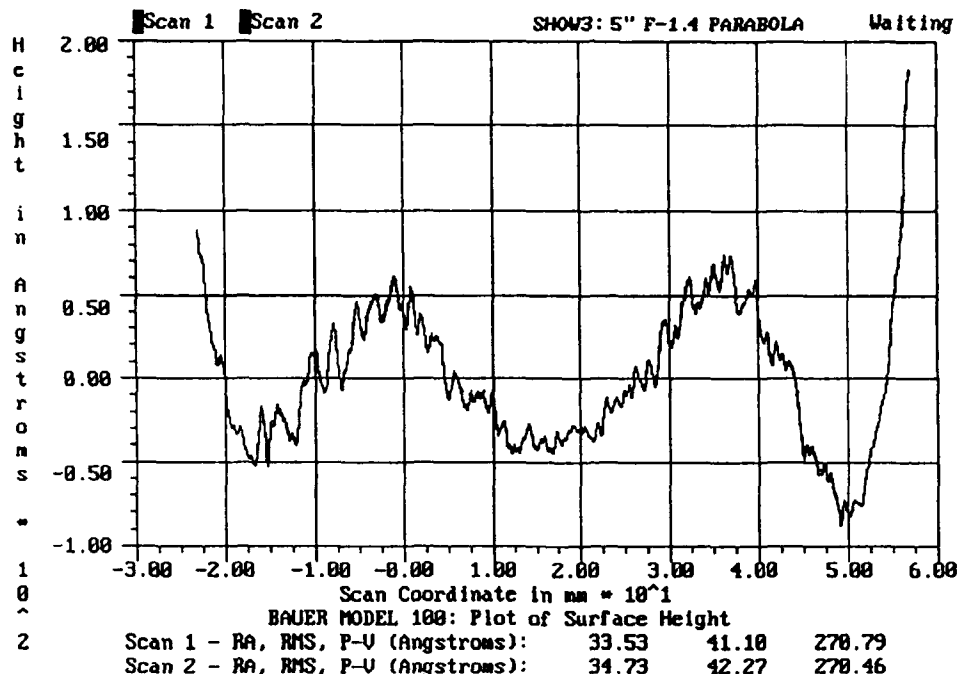
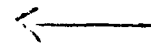


Figure 2. Two scans of a five inch F-1.4 glass parabola.

We are in the process of upgrading the instrument in two important ways to make it able to provide full aperture metrology of steep aspheres, rather than simple line scans. The first upgrade is in hardware, where we are integrating a second translation stage to allow two dimensional scanning. A second calcite plate oriented at right angles to the first can be substituted under computer control to allow the second scanning direction, which can be configured as either an orthogonal linear stage, or a rotary stage. The second upgrade is in software, where we are implementing new algorithms to take full account of the steep angles, large asphericities, and curved scan trajectories on the test piece. We are also implementing the algorithms required to combine the multiple line scans to obtain a full figure profile, and to fit and remove standard functions such as Zernike polynomials.

#### References

1. "Angstrom Level Profilometry for Sub Millimeter to Meter Scale Surface Errors," P. Glenn, Proc. SPIE 1333 (1990)
2. "Robust, Sub Angstrom Level Mid Spatial Frequency Profilometry," P. Glenn, Proc. SPIE 1333 (1990)
3. "Robust, Angstrom Level Circularity Profilometry," P. Glenn, Proc. SPIE 1333 (1990)





## Nonspecular Scattering from X-Ray Multilayer Structures

J. B. Kortright

*Center for X-Ray Optics, Lawrence Berkeley Laboratory, University of California,  
Berkeley, California 94720*

# 92-19512



Measurements of non-specular x-ray scattering from a W/C multilayer structure are presented which demonstrate that in-plane heterogeneities exist in high quality multilayer structures on high quality substrates. Certain features of the non-specular scattering are presented and discussed. The implications of these observations for soft x-ray imaging using multilayer-coated focussing mirrors are discussed.

### Introduction

High specular reflectance of nanometer period multilayer interference structures is the property which enables research into soft x-ray projection lithography, as well as many other applications. Real multilayers are not ideal, but have structural imperfections associated with their interfaces or layers which reduce their specular reflectance and contribute to scattering into non-specular directions. This paper reports on early measurements of non-specular x-ray scattering from a high quality W/C multilayer structure on a high quality substrate, and discusses some of the implications of this non-specular scattering to soft x-ray imaging applications. A more detailed description of these experiments and observations is found in ref. 1.

Figure 1 shows several different hypothetical types of structural imperfections in multilayers which would affect their x-ray reflectance. The ideal multilayer in Fig. 1a would have flat, atomically abrupt interfaces between homogeneous layers of materials A and B. This structure would yield the highest specular reflectance in the first peak obtainable from a multilayer of materials A and B, and no non-specular scattering. Interdiffusion between materials A and B is illustrated in Fig. 1b, where it is depicted to occur in such a way that the structure remains homogeneous

in the x-y plane of the interfaces. This type of intermixing results in a reduced specular reflectance profile, which is essentially the autocorrelation function of the composition profile in the z direction. Figure 1c shows a situation where the local composition gradient across the interfaces is atomically abrupt, but the interfaces are not flat. This structure would exhibit reduced reflectance in the specular direction, in addition to scattering into non-specular directions. Combined interdiffusion and lateral roughness are illustrated in Fig. 1d, and would again result in a reduced specular component and a non-specular com-

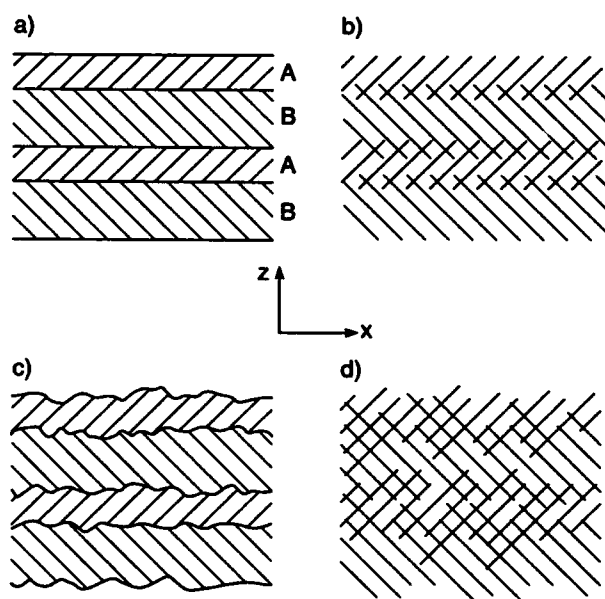


Figure 1. Several hypothetical multilayer structures are shown, illustrating different types of structural imperfections.

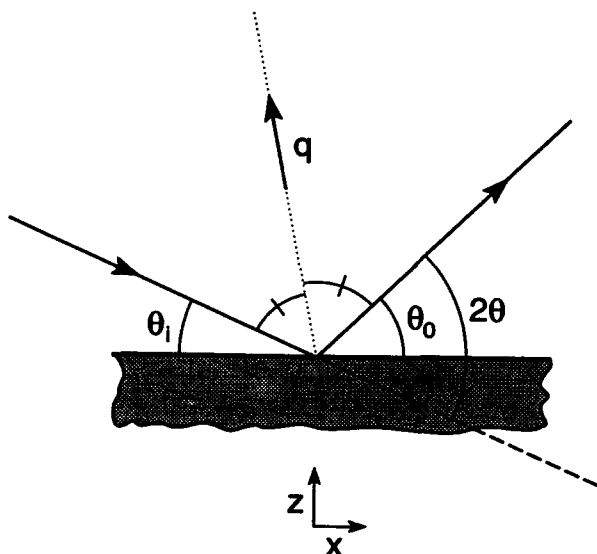


Figure 2. The geometry and angles used to define the scattering vector  $q$  in these scattering measurements.

ponent to the scattering. In general, structural inhomogeneities in the  $x$ - $y$  plane will result in scattering into non-specular directions, accompanied by reduced specular intensity.

In addition to providing a measure of the in-plane structural heterogeneities, the non-specular scattering contributes directly to the point-spread function of the reflective multilayer optic. As such, the magnitude and distribution of the non-specular scattering have an important bearing on the imaging capabilities of multilayer coated optics in the  $x$ -ray region.

Theoretical treatments of the reduction in specular reflectance by imperfections in  $x$ -ray multilayer structures have been developed by several authors [2-6], but the non-specular scattering has received relatively little attention. Several theories have been developed to describe non-specular scattering motivated by multilayer structures for use at longer wavelengths in the visible and ultraviolet [7,8].

### Experiment

Experimental results presented here are confined to scattering from a single tungsten/carbon multilayer. The W/C sample was prepared by magnetron sputtering in 2.5 mtorr Ar to have 40 periods with each period 3.90 nm thick. The substrate was a superpolished fused silica flat, in an effort to minimize any contribution to multilayer imperfections from the substrate. The substrate had rms microroughness of roughly 1 Å over a range of spatial wavelengths ranging from 0.8  $\mu$ m to 0.6 mm as measured by a WYKO optical profilometer, and was flat to better

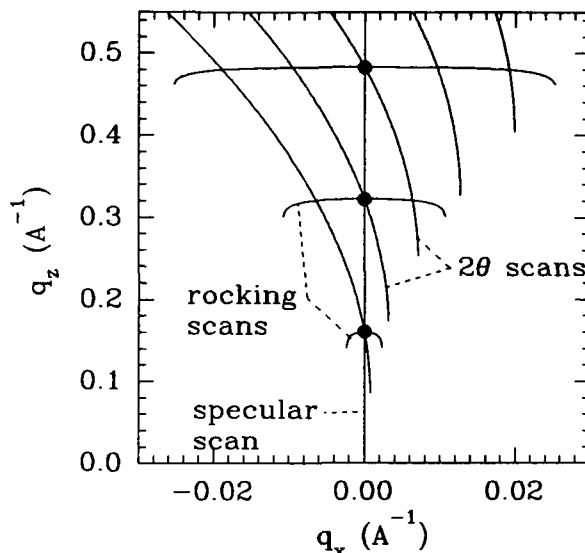


Figure 3. The range of scattering vectors available for measurement of scattering from the W/C multilayer studied here is illustrated by the refraction-corrected scan trajectories through  $q$  space. (from ref. 1).

than  $\lambda/10$  ( $\lambda$  visible). Non-specular intensity features described here were observed from several different multilayers on similar substrates.

X-ray measurements were made using Cu  $K\alpha$  radiation from a 12 kW rotating anode source. A Ge 111 monochromator crystal followed by a slit passing only the  $K\alpha_1$  was used to illuminate the sample with a parallel, high resolution beam. The sample was positioned on the axis of a 2-circle diffractometer with its normal in the scattering plane. A 0.5 mm slit positioned 0.5 m from the sample provided angular resolution in the scattered beam. Reflectance was measured over 8 orders of magnitude. Several types of angular scans were made and are defined in terms of the incidence angle  $\theta_i$ , the observation angle  $\theta_o$ , and the scattering angle  $2\theta = \theta_i + \theta_o$  shown in Figure 2. Whenever  $\theta_i = \theta_o$  the symmetric or specular condition is met, in which the scattering vector  $q$  is directed along the sample normal or the  $z$ -direction. Whenever  $\theta_i \neq \theta_o$ ,  $q$  is directed along a non-specular direction characterized by both a  $q_x$  and a  $q_z$  component. The scattering vector or momentum transfer  $q$  is the appropriate dependent variable with which to measure the specular and non-specular scattering.

The range of scattering vector space available for measurement of non-specular  $x$ -ray scattering from nanometer period multilayer structures is limited by refraction. It is  $q$  inside of the multilayer, not in vacuum or air, that is the quantity of interest as the dependent variable in these measurements. To obtain this  $q$  a refraction correction must be made, as in ref.

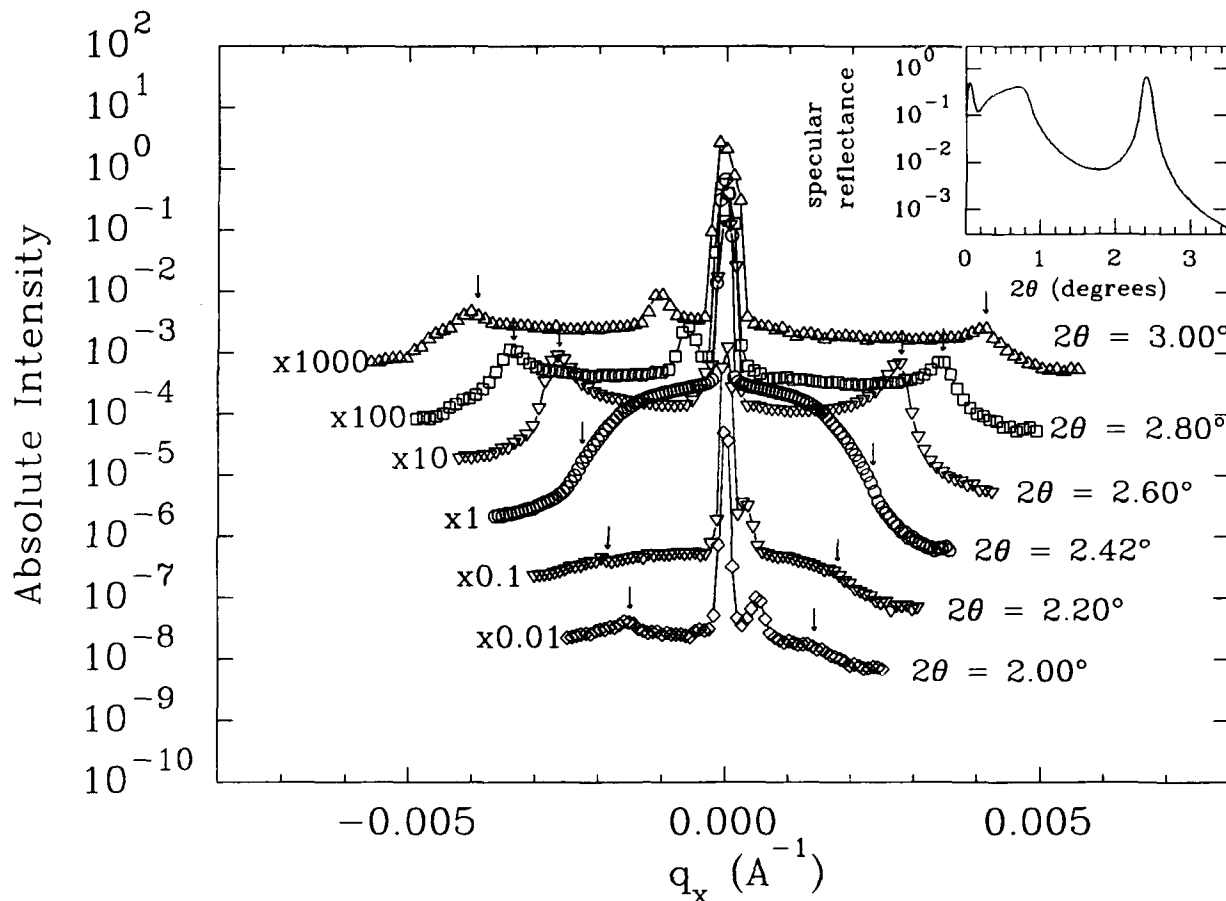


Figure 4. Rocking scans at different  $2\theta$  values near the first order Bragg peak. Different scans are offset by orders of magnitude as noted. Vertical arrows indicate positions in the rocking scans when  $\theta_i$  or  $\theta_o = \theta_c$ . The inset shows the specular reflectance scan near the first peak. (after ref. 1)

1. Refractive effects are especially strong and rapidly varying with angle at the small values of scattering vector near the first order multilayer Bragg peak, and when  $\theta_i$  and  $\theta_o$  are near to the critical angle for total external reflection,  $\theta_c$ . Figure 3 shows the region of refraction-corrected  $q$  space available for measurement, as well as several features within this space. The specular scan corresponds to the straight line at  $q_x = 0$ , and the evenly spaced points along this scan at multiples of  $0.161 \text{ \AA}^{-1}$  correspond to the multilayer Bragg peak orders for this sample having  $d = 39.0 \text{ \AA}$ . The total reflection condition along the specular scan corresponds to  $q_x = 0$ . The additional solid lines in Fig. 3 correspond to rocking and  $2\theta$  scan trajectories which pass through the Bragg points. The endpoints of the rocking and  $2\theta$  scans correspond to the conditions when either  $\theta_i$  or  $\theta_o$  equals  $\theta_c$ , and thus set the limit of  $q_x$  from which scattering can be measured from within the multilayer sample. The range of  $q_x$  available for measurement is proportional to  $q_x^{\frac{1}{2}}$ . At  $q_x$  corresponding to the first order Bragg peak, measurements of non-specular scattering can be made only with  $|q_x| \leq 0.003 \text{ \AA}^{-1}$ , corresponding to

in-plane spatial wavelengths greater than  $2094 \text{ \AA}$ .

### Results

Data were collected by making a scan along the specular direction as well as a series of rocking and  $2\theta$  scans across the available  $q$  space from the origin through the 3rd order multilayer Bragg peak region. A rich variety of different features can be observed (see ref. 1 for details). Here we concentrate on those features near to the first order multilayer Bragg peak, since only these features would contribute unwanted background to normal incidence imaging experiments.

Figure 4 shows a series of rocking scans near the first order multilayer Bragg peak at different  $2\theta$  values. In addition to the specular reflectance peaks at  $q_x = 0$ , several other features are evident in these scans. A featureless, diffuse intensity extends across the entire region of  $q$  space available for measurement. This diffuse intensity becomes stronger relative to the specular intensity as  $q_x$  increases.

The predominant non-specular feature is a region of diffuse intensity centered around the first Bragg peak. In the  $2\theta$  scans in Fig. 4 this region is



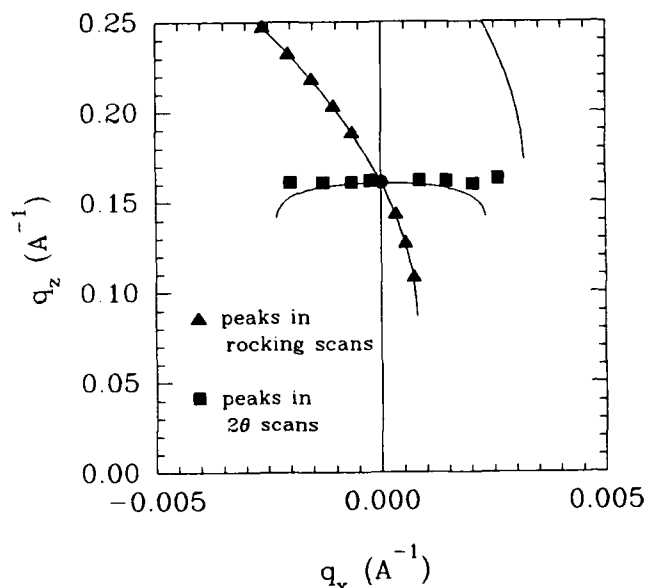


**Figure 5.** Positions of non-specular intensity features in  $q$  space near the first order Bragg peak. Lines are the specular scan and the rocking and  $2\theta$  scans which pass through the first order Bragg peak.

most evident in the scan through the Bragg peak ( $2\theta = 2.42^\circ$ ) as intensity extending across the entire available  $q_x$  range. Rocking scans with  $2\theta > 2.42^\circ$  also show diffuse intensity extending across the entire  $q_x$  range, but with an increase near  $\theta_c$ .  $2\theta$  scans across this predominant diffuse intensity feature show peaks, whose positions in  $q$  space are plotted in Fig. 5, and form a streak along  $q_x$  at constant  $q_z$  corresponding to the first order Bragg peak. The rocking scans in Fig. 4 pass through this diffuse non-specular feature in the curved trajectories shown in Fig. 3. This explains the peaks near  $\theta_c$  in the rocking scans with  $2\theta > 2.42^\circ$ , and the absence of these peaks in rocking scans with  $2\theta < 2.42^\circ$ . Very weak Yoneda features [9] can be seen when  $\theta_i$  or  $\theta_o = \theta_c$  for scans with  $2\theta \leq 2.2^\circ$ .

Another feature in the non-specular intensity near the first order Bragg peak is a small peak which changes position in  $q_x$  in the rocking scans in Fig. 4. The positions of these peaks in the rocking scans in Fig. 4 are plotted in  $q$  space in Fig. 5. These peaks form a ridge of intensity which occurs when  $\theta_i = 2.42^\circ$ , the first order Bragg angle. This feature is interpreted to result from standing wave enhanced scattering [10]. Standing waves are set up within the multilayer structure when the first order reflection is strong, and can increase the electric field amplitude by as much as 2 times. These standing waves enhance intensity from structural inhomogeneities which yield non-specular scattering. The observed ridge has intensity roughly 3 times the diffuse background,

which together with its position at  $\theta_i = 2.42^\circ$ , suggests this standing wave enhanced scattering mechanism.

### Discussion

The observation of non-specular scattering is direct evidence that structural heterogeneities exist in the  $x$ - $y$  plane of the multilayer sample. Near the first peak non-specular scattering is observed across the entire  $q_x$  range available for measurement, which means that spatial wavelengths in the  $x$ - $y$  plane greater than roughly 2000 Å cause this non-specular scattering. The most intense non-specular scattering is at the base of the specular first order peak along  $q_x$ , and is roughly 3 orders of magnitude less than the specular intensity.

The specific nature of the lateral structural inhomogeneities which result in this non-specular scattering is not uniquely revealed by these measurements alone. Any structural imperfection characterized by compositional fluctuations in the  $x$ - $y$  plane would yield non-specular scattering. Imperfections could originate in the substrate, or could be intrinsic to the multilayer itself. Inhomogeneities intrinsic to the multilayer could be localized at the interfaces between the individual W-rich and C-rich layers, such as rough interfaces between two regions of well defined composition as in Fig. 1c. Or they could be the result of inhomogeneous diffusion between the two layers as in Fig. 1d. Alternatively the heterogeneities could be defects within the individual layers, such as grain boundaries, or regions of varying density or composition. The multilayer period of 3.9 nm is of order ten atoms wide, and W/C multilayers with these short periods are known to have highly disordered interatomic arrangements [11,12]. Thus it may be difficult to distinguish between these different types of in-plane heterogeneities. From the available region of  $q$  space near the 1st order Bragg peak it is clear that the measured non-specular scattering results from inhomogeneities with spatial wavelengths several orders greater than the multilayer period.

The in-plane imperfections yielding the non-specular scattering may or may not be correlated from one layer to the next, or may show partial correlation. Perfectly correlated roughness from one layer to the next would be expected to give rise to streaks in the non-specular intensity directed along  $q_x$  at constant  $q_z$ , corresponding to the Bragg peak, as observed [13]. The effect of correlated roughness can be understood by thinking of a multilayer with correlated roughness as a mosaic diffracting structure (analogous to a mosaic crystal) in which the angular spread in the diffracting structure exists in the  $x$ - $y$  plane. This angular spread will give rise to a circular

streak of intensity having the same  $|q|$  as the Bragg peak and centered at  $q = 0$ . In the limited  $q$  range available for measurement, this circular streak would appear straight and directed along  $q_x$ . Thus, the observed streak along  $q_x$  is consistent with correlated roughness. If correlated roughness results in this diffuse streak along  $q_x$ , it is possible that this roughness propagates into the multilayer film from the substrate. However, the extent to which correlated roughness is required for the enhancement of diffuse scattering at  $q_x$  corresponding to the Bragg conditions, as observed here, requires theoretical investigation beyond the scope of this paper. Non-specular scattering is also clearly measured at  $q_x$  values well away from Bragg peaks, so that uncorrelated roughness is evidently also present in this structure.

Non-specular x-ray scattering from multilayers contributes to the point spread function of any multilayer-coated x-ray optic, and hence has important implications for image formation in lithography applications. The measurements reported here are essentially a detailed map of the non-specular scattering in  $q$  space. To relate such measurements to the point spread function in an imaging application, one must consider the angular and spectral distribution of the incident radiation, the specific optical design, and the detector, which together define the range of  $q$  from which non-specular scattering can contribute to the point spread function. In considering compound, multilayer-coated reflective optics of interest in projection x-ray lithography, it is the non-specular scattering from the last multilayer-coated reflector before the image which will make the primary contribution of unwanted components to the point spread function of the system.

### Summary

In summary, measurements of non-specular x-ray scattering from a W/C multilayer provide direct evidence that in-plane structural inhomogeneities contribute to degraded multilayer reflectance performance. Several different features of non-specular scattering can be observed. This non-specular scattering has important implications for normal-incidence imaging experiments utilizing multilayer coated reflecting optics, in addition to being a direct measure of the effect of structural heterogeneities on the reflectance properties of multilayers. As such, measurements of this non-specular scattering will become a useful aid in assessing the structural perfection of multilayers for optical and other applications. Theoretical developments are called for to aid in interpretation of these non-specular features.

### Acknowledgment

This work was supported by the Director, Office of Energy Research, Office of Basic Energy Sciences, Materials Sciences Division, of the U.S. Department of Energy under contract No. AC03-76SF00098.

### References

1. J.B. Kortright, "Non-specular x-ray scattering from multilayer structures," to be published.
2. J.H. Underwood and T.W. Barbee, "Layered synthetic microstructures as Bragg diffractors for x-rays and extreme ultraviolet: theory and predicted performance," *Appl. Opt.*, **20**, 3027-3034 (1981).
3. E. Spiller and A.E. Rosenbluth, "Determination of thickness errors and boundary roughness from the measured performance of a multilayer coating," *Proc. Int. Soc. Opt. Eng.*, **563**, 221-235 (1985).
4. B. Vidal and P. Vincent, "Metallic multilayers for x-rays using classical thin film theory," *Appl. Opt.*, **23**, 1794-1801 (1984).
5. C.K. Carniglia, *Opt. Eng.*, **18**, 104 (1979).
6. D.G. Stearns, "The scattering of x-rays from nonideal multilayer structures," *J. Appl. Phys.*, **65**, 491-506 (1989).
7. J.M. Elson, J.P. Rahn, and J.M. Bennett, "Light scattering from multilayer optics: comparison of theory and experiment," *Appl. Opt.*, **19**, 669-679 (1980).
8. J.M. Eastman, "Scattering by all-dielectric multilayer bandpass filters and mirrors for lasers," in *Physics of Thin Films, Advances in Research and Development*, G. Hass and M.H. Francombe, eds. (Academic Press, New York, 1978), 167-226.
9. Y. Yoneda, "Anomalous surface reflection of x-rays," *Phys. Rev.*, **131**, 2010-2013 (1963).
10. J.B. Kortright and A. Fischer-Colbrie, "Standing wave enhanced scattering from multilayer samples," *J. Appl. Phys.*, **61**, 1130-1133 (1987).
11. J.B. Kortright and J.D. Denlinger, "Tungsten-Carbon multilayer system studied with x-ray scattering," *Mat. Res. Soc. Symp. Proc.*, **103**, 95-100 (1988).
12. T.D. Nguyen, R. Gronsky, and J.B. Kortright, "High resolution electron microscopy study of as-prepared and annealed tungsten-carbon multilayers," *Mat. Res. Soc. Symp. Proc.*, **139**, 357-362 (1989).
13. D.E. Savage, J. Kleiner, N. Schimke, Y.-H. Phang, T. Jankowski, J. Jacobs, R. Kariotis, and M.G. Lagally, "Determination of roughness correlations in multilayer films for x-ray mirrors," *J. Appl. Phys.*, **69**, 1411-1424 (1991).



## National Institute of Standards and Technology Metrology for Soft-X-Ray Multilayer Optics

R. N. Watts, D. L. Ederer, and T. B. Lucatorto

*Physics Laboratory, National Institute of Standards and Technology,  
Gaithersburg, Maryland 20899*

M. Isaacson

*School of Applied and Engineering Physics, Clark Hall, National  
Nanofabrication Facility, Cornell University, Ithaca, New York 14853*

### Abstract

We describe the capabilities of the existing NIST soft X-ray reflectometry program and outline our proposed new characterization facility.

### Introduction

As part of its commitment to support the microelectronics industry, NIST has begun a metrology program aimed at characterizing normal incidence, soft X-ray optical systems for both basic research and industrial applications. At present, this program has two components: the characterization of surface figure (geometric shape) and surface finish (smoothness) and the measurement of XUV reflectivity. In this paper, we will focus our discussion on the existing soft X-ray reflectometer and the work being performed with it, the design characteristics of a new reflectometer that will replace the present instrument, and our plans to build an optical characterization facility based on a quasi-real time, two dimensional, soft X-ray imaging system with an ultimate resolution of a few tens of nanometers.

### NIST Reflectometer

The existing soft X-ray characterization facility has been described in detail elsewhere. [1,2] Briefly though, the reflectometer is composed of a multi-axis sample manipulator having a single axis of

rotation and three orthogonal axes of translation and is attached to the moving exit slit of a 2.2 m grazing incidence grating monochromator. The monochromator is illuminated by the NIST SURF II electron storage ring, a 280-300 MeV device with a peak photon flux between 13 and 15 nm. [3] Both the monochromator movement and the data acquisition are under computer control. The important parameters of the reflectometer/monochromator system are listed in Table 1. Note that it is possible, for a particular measurement on a specific sample, to set special tolerances on some of these parameters, however, optimizing some of these parameters usually results in comprising accuracy or precision in other parameters.

The computer and software controlling the data acquisition have both been upgraded recently and the reflectometer sample stage and detector movement have been motorized so as to make the facility more flexible and more accommodating, both in terms of data taking and in data reduction and display. A motorized facility will allow us greater reproducibility and far greater resolution both in sample placement and sample and detector rotation than is available manually. We are also completing software development that will allow us greater flexibility in determining reflectivity. Currently, we are limited to measuring reflectivity as a function of wavelength for a particular angle of incidence. When the new software is fully operational, we hope to be

Table 1  
Characteristics of the NIST Reflectometers

| Characteristic                      | Present Apparatus   | New Apparatus (Under design) |
|-------------------------------------|---|------------------------------|
| Wavelength Range                    | 8-60 nm   | 4-50 nm                      |
| Resolution at 13 nm                 | 0.2 nm  | 1 - 0.01 nm adjustable       |
| Polarization at sample              | $87 \pm 2$ % s  | 97% s                        |
| Divergence at sample                | 12 mrad x 16 mrad<br>(FWHM horiz x vert as ray traced at 17 nm) | 10 x 10 mrad                 |
| Spot size at sample                 | 2 mm x 2 mm   | variable                     |
| Maximum substrate size              | 11 cm $\phi$  | 15 cm $\phi$                 |
| Maximum area sampled                | 5 cm (h) x 2.5 cm (v)   | 15 cm $\phi$                 |
| Angle of incidence                  | $\pm(3 - 80)^\circ$   | $\pm(1 - 90)^\circ$          |
| Plane of detector                   | s only  | s and p                      |
| Minimum radius of curvature allowed | $\pm 4$ cm  | $\pm 1$ cm                   |

able to scan, in addition to wavelength, angle of incidence, angle of detection, and sample position. We have also installed a XUV silicon photodiode detector in the reflectometer. This has increased the sensitivity of the reflectometer by several orders of magnitude and allows us to measure reflectivities of  $10^{-4}$ .

## Results

This instrument has been used, over the the past year, in a variety of interesting measurements that include measuring the reflectivities of soft X-ray multilayer structures, the transmission of soft X-ray filters, the dosimetry of soft X-ray films, and performing studies of the magnetic properties of the transition metals. One measurement of particular interest involved an intercomparison of the results of our facility with those of the BESSY reflectometry facility in West Berlin. Both laboratories measured a set of multilayer mirrors supplied by Lawrence Livermore National Laboratory, within a one month period, and found the measured reflectivity as a function of wavelength to be virtually identical. This test, we feel, gives an important confirmation to the accuracy of the NIST apparatus.

## Future Plans

We are in the process of designing and constructing a new monochromator/reflectometer beam line at SURF to upgrade and extend our XUV capabilities. The design characteristics of the new

reflectometer are listed in Table 1 and the new system is scheduled for completion in 1992-93. As is obvious, the new reflectometer will be an improvement over the old device in every aspect. We note in particular that this new instrument should be able to reach energies slightly above the carbon edge, the limit imposed by the output of SURF II. In addition, the fixed entrance and exit slit design of the new monochromator should allow a larger, fixed reflectometer chamber which, in turn, should allow larger samples to be examined using more sophisticated measurement methods. The new apparatus will incorporate a higher order filter that should decrease the amount of higher order light present at the sample, the main source of systematic error in the present device. Lastly, we plan to be able to make measurements of reflectivity for both s and p polarized light and to make non-specular, diffuse scattering measurements of the substrate/ multilayer via a sensitive two-dimensional CCD detector.

In addition to characterizing the reflectivity of individual optical components, we intend to develop an optical test bed able to characterize the image forming capabilities and throughput of complete XUV optical systems. The heart of this test bed will be a device we call a "nanodetector". At present, the image forming capability of optical systems producing feature sizes less than  $0.25 \mu\text{m}$  can only be tested by projecting those features onto a resist which is subsequently developed and "read" using an electron microscope. The "nanodetector"

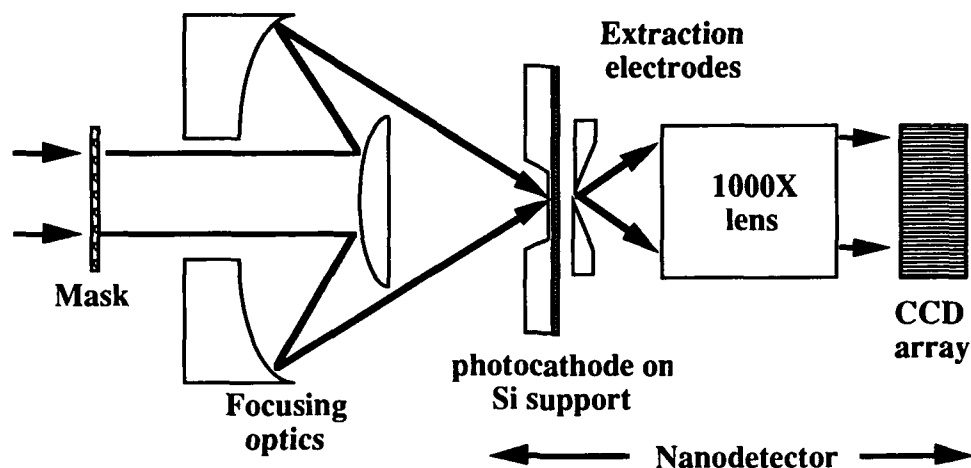


Figure 1. Conceptual design of the "nanodetector"

that we have begun to design is a device that would allow quasi-real time, electronic imaging with 25 nm resolution, thus eliminating the present time consuming and non-interactive approach. In addition such a nanodetector should allow mask inspection and the rapid optimization of focus for complex, multi-element optical systems.

A tentative conceptual design, sketched in Fig. 1, shows the nanodetector being used to check the alignment of a Schwarzschild projection system. Here, an XUV image of a mask is reduced by the optics and projected onto a thin membrane photocathode where it is converted into a photoelectron image. The photoelectrons are accelerated into a 1000X magnifying lens by the extraction electrode and the resulting magnified electron image is projected onto a commercial, thinned, back-side illuminated CCD array with 20  $\mu\text{m}$  pixels. The CCD provides a real time electronic image with one CCD pixel corresponding to a 20 nm feature of the original XUV image at the photocathode.

Two important technical issues must be addressed in our research: optimizing the photoelectron image obtained from the photocathode membrane and providing adequate image brightness. Our preliminary design uses a back-illuminated photocathode with a two-component thin membrane. The first component is a 100 nm thick silicon nitride ( $\text{Si}_3\text{N}_4$ ) membrane several hundred microns in diameter and the second is a 10 nm thick layer of either Cr or Ni. The  $\text{Si}_3\text{N}_4$  layer

would be essentially transparent to the XUV (13 nm radiation for our first device) and would be there to support the thinner metal layer that forms the photocathode. Cr and Ni are both fairly absorbant and would convert most of the XUV photons to photoelectrons which in turn would produce low energy secondary electrons as they travel through the metal. The electrons exiting the film would be primarily these secondaries with an energy spread of several electron volts. The design of the extraction and lens system must account for this energy spread since the lens is not achromatic. Preliminary calculations show that a resolution of 30 nm can be maintained with a 3 eV spread in initial secondary electron energy if we use an overall accelerating voltage of 25kV, a relatively modest value.

## References

1. J. R. Roberts, J. Kerner and E. B. Saloman, "Soft X-Ray Optics Characterization on SURF II", *Physica Scripta* **41**, 9 - 12 (1990).
2. J. Rife and J. Osantowski, "Mirror Reflectivities From 50 - 150 eV", *Nucl. Inst. and Meth.* **172**, 297 - 301 (1980).
3. A. C. Parr and S. Ebner, ed., SURF II Users' Guide (U. S. Department of Commerce, National Institute of Standards and Technology, Gaithersburg, MD 20899).

## Surface Figure Metrology for X-ray Optics

W. Tyler Estler and Chris J. Evans

National Institute of Standards and Technology  
Precision Engineering Division  
Gaithersburg, MD 20899

AD-P007 258



A soft-X-ray projection lithography system will require diffraction limited performance at wavelengths near 13 nm. A typical conceptual design for such a system consists of an x-ray source, a reflecting mask, and a series of normal incidence, multilayer coated mirrors used to image the mask upon a resist-coated wafer. System throughput and image field flatness demands will require aspheric mirrors with figure accuracies of  $\lambda/200$  or better at 633 nm. Commercial phase measuring interferometers (PMIs) offer  $\lambda/1000$  resolution and, with care,  $\lambda/300$  repeatability. For flats and spheres, absolute figure accuracy is limited by one's knowledge of the reference optics, since such PMIs are differential devices. At the National Institute of Standards and Technology (NIST) our present absolute figure uncertainty is about  $\lambda/20$  for flats up to 150 mm in diameter and no better than  $\lambda/10$  or so for spheres. For an asphere, compared with a reference sphere of no more than a few waves of figure departure, we can perhaps attain an absolute accuracy of  $\lambda/5$  or so, but we are fundamentally limited by errors in the interferometer system due to non-common mode optical paths of the test and reference beams.

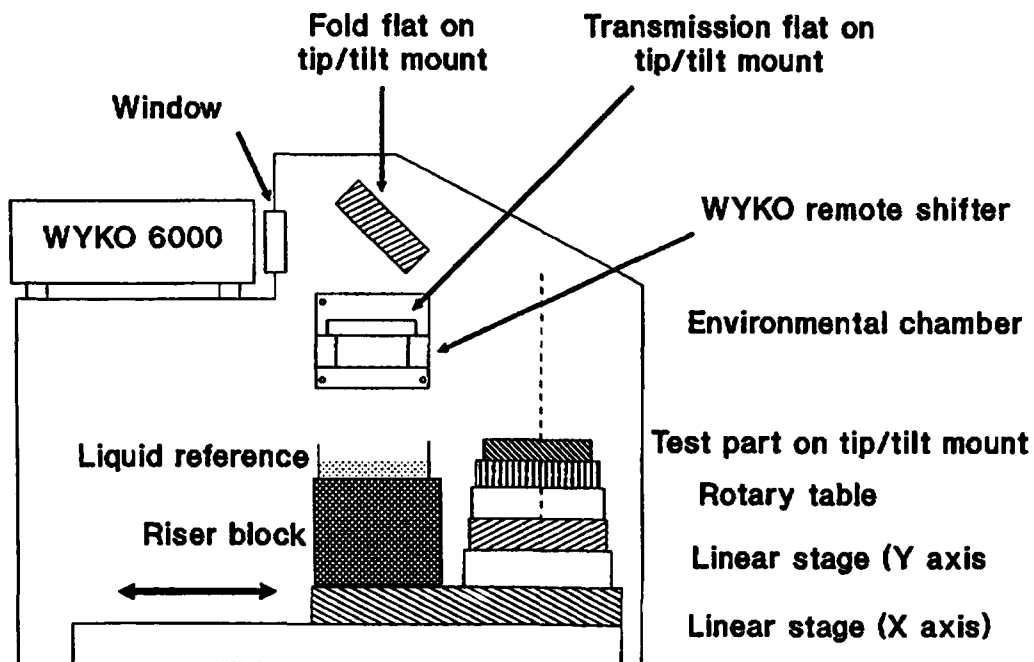
At NIST, we are in the initial phases of a five-year program aimed at improving the accuracy of optical figure measurements as a part of an Institute Competence Program in support of X-ray projection lithography. Our first technical goal is to demonstrate the calibration of an optical flat (150 mm diam.) with an absolute accuracy of  $\lambda/200$  or better. PMI measurements will be referenced to a fluid surface with diameter large enough to avoid meniscus errors. As a useful crosscheck, the same flat will be measured using multi-setup absolute calibration procedures such as the optical analog of the classic Whitworth three-flat test and the methods due to Parks, and Fritz. In the later evolution of our program, spheres and mild aspheres will be measured with reference to ideal parabolae generated by ultrastable rotation of the fluid. We ultimately plan to provide high-accuracy calibration services for PMI reference optics to be used by optical manufacturers for in-process quality control.

In this paper we first describe the program and then present the preliminary results of a small set of experiments designed to explore the systematic errors of a commercial 150 mm aperture PMI system. We have observed a significant system sensitivity to changes in tilt between 150 mm diameter test and reference flats in a short (15 mm) cavity. Peak-to-valley (P-V) and RMS surface errors, with setup tilt removed by the analysis software, are both observed to increase quadratically with increased tilt between the flats. The errors are not symmetric with respect to rotation about the cavity optical axis. We have not developed a quantitative physical model which would explain these effects, but the nature of the residual errors suggests some combination of spherical aberration, coma, and misalignment of the interferometer collimating lens. Qualitatively similar effects have been observed in sphere testing.

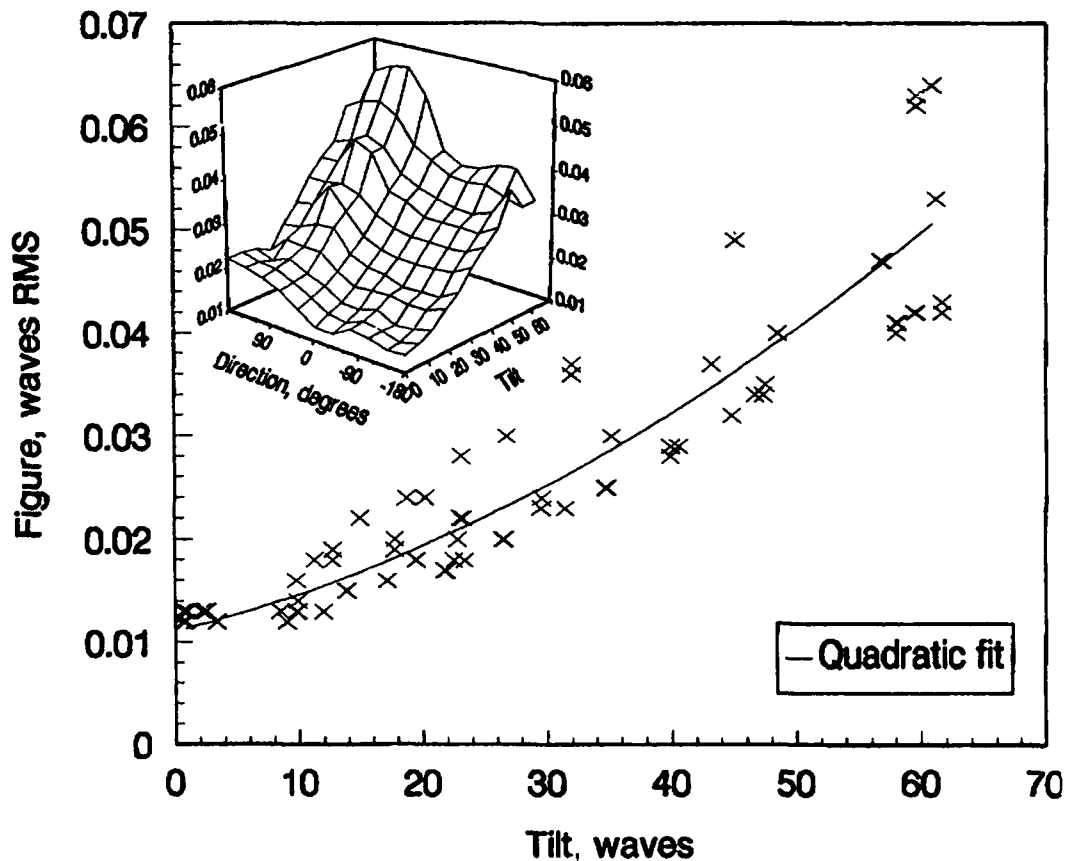
The measured (P-V) figure error is also sensitive to the averaging procedure used when attempting to minimize the effects of air turbulence. For example, if one measures the sample P-V error four times and computes an average, the result is in general larger than when the PMI system is asked to take a series of four measurements and averages the data in the analysis software. A simple model, assuming a Gaussian noise distribution for each detector pixel in the imaging CCD array, provides a plausible explanation of this behavior and serves as a guide for efficient PMI data acquisition.

92-19514





PMI, 150 mm flat, 15 mm cavity, RMS figure vs tilt



# **Proximity X-Ray Lithography**



Proximity X-ray Nanolithography  
by  
Henry I. Smith<sup>(a)</sup>  
and  
M. L. Schattenburg<sup>(b)</sup>  
Massachusetts Institute of Technology  
Cambridge, MA 02139

(a) Department of Electrical Engineering and Computer Science  
(b) MIT Center for Space Research

Summary

The use of x-ray lithography in the fabrication of integrated electronics at 0.5  $\mu\text{m}$  minimum feature sizes, and its extension to 0.1  $\mu\text{m}$  features, is well documented in the technical and popular literature. The primary advantage of x-ray relative to optical-projection lithography in the 0.5 to 0.25  $\mu\text{m}$  range is process latitude, which follows from a high contrast aerial image and absence of coherent scattering (e.g., standing waves). The potential of x-ray lithography in the nanometer domain (i.e., sub-100 nm features) has been appreciated since the late 70's when 18 nm lines and spaces were demonstrated by Flanders [1]. Over the past 5 years, a concerted effort to develop a reliable, manufacturing-compatible technology for sub-100 nm lithography has been pursued at MIT; our motivation being the eventual manufacture of quantum-effect electronic systems. A number of options were considered. Our results indicate that x-ray nanolithography using 1 to 1 masks will meet all the needs of manufacturing down to 50 nm features, and probably also from 50 down to 10 nm. The techniques of x-ray nanolithography will be reviewed and the factors that limit resolution and drive mask architecture described.

A wavelength around 1.3 nm is optimal for features from 100 to 50 nm because the absorber (W or Au) need be only 0.2  $\mu\text{m}$  thick to provide 10 db contrast, and because membranes of Si,  $\text{SiN}_x$  or SiC can be used. Such membranes are extremely strong and clearly compatible with manufacturing. For example, a 1  $\mu\text{m}$ -thick  $\text{SiN}_x$  membrane can sustain more than 1 atmospheric pressure differential across a 20 mm diameter. (We currently use such membranes as vacuum windows.) For linewidths below 50 nm an x-ray wavelength at the carbon edge (4.5 nm) is optimal because the absorber need be only 80 nm thick. The membrane must be carbonaceous (e.g. diamond) and soft contact between membrane and substrate is required to avoid diffraction effects.

Electron-bombardment sources are suitable for research but for manufacturing laser-plasma or synchrotron sources will be required. X-ray masks can be made free of distortion by controlling the absorber stress. Both e-beam and focused-ion-beam techniques have been used to make

AD-P007 259  

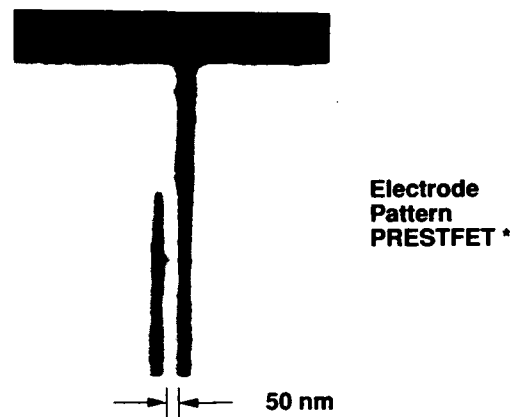



nanolithography masks. Our mask fabrication procedures will be presented and results of exposures and device fabrication shown. Methods of aligning x-ray masks to less than 5 nm have been known for several years and will be described.

[1] D.C. Flanders, Appl. Phys. Lett. 36, 93 (1980).

This work is sponsored by the National Science Foundation, the Joint Services Electronics Program and the National Aeronautics and Space Administration.

### Proximity X-ray Nanolithography



• 50 nm lines and spaces

•  $\lambda = 1.34 \text{ nm}$   $G = 2.72 \text{ }\mu\text{m}$

$$G = \alpha W^2 / \lambda$$

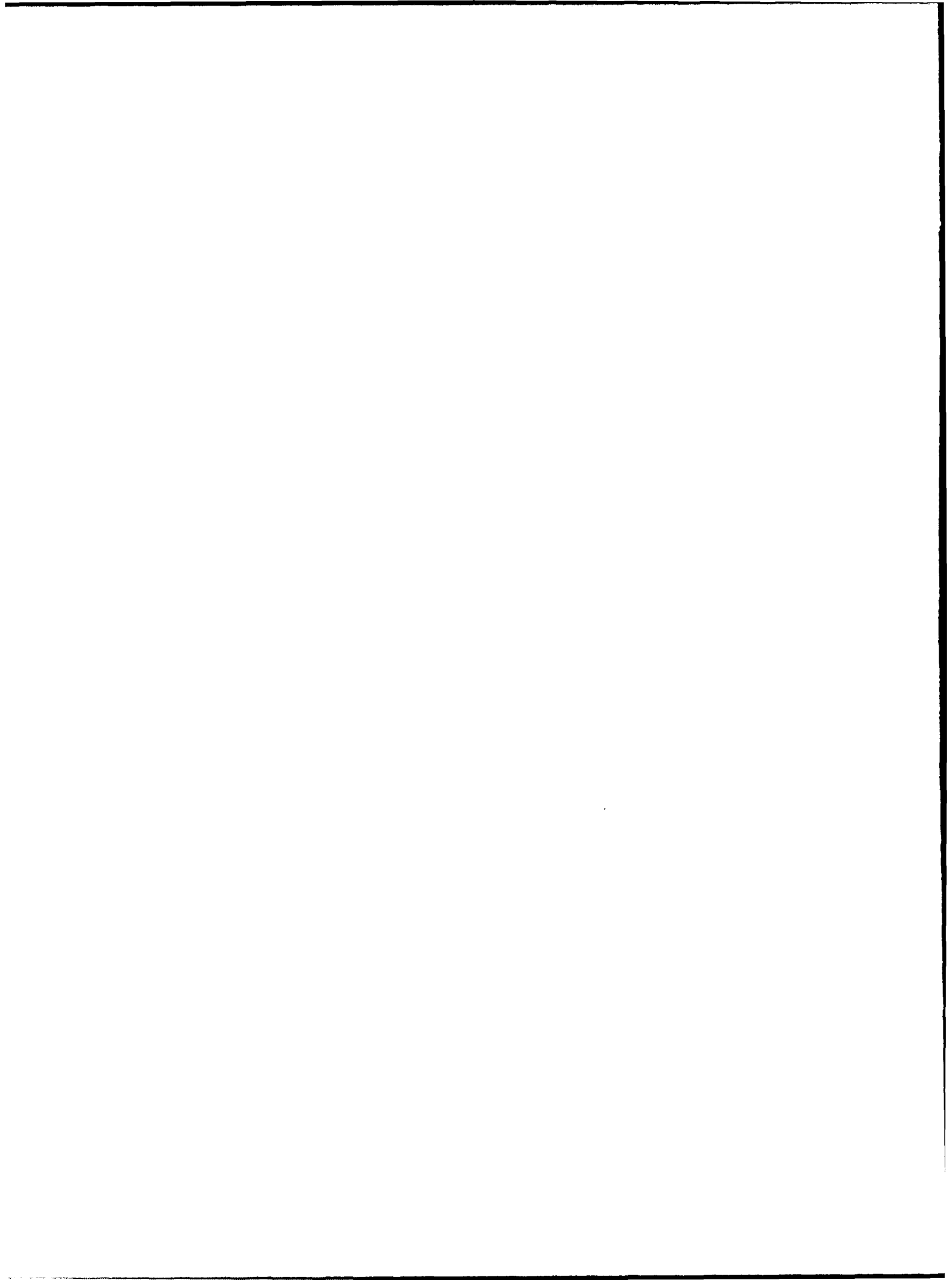
$$\alpha = 1.5$$

• Implication: if  $W = 0.1 \text{ }\mu\text{m}$ ,  $\lambda = 1 \text{ nm}$

$$G = 15 \text{ }\mu\text{m} !$$

\* PRESTFET  $\rightarrow$  Planar Resonant-Tunneling Field-Effect Transistor

Figure 1 is a scanning-electron micrograph of a 100 nm-pitch interdigital electrode pattern (~50 nm nominal linewidth, W) exposed using the  $\text{Cu}_L$  x-ray and mask-to-substrate gap, G, of 2.72  $\mu\text{m}$ . W. Chu et al, to be published Appl. Phys. Lett.



**A**

Attwood, David, 62

**B**

Berger, Kurt W., 54, 76, 124

Bijkerk, F., 51

Bjorkholm, J. E., 2, 54, 97,  
124, 129

Bobroff, Norman, 42

Bokor, J., 2

Brown, L. A., 54

Browning, R., 45

Bruning, J. H., 2

**C**

Ceglio, N. M., 5, 45

Cerjan, C., 72

**D**

Daido, H., 58

D'Souza, R. M., 129

**E**

Economou, N., 45

Ederer, D. L., 142

Eichner, L., 2, 97

Estler, W. Tyler, 145

Evans, Chris J., 145

**F**

Freeman, R. R., 2, 54, 97, 129

**G**

Gaines, D. P., 45

Glenn, Paul, 134

Goodman, Douglas S., 27

Gustafson, T. K., 62

**H**

Haga, T., 11

Haney, S. J., 54

Hartney, Mark A., 120

Harvey, James E., 34

Hawryluk, A. M., 5, 45

Howells, Malcolm R., 108

Hull, R., 82

Hunter, John A., 76

**I**

Isaacson, M., 142

Ishii, Y., 11

Itou, Masaaki, 18

**J**

Jacobsen, Chris, 108

Jewell, Tanya E., 2, 54, 97,  
113

**K**

Kado, M., 58

Kauffman, Robert L., 68

Kensek, Ron, 76

Kinoshita, H., 11

Kitamoto, S., 58

Kneedler, E. M., 124

Koike, Masato, 87

Kortright, J. B., 92, 137

Kubiak, Glenn D., 54, 76, 124

Kurihara, K., 11

**L**

Louis, E., 51

Lucatorto, T. B., 142

**M**

MacDowell, A. A., 2, 97, 129

Malinowski, M. E., 54

Mansfield, W. M., 2, 54, 97,  
124, 129

Mizota, T., 11

Moriyama, Shigeo, 18

Murakami, Katsuhiko, 101

**N**

Nakai, S., 58

Nakamura, Hiroshi, 101

Namioka, Takeshi, 87

Neureuther, A. R., 129

Newnam, Brian E., 30

Nguyen, Khanh, 62

Nikaido, Hideo, 101

**O**

Olson, Richard E., 76

Oshino, Tetsuya, 101

**P**

Pease, R. F., 45

Phillion, Donald W., 45, 68

Puik, E. J., 51

**R**

Rockett, Paul D., 76

Romijn, J., 51

Rosen, M. D., 72

Rosenbluth, Alan E., 42

Rousseuw, B. A. C., 51

**S**

Schattenburg, M. L., 148

Shafer, David, 16

Shealy, David L., 22

Smith, Henry I., 148

Stewart, D., 45

Stulen, R. H., 37, 54, 124

Szeto, L. H., 2, 97, 129

**T**

Takenaka, H., 11

Tanaka, K. A., 58

Taylor, G. N., 129

Tennant, D. M., 2, 54, 97, 129

Terasawa, Tsuneo, 18

Tichenor, D. A., 54

Torii, Y., 11

**V**

van der Drift, E. W. J. M., 51

van der Wiel, M. J., 51

van Dorssen, G. E., 51

Verhoeven, J., 51

Viswanathan, V. K., 22, 30

Voorma, H. -J., 51

**W**

Wang, Cheng, 22

Waskiewicz, W. K., 2, 54, 82,  
97, 129

Watson, R. D., 37

Watts, R. N., 92, 142

White, D. L., 2, 54, 97, 129

Windischmann, H., 124

Windt, David L., 2, 54, 82,  
97, 129

Wood II, O. R., 2, 54, 97, 129

**Y**

Yamamoto, Masaki, 87

Yamanaka, T., 58

Yamashita, K., 58

Yanagihara, Mihiro, 87